Title
Conformational Coordination of Strand Passage by Type IIA and Type IIB Topoisomerases

Author
Wendorff, Timothy John

Publication Date
2017

Peer reviewed|Thesis/dissertation

Conformational Coordination of Strand Passage by Type IIA and Type IIB Topoisomerases

By

Timothy J Wendorff

A dissertation submitted in partial satisfaction of the

requirements for the degree of

Doctor of Philosophy

in

Biophysics

in the

Graduate Division

of the

University of California, Berkeley

Committee in charge:

Professor James M Berger, co-Chair

Professor Andreas Martin, co-Chair

Professor Ahmet Yildiz

Professor Donald Rio

Spring 2017

Abstract
Conformational Coordination of Strand Passage by Type IIA and Type IIB Topoisomerases
by
Timothy J Wendorff
Doctor of Philosophy in Biophysics
University of California, Berkeley
Professors James M. Berger and Andreas Martin, Co-Chairs

Topoisomerases are essential molecular machines that manage physical challenges presented by DNA topology. Life has evolved two classes of enzyme, type IIA and type IIB topoisomerases, which unlink entangled chromosomes by coordinating a complex, ATP-dependent passage of one DNA segment through a transient double strand break generated in a second DNA segment. Both classes share functional modules and an overall mechanism, yet they possess distinct architectures. Type IIA topoisomerases must coordinate transient strand scission with the association and dissociation of three distinct dimer interfaces, whereas type IIB topoisomerases must accomplish the same using only two interfaces. The biophysical basis of communication between these interfaces underlies the action of frontline small-molecule therapeutics which corrupt these concerted movements. To address how type IIA topoisomerases coordinate strand scission with the dimerization status of their unique third interface, I used X-ray crystallography to determine the first structure of the DNA cleavage core of human topoisomerase IIα. Comparative analyses to previously determined structures revealed that the principal site of DNA engagement in type IIA topoisomerases undergoes highly-quantized conformational transitions between distinct binding, cleavage, and drug-inhibited states that correlate with the control of subunit-subunit interactions. Additional consideration of this model in light of an etoposide-inhibited complex of human topoisomerase IIβ suggests possible strategies for developing inhibitors specific to topoisomerase IIα, the primary target of these therapies. To address how type IIB topoisomerases faithfully coordinate strand scission using only two interfaces, I performed biochemical analyses which show that these enzymes actively recognize and utilizes DNA bends and crossings formed in supercoiled DNA to stimulate ATP binding and hydrolysis as a prerequisite for efficient DNA cleavage and strand passage. This finding indicates that binding of two DNA segments preferentially drives the ATP-triggered dimerization, a coordinated action with important ramifications for how both type II topoisomerase machineries control of double-strand break formation.

Table of Contents

Acknowledgements

I first wish to acknowledge the many teachers and mentors who have guided and encouraged me towards pursuit of a doctorate of philosophy in the natural sciences. These include Gerald Gunderson, Julie Jensen, Tim Simon, Jack Markin, and Kathryn Eilert in my early years and secondary education. I wish to thank Robert Erdmann, Justin Shorb, Doug Wiebel, Kerstin Wiss, Patrick Theato, John Moore, and Janet Batzli, who honed my scientific interests while I pursed my bachelor's degree, with particular thanks to Tom Record who nurtured and focused my interest in scientific research in general, and the field of biophysics in specific.

In pursing my doctorate, I first and foremost wish to thank my thesis advisor, James Berger, from whom I have learned a breadth of techniques and depth of intellectual rigor that have fundamentally shaped and defined my approach to science. I also wish to thank Andreas Martin, Ahmet Yildiz and Donald Rio, who have provided great insight, support and direction as members of my thesis committee. I wish to thank the many members and visiting scholars in the Berger laboratory who have helped me out over the years in ways large and small, including Karl Duderstadt, Allesandro Costa, Melania Strechaska, Richard Rymer, Elsa Tretter, Seychelle Vos, Karl Drlica, Art Lyubimov, Kevin Jude, Tim Blower, Iris Hood, Valerie O'Shea, Alexia Miller, Franziska Bleichert, Ernesto Arias-Palomo, Glenn Hauk, Matt Hobson, Joyce Lee, Mathew Parker, Afif Bandak, and Frederic Stanger. In particular, I want to thank fellow lab members Bryan Schmidt, whose mentorship was invaluable for my work pertaining to human topo IIα and for my development as a scientist in general; Tom Murray and Imsang Lee, who provided essential guidance on fluorescence microscopy and FRET based experiments; Kevin Corbett for guidance pertaining to topoisomerase VI, and Michael Lawson, whom in addition to being a valuable colleague has become a dear and irrevocable friend.

A number of collaborators and colleagues have also been invaluable my thesis work, including James Holton and George Meigs of ALS Beamline 8.3.1; Caroline Austin; Louis Fernandes and Paul Lebel from Zev Bryant's laboratory; Laura Nevin and Nick Guydosh from Rachel Green's laboratory; Scott Kuo; Xinxing Yang and Carla Coltharp from Jie Xiao's laboratory; and Boyang Hua and Byoung Choul Kim from Taekjip Ha's laboratory. I thank Teri Pennington and Kate Chase for saving me from the perils of bureaucracy more times than I can count. Lastly, I wish to acknowledge an NSF Graduate Fellowship which funded me through much of my doctorate work.

The friendships I have made during my doctorate work have been invaluable, thank you Vlad Belyy, Mike Souza, Kris Nyquist, Piere Rodriguez, for helping me get through the difficult and fun times!

Lastly and most importantly, I wish to thank my extended family, my sister Emily Wendorff, and my loving parents, Eric and Kathleen Wendorff, who raised me, guided me, and believed in my ability accomplish whatever task I have at hand, even when I have doubted. And finally, I thank Samantha Bomotti, who gives me reason to wake up each morning, and whose love I cherish more than anything else and hold dear to my heart.

Chapter 1—A comparative introduction to type IIA and type IIB topoisomerases

Topoisomerase solve challenges to DNA metabolism generated by the double helix

As the genetic material of all cellular organisms and many viruses, DNA must serve two critical tasks: storing information and providing a template from which to read out that information. The interlinked double helix structure of DNA provides an elegant solution for information preservation and flow, but also poses a physical challenge. When the DNA double helix is bounded, either as a closed circular chromosome in most bacteria and archaea, or as an anchored, higher-order nucleoprotein superstructure (chromatin) in eukaryotes, the number of times both strands of a DNA helix cross each other (the DNA "linking number") cannot change unless one or both of the strands are cut (Bates & Maxwell, 2005; Crick, 1976; White, 1969). This property creates fundamental problems for both transcription and replication machinery (Liu & Wang, 1987; Peter, Ullsperger, Hiasa, Marians, & Cozzarelli, 1998). The simple act of opening the duplex to initiate transcription or replication requires a compensatory over-twisting or writhing of the duplex upon itself in the form of a supercoil. Processive polymerization introduces over-winding (positive supercoiling) in the front of the transcriptional or replicative machinery (**Figure 1.1a-b**), creating a torsional "backpressure" that can stall such processes if not relieved (Brill, DiNardo, Voelkel-Meiman, & Sternglanz, 1987; Khodursky et al., 2000; Mondal et al., 2003). Topological issues also arise behind replicating and transcribing complexes, in the form of compensatory under-winding (negative supercoiling) (**Figure 1.1b**). Superhelical tension causes the replisome to rotate, leading to interlinking daughter chromosomes that physically impede segregation (**Figure 1.1a**).

To address these challenges presented by the double helix, biology has evolved a large and diverse set of enzymes, termed topoisomerases, that change the linking number of DNA in a controlled fashion. To date, five architecturally distinct families of topoisomerases have been identified, which are classified by whether they cleave one (type I) or both (type II) strands of a DNA duplex to modify DNA topology (Forterre, Gribaldo, Gadelle, & Serre, 2007). The three families of type I topoisomerases use two distinct mechanisms to relax DNA. Type IA topoisomerases form or bind to a region of unpaired single strand DNA (ssDNA), cleave it, and pass the complementary ssDNA strand through the gap (Brown & Cozzarelli, 1981; Tse, Kirkegaard, & Wang, 1980). Type IB and Type IC topoisomerases, which are structurally unrelated, use a "swivelase" mechanism where they nick duplex DNA and relax superhelical build-up by controlled rotational diffusion about the intact phosphodiester bond on the uncut strand (Koster, Croquette, Dekker, Shuman, & Dekker, 2005; Slesarev et al., 1993; Taneja, Schnurr, Slesarev, Marko, & Mondragon, 2007). Type II topoisomerases are divided into two architecturally distinct families – type IIA and type IIB – yet both operate by passing one double strand DNA (dsDNA) through a transient, enzyme-mediated double-strand break introduced in a second duplex. Unlike members of nearly all type I topoisomerase families, type II

topoisomerases generally require ATP for strand passage, even when they are performing thermodynamically favorable transactions, such as the relaxation of supercoiled DNA (Bergerat, Gadelle, & Forterre, 1994; Brown & Cozzarelli, 1979; Liu, Liu, & Alberts, 1979; Mizuuchi, Fisher, O'Dea, & Gellert, 1980).

The different mechanisms of DNA segment manipulation used by topoisomerases are well-suited for resolving distinct topological challenges, and partition each family of topoisomerase into specific cellular roles. As type IA topoisomerases utilize a non-paired stretch of ssDNA, they tend to preferentially relax under-wound DNA (Kirkegaard & Wang, 1985; J. C. Wang, 1971). In bacteria these enzymes remove the negative supercoils formed behind transcribing complexes and help to balance superhelical homeostasis (**Figure 1.1b**). Type IA topoisomerases can unlink DNA precatenanes formed by daughter chromosomes before DNA nicks and gaps are filled (DiGate & Marians, 1988); when paired with a helicase, their cellular roles can expand to: 1) unlink hemicatenanes ahead of converging replication forks (Chan, North, & Hickson, 2007; Nurse, Levine, Hassing, & Marians, 2003; Suski & Marians, 2008), 2) resolve double Holliday junctions formed by homologous recombination and repair across all domains of life (**Figure 1.1a,c-d**)(Harmon, DiGate, & Kowalczykowski, 1999; Plank, Wu, & Hsieh, 2006; Wallis, Chrebet, Brodsky, Rolfe, & Rothstein, 1989), and 3) renature melted DNA in hyperthermophilic archaea and bacteria (Confalonieri et al., 1993; Forterre & Gadelle, 2009; Hsieh & Plank, 2006; Kikuchi & Asai, 1984). The swivelase mechanism allows type IB (and likely type IC (Forterre & Gadelle, 2009)) topoisomerases to relax both negative supercoils generated behind transcribing complexes and positive supercoils generated ahead of both replication and transcription machinery in eukaryotes, where they are predominantly found (**Figure 1.1a-b**)(Durand-Dubief, Persson, Norman, Hartsuiker, & Ekwall, 2010; Forterre & Gadelle, 2009; Kim & Wang, 1989). The dsDNA passage mechanism of type II topoisomerases confers a unique ability to unlink catenated and knotted DNA molecules and thereby promote chromosome segregation in all domains of life (Bergerat et al., 1997; Holm, Goto, James, & Botstein, 1985; Zechiedrich & Cozzarelli, 1995). Type II topoisomerases also relax both positive and negative supercoils, and in the case of DNA gyrase can processively introduce negative supercoils, making this class highly functionally versatile (Bergerat et al., 1994; Gellert, Mizuuchi, O'Dea, & Nash, 1976; Goto & Wang, 1982; Kato, Suzuki, & Ikeda, 1992; Liu et al., 1979).

Overview of type II topoisomerases

In terms of phylogenetic distribution and cellular role, the commonalities and differences between type IIA and type IIB topoisomerases at the molecular level are non-trivial. The two families preferentially segregate to different branches of the three domains of life, where they perform similar cellular roles (reviewed in (Forterre et al., 2007; Schoeffler & Berger, 2008)). For instance, the type IIB topoisomerase, topo VI, is the primary archaeal decatenase involved in chromosome segregation, and for most archaea is also believed to be the primary supercoil relaxase (**Figure 1.1a-b**). By contrast, the type IIA family constitutes the principal type II topoisomerase activity in bacteria and eukaryotes. Eukaryotic topoisomerase II (topo II) serves as both a decatenase in chromosome segregation, and aids type IB topoisomerases in relaxing DNA supercoils (**Figure 1.1a-b**)(Brill et al., 1987). Most bacteria encode two type IIA topoisomerases, DNA gyrase and topoisomerase IV (topo IV), and partition

the cellular workload between them; gyrase introduces negative supercoils to help maintain bacterial genomes in an under-wound state, whereas topo IV serves as the primary decatenase for aiding chromosome segregation (**Figure 1.1a-b**) (Zechiedrich & Cozzarelli, 1995). This division of labor is not universal across bacteria, however, as some species employ a single type IIA topoisomerase to accomplish both sets of tasks (Forterre et al., 2007). Moreover, the general phylogenetic distribution of type II topoisomerases is inadequate to describe the true dispersal of the enzyme family. For example, some archaea possess a DNA gyrase of bacterial origin, while certain bacteria possess topo VI. Similarly, plants also possess topo VI, which is required for endoreduplication (a form of DNA replication that is not accompanied by cell division and is used to increase cell size), and the type IIB scaffold has been further coopted into eukaryotes as the meiotic recombination machinery architecture (Bergerat et al., 1997; Hartung et al., 2002; Sugimoto-shirasu, Stacey, Corsar, Roberts, & Mccann, 2002; Yin et al., 2002).

At a molecular level, the type IIA and IIB topoisomerase families share a dyadic symmetry, forming dimers in eukaryotes (Goto, Laipiss, & Wang, 1984; Miller, Liu, & Englund, 1981; Sander & Hsieh, 1983), A_2B_2 heterotetramers in prokaryotes (Bergerat et al., 1994; Kato et al., 1990; Klevan & Wang, 1980), and an $A_2B_2C_2$ heterohexamer in some phage (Liu et al., 1979) (**Figure 1.2a-b**). Both topoisomerase families are composed of a "breakage-reunion region," which introduces double-stranded breaks into DNA (Berger, Gamblin, Harrison, & Wang, 1996; Buhler, Lebbink, Bocs, Ladenstein, & Forterre, 2001; Morais Cabral et al., 1997; Morrison & Cozzarelli, 1979; Nichols, DeAngelis, Keck, & Berger, 1999; Sander & Hsieh, 1983; Tse et al., 1980), and an ATPase region, which coordinates strand passage (Buhler, Gadelle, Forterre, Wang, & Bergerat, 1998; Classen, Olland, & Berger, 2003; Corbett & Berger, 2003, 2005; Gellert et al., 1976; Harkins, Lewis, & Lindsley, 1998; Harkins & Lindsley, 1998; Wigley, Davies, Dodson, Maxwell, & Dodson, 1991). The reciprocal action of these two regions leads to a so-called "two-gate" mechanism (**Figure. 1.3**), in which a dimer related interface present in the breakage-reunion region, termed the "DNA-gate" alternates opening and closing in accord with a dimer interface formed by the ATPase elements (the "N"- or "ATP"-gate) (Mizuuchi et al., 1980; Roca & Wang, 1994; Roca, Berger, Harrison, & Wang, 1996; Roca & Wang, 1992). The DNA gate binds to the prospective DNA duplex to be cleaved, termed the gate or "G"-segment (Dong & Berger, 2007; Roca & Wang, 1992). A second duplex, termed the transport or "T"-segment DNA, can be captured by ATP-gate dimerization, which occurs during nucleotide binding (Ali, Orphanides, & Maxwell, 1995; Corbett & Berger, 2003; Olland & Wang, 1999; Roca & Wang, 1992; Wigley et al., 1991). Both ATP binding and T-segment capture induce cleavage of the G-segment through a metal-dependent reaction that leads to G-segment strand scission and the formation of a covalent phosphotyrosine intermediate between each strand of the G-segment and the two halves of the DNA gate (Baird, Harkins, Morris, & Lindsley, 1999; Buhler et al., 2001; Corbett, Zechiedrich, & Osheroff, 1992; Lindsley & Wang, 1993; Morrison & Cozzarelli, 1979; Schmidt, Burgin, Deweese, Osheroff, & Berger, 2010; Tingey & Maxwell, 1996; Tse et al., 1980). Opening of the G-segment allows for T-segment passage through the DNA gate, inverting the chirality an intramolecular crossing to change DNA supercoiling or altering an intermolecular crossing to promote DNA (de)catenation or (un)knotting (Berger et al., 1996; Brown & Cozzarelli, 1979; Liu, Liu, & Alberts, 1980; Mizuuchi et al., 1980; Morais Cabral et al.,

1997; Roca & Wang, 1994; Williams & Maxwell, 1999). In the case of type IIA topoisomerases, the T-segment passes through an additional C-terminal interface (the "C"-gate) (Roca et al., 1996; Williams & Maxwell, 1999), which is not present in type IIB topoisomerases. The mechanistic role for the third gate is unclear; it may serve as a safety mechanism, or as a means to proofread T-segment passage and promote decatenation over catenation (Martinez-Carcia et al., 2014).

Although DNA strand passage is required for DNA (de)catenation and (un)knotting, this reaction also generates transient double-strand breaks in DNA. These intermediates have the potential to be highly catastrophic to the cell. In considering the enzyme alone, dissociation of all symmetry-related interfaces at this step would prevent religation and transform the topoisomerase into an indiscriminant endonuclease (Bates, Berger, & Maxwell, 2011). In a cellular context, a stalled type II topoisomerase-DNA cleavage intermediate would act as a roadblock to transcription and replication (Arpa, Beardmore, & Liu, 1990; Hiasa, Yousef, & Marians, 1996; Wentzell & Maxwell, 2000; Willmott, Critchlow, Eperon, & Maxwell, 1994). To avoid creating such cytotoxic lesions, type II topoisomerases appear to have evolved various means to both avoid inappropriate dimer interface dissociation and minimize unnecessary DNA cleavage and time spent in the covalent phosphotyrosine intermediate state.

The underlying purpose of ATP hydrolysis in type II topoisomerases is likely to coordinate specific conformational changes and nucleolytic reactions to minimize aberrant DNA cleavage. As yet, a detailed understanding of how cleavage control is physically linked to the ATPase cycle is fragmented. In both type IIA and type IIB enzymes, communication occurs between ATPase and DNA cleavage centers that are separated spatially by ~70Å (Corbett, Benedetti, & Berger, 2007; Papillon et al., 2013; Schmidt, Osheroff, & Berger, 2012). In type IIA enzymes the DNA gate must additionally coordinate with the C-gate, which lies ~50Å away (**Figure 1.2a-b**)(Bax et al., 2010; Fass, Bogden, & Berger, 1999; Laponogov et al., 2009; Schmidt et al., 2010). Beyond communicating gate status within the enzyme, the engagement of T-segment and G-segment DNA likely also serves to influence the coordination needed to prevent potential enzyme stalling. Whether these coordination mechanisms are shared or distinct between the type IIA and type IIB families remains an important unanswered question. Given that the two classes diverge in the breakage reunion domain architecture, it seems likely that the holoenzyme machineries may regulate strand passage by different mechanisms as well.

Structural and mechanistic overview of type IIA topoisomerases

Strand passage coordination in type IIA topoisomerase is dependent upon three functional modules that comprise the ATP- and DNA-gates. The ATP-gate region is composed of a Gyrase, Hsp90, histidine kinase and MutL (GHKL) superfamily ATPase fold (Dutta & Inouye, 2000), coupled to a second, ribosomal protein S5 domain 2-like superfamily fold, termed the "transducer" domain (Murzin, 1995). The GHKL fold is found in a variety of molecular machines, including Hsp90, MutL proteins, histidine kinases for which the fold is in part named, as well as MORC ATPases (Iyer, Abhiman, & Aravind, 2008). ATP binding induces GHKL domain dimerization, with a domain-swap exchange of the extreme N-termini between the two protomers that helps to seal off the ATP binding pocket. ATP binding also induces a

conformational change in the transducer domain, relative to the GHKL fold, which allows a "sensor" lysine on the transducer to engage the γ-phosphate of ATP (**Figure 1.2c**) (Classen et al., 2003; Corbett & Berger, 2003; Lamour, Hoermann, Jeltsch, Oudet, & Moras, 2002; Wei, Ruthenburg, Bechis, & Verdine, 2005; Wigley et al., 1991). Upon ATP hydrolysis and product release, the GHKL domains can dissociate to reset for another cycle (Baird et al., 1999; Corbett & Berger, 2005; Harkins & Lindsley, 1998). In type IIA topoisomerases, a cavity formed by the dimerized GHKL and transducer domains has been proposed to help capture the T-segment (Papillon et al., 2013; Tingey & Maxwell, 1996; Wigley et al., 1991).

The dimeric breakage-reunion region contains two, bipartite nucleolytic centers, in which one protomer of the dimer contributes a Mg^{2+}-ion binding Topoisomerase/Primase (TOPRIM) domain (Aravind, Leipe, & Koonin, 1998; Noble & Maxwell, 2002) to a winged helix domain (WHD) bearing the catalytic tyrosine of the other. The tyrosine, aided by the Mg^{2+}-ion, forms a covalent bond with the 5' scissile phosphate of a G-segment DNA (**Figure. 1.2d**) (Laponogov et al., 2009; Morrison & Cozzarelli, 1979; B.H. Schmidt et al., 2010; Tse et al., 1980). Although ATP promotes DNA cleavage by type IIA topoisomerases, it is not strictly required for strand scission (Gellert, Mizuuchi, O'Dea, Itoh, & Tomizawa, 1977; Kato et al., 1992; Sander & Hsieh, 1983; Sugino, Peebles, Kreuzer, & Cozzarelli, 1977). Interestingly, it is between the TOPRIM and WHD that the two subunits that make up the bacterial heterotetramer split (GyrB and GyrA for DNA gyrase, ParE and ParC for topo IV), not between the ATPase and breakage-reunion region (Brown, Peebles, & Cozzarelli, 1979; Gellert, Fisher, & O'Dea, 1979; Kato et al., 1990). The WHD and TOPRIM domains, in conjunction with a so-called "tower" domain, bind and bend the G-segment by ~150˚ (Dong & Berger, 2007; Hardin et al., 2011; Lee, Dong, & Berger, 2013; Lee et al., 2012).

A third module found in type IIA topoisomerases is a variable C-terminal region (CTR) that imparts homolog specific activities. In certain cases (i.e. yeast topo II), the region appears to have no mechanistic role *in vitro* (Caron, Wayt, & Wang, 1994), and may instead be used for binding DNA recruitment or repair factors ((Chen, Chan, & Hsieh, 2013; Vos, Tretter, Schmidt, & Berger, 2011) provide recent reviews of known eukaryotic topo II interactors). By contrast, the human topo IIα CTR interacts with DNA, imparting a preference for positively supercoiled substrates on the enzyme (McClendon et al., 2008; Seol, Gentry, Osheroff, & Neuman, 2013). The C-terminal domain (CTD) of bacterial gyrase, which forms a β-propeller-type fold not found in eukaryotic topo IIs, positively wraps G-segment DNA to provide a T-segment to the enzyme *in cis*, aiding the unidirectional introduction of negative supercoils during strand passage (Corbett, Shultzaberger, & Berger, 2004; Gellert et al., 1976; Papillon et al., 2013; Reece & Maxwell, 1991). For its part, the CTD of topo IV, which is a degenerate form of the GyrA CTD, is crucial for the preferential engagement positive supercoils and resolution of catenated daughter chromosomes (Corbett, Schoeffler, Thomsen, & Berger, 2005; Hsieh, Farh, Huang, & Chan, 2004; Vos, Lee, & Berger, 2013).

Although the type IIA topoisomerase modules each have a self-contained function, they collectively influence each other through a number of physical mechanisms. For instance, the ATPase domain in eukaryotic topo II can engage with a bent G-segment bound by the DNA gate

(Schmidt et al., 2012). Structures have revealed that the ATPase regions of both topo II and DNA gyrase are offset with respect to the related breakage-reunion region (Papillon et al., 2013; Schmidt et al., 2012), forming a crisscrossed subunit arrangement that may serve as a mechanism to block a newly-transported T-segment from back-tracking through the G-segment. When open, the ATPase region may dock onto the tower domain of the breakage-reunion region in an auto-inhibited pose (Laponogov et al., 2013), and in E. coli gyrase at least, may further bind an autoinhibitory element on GyrA's CTD to control DNA wrapping by this region (Tretter & Berger, 2012). Finally, a coiled-coil pair of α-helices that connect the C-gate to the DNA-gate appear to act like a lever arm to communicate the cleavage status of the G-segment to the C-gate, holding the C-gate shut when DNA is cleaved, and allowing it to open when DNA is intact (Schmidt et al., 2010). Chapter 2 presents a comparative study of the coordinated conformational changes between the DNA- and C-gates that has helped to explain this allosteric communication.

Given their central role in chromosome segregation and cell proliferation, type IIA topoisomerases are important biomedical targets. Interestingly, many anti-topoisomerase therapeutics act by stalling or corrupting both enzyme chemistry and conformational flexion. For instance, novobiocin competes with ATP binding to the GHKL fold to promote ATP-gate monomerization (**Figure 1.3a**, step 2) (Lamour et al., 2002),whereas bisdioxopiperazines bind to the dimerized N-gate interface of eukaryotic topo II to preventing ATP-gate re-opening (**Figure 1.3a**, step 5) (Classen et al., 2003; Roca, Ishidat, Berger, Andoht, & Wang, 1994), Simocyclinone D8 blocks DNA binding, but the compound GSK299423 blocks DNA cleavage **(Figure 1.3a**, step 1 and 3 respectively) (Bax et al., 2010; Edwards et al., 2009). A significant number of small-molecule inhibitors bind to the breakage-reunion domain to halt strand passage while the enzyme is in a covalent cleavage complex, thereby "poisoning" the topoisomerase and turning it into a DNA damaging agent. Medically-relevant compounds include the fluoroquinolone antibiotics (Blower, Williamson, Kerns, & Berger, 2016; Drlica, Hiasa, Kerns, Malik, & Mustaev, 2009; Laponogov et al., 2009), and a suite of anti-cancer drugs, such as etoposide, mAMSA, and doxorubicin (Pommier, Leo, Zhang, & Marchand, 2010; C.-C. Wu et al., 2011). Although some poisons can specifically target bacterial vs. eukaryotic type IIA topoisomerases, there is growing evidence many of these agents exhibit a degree of cross-reactivity (Chan et al., 2015; Hawtin et al., 2010). The shared binding site exploited by the bacterial and eukaryotic type IIA topoisomerase poisons highlights the need for atomic structural information for both gyrase and topo IV bound to antibiotics, and for the human type II topoisomerases bound to chemotherapeutics. This rationale was a primary motivation for determining the first structure of the human topoisomerase IIα breakage-reunion domain presented in Chapter 2, and for performing comparative structural analyses to highlight general mechanisms of how poisons corrupt the normal conformational modes of the DNA gate. The similarities in the etoposide binding pocket between the two human type IIA topoisomerase isoforms, topo IIα and topo IIβ, also have ramifications pertaining to the development of drugs with diminished cross-reactivity between the paralogs.

Structural and mechanistic overview of type IIB topoisomerases

Type IIB topoisomerases share many biochemical and structural features with type IIA topoisomerases. Although they have been less well-studied than their type IIA counterparts, our current understanding of type IIB topoisomerase mechanism has benefited greatly from analyses of their type IIA counterparts. Similar to bacterial type IIA topoisomerases, the type IIB topoisomerase (topo VI) is an A_2B_2 heterotetramer with dyadic symmetry (**Figure 1.2b**) (Bergerat et al., 1997; Corbett & Berger, 2003; Nichols et al., 1999). However, unlike gyrase and topo IV, the topo VI B-subunit (Top6B) is entirely composed of the ATPase region, while the A-subunit (Top6A) forms the complete breakage-reunion element. Like type IIA topoisomerases, Top6B consists of a GHKL ATPase domain and transducer domain which help coordinate strand passage (Bergerat et al., 1997; Corbett & Berger, 2003). Dimerization of the GHKL fold by exchange of Top6B N-termini and γ-phosphate engagement by the sensor loop lysine in the transducer domain are conserved with the type IIA topoisomerases (**Figure 1.2c**) (Corbett & Berger, 2003). Top6A is likely to utilize a nucleolytic chemistry similar to that of type IIA enzymes as well, in which a metal-binding TOPRIM fold and a catalytic tyrosine donated from a dimer-related WHD form a bipartite active site for strand scission (**Figure 1.2b,d**) (Buhler et al., 1998; Nichols et al., 1999).

Although the biochemical properties of type IIB topoisomerases are reminiscent to the type IIA enzymes, some major differences exist. For example, unlike their type IIA counterparts type IIB topoisomerases absolutely require ATP to promote G-segment cleavage (Buhler et al., 1998, 2001). A number of architectural features might account for this difference in the coordination of strand scission. Although the ATPase regions of type IIA and type IIB topoisomerases are homologous, the enzyme classes diverge in two notable ways. First, Top6B contains an auxiliary helix-two-turn-helix (H2TH) domain inserted between its GHKL and transducer folds (**Figure 1.2b**) (Corbett & Berger, 2003). The function of this element is unknown. Second, whereas the C-terminus of the type IIA topoisomerase transducer domain links directly the breakage-reunion region by a flexible linker (Papillon et al., 2013; Schmidt et al., 2012), the type IIB transducer domain lacks such a connection and instead interacts with the cleavage reunion region by protein/protein contacts (Corbett et al., 2007; Graille et al., 2008).

Even larger differences exist between the breakage-reunion domains of type IIA and IIB topoisomerases. Although Top6A retains a WHD and TOPRIM domain, their relative organization in primary sequence space is swapped compared to that type IIA topoisomerases. Accordingly, the catalytic tyrosine in the WHD resides on a different WHD secondary structural element between the two topoisomerase families (Bergerat et al., 1997; Nichols et al., 1999) (**Figure 1.2a-b**). In all structures observed to date, the catalytic tyrosine residues of dimer-apposed Top6A subunits are positioned too far away from the TORPIM metal binding motif to correspond to a DNA cleavage competent configuration (Corbett et al., 2007; Graille et al., 2008; Nichols et al., 1999). It has been proposed the WHD rotates with respect to the TOPRIM domain to cleave DNA, and this rotation would require Top6B dimerization (Buhler et al., 2001; Corbett et al., 2007; Graille et al., 2008). It is curious that topo VI both cleaves DNA more stringently and accomplishes similar cellular roles to type IIA topoisomerases given that it is predicted to lack an extended G-segment binding interface, as well as the C-gate and auxiliary

C-terminal regions that most type IIA topoisomerases require to support activity. The data presented in Chapter 3 address how topo VI accomplishes strand passage, and provides a new and unanticipated model both for G-segment binding by type IIB topoisomerases and for a mechanism as to why Top6B is absolutely required to promote G-segment cleavage.

Understanding how type IIB topoisomerases promote strand scission may also provide insights into a seemingly unrelated biological activity, meiotic recombination. The meiotic recombination protein, Spo11, is homologous to Top6A, and forms double-strand DNA breaks to initiation chromosome crossover (Bergerat et al., 1997; Keeney, Giroux, & Kleckner, 1997). As topo VI requires Top6B and ATP to generate double-strand breaks, it has been long postulated that a similar partner exists for Spo11 (Buhler et al., 1998, 2001); the recent discovery of such a protein (Top6BL in mammals and MTop6B in plants) reveals that this is indeed the case (Robert et al., 2016; Vrielynck et al., 2016). Interestingly, well known partners of Spo11, i.e. Rec102 in yeast and Mei-P22 in flies, also are structurally homologous to the Top6B transducer domain upon reexamination (Robert et al., 2016). Nevertheless, whether Spo11 is truly an ATP dependent endonuclease, why the transducer and helical stalks of Top6B seem to be the most conserved features of Top6B in meiosis, or what might be the roles of other meiotic recombination machinery components without defined homology to Top6B remain unknown. Chapter 3 reveals some insights into the mechanistic role of Top6B in strand passage that address some, though certainly not all, of these questions.

Concluding remarks

Topoisomerases are essential for overcoming the complications of DNA topology. A duplex strand passage mechanism makes type II topoisomerases the most versatile of these enzymes, but requires a dangerous double-strand break intermediate. Decades of study have revealed the biochemical and biophysical activities of the functional modules comprising these molecular machines, but major questions remain as to how they act in concert. Considering type IIA topoisomerases, the studies presented in Chapter 2 of this dissertation address how the dimer interfaces of the type IIA topoisomerase cleavage-reunion domain are coordinated with respect to DNA engagement and cleavage, and suggest a framework for how small molecule poisons corrupt this coordination. Determining the structure of the human topoisomerase IIα breakage-reunion region also provides a useful tool in addressing the biomedical goal of targeting human cancer cells while minimizing off-target poisoning of constitutively expressed human topoisomerase IIβ. By comparison, how type IIB topoisomerases transact strand passage is quite poorly understood. The studies presented in Chapter 3 help fill this gap, providing a new model for how type IIB topoisomerases prevent double strand breaks, and how their mechanisms of conformational coordination differ from their type IIA counterparts.

Figures

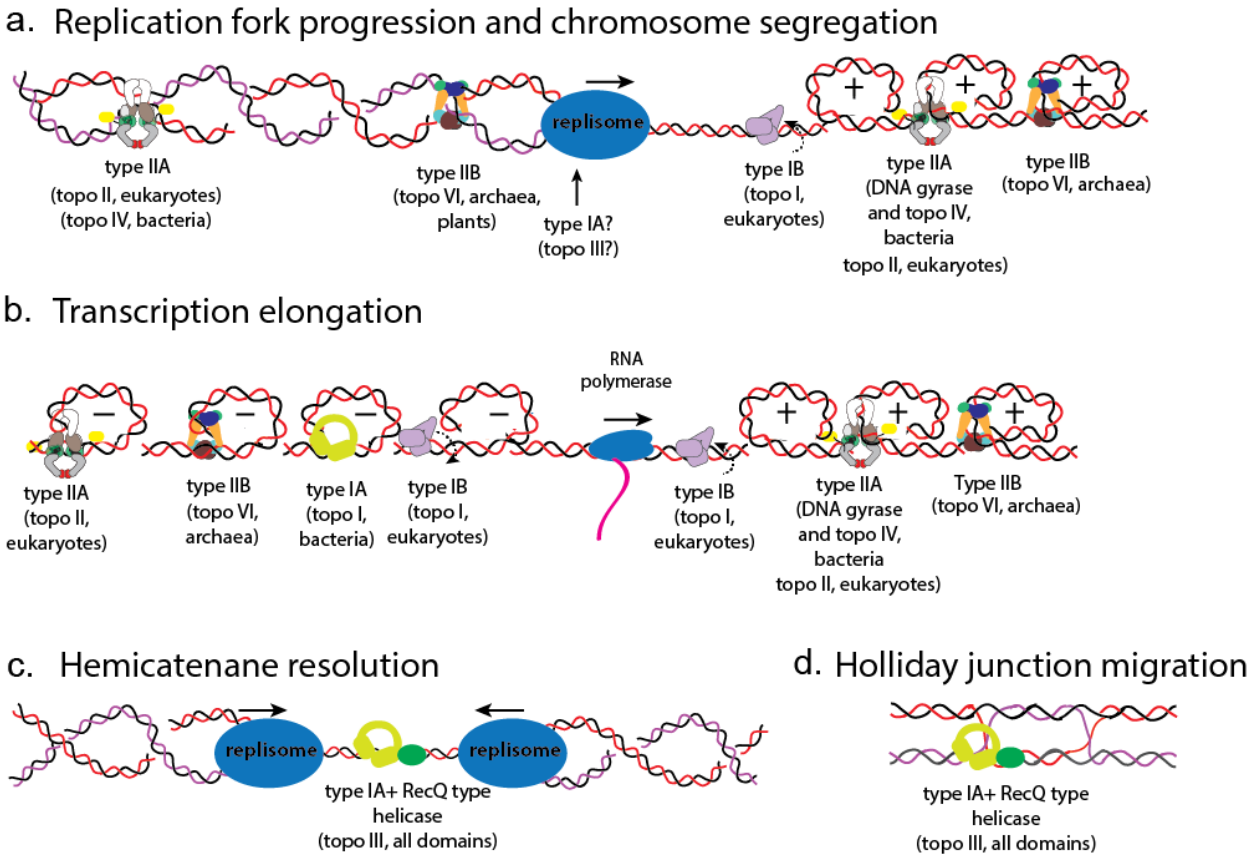

Figure 1.1. Summary of topological challenges generated by DNA metabolism, and the topoisomerases responsible for their resolution.

(**a**) Positive supercoils generated ahead of the replisome are relaxed by type IB topoisomerases with aid from type IIA topoisomerases in eukaryotes, by type IIA topoisomerases in bacteria, and by the type IIB topoisomerases in archaea. Catenated daughter strands are resolved by type IIA topoisomerases resolved in eukaryotes and bacteria, and type IIB topoisomerases in archaea. Type IIB topoisomerases also resolve the interlinked products of endoreduplication in plants. The type IA topoisomerase topo III has been shown to resolve nicked precatenanes *in vitro*.

(**b**) Positive supercoils generated ahead of a transcribing RNA polymerase are resolved by the same topoisomerases that address positive supercoils in replisome progression. Negative supercoils generated behind RNA polymerase are resolved by type IA topoisomerases in bacteria, type IB topoisomerases aided by type IIA topoisomerases in eukaryotes, and by type IIB topoisomerases in archaea.

(**c**) When aided by a RecQ type helicase, the primary role of topo III, a type IA topoisomerase is to resolve hemicatenanes, and (**d**) double Holliday junction products produced by replication repair.

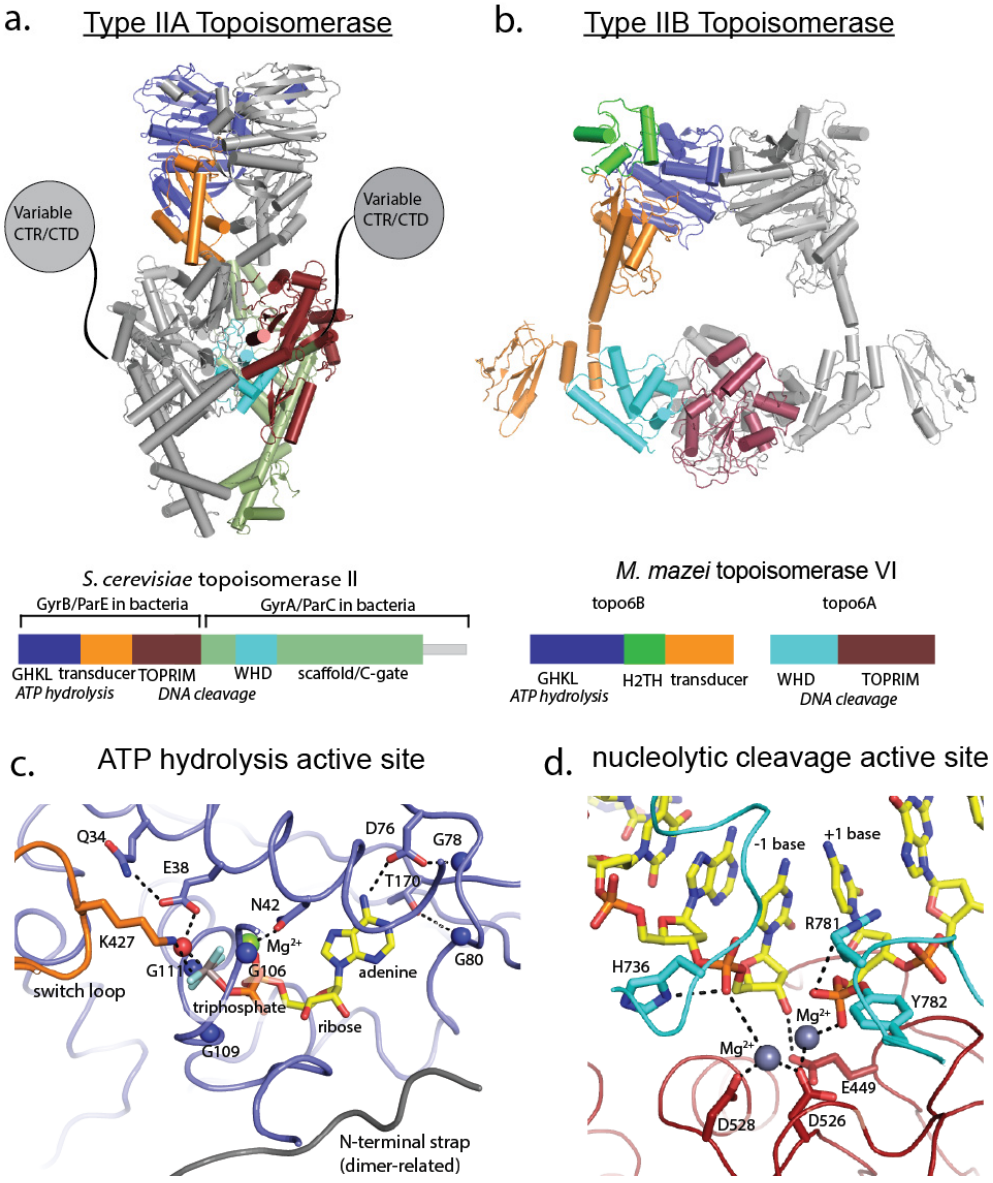

Figure 1.2. Structural comparison between type II topoisomerases.

(**a**) type IIA and (**b**) type IIB topoisomerases both classes show a two-fold symmetry, with each half-enzyme either a single chain (topo II), or a heterodimer (DNA gyrase, topo IV, and topo VI) as noted. Primary structure is shown below an exemplar crystal structure model (*S. cerevisiae* topo II, PDB ID = 4GFH (Schmidt et al., 2012); *M. mazei* topo VI, PDB ID = 2Q2E (Corbett et al., 2007)) for each family, and the variable C-terminal region of the type IIA enzymes depicted by cartoon. Domain name and catalytic function is noted below the primary structure. (**c**) The ATP hydrolysis site is conserved between both families, including an adenine binding pocket(D76, G78, G80), catalytic glutamate (E38, potentiated by Q34), Mg^{2+} binding asparagine (N42), glycine rich triphosphate binding loop(G106, G109, G111) Numbering is for *S. shibatae* topo6B (PDB ID 1Z5B)(Corbett & Berger, 2005). (**d**) Nucleolytic cleavage site in the type IIA

topoisomerase breakage-reunion region. While this intermediate has not been visualized for type IIB topoisomerases, important residues are conserved. Formation of the phosphotyrosine (Y782) 5'-phosphate adduct is potentiated by a conserved arginine (R781) interaction with the +1 base phosphate and a Mg^{2+} cation coordinated by the DxD motif (D526, D528). A conserved glutamate (E449) coordinates the 3' hydroxyl of the -1 base, while a second metal coordinated by the DxD motif and a conserved histidine (H736) coordinate the 5' phosphate of the -1 base. Numbering is for *S. cerevisiae* topo II (PDB ID = 3L4K)(Schmidt et al., 2010).

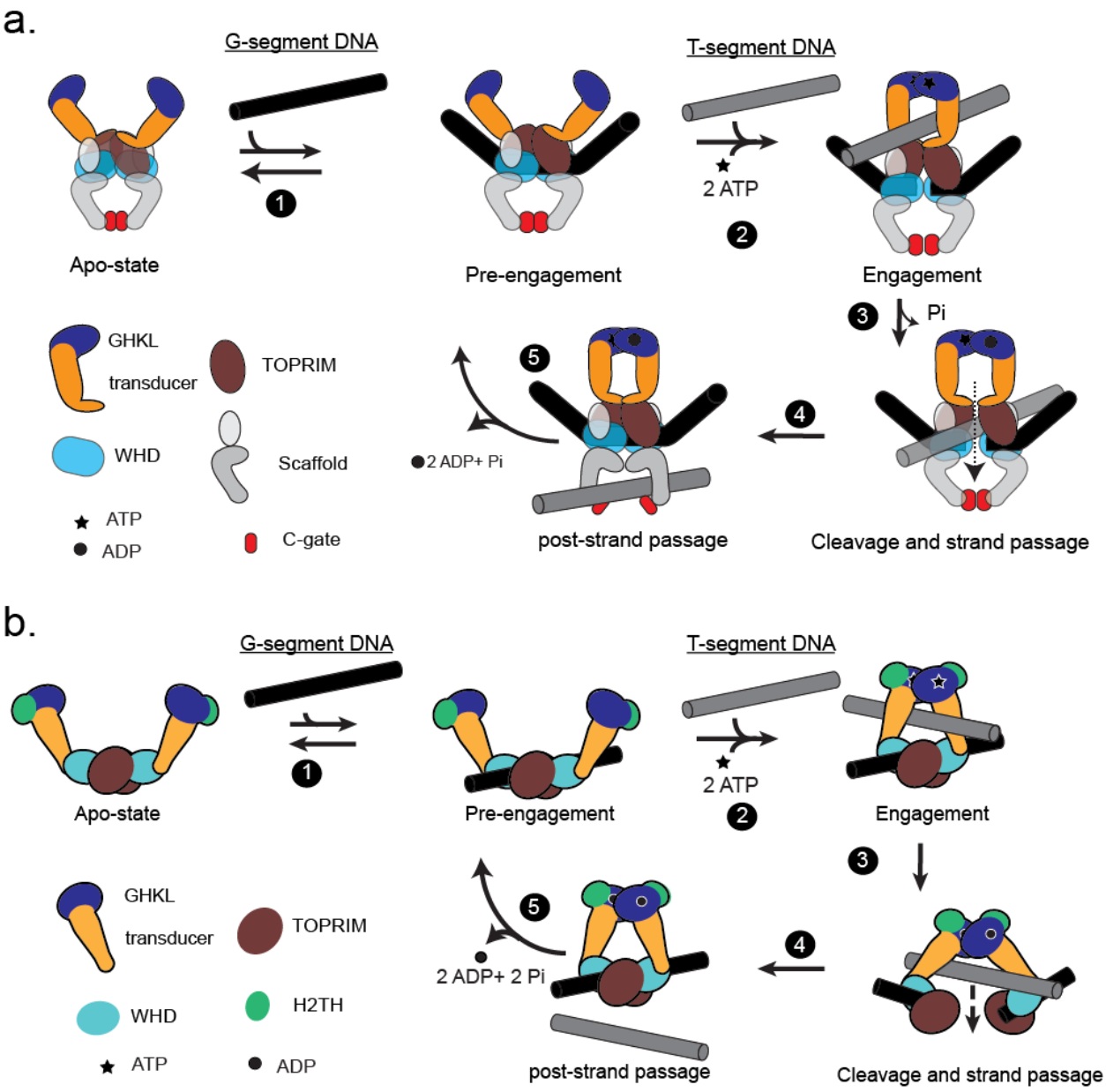

Figure 1.3. Model of the two-gate strand passage mechanism.

For (**a**) type IIA and (**b**) type IIB topoisomerases: (1) the DNA-gate formed by a pair of dimer-related TOPRIM and winged-helix domains bind a G-segment DNA. (2) Binding of two ATP molecules promotes GHKL domain dimerization and capture of a T-segment. (3) In type IIA topoisomerases, hydrolysis of one ATP promotes G-segment cleavage. ATP binding is required for cleavage in type IIB topoisomerases, but the timing of hydrolysis is unknown. (4) The T-segment passes through an open DNA gate, inverting the chirality of the G-segment/T-segment crossing. (5) Release of ADP and Pi cause the GHKL domains to dissociate, resetting the enzyme.

Chapter 2—The structure of DNA-bound human topoisomerase II alpha: conformational mechanisms for coordinating inter-subunit interactions with DNA cleavage

(This chapter has been reproduced from Wendorff TJ, Schmidt B.H, Heslop P., Austin CA, and Berger JM; The Journal of Molecular Biology, 2012).

Introduction

Topoisomerases are essential enzymes that manage the higher-order structural state of DNA. By selectively cleaving, rearranging, and religating DNA strands, topoisomerases can both alter the superhelical state of DNA and help disentangle interlinked chromosomes (Schoeffler & Berger, 2008). Topoisomerases fall into two general categories, termed type I or type II, depending on whether one or both DNA strands of a single duplex are cut during a catalytic cycle, respectively. Although necessary for activity, the DNA breaks generated by topoisomerases can be subverted to give rise to mutagenic or cytotoxic lesions (Deweese & Osheroff, 2009). A variety of small molecule agents capable of inducing such effects have been identified to date, many of which serve as front-line antibiotics or anti-cancer agents (Pommier et al., 2010).

Type II topoisomerases operate by a complex mechanism that involves the controlled association and dissociation of subunit dimerization elements (Roca & Wang, 1994; Roca et al., 1996; Roca & Wang, 1992; Wigley et al., 1991; Williams & Maxwell, 1999). In this reaction, one DNA duplex (termed the "G-segment") is bound and cleaved by the enzyme, while a second double-stranded DNA (the "T-segment") is transported through the break. G-segment breakage is catalyzed by a pair of symmetrically-related tyrosines (Buhler et al., 2001; Morrison & Cozzarelli, 1979; Tse et al., 1980) forming a transient, but covalently-linked, topoisomerase•DNA assembly termed the cleavage complex. Strand passage is typically dependent upon ATP (Baldi, Benedetti, Mattoccia, & Tocchini-Valentini, 1980; Gellert et al., 1976; Goto & Wang, 1982; Liu et al., 1979), a cofactor that not only promotes T-segment capture and stimulates G-segment cleavage, but that also triggers the successive opening and closing of inter-protomer interfaces, or "gates" (Baird et al., 1999; Corbett et al., 2007; Graille et al., 2008; Harkins et al., 1998; Roca & Wang, 1994; Roca et al., 1996; Roca & Wang, 1992). Type IIA topoisomerases, which comprise one of two type II topoisomerase subfamilies found predominantly in bacteria and eukaryotes (Forterre et al., 2007), possess three such regions, termed the ATP-gate, DNA-gate, and C-gate (Bates et al., 2011; Schoeffler & Berger, 2008). Although a general structural framework for type IIA topoisomerase action has been established for some time (Berger et al., 1996), many mechanistic questions, such as the role of metal ions in DNA cleavage, or how specific catalytic events are coordinated with gate actuation, remain ill-defined.

Humans express two type IIA topoisomerase paralogs, or isoforms, termed topoisomerase IIα (TOP2A) (Tsai-Pflugfelder et al., 1988) and topoisomerase IIβ (TOP2B) (Austin

& Fisher, 1990; Chung et al., 1989). Type IIA topoisomerases share significant amino acid sequence homology between species, with the human type II topoisomerases being ~40% identical to *Saccharomyces cerevisiae* topoisomerase II (Top2) (**Fig. S2.1**). Overall, the two human enzymes are 68% identical to each other (Austin et al. 1993), with the catalytic portions of the proteins sharing ~78% identity. TOP2A and TOP2B have different expression patterns in mouse (Capranico, Tinelli, Austin, Fisher, & Zunino, 1992), with TOP2A produced in proliferating tissues and TOP2B expressed more systemically. Expression of both isoforms are cell-cycle dependent; levels for both are highest in dividing cells, but TOP2B is the predominant paralog in non-dividing and post-mitotic cells (Lyu & Wang, 2003; Padget, Pearson, & Austin, 2005; Tsutsui et al., 1993; Tsutsui, Sano, Kikuchi, & Tokunaga, 2001). In general, TOP2A plays a more central role in chromosome segregation and DNA replication (Grue et al., 1998; Niimi, Suka, Harata, Kikuchi, & Mizuno, 2001) whereas TOP2B seems to be involved primarily in transcriptional regulation (Ju et al., 2006; McNamara, Wang, Hanna, & Miller, 2008; Perillo et al., 2008).

Due to its role in cell proliferation, TOP2A expression has been used as a cancer cell marker (Boege, Andersen, Jensen, Zeidler, & Kreipe, 1995; Dingemans, Pinedo, & Giaccone, 1998; Fry et al., 1991; Kasahara et al., 1992). Both human type II topoisomerases are targets of highly effective anticancer drugs such as epipodophyllotoxins (e.g., etoposide); however, in some human patients these agents also increase the likelihood of therapy-related malignancies, such as acute myeloid leukemia (Felix, 1998, 2001; Pedersen-Bjergaard, 2002). Several studies have suggested these secondary cancers may be linked to the undesired action of such drugs on TOP2B (Azarova et al., 2007; Cowell et al., 2012; Haffner et al., 2010; Lyu et al., 2007), raising the possibility that TOP2A-specific inhibitors (e.g., NK314, (Toyoda et al., 2008)) might be useful for improving therapeutic outcomes. One challenge to identifying such compounds arises from the fact that the principal drug-binding locus, the DNA-gate, is one of the most highly-conserved regions between the two enzymes. Structural insights from both drug-bound and drug-free states of DNA-bound TOP2A and TOP2B complexes are ultimately needed to aid efforts aimed at improving specificity. Currently, only an etoposide-inhibited form of the human TOP2B DNA cleavage core has been imaged crystallographically (Wu et al., 2011).

To better understand both type IIA topoisomerase mechanism and identify features that can distinguish between closely related epipodophyllotoxin-binding sites, crystallized and solved the structure of the central catalytic region of human TOP2A bound non-covalently to a doubly-nicked DNA substrate. The complex exhibits the now-canonical DNA bend imparted by type IIA topoisomerase family members (Charvin, Strick, Bensimon, & Croquette, 2005; Dong & Berger, 2007; Hardin et al., 2011; Laponogov et al., 2009; Schmidt et al., 2010; Wohlkonig et al., 2010; Wu et al., 2011), but also fosters comparative studies that provide new insights into how the relative configuration of the active site for DNA cleavage correlates with both metal-ion occupancy and the opening and closing of a distal C-terminal dimer interface. Analysis of the TOP2A structure in light of the etoposide-inhibited state of human TOP2B confirms the close relationship between the two isoforms that favors inhibitor cross-reactivity, while also highlighting two positions in the drug-binding pocket that could serve as differentiating features for developing more selective anti-topoisomerase agents.

Results and Discussion

Overview of the human topoisomerase IIα-DNA complex

As no structure of the human TOP2A DNA binding and cleavage core had been determined previously, we used sequence homology and existing type IIA topoisomerase structures as a guide for constructing a minimal, crystallizable fragment (residues 431-1193, **Figure 2.1a**). This protein was expressed and purified (**Methods**), and subsequently co-crystallized with a duplex DNA 13mer containing complementary 4-base, 5' overhangs (**Figure 2.1b**). Following data collection and phasing by molecular replacement (**Methods**), the resultant electron-density maps readily permitted modeling of the entire DNA substrate and essentially all of the protein (**Figure 2.2a, b**). The final model was refined to 2.9Å resolution with an R_{work}/R_{free} of 22.93/27.44% and excellent stereochemistry (**Table 2.1**).

The TOP2A•DNA complex forms a homodimer (**Figure 2.2c**), in which the two protomers derive from a pair of asymmetric units related by crystal symmetry. One DNA oligo associates with each protomer, forming a doubly-nicked, pseudo-continuous duplex in which the complementary overhangs pair with one another across the molecular dyad. Dimerization at the site of DNA binding (corresponding to the DNA-gate) buries 2560 $Å^2$ of surface area between three elements – a metal-ion binding TOPRIM (TOpoisomerase/PRIMase) domain, a Winged-Helix Domain (WHD) bearing the active site tyrosine, and the "tower" domain – which reside on both halves of the dimer (**Figures 2.1a, 2.2c**). Two isoleucines, one on each protomer (Ile856), intercalate into the minor groove of DNA, together bending the duplex by 130°; additional DNA contacts are manifest by numerous non-specific, electrostatic interactions within the large (~3130 $Å^2$), positively-charged DNA-binding surface of the protein. The degree of bending seen in the structure coincides with that reported for TOP2A by FRET (136±17˚) (Hardin et al., 2011), and with structures of other type IIA topoisomerase•DNA complexes (Dong & Berger, 2007; Laponogov et al., 2010; Schmidt et al., 2010; Wohlkonig et al., 2010).

Within each protomer, a cluster of invariant amino acids forms the active site for DNA cleavage (**Figure 2.2a**). The catalytic tyrosine (Tyr805), responsible for nucleophilic attack on the DNA, resides ~6 Å from the backbone, opposite the nick; the two aspartates (Asp541, Asp543) that form the conserved DxD motif of the TOPRIM region sit nearby, coordinating a single Mg^{2+} ion. A third invariant acidic moiety of the TOPRIM domain, Glu461, hydrogen bonds to the 3' OH of the DNA strand, while Arg804, which ligands the scissile phosphate in covalent cleavage complexes determined for type IIA topoisomerases, coordinates the -1 phosphate in this structure. In general, these contacts comport well with the active-site environments seen in other structures of type IIA topoisomerases complexed with DNA (Bax et al., 2010; Dong & Berger, 2007; Laponogov et al., 2009, 2010; Schmidt et al., 2010; Wohlkonig et al., 2010; Wu et al., 2011).

Implications for inhibition of TOP2A by exogenous agents

Type IIA topoisomerases are targets of both small-molecule inhibitors and post-translational regulatory events that can alter enzyme activity. The structure of the TOP2A•DNA complex affords a new understanding of two such strategies. One is SUMOylation, which

recently has emerged as an important, albeit poorly understood, modification of topo II (Bachant, Alcasabas, Blat, Kleckner, & Elledge, 2002; Dawlaty et al., 2008). Most post-translational modification sites, SUMOylation loci included (Lee & Bachant, 2009), reside in the highly divergent C-terminal region of eukaryotic type IIA topoisomerases. However, a recent study found that a catalytic core residue, Lys660 of *Xenopus laevis* TOP2A, could be SUMOylated by **P**rotein **I**nhibitor of **A**ctivated **S**TAT-**g**amma (PIAS-γ), resulting in loss of decatenation activity (Ryu, Furuta, Kirkpatrick, Gygi, & Azuma, 2010). In human TOP2A, this residue (Lys662) is directly involved in binding G-segment DNA (**Figure. S2.2**). This contact indicates that SUMOylation likely inhibits TOP2A by interfering with G-segment binding, or by preventing the TOPRIM domain from properly forming a functional DNA-gate. Curiously, SUMOylation of *Xenopus* TOP2A *in vitro* was observed only in the presence of DNA, even though the reactive lysine is buried in the DNA binding interface. Moreover, Lys662 does not reside in a typical ϕ-K-X-E/D SUMOylation target motif (where ϕ is a hydrophobic residue) recognized by the *Xenopus* or human enzyme (Hay, 2005; Rodriguez, Dargemont, & Hay, 2001). These peculiarities suggest PIASγ may be SUMOylating Lys662 in an unusual fashion, perhaps capturing a state of the enzyme where the G-segment binding site has undergone a marked rearrangement from the conformations seen crystallographically.

Our TOP2A model also provides useful insights into epipodophyllotoxin inhibition, particularly with respect to efforts aimed at engineering compounds that discriminate between the two human isoforms. A recent landmark structure of human TOP2B in complex with etoposide establishes the binding pocket and modality for this class of topoisomerase II poisons (Wu et al., 2011). This pocket is solvent accessible in our TOP2A structure, but insufficiently large to accommodate drug. In TOP2B the expanded pocket derives from changes in global protein conformation: association of the relatively non-planar compound alters the disposition of the two WHDs in the dimer interface with respect to each other, deforming the DNA and pushing each TOPRIM domain away from the WHD of its partner protomer. These observed structural changes comprise rigid-body, *en bloc* movements between the WHDs and TOPRIM domains in the dimer, suggesting that following DNA cleavage, drug binding occurs during transient opening or breathing of the DNA-gate.

To investigate how etoposide might interact with human TOP2A, we individually superposed both the WHD and TOPRIM domain from our structure onto that of TOP2B. A single superposition using both domains simultaneously was not feasible due to the aforementioned conformational changes in the region (**Figure 2.3a**); however, the backbones of both domains individually align well with those of TOP2B (WHD Cα RMSD =0.70Å, TOPRIM Cα RMSD = 0.51Å). Of the four TOP2B residues that make side-chain contacts with the drug, the only residue that is different in the corresponding TOP2A binding site is the substitution of a methionine (Met762) for glutamine (Gln778 in TOP2B) (**Figure 2.3b, c**). The sulfur atom in methionine is unlikely to participate in the hydrogen-bonding interaction seen to occur between the glutamine amide of TOP2B and the O12 moiety on the "D" ring of etoposide. Nevertheless, etoposide is known to act *in vitro* against both human paralogs (Gentry et al., 2011), and targets both proteins in cells (Bandele & Osheroff, 2008; Willmore, Frank, Padget, Tilby, & Austin, 1998). Since Gln778

adopts two conformations in the TOP2B structure (Wu et al., 2011), its observed contacts with etoposide likely are not crucial for inhibitor activity.

A comparison of the two structures suggests a few possible avenues by which etoposide might be modified to better discriminate between TOP2A and TOP2B. Adding different substituents to the lactone group of etoposide to take advantage of the different chemistries, steric bulk, and rotamer preferences of glutamine *vs.* methionine could constitute one approach. The reactivity of methionine might also be exploited, for instance through platinum conjugates (Dedon & Borch, 1987; Fuertes, Alonso, & Pérez, 2003), to select for TOP2A reactivity. Our modeling suggests that the glycosidic moiety on the etoposide "C" ring is another possible candidate for modification (**Figure 2.3c**). In the TOP2B complex, this group resides within a large binding pocket on the enzyme, but makes few contacts with the protein surface. NMR studies have corroborated this paucity of contacts (Bender et al., 2009), and removal of the sugar is known to cause little change in drug activity *in vitro* (Bender et al., 2009; Wilstermann et al., 2007). Comparison of this region between human TOP2A and TOP2B reveals a single point difference between the two isoforms, with Ser800 of TOP2A replacing Ala816 of TOP2B (**Figure 2.3c**). This substitution suggests that the addition of a hydrogen-bonding or serine-reactive extension to the 8'' carbon position of the glycosidic group of etoposide might be useful for increasing TOP2A selectivity. Interestingly, teniposide, an etoposide analog that shows a 4-fold greater inhibitor effect against TOP2A as compared with TOP2B *in vitro* (Drake et al., 1989) may already employ such an approach: teniposide possesses a thienyl sulfur in lieu of the methyl group found on etoposide's glycosidic C-ring, which modeling suggests could make van der Waals contacts with Ser800.

Distinguishing features between TOP2A and other eukaryotic type II topoisomerases

Outside of the active site, various structures have captured a range of conformational states for the DNA binding and cleavage core of type IIA topoisomerases as a whole. Our present TOP2A model bears greatest resemblance to a noncovalent complex between a doubly-nicked, duplex DNA and the corresponding region of *Saccharomyces cerevisiae* topoisomerase II (**Figure 2.4a**) (Dong & Berger, 2007). Both models retain a closed DNA-gate, and exhibit similar DNA-bend angles and catalytic-tyrosine positions relative to the DNA backbone. More strikingly, the C-terminal dimerization interface that regulates DNA transport through type IIA topoisomerases (the "C-gate") is separated in both structures.

Aside from single amino-acid substitutions, the most significant differences between human TOP2A and yeast Top2 map to two regions of secondary structure. One is an insertion in helix α11 (residues 670-686 of human TOP2A, **Fig. S2.1**) of the three-helix bundle that both connects the TOPRIM domain to the WHD, and forms part of the DNA binding interface (**Figure 2.4b**). This insertion packs against a flexible "Greek-key" element, which constitutes a distinct augmentation to the TOPRIM fold of type IIA topoisomerases, pinning this subdomain against the WHD of the partner subunit. The second difference maps to the C-gate (**Figure 2.4c**), where a short α-helix in human TOP2A (residues 1086-1092) replaces a β-hairpin in the yeast model, thereby forming an interface with one of the two long α-helical arms (residues 1015-1060) that

extend from the DNA-gate. The functional significance of these modifications, if any, is not known at present.

By contrast to these respective similarities and differences with yeast Top2, the human TOP2A•DNA complex is more akin to human TOP2B in terms of local structure, but distinct insofar as global conformation. Like TOP2A, TOP2B contains the extended helix in the three-helix bundle between the TOPRIM and WHD, as well as the extra helix near the C-gate. However, the TOPRIM-associated Greek-key domain is not visible in the TOP2B structure, despite the high resolution of the model (2.2 Å) (Wu et al., 2011). This element may be disordered in TOP2B due to natural substitutions of Tyr684 for phenylalanine and Thr689 for alanine, which together would abrogate interactions between the α11 extension and the Greek-key motif seen in TOP2A (**Figure 2.4b**). Alternatively, this subdomain may become disordered due to conformational differences in the DNA-gate between the two enzymes. In particular, in accommodating etoposide, the TOPRIM domain of TOP2B is rotated by ~7˚ toward the dimer interface compared to TOP2A (**Figure 2.3a**), concomitant with a lateral displacement of ~3Å between its dyad-related WHDs. This movement leads the DNA-gate to crack open, decreasing the buried surface area in this region of TOP2B by ~2000Å^2. Even more strikingly, the C-gate of TOP2B is fully dimerized, compared to the separated, or "open", state seen in TOP2A (**Figure 2.3a**).

Inter-subunit conformational states correlate with DNA cleavage status

The TOP2A•DNA complex presented here joins a growing number of structures for the DNA binding and cleavage core of type IIA topoisomerases. This collection in turn provides a wealth of data for comparative analyses. While considering our TOP2A model in light of these related systems, we noted that the majority of structures (22 out of 25) retained an associated, or "closed", C-gate (Bax et al., 2010; Berger et al., 1996; Corbett et al., 2005; Fass et al., 1999; Laponogov et al., 2007, 2009, 2010; Morais Cabral et al., 1997; Schmidt et al., 2010; Schoeffler, May, & Berger, 2010; Tretter, Schoeffler, Weisfield, & Berger, 2010; Wohlkonig et al., 2010; Wu et al., 2011). However, three completely distinct complexes – *S. cerevisiae* Top2 (Dong & Berger, 2007), *A. baumannii* topoisomerase IV (Wohlkonig et al., 2010), and human TOP2A (the present study) – also have been obtained in which the C-gate interface is dissociated. The existence of multiple models that derive from different topoisomerase homologs and crystal packing environments, yet still exhibit an "open" C-gate, strongly argues against suggestions that this conformation represents a non-physiologic state (Laponogov et al., 2009).

The factors that control C-gate status have been the subject of debate. One proposal has suggested that the formation of a covalent protein•DNA cleavage complex favors C-gate association, whereas G-segment binding alone promotes (but does not strictly enforce) C-gate opening (Schmidt et al., 2010). Support for this argument centers on the existence of a physical linkage between the active-site tyrosine and the α-helical arms that extend into the C-terminal interface (α14 and α18 in human TOP2A); this connection would appear to allow DNA-gate movements, triggered by entry into a cleavage-competent conformational state, to lever the arms toward each other and shut the gate. By contrast, the imaging of certain non-covalent, DNA-bound type IIA topoisomerases with a closed C-gate (Bax et al., 2010; Laponogov et al.,

2010) has raised the possibility that an alternative mechanism may account for the opening of this region. Entrapment of the T-segment in the cavity between the DNA-gate and C-gate could constitute one such approach (Roca, 2004).

A close inspection between all 22 published type IIA topoisomerase structures bearing a closed DNA-gate helps resolve this question (Bax et al., 2010; Dong & Berger, 2007; Laponogov et al., 2007, 2009, 2010; Morais Cabral et al., 1997; Schmidt et al., 2010; Schoeffler et al., 2010; Tretter et al., 2010; Wohlkonig et al., 2010; Wu et al., 2011). In particular, superposition between the WHDs of these models reveals that the DNA-gate samples only a limited number of conformational states as the region engages a duplex substrate. For example, in comparing apo and substrate-bound forms, the presence of DNA correlates with a single, quantized sliding motion of the WHDs with respect to each other, along a vector that is both perpendicular to the dyad axis of the topoisomerase dimer, and roughly parallel with the axes of the two α-helices that abut each other at the dimer interface (α3 in bacterial GyrA, and A'α3 in eukaryotic topo II) (**Figure 2.5a, b**). This movement corresponds to a translational shift of the helix-turn-helix (HTH) motif of each WHD past each other by a distance corresponding to single helical turn, clamping the TOPRIM and tower domains around the G-segment DNA. Interestingly, the etoposide-bound TOP2B•DNA structure exhibits an analogous shift of two helical turns, along with a rotational reorientation of the TOPRIM domain (**Figure 2.5b**), as its DNA-gate cracks open.

The relative rotational status of the two WHDs and their associated active-site tyrosines is similarly quantized, and correlates with both DNA cleavage status and the dimerization state of the C-gate (**Figure 2.5a, c**). An open C-gate is observed only at one end of the rotational range, which is populated by two non-covalent topoisomerase•DNA complexes, as well as one apo-enzyme structure (Dong & Berger, 2007; Wohlkonig et al., 2010). By contrast, all other apo and DNA-bound complexes occupy a distinct set of alternate WHD•WHD juxtapositions that coincide with C-gate closure. For instance, all DNA-cleavage complexes stabilized by small-molecule poisons not only have an associated C-gate, but also exhibit a consistent counterclockwise rotation of the two WHDs with respect to each other (Bax et al., 2010; Laponogov et al., 2009, 2010; Wohlkonig et al., 2010). This conformational change is preserved in the etoposide-inhibited structure between DNA and human TOP2B (C.-C. Wu et al., 2011), where an extra translational shift between WHDs also has occurred (**Figure 2.5b**). A less-extreme, but still evident, counterclockwise movement is seen in every DNA-free structure that displays a closed C-gate (Morais Cabral et al., 1997; Schoeffler et al., 2010; Tretter et al., 2010) and in a *S. cerevisiae* Top2 cleavage complex that was obtained using a phosphorothiolated suicide substrate (Schmidt et al., 2010).

Overall, in instances where DNA is present, these comparisons reveal a tight correlation between a relative movement on the part of the WHDs to elicit DNA cleavage, and the predisposition of the C-gate to be closed. Indeed, out of the 15 topoisomerase II•DNA co-crystal structures in the database, only two appear to violate this correspondence. However, a closer consideration of these outliers (which represent non-covalent, DNA-bound states) demonstrate that neither structure in fact violates the dependence of C-gate dimerization on DNA gate status proposed above: both structures actually derive from topoisomerase/DNA

complexes that were exposed to a small-molecule agent that interferes with the normal cleavage cycle of the enzyme. In one example, the cleavage core of *S. aureus* gyrase was co-crystallized with an intact DNA duplex and a non-intercalative inhibitor of strand scission (GSK299943). Interestingly, this inhibitor binds at the interface between the two apposed WHDs, in a pocket that materializes when the domains adopt a cleavage-like orientation relative to each other (Bax et al., 2010). This concurrence suggests that GSK299943 traps the DNA-gate of bacterial type IIA topoisomerases in a conformation similar to that adopted *after* the action of fluoroquinolone poisons, which are known to impede normal phosphotransfer chemistry (Bax et al., 2010; Laponogov et al., 2009, 2010; Wohlkonig et al., 2010). In the other instance, the core region of *S. pneumoniae* topo IV was first crystallized with the dione PD 0305970 to stabilize a cleavage complex, after which religation was promoted *in situ* by first soaking out the drug in the presence of EDTA, and then re-soaking the crystals with Mg^{2+} ions (Laponogov et al., 2010). Thus, this latter structure derives from a state in which the topoisomerase•DNA complex had already been captured with a rotated WHD configuration and closed C-gate. An inspection of the contacts arising from the crystal lattice indicates that molecular packing interactions would prevent subsequent WHD/WHD rearrangements or C-gate opening upon removal of the drug.

These findings have additional intriguing implications for the mechanism of DNA cleavage. Based on biochemical data, there is a general consensus that type IIA topoisomerases rely on two metal ions for DNA cleavage (Deweese, Guengerich, Burgin, & Osheroff, 2009; Noble & Maxwell, 2002; West et al., 2000). Crystallographic efforts have refined this picture to suggest that only one metal ion (metal A) actively assists with the chemistry of strand scission and religation, whereas the other (metal B) serves a more structural role, anchoring the DNA at the -1 phosphate position (Bax et al., 2010; Dong & Berger, 2007; Laponogov et al., 2009, 2010; Schmidt et al., 2010; Wohlkonig et al., 2010; Wu et al., 2011). The use of a single metal for phosphodiester bond breakage and reformation parallels the mechanism of strand cleavage employed by $\beta\beta\alpha$-Me and HUH nucleases (Yang, 2008). However, there is debate as to whether the two metals found in the type II topoisomerase active site bind simultaneously during DNA breakage and religation, or if a single "dynamic" ion hops between the two coordination sites at different stages of the reaction.

Support for the simultaneous two-metal mechanism has derived from thiol-rescue studies (Deweese et al., 2009; Noble & Maxwell, 2002), and from a structure of *S. cerevisiae* Top2 captured in a covalent product complex with a phosphorothiolated DNA that was soaked with Zn^{2+} ions (Schmidt et al., 2010) (**Figure 2.6a**). By comparison, the dynamic metal concept derives from a number of type IIA topoisomerase•DNA complex structures that exhibit only a single metal in either one position or the other (Bax et al., 2010; Dong & Berger, 2007; Laponogov et al., 2009, 2010; Wohlkonig et al., 2010; Wu et al., 2011). However, each of these one-metal structures correspond to, or derive from, either drug-inhibited states of the enzyme, or complexes in which the DNA substrate is not competent to support cleavage. For instance, in all structures where the protein is bound to an intercalative poison, or where the DNA is nicked at the scissile position (as in the present TOP2A model), only metal B is visible **(Figures 2.6b-c,**

S2.3a). Alternatively, in the two topoisomerase•DNA complexes where the duplex backbone is intact and a poison is not present – either because the protein is bound to a non-intercalative drug (e.g., GSK29994), or because the enzyme was first co-crystallized with a poison before removal of the drug – only site A is filled **(Figures 2.6d, S2.3b-c)**. The inability of poisoned or nicked DNAs to support metal binding at the A-position is readily understandable, as the phosphate which coordinates this metal ion is either shifted out of the active site pocket (in drug-bound states), or missing altogether. Similarly, the physical impediment to metal binding at site B in the GSK29994-associated, or dione-pretreated complexes coincides with a misalignment of the coordinating residues in the DxD motif. This alteration likely is coupled to the more extreme WHD juxtaposition exhibited by these structures, which matches that of other cleavage-impaired drug-bound complexes (**Figure 2.5**). These shifts may also explain why metal A remains present in the enzyme active site even after EDTA treatment of the dione-soaked crystals, and why no other divalent species appear following the addition of Mg^{2+}: this behavior suggests that the presence of drug reconfigures the active site to tightly bind only a single cofactor, which is sufficient to promote religation in a non-ideal crystalline environment once drug is removed. Overall, the most parsimonious interpretation of these data is that under normal circumstances, two metals are present in the active site during strand scission, whereas inhibitor binding introduces new conformational constraints that allow for occupancy of only a single metal ion. This mode of action would be expected to perturb the cleavage/religation equilibrium of the enzyme, a well-established property of type IIA topoisomerase poisons in general.

Together, this pattern of coupled conformational changes and DNA binding/cleavage status not only supports the idea that a direct allosteric connection exists between the state of the DNA-gate and C-gate actuation, but also highlights probable substeps in the type IIA topoisomerase reaction (**Figure 2.7**). Prior to G-segment binding, the DNA-gate can oscillate between dissociated and associated conformers that are accompanied by a dimerized (closed) C-gate (**1**) (Berger et al., 1996; Corbett et al., 2005; Fass et al., 1999; Laponogov et al., 2007; Morais Cabral et al., 1997; Schoeffler et al., 2010; Tretter et al., 2010). Occasionally, when the DNA-gate adopts a closed configuration the C-gate can sample an open state (**2**), as is seen in *A. baumannii* topo IV (Wohlkonig et al., 2010). We propose that binding of an intact G-segment promotes the transition from this "pre-engagement" state to an "engagement" configuration (**3**), in which subunit-related TOPRIM and WHD elements shift with respect to each other to both clamp around DNA; this structural change simultaneously imposes a WHD/WHD juxtaposition that modestly destabilizes the C-gate and more readily allows for separation (**4**), possibly by introducing strain into the coiled-coil arms that link the DNA-gate and C-gate together. ATP- and/or T-segment binding would subsequently promote entry into a new physical state – one that promotes DNA cleavage – by inducing the WHDs to rotate with respect to each other and bring the active-site tyrosines in-line to attack DNA (**5**). This movement also would serve to relieve any strain imposed by the engagement state and thereby maintain C-gate closure. Resealing of the G-segment would return the DNA-gate to a conformation promoting C-gate dissociation and allow for T-segment release (**6**). Interestingly, our comparative studies indicate that the binding of either small-molecule poisons (which push

apart the 3' and 5' ends of a cleaved DNA), or other interfacial inhibitors that associate with the DNA-gate interface, can promote the formation of a more extreme rotation of the WHDs with respect to each other (**7**). This action may help such drugs trap the enzyme in an off-pathway state, thereby impeding recovery to a religation-competent form. Consistent with this model, the binding of etoposide, which is substantially non-planar compared to its fluoroquinolone counterparts, promotes an even more pronounced WHD rotation and partial separation of the DNA-gate. An interesting secondary feature of this model is that it suggests that the energy landscape between conformational transitions controlling DNA cleavage and gate opening is relatively flat, with only subtle energetic differences needed to shift from one structural intermediate to another.

Concluding remarks

In summary, this work presents the first structure of the DNA binding and cleavage core of human TOP2A bound to DNA. Consideration of the model in light of existing structures of homologous enzymes has enabled us to better understand several important facets of type IIA topoisomerase mechanism and inhibition. In particular, we find that the two winged-helix domains of a topoisomerase dimer, which form part of the region responsible for cleaving and opening DNA (the DNA-gate), adopt only a small set of positional configurations with respect to each other. These quantized conformations appear to couple DNA cleavage status with the allosteric control of interactions at a distal subunit interface, the C-gate, which sits more than 50 Å away from the enzyme active site. Anti-topoisomerase agents that bind within the DNA-gate appear to subvert these movements, altering the position and occupancy of reactive elements to either impede or stabilize cleavage and religation events. Comparisons of our model with an etoposide-inhibited state of the second human type IIA topoisomerase, TOP2B, highlight the similarities between the two isoforms, but also suggest avenues for promoting epipodophyllotoxin selectivity that might be of use in countering secondary malignancies. Future efforts aimed at imaging additional intermediates and drug-bound states will be needed to investigate these ideas further.

Materials and Methods

A truncation of the DNA binding and cleavage core from the human gene TOP2A(Tsai-Pflugfelder et al., 1988) (residues 431-1193, **Figure 2.1a**) was cloned into a GAL1-based yeast shuttle vector, in frame with an N-terminal tobacco etch virus (TEV) protease-cleavable His_6-MBP tag. Protein was expressed in *Saccharomyces cerevisiae* strain BCY123 (*MATα pep3::HIS3 prb1::LEU2 bar1::HISG lys2::GAL1/10-GAL4 can1 ade2 trp1 ura3 his3 leu2-3,112* (Wasserman & Wang, 1994), originally from the laboratory of R. Kornberg) grown in CSM-Ura^- media with a 2% lactic acid and 1.5% glycerol carbon source at 30°C. Overexpression was induced by the addition of 2% galactose at A_{600}=0.9. Six hours after induction, cells were centrifuged (4500 rpm, 4°C, 15min), resuspended in 1mM EDTA and 250mM NaCl (1 mL per liter liquid culture), and flash frozen drop-wise in liquid nitrogen.

For purification, frozen cells were first lysed under liquid nitrogen by grinding with a mortar and pestle, and resultant powder thawed and re-suspended in 20mM Tris-HCl (pH 8.5),

300mM KCl, 20mM imidazole, and 10% glycerol (20 mL per liter liquid culture) supplemented with protease inhibitors (1mM PMSF, 2.34µM leupeptin, and 1.45µM pepstatin). Lysate was clarified by centrifugation (15000 rpm, 4°C, 20 min) and run over a nickel-chelating sepharose column (GE) at 4˚C. Following a column wash in resuspension buffer, tagged TOP2A was eluted stepwise with resuspension buffer plus 200mM imidazole. Eluted protein was concentrated using a 100kDa cutoff centrifugal filter (Amicon), buffer exchanged with resuspension buffer, and then incubated overnight with His-tagged TEV protease at 4°C (Tropea, Cherry, & Waugh, 2009). Protease and uncleaved protein were removed by running over a second nickel column, and the eluted cleaved protein was run over a gel filtration column (S300, GE) equilibrated in 500mM KCl, 20mM Tris-HCl (pH 7.9), and 10% glycerol. Purity was estimated by SDS-PAGE, and peak fractions were combined and concentrated to ~15.8mg/ml protein using a 100 kDa cutoff filter.

Oligonucleotides were ordered from Integrated DNA Technologies. After receipt, DNAs were purified by urea-formamide PAGE, resuspended in 200 mM KCl, 10 mM Tris-HCl (pH 7.9), and annealed to form a 13bp duplex with a complementary 4-base 5'overhang. This construct results in the formation of a doubly-nicked, 30 base pair DNA substrate (**Figure 2.1b**) when bound to a TOP2A homodimer. DNA and protein were combined in a 1.1:1 molar ratio of DNA 30mer:TOP2A dimer and dialyzed stepwise against 20mM Tris-HCl (pH 7.9), 10mM $MgCl_2$ and decreasing concentrations of KCl (500mM, 250mM, 100mM). Dialysis ran over the course of 16 h at 4°C to a final condition of 20mM Tris-HCl (pH 7.9), 10mM $MgCl_2$ and 100mM KCl using a 1000 Dalton cut-off mini-capillary dialyzer (Harvard Apparatus). Crystals grew within a day of setting hanging drops by mixing 150 nL of a 5 mg/mL protein/DNA sample with 150 nL 10% (w/v) PEG 3000, 100 mM Na-cacodylate (pH 6.5) and 200 mM $MgCl_2$ solution at 18°C. Crystals were looped and cryoprotected with well solution plus 29% glycerol before being flash frozen in liquid nitrogen.

Diffraction experiments were performed at the 8.3.1 beamline of the Advanced Light Source at Lawrence Berkeley National Laboratory.(MacDowell et al., 2004) Data were collected on an ADSC Q210 CCD detector using a wavelength of 1.1159Å, and crystals maintained at 100 K by a gaseous N_2 cyrostat. Data were integrated and scaled using HKL2000 (Otwinowski & Minor, 1997) and reduced using CCP4 software (Winn et al., 2011). Based on BLAST analysis of type IIA topoisomerase homologs at the time (the human TOP2B model had not yet been published) (Altschul et al., 1997; Altschul et al., 2005), a molecular replacement search model comprising the DNA gate (residues 431-1014 and 1165-1189, TOP2A numbering) of a single protomer bound to half the DNA substrate but excluding the α-helical arms and C-gate was prepared from the crystal structure of the yeast topoisomerase II DNA binding and cleavage core bound to DNA (residues 419-989 and 1153-1177, PDB ID = 2RGR, (Dong & Berger, 2007)). Sidechain lengths in the search model were reduced to the last common atom using CHAINSAW (Stein, 2008). From this model, PHASER was used to find a positional solution and determine initial phases (McCoy et al., 2007); molecular replacement performed with the same initial search model, but without DNA, yielded an identical solution with strong positive difference density confirming the DNA substrate was present. A second molecular replacement search using only the globular domains of the C-gate was performed against the first solution to

determine placement of this region, again using the yeast topoisomerase II DNA structure as a search model (residues 1029-1136, PDB ID = 2RGR). The resultant asymmetric unit consists of a single protomer and half the DNA substrate; the protein dimer is generated by a crystallographic two-fold axis. After a round of rigid body refinement using PHENIX (Adams et al., 2010), the model was improved by building in COOT (Emsley, Lohkamp, Scott, & Cowtan, 2010) and refinement in PHENIX using individual site refinement, individual ADP refinement, and TLS. The TLS Server (Painter & Merritt, 2006a, 2006b) was used to inform decisions for TLS groups. The final model included the entire DNA substrate and the entire protein construct, excluding residues 1092-1124, the N-terminus (residues 431-2) and the C-terminus (residues 1190-1193). Model validation was performed by Molprobity (Chen et al., 2010); comparisons between different topoisomerase models were conducted using PYMOL (The PyMOL Molecular Graphics System, Version 1.5.x, Schödinger, LLC).

Accession numbers

Structure factors and atomic coordinates are deposited in the Protein Data Bank with accession number 4FM9.

Tables

Table 2.1. Diffraction and refinement statistics for the DNA bound human topoisomerase IIα complex

Structure	Human topo IIα- DNA complex
Space group	$C222_1$
Unit cell dimensions	
a, b, c (Å)	85.91, 215.08, 128.65
α, β, γ (˚)	90, 90, 90
Data collection	
Wavelength (Å)	1.1159
Resolution (highest shell)	49.6-2.9 (3.00-2.90)
Observed reflections	552602
Unique reflections	25373
R_{sym}* (%)(3.00-2.90Å)	9.3 (71.2)
I/σI (3.00-2.90Å)	15.4 (2.0)
Completeness (3.00-2.90Å)	95.3 (91.6)
Redundancy (3.00-2.90Å)	7.2 (4.5)
Refinement	
R_{work}†	22.7%
R_{free}†	27.0%
Reflections in test set (% of total)	1285 (5.1%)
No. atoms	
Protein/DNA	6538
Solvent	44
Average B factor (Å^2)	
Protein/DNA	80.2
Solvent	37.6
Bond length deviations from ideal	0.006 Å
Bond angle deviations from ideal	0.847˚
Ramachandran outliers‡	0
Ramachandran favored‡	96.4%

*$R_{sym} = \Sigma|I-I\sigma|/\Sigma I$, where I is the integrated intensity for a given reflection.

†$R_{work} = \Sigma|F_{obs}-F_c|/\Sigma F_{obs}$, where F_{obs} and F_c are the observed and calculated structure factor amplitudes. R_{free} is calculated as for R_{work}, but from a subset of the data (5.1%) that was withheld from crystallographic refinement.

‡As defined by Molprobity (Chen et al., 2010).

Figures

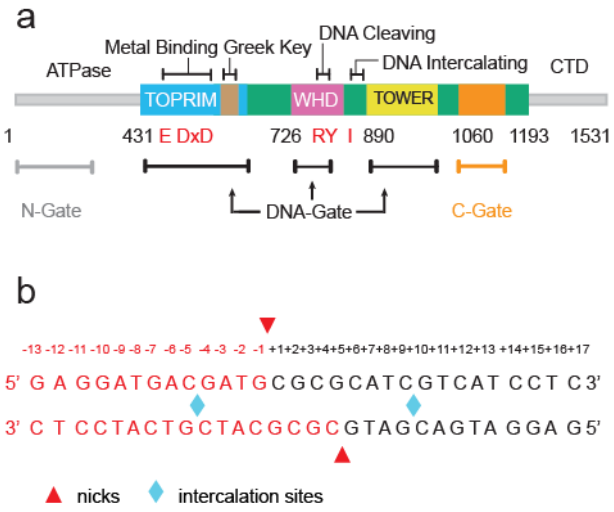

Figure 2.1. Crystallization constructs.

a. Primary structure of human topoisomerase IIα. The region crystallized (residues 431-1193) is shown in color. Specific domains (TOPRIM, WHD, tower) and dimerization gates are labeled with important residues and features highlighted: catalytic tyrosine and associated arginine – RY; intercalating isoleucine – I; metal-binding triad – DxD and E.

b. Schematic of the doubly-nicked, 30 basepair DNA substrate. Nicks and intercalation sites are highlighted.

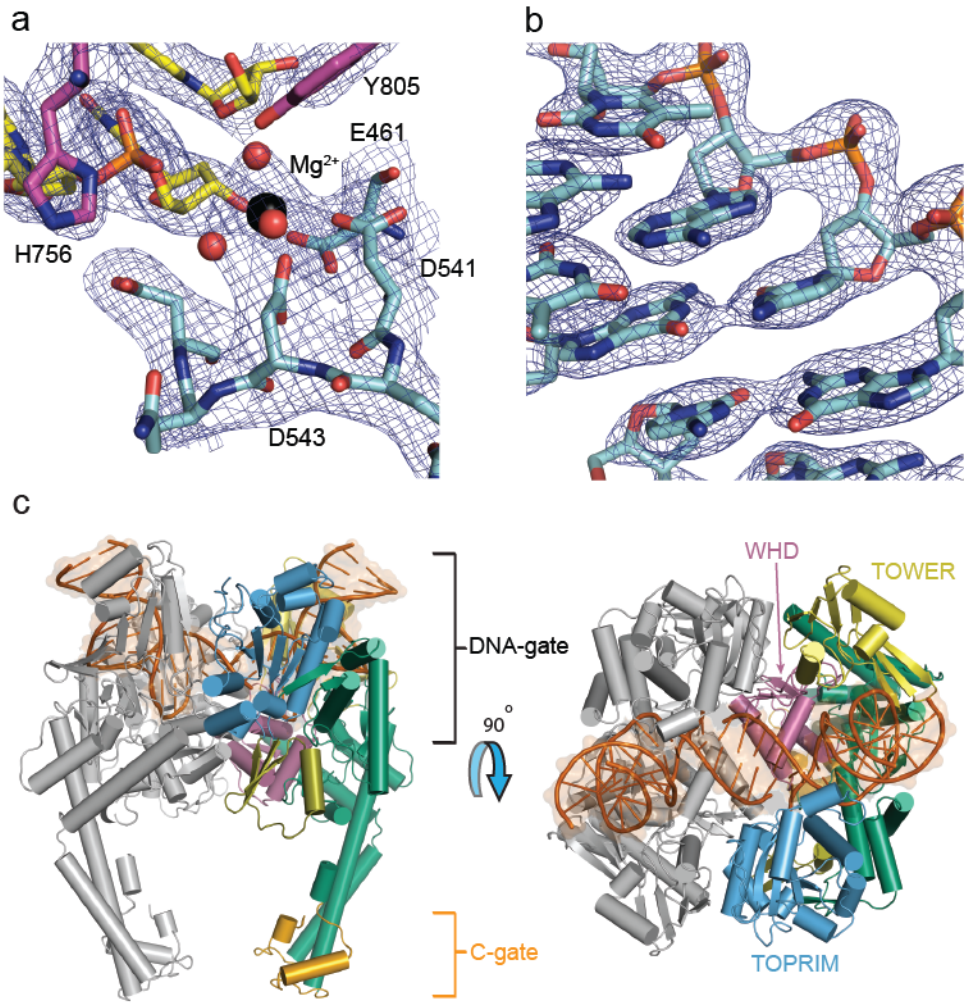

Figure 2.2. Structure of the human TOP2A DNA binding and cleavage core bound to DNA.

a. Refined $2F_o$-F_c map around the nucleolytic center (1.4σ contour). The active site is formed around DNA (yellow) at the interface between the TOPRIM domain (cyan) and WHD (magenta) of opposing protomers.

b. Refined $2F_o$-F_c electron density map (2σ contour) clearly shows the bound DNA substrate.

c. The human TOP2A•DNA complex as viewed from the front (*left*) and above (*right*). Domains are colored as in **Fig. 2.1a**, with DNA in dark orange. The G-segment is bound in the DNA gate, and the C-gate dimerization interface is dissociated.

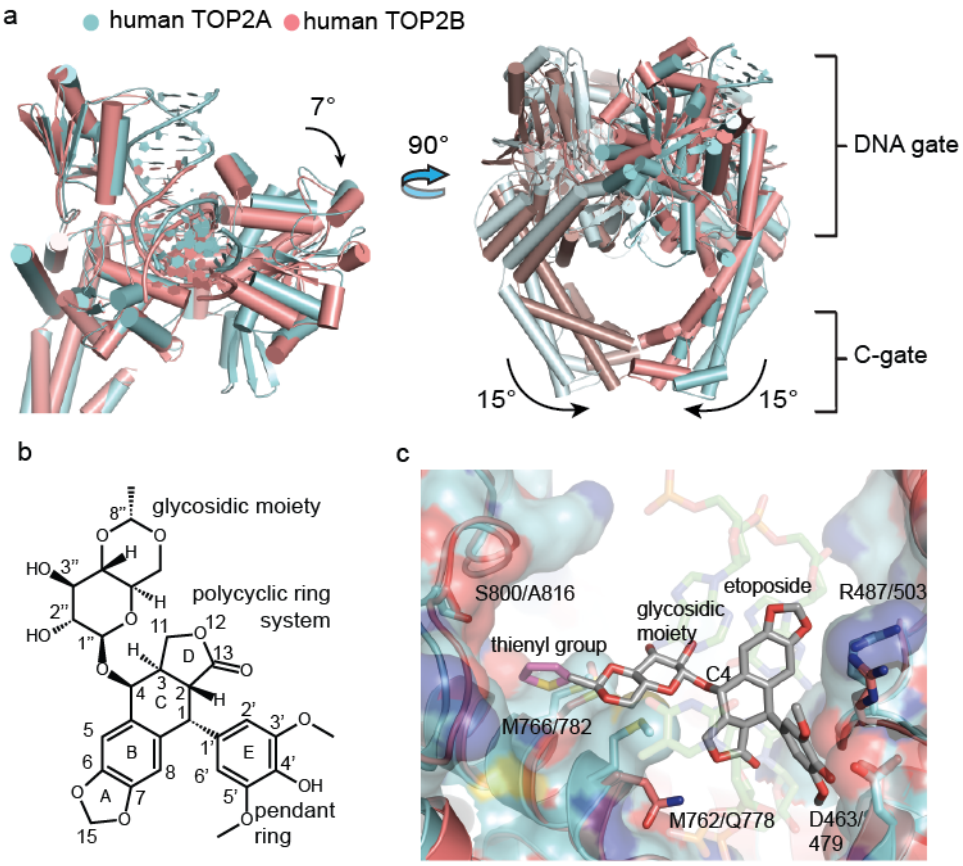

Figure 2.3. Comparison of TOP2A and etoposide-bound TOP2B.

a. The global conformation of TOP2A and TOP2B differs. Superposition of the two human isoforms shows that the TOPRIM domain in the etoposide-bound TOP2B cleavage complex (PDB ID 3QX3) is rotated relative to the WHD and tower domain in the TOP2A structure (*left panel,* only one protomer shown). The dimeric TOP2B cleavage complex has a closed C-gate compared to TOP2A (*right panel*).

b. Structure and ring numbering of etoposide.

c. Only two amino acids differ in the etoposide-binding pocket of TOP2A and TOP2B. The WHD and TOPRIM of TOP2A are shown individually superposed on the TOP2B drug-binding site. Two residues that differ – Met762 in TOP2A *vs*. Gln778 in TOP2B, and Ser800 *vs*. Ala816 – are labeled, as are three amino acids that are preserved (Arg487/503, Asp463/479, and Met766/782). Etoposide is shown as gray/red sticks; the additional thienyl group of the related anticancer drug teniposide is modeled in magenta to show its relation to the Ser800/Ala816 region.

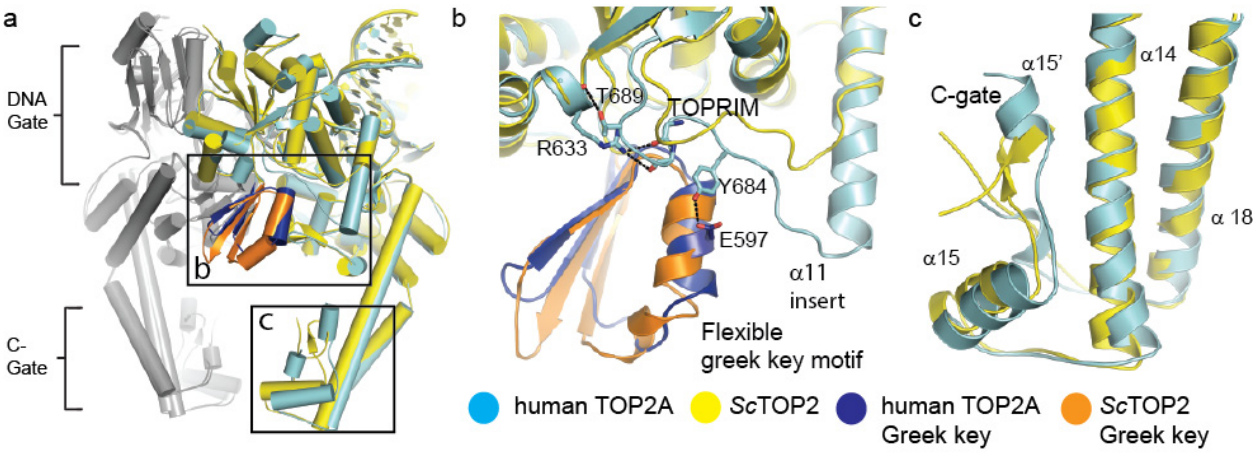

Figure 2.4. Comparison of TOP2A and *S cerevisiae* topoisomerase II.
a. The quaternary conformation of the human TOP2A•DNA complex most closely resembles the yeast Top2-DNA complex with a double nicked substrate. Architectural differences between the two structures are most pronounced in the Greek key motif and in the C-gate (boxed regions).

b. Differences in the TOPRIM insert region. A tyrosine (Tyr684) in the 670-686 insert of TOP2A forms hydrogen bonds with Glu597 in the Greek key element of the TOPRIM domain. Interactions seen in TOP2A, but not yeast topoisomerase II, are shown as sticks/dashed lines, and labeled.

c. Differences in the C-gate. A β-hairpin in the yeast topoisomerase II C-gate is replaced by an α helix (A'α15') in TOP2A.

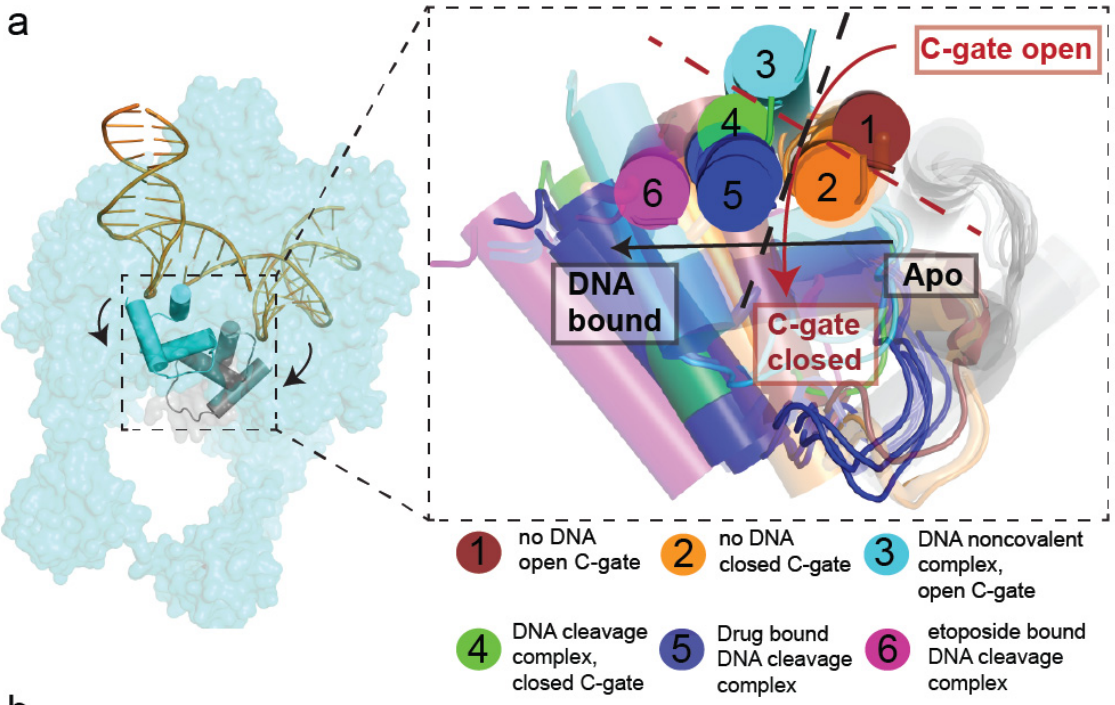
a
C-gate open
3
4
1
6
5
2
DNA bound
Apo
C-gate closed
1 no DNA open C-gate
2 no DNA closed C-gate
3 DNA noncovalent complex, open C-gate
4 DNA cleavage complex, closed C-gate
5 Drug bound DNA cleavage complex
6 etoposide bound DNA cleavage complex

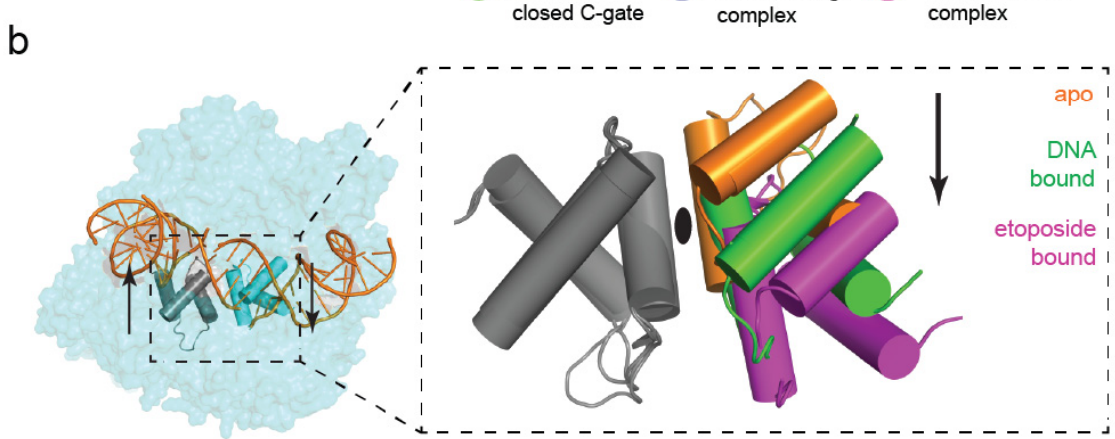
b
apo
DNA bound
etoposide bound

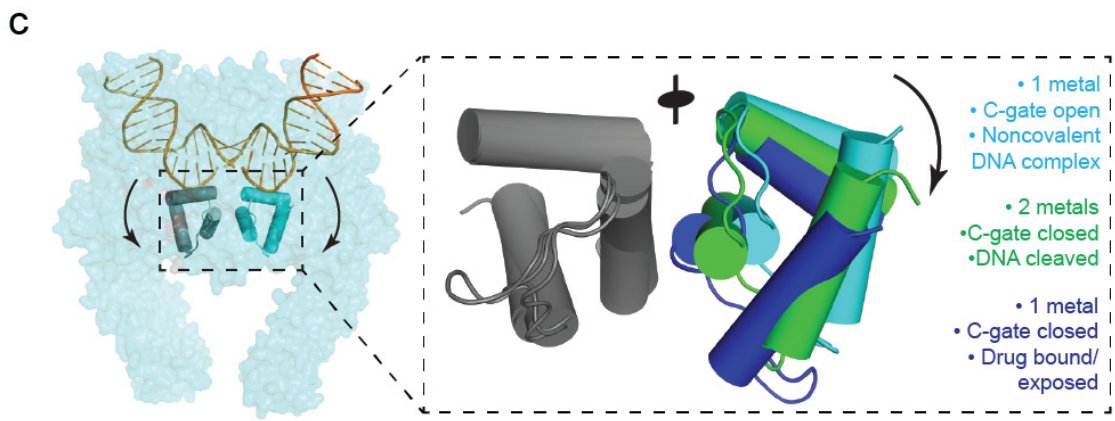
c
• 1 metal
• C-gate open
• Noncovalent DNA complex
• 2 metals
•C-gate closed
•DNA cleaved
• 1 metal
• C-gate closed
• Drug bound/ exposed

Figure 2.5. Substrate-dependent movements in the type IIA topoisomerase DNA gate are quantized.

This figure depicts the superposition of 22 type IIA topoisomerase structures, aligned using the WHD of one protomer to reveal the relative displacements of its partner WHD. The juxtapositions fall into six groups. Cartoons depict just the three-helix bundles of the two WHDs; surface representations are provided for orientation.

a. Overview of the six juxtapositions: *1)* no DNA bound, C-gate open (*A. baumanni* topo IV(2XKJ)); *2)* no DNA bound, C-gate closed (*E. coli* gyrase (3NUH), also *E. coli* gyrase (1AB4), *M. tuberculosis* gyrase (3ILW)); *3)* DNA noncovalently bound, C-gate open (human TOP2A, also *S. cerevisiae* topoisomerase II (2RGR)); *4)* DNA cleavage complex, C-gate closed (*S. cerevisiae* topoisomerase II (3L4K)); *5)* DNA cleavage complex, C-gate closed, initial crystallization with drug bound (*A. baumanni* topo IV bound to moxifloxacin (2XKK), also *S. pneumoniae* topo IV cleavage complex bound to moxifloxacin (3FOF), clinafloxacin (3FOE), levofloxacin (3K9F) a dione inhibitor (3LTN), the dione complex back soaked with EDTA (3KSA), and the EDTA soaked complex resealed by a $MgCl_2$ soak (3KSB). The *S. aureus* gyrase noncovalent complex bound to GSK299943 (2XCR, 2XCS) and cleavage complex bound to ciprofloxacin (2XCT) further map to this group); *6)* DNA cleavage complex, C-gate closed, etoposide bound (human TOP2B (3QX3)). The red dashed line indicates the demarcation in relative WHD rotation angles between open and closed C-gate states. The black dashed line indicates the demarcation of lateral WHD displacement between DNA bound and free forms.

b. Binding of DNA causes the WHDs in opposing protomers to slide past each other by one helical turn along the α3 helix (A'α3 helix in eukaryotic topoisomerase IIs). This sliding can be quantized into juxtapositions taken by the apo-enzyme (conformations 1 and 2 in panel **a**) and juxtapositions taken by DNA bound enzymes (conformations 3-5 in panel **a**). A more extreme lateral shift is seen in the etoposide bound TOP2B complex where the DNA-gate interface has been disrupted (conformation 6 in panel **a**).

c. DNA cleavage and C-gate dimerization are correlated to a rocking of the WHDs against each other. This rotation is quantized into juxtapositions with an open C-gate and non-covalently bound DNA (conformations 1, 3 in panel **a**), a closed C-gate and covalently bound DNA (conformations 2, 4 in panel **a**), and a closed C-gate, covalently bound DNA, and drug binding (conformation 5, 6 in panel **a**).

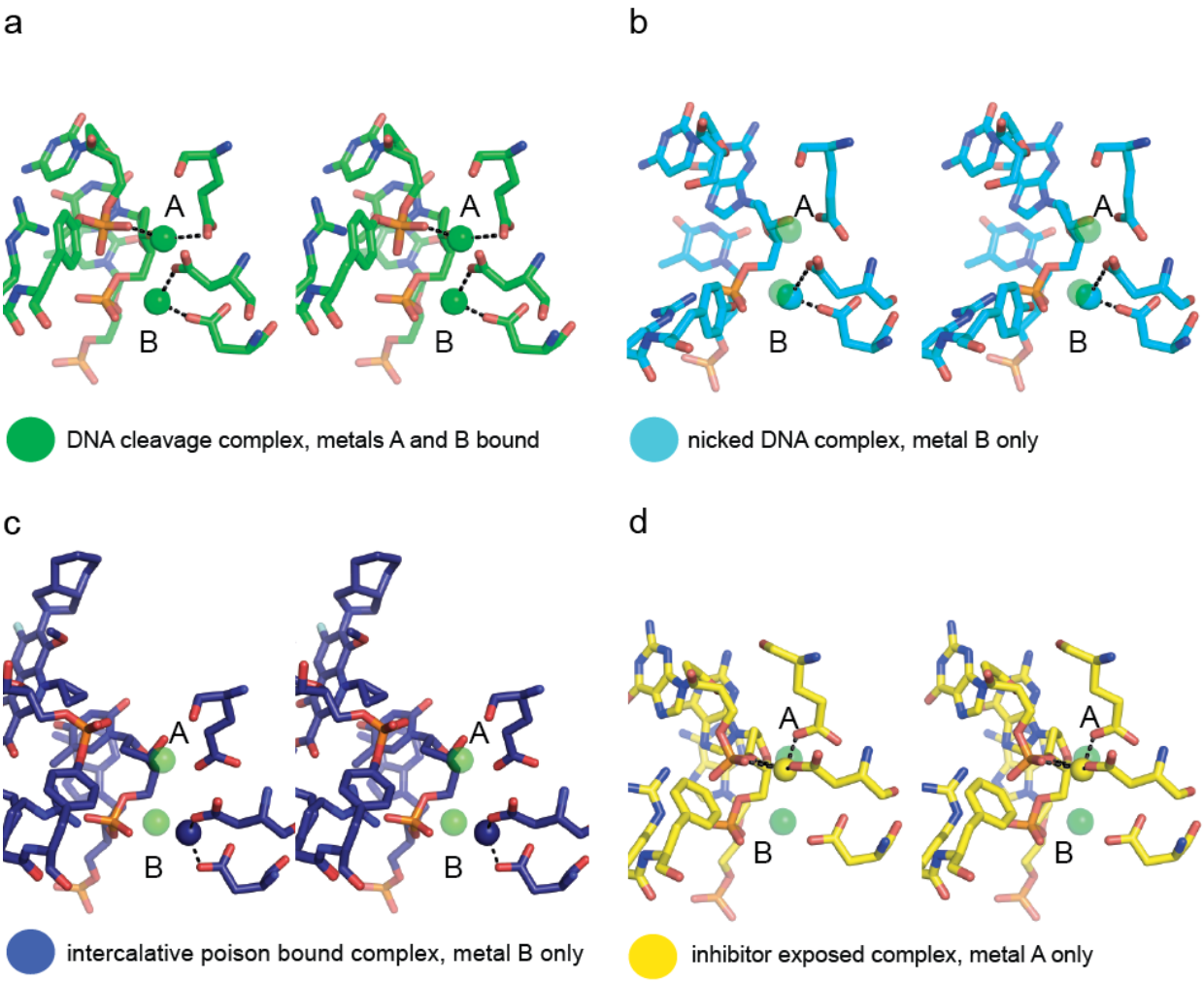

Figure 2.6. Comparison of metal occupancy between type IIA topoisomerase structures.

a. The structure of *S. cerevisiae* topoisomerase II trapped in a cleavage intermediate by a phosphorothiolate suicide substrate has two metals, A and B, bound in the active site (PDB 3L4K shown).

b. In structures solved with nicked substrates, only metal B is present, as metal A binding requires coordination by the missing scissile phosphate (PDB 4FM9 shown).

c. Structures bound to a type IIA topoisomerase poison bind only metal B, due to a shift of the phosphotyrosine out of the metal A binding site (PDB 2XKK shown).

d. In structures bound to a non-intercalative drug (e.g., GSK29994), or where poison has been removed following co-crystallization, only metal A is present. In these structures, residues in the DxD motif do not form appropriate geometry for metal B coordination, due possibly to the retention of an altered DNA gate state (c.f. Fig. 2.5) (PDB 2XCS shown).

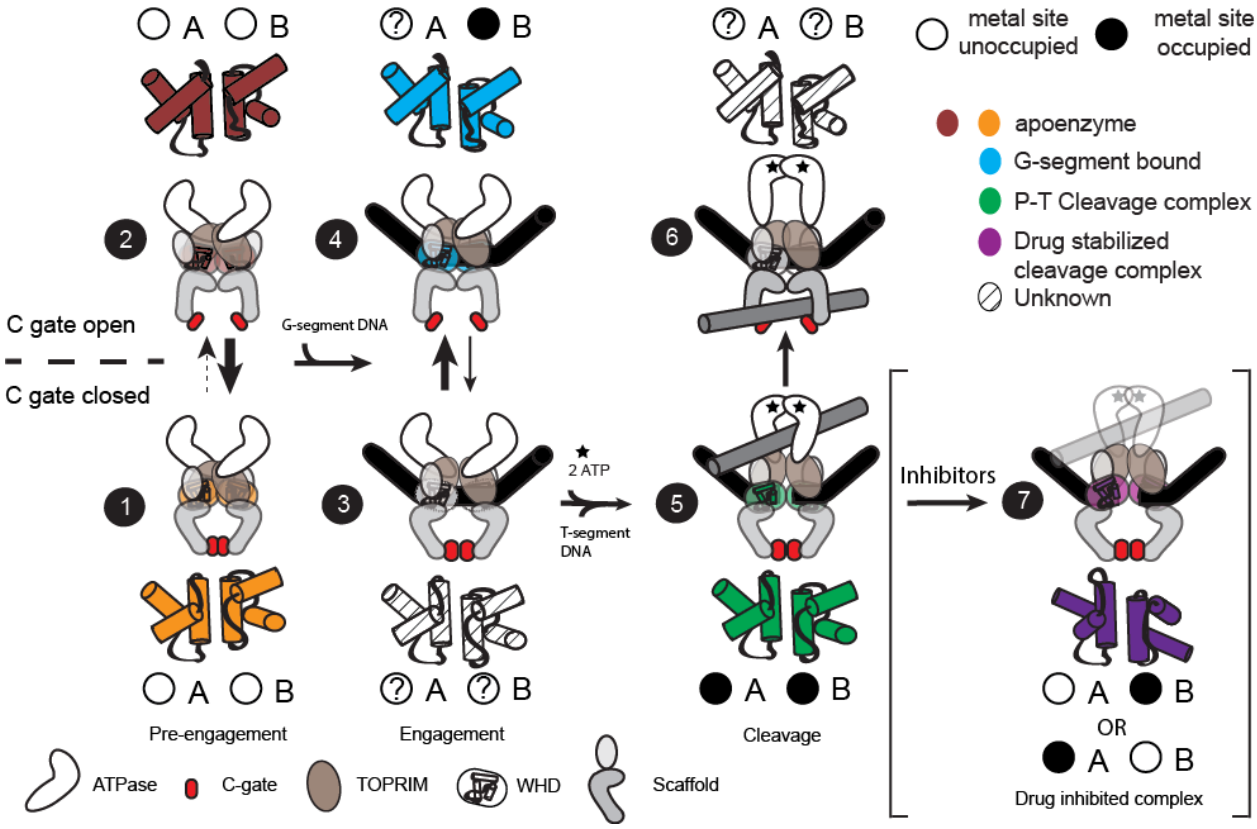

Figure 2.7. A Model relating DNA-gate status to C-gate dimerization and metal occupancy in the context of the type IIA topoisomerase reaction.

Topoisomerase IIA dimers exist in an equilibrium between different combinations of associated or dissociated proteinaceous interfaces. Where double-arrows are shown, the relative thickness of the arrows denotes the likely weighted distribution of the two states. Prior to DNA binding, DNA-gate closure can occur with either a closed (1) or an open C-gate (2). G-segment binding promotes the TOPRIM domain, WHD, and tower domain of both protomers to clamp around the DNA (3); this event may promote C-gate opening (4). ATP binding and capture of a second duplex, the T-segment, promote cleavage of the G-segment (5), favoring C-gate closure. The T-segment exits through an open C-gate following its passage through the G-segment, and resealing of the cleaved DNA (6). Binding of topoisomerase II poisons and inhibitors like GSK299943 perturb the DNA-gate interface to a more extended rotation that is impaired for religation, and may help maintain the C-gate in a closed conformation (7). Relative WHD displacements as observed between different ligand bound and/or free states are shown as cartoon cylinders and colored as per **Figure 2.5**. The relative occupancies of the two metal-binding sites are also shown, with question marks denoting states that have yet to be imaged. The lone question mark associated with site A, state (4), reflects that fact that the DNAs found in these models lack a scissile phosphate, and hence may not capable of binding a metal ion accordingly.

Supplementary Material

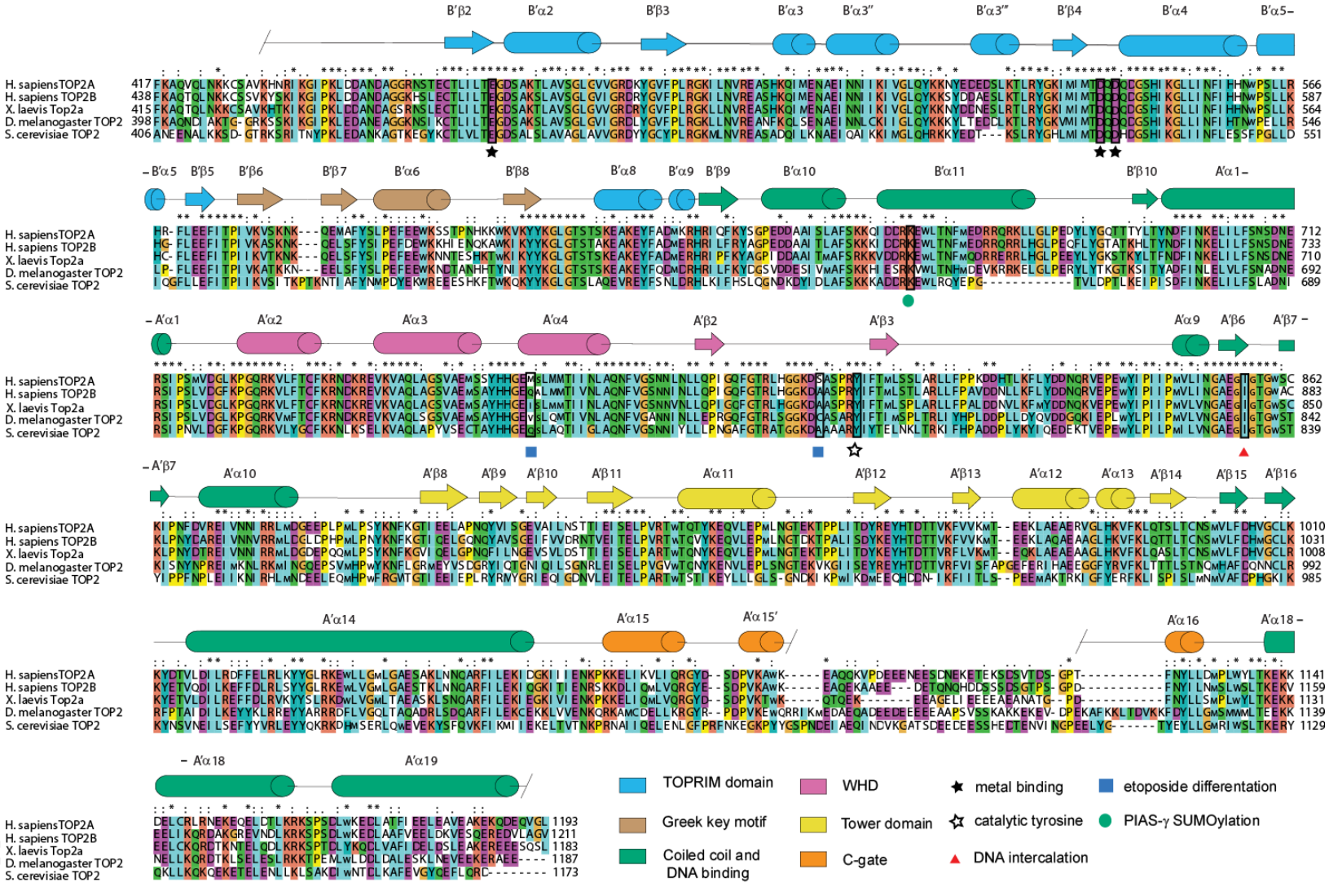

Figure S2.1. Sequence alignment of select type IIA topoisomerases.

The breakage-rejoining domain amino acid sequences of human TOP2A, human TOP2B, *X. laevis* Top2a, *S. cerevisiae* Top2 and *D. melanogaster* Top2 were aligned using the ClustalX software.(Larkin et al., 2007) A map of secondary structure features from the human TOP2A model is overlaid on the alignment. Metal-binding residues, the catalytic tyrosine, and the DNA intercalating isoleucine are marked. Non-conserved residues between TOP2A and TOP2B in the drug-binding pocket and the SUMOylated lysine from *X. laevis* are also indicated.

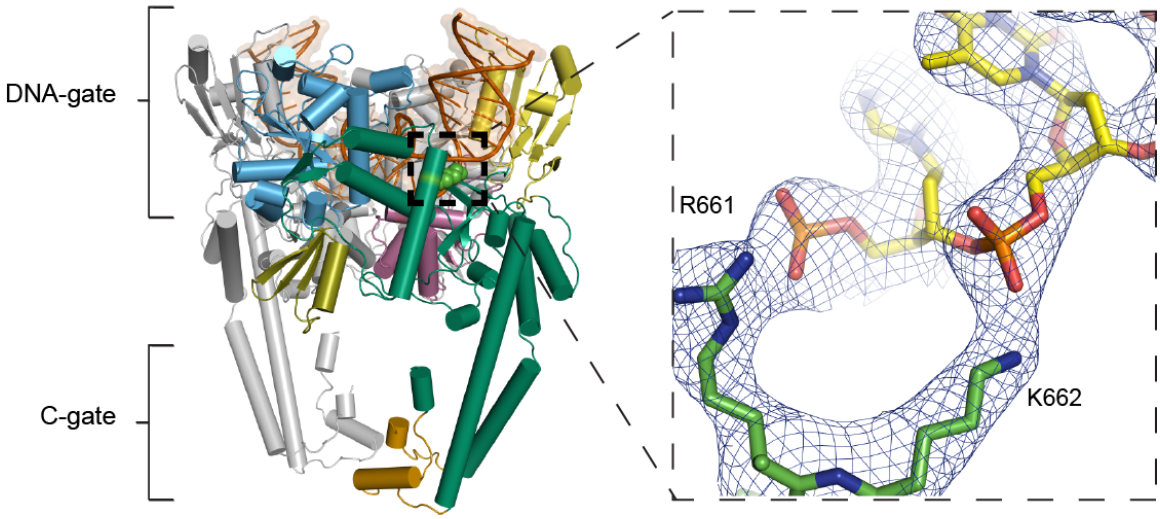

Figure S2.2. Location of the PIAS-γ SUMOylation site.

Lys662 has been implicated as a SUMOylation target (Ryu et al., 2010). A 2Fo-Fc electron density map contoured to 1.5σ shows that Lys662 is directly involved in binding DNA. (*Left*) Cartoon view of the human TOP2A dimer bound to DNA. Domain coloring as per **Figure 2.1a**. (*Right)* Close-up of interaction site.

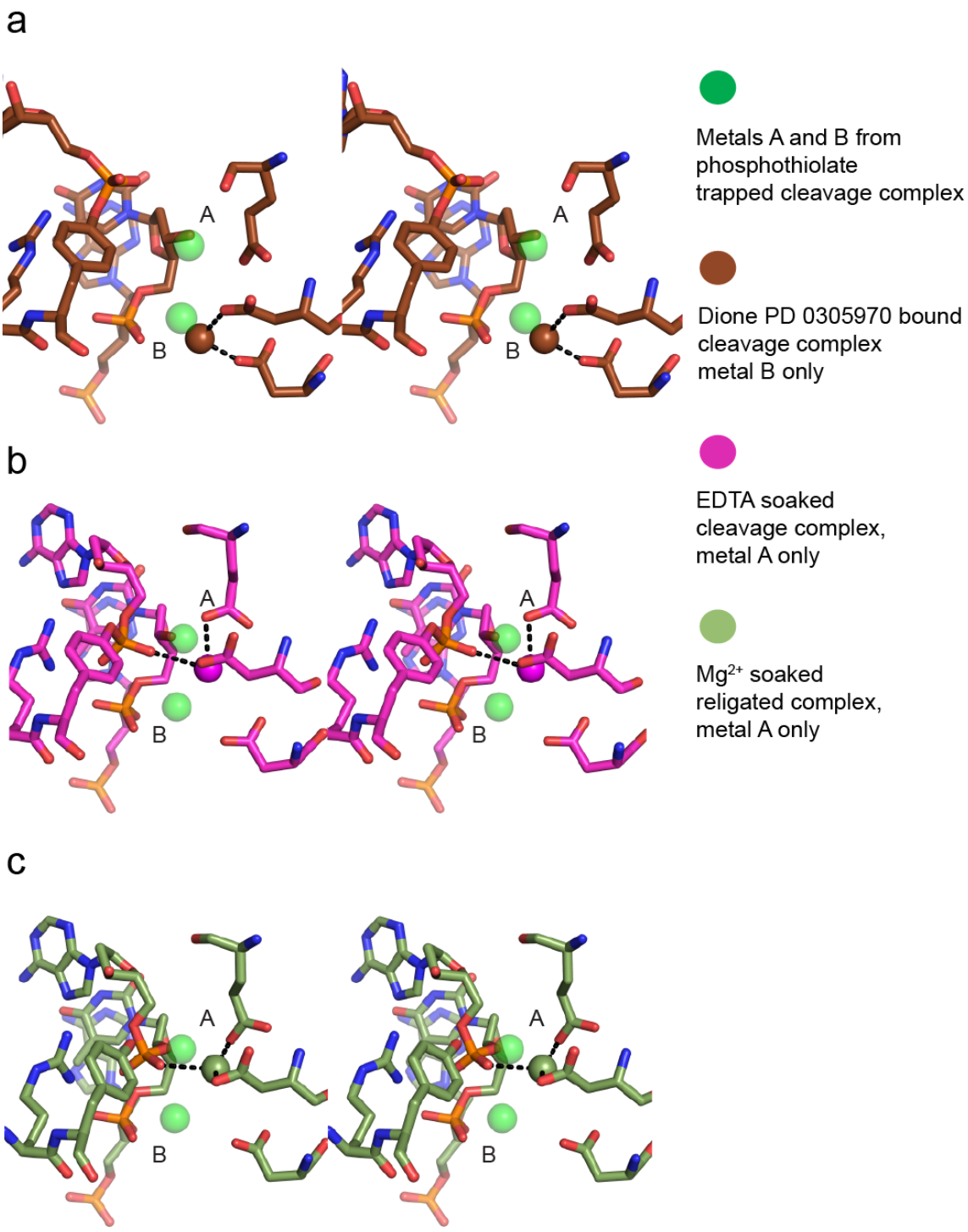

Figure S2.3. Metal occupancy trends in drug-exposed topo IV structures.
Stereo images (as per **Figure 2.6)** depicting metal occupancy of the *S. pneumoniae* topo IV active site.(Laponogov et al., 2010) **a)** Co-crystal structure with the dione PD 0305970 (drug is not shown for clarity) (PDB ID 3LTN). **b)** PD 0305970 co-crystals treated with EDTA to remove

the dione (PDB ID 3KSA). **c)** EDTA treated crystals deriving from the PD 0305970 complex, resoaked with Mg^{2+} to promote DNA religation (PDB ID 3KSB).

Chapter 3—Topoisomerase VI senses and exploits both DNA crossings and bends to facilitate strand passage.

(Portions of this chapter are reproduced from a manuscript in preparation by T.J. Wendorff and J.M. Berger).

Introduction

Transcription, DNA replication and the segregation of genetic material are essential processes for all DNA-based life. These processes are antagonized by the double helix structure of DNA, which counteracts both RNA polymerase and replisome processivity by storing the super-helical backpressure, and leads to physically interlinked chromosomes upon replication (reviewed in (Vos et al., 2011; Wang, 2002)). To overcome these topological impediments to DNA metabolism, cells and viruses employ topoisomerases. These ubiquitous and essential molecular machines relieve super-helical tension and DNA entanglements through mechanisms that rely on either single strand (Type I) or double strand (Type II) breaks (reviewed in (Chen et al., 2013; Forterre & Gadelle, 2009; Schoeffler & Berger, 2008)).

By generating transient double strand breaks, type II topoisomerases are the only enzymes capable of unlinking catenated DNA molecules (Holm et al., 1985; Spell & Holm, 1994; Zechiedrich & Cozzarelli, 1995). This activity is accomplished by a so-called "two-gate" mechanism for strand passage, whereby a topoisomerase binds to one DNA segment (termed the gate or "G"-segment DNA) using a dimer-related interface (termed the DNA gate) and captures a second DNA segment (termed the transfer or "T"-segment DNA) upon ATP-dependent closure of a second, N-terminal dimer related interface (termed the N-gate). A pair of catalytic tyrosine residues in the DNA gate breaks the G-segment by forming covalent intermediates with the phosphate backbone. Transient dissociation of the DNA gate allows the T-segment to pass through the cleaved G-segment, resulting in either the unlinking of two catenated DNA molecules or in changes to DNA superhelicity (reviewed in (Chen et al., 2013; Schoeffler & Berger, 2008; Vos et al., 2013)). If not properly controlled, the type II topoisomerase mechanism can jeopardize genomic stability by promiscuously cutting DNA (Deweese & Osheroff, 2009). A number of clinically relevant antibiotic and anticancer small molecule "poisons" exploit this vulnerability by stabilizing a cleaved G-segment (Pommier et al., 2010). Understanding how type II topoisomerases naturally mitigate aberrant cleavage events and how these intrinsic feedback mechanisms can be subverted is thus of significant biological and clinical importance. Interestingly, while strand scission mediated by the type IIA class of topoisomerases has been the subject of numerous studies, how the architecturally distinct type IIB family controls cleavage remains relatively unknown.

Topoisomerase VI (topo VI) is the prototypical type IIB topoisomerase, an A_2B_2 heterotetramer comprised of two Top6A protomers, which cleave DNA, and two Top6B protomers, which promote strand passage through ATP turnover (Buhler et al., 1998, 2001). Topo VI is thought to serve as the primary topoisomerase for DNA decatenation and the

relaxation of DNA supercoils in archaea, and also is required for endoreduplication and cell growth in plants (Bergerat et al., 1994; Bergerat et al., 1997; Hartung et al., 2002; Sugimoto-shirasu et al., 2002; Yin et al., 2002). Topo VI is found in sporadically throughout the bacterial domain, and a single chain variant, topo VIII, is found in certain plasmid-based mobile elements as well (Forterre et al., 2007; Gadelle, Krupovic, Raymann, Mayer, & Forterre, 2014). Interestingly, the type IIB topoisomerase scaffold is found across eukaryotes in the spo11 meiotic recombination initiation machinery, where it introduces double-strand breaks which lead to homologous crossovers (Bergerat et al., 1997; Keeney et al., 1997; Robert et al., 2016; Vrielynck et al., 2016) Type IIB topoisomerases use a similar set of functional domains to type IIA topoisomerases, and the ATPase region of the two enzyme classes share a similar architecture (Bergerat et al., 1997; Corbett & Berger, 2003; Wigley et al., 1991). The domains in the breakage-reunion region, however, take on a starkly different tertiary and quaternary structure, with type IIB enzymes lacking the third dimerization interface present in their type IIA counterparts (Berger et al., 1996; Corbett et al., 2007; Graille et al., 2008; Nichols et al., 1999; Schmidt et al., 2012).

Of the type II topoisomerase classes, the type IIB enzymes have evolved a particularly stringent set of controls against promiscuous strand scission (Buhler et al., 1998, 2001). At present, type IIB topoisomerases are thought to employ a gating strategy where the ATPase region must stably dimerize before the breakage-reunion region dissociates and separates the transiently cleaved G-segment DNA. How topo VI physically coordinates ATP binding and hydrolysis to DNA strand passage, and prevents uncontrolled double strand breaks remains obscure. For type IIA topoisomerases, the third dimerization interface in their breakage-reunion region introduces redundancy that may ensue at least two interfaces are associated when the T-segment passes through the G-segment. That topo VI lacks a redundant third dimer interface introduces a greater risk for double-strand break formation through holoenzyme dissociation (Bates et al., 2011). No DNA-bound structure of topo VI has yet been determined, although structures of the Top6A-subunit dimer reveal a ~55 Å long DNA binding channel that could accommodate ~18-20 bp of duplex DNA (K. D. Corbett et al., 2007; Graille et al., 2008; Nichols et al., 1999). It is unclear how tight control of strand cleavage, specific targeting of supercoiled or interlinked DNA molecules, or a recently reported DNA bending activity of topo VI (Thomson et al., 2014) could arise from such a minimal interface. Why the nucleolytic elements of top6A require activation by nucleotide binding to top6B, when similar control is not observed in type IIA topoisomerases systems, is also unknown (Gellert et al., 1977; Kato et al., 1992; Sander & Hsieh, 1983; Sugino et al., 1977).

To better understand how type IIB topoisomerases stringently couple ATP hydrolysis to the introduction of double-strand DNA breaks, we performed a broad biochemical investigation of *Methanosarcina mazei* topo VI, a model mesophilic type IIB topoisomerase., We find that topo VI possesses an ability to discriminate between linear and supercoiled DNA using an extensive and unanticipated DNA binding interface. Both nucleolytic activity by Top6A and gate closure and ATP hydrolysis by Top6B require DNA engagement along this entire interface. Functional mutagenesis shows that three conserved positively charged regions on the B-subunit are responsible for sensing the DNA bends and crossings present in supercoiled substrates, for

engaging both G- and T-segment DNA, and for coupling DNA binding to B-subunit dimerization, nucleotide binding, and DNA strand scission. Our results explain why type IIB topoisomerases absolutely depend upon the ATPase activity of the B-subunit to generate double strand breaks. These observations reinforce the functional importance for DNA bending and potential T-segment sensing elements in the related type IIA topoisomerases, and also suggest how the recently discovered meiotic Top6B homologs might promote Spo11 mediated strand scission during meiotic recombination.

Results

Topo VI is a distributive DNA relaxase that preferentially recognizes DNA crossings

We began our investigations of type IIB topoisomerase mechanism by measuring the affinity of *M. mazei* topo VI for DNAs of varying length or topological status. The relative affinity of the holoenzyme was first assessed for DNAs ranging from 20bp (the predicted length of the G-segment DNA binding channel of the A subunits (Nichols et al., 1999)) to 70bp in length. Topo VI was incubated with fluorescein-labeled duplex DNAs based on a previously-determined, DNA-cleavage hotspot (Buhler et al., 2001) (**Supplemental Materials**) and measurements were performed by fluorescence anisotropy. Binding assays with our substrate panel showed that whereas a 20bp duplex binds relatively weakly to topo VI, apparent affinity increased with length, plateauing between 40-70bp (**Figure 3.1a**). As the binding isotherms did not show any sign of complex interactions, such as cooperativity, and could be fit well by a single-site binding model (Heyduk & Lee, 1990; Inglese, Blatchly, & Benkovic, 1989), this result provided the first clue that topo VI might have a more extensive interaction with DNA with than previously hypothesized.

To determine whether topo VI displayed any preference for certain DNA topological states, the relative binding affinities of the holoenzyme were next assessed for supercoiled plasmid *vs*. sheared, linear salmon-sperm DNA using a competition assay. Topo VI was first bound to the fluorescein-labeled 70bp duplex DNA and varying amounts of unlabeled, supercoiled plasmid or sheared salmon-sperm DNA were added to the binding reactions. The relative affinity of topo VI for each substrate was determined by monitoring how well the competitor DNAs interfered with binding of the labeled probe. The response to the titration of supercoiled DNA or sheared salmon sperm DNA was fit to an explicit competitive binding model (Wang, 1995) to indirectly estimate affinities for the unlabeled substrates. Based on these measurements, topo VI showed a ~60-fold preference for supercoiled DNA ($K_{I,app}$ = 0.6±0.3nM) compared to sheared salmon sperm DNA ($K_{I,app}$ = 39.3±2.6nM) (**Figure 3.1b**). This finding shows that topo VI preferentially recognizes features in supercoiled DNA not present in torsionally-unconstrained linear substrates.

In principle, topo VI might preferentially engage supercoiled DNA crossings, bends, or both. To distinguish between these recognition modes, we examined the time-dependent processivity of topo VI in relaxing negatively-supercoiled DNA. For type II topoisomerases in general, processivity relates to the ability of a single enzyme to remain bound to a DNA

segment during multiple passage events. For topo VI, the progress of ATP-dependent supercoil relaxation was followed by native agarose-gel electrophoresis, using a slight molar excess of plasmid over enzyme to disfavor the binding of two topo VI molecules to a single DNA substrate (**Figure 3.2a**). A processive topoisomerase, such as *Saccharomyces cerevisiae* topo II, shows high processivity (**Figure S3.1a**), as evidenced by an absence of DNA topoisomers between the supercoiled substrate and fully-relaxed product plasmids. In contrast, topo VI produced a broad distribution of intermediate topoisomers that are gradually converted to the fully-relaxed distribution. This behavior suggests that topo VI operates by a predominantly distributive enzymatic mechanism.

To more thoroughly investigate supercoil processing by topo VI, we followed plasmid relaxation using two differently-sized plasmids in a chase experiment. Following pre-incubation of a defined amount of topo VI with a slight molar excess of a primary 2.9 kb plasmid, a second, larger plasmid (13.5 kb) was added along with ATP to serve as a competing substrate for any dissociated enzymes (**Figure 3.2b**). In the case of a processive enzyme such as topo II, a fully relaxed topoisomer distribution of the primary plasmid can be seen before relaxation of the chase plasmid is observed (**Figure S3.1b**). By contrast, topo VI again displayed clearly distributive behavior, relaxing both plasmids simultaneously. Although assay conditions can modulate whether a topoisomerase acts processively or distributively (salt concentration in particular), both timecourse experiments were run under low-salt conditions where type IIA topoisomerases are processive. Collectively, these findings demonstrate that topo VI operates by a strongly distributive mechanism, indicating that once a DNA crossing is resolved by strand passage, topo VI will tend to dissociate from the substrate, and that engagement of a new crossing and/or bent DNA segment is an important factor for DNA rebinding.

Topo VI actively uses DNA crossings to couple ATP hydrolysis with DNA strand passage

A defining characteristic of type II topoisomerases is a need for ATP in driving efficient and rapid strand passage. In type IIA topoisomerases, DNA binding strongly stimulates ATPase activity (Lee et al., 2013; Lindsley & Wang, 1993; Liu et al., 1979; Mizuuchi, O'Dea, & Gellert, 1978; Osheroff, Shelton, & Brutlag, 1983; Akio Sugino & Cozzarelli, 1980). The coupling of DNA topological state to the magnitude of the ATP hydrolysis stimulation is variable, with examples of increased stimulation by a preferred topology (Anderson, Gootz, & Osheroff, 1998; Osheroff et al., 1983; Sugino & Cozzarelli, 1980), increased stimulation by a disfavored topology (Gubaev & Klostermeier, 2011; McClendon, Rodriguez, & Osheroff, 2005), or lack of topological preference reported in the literature (Harkins & Lindsley, 1998; Vaughn et al., 2005). To determine whether type IIB topoisomerases display any topology-dependent ATPase stimulation, we examined nucleotide turnover by topo VI in the absence and presence of either linear or supercoiled DNA substrates. ATP hydrolysis was measured by following depletion of NADH in a coupled assay at varying ATP concentrations to determine kinetics parameters (**Figure 3.2c**). Topo VI showed very low basal ATPase activity, with a K_m ~5-fold weaker than observed for type IIA topoisomerases (Göttler & Klostermeier, 2007; Lee et al., 2013; Lindsley & Wang, 1993; Osheroff et al., 1983; Sugino & Cozzarelli, 1980; Vaughn et al., 2005). Activity and ATP affinity (as judged by K_m) both increased upon addition of sheared salmon sperm DNA;

however, incubation with supercoiled DNA increased the maximal hydrolysis rate and decreased K_m further, yielding a catalytic efficiency (k_{cat}/K_m) ~4-fold greater than linear DNA and ~30-fold greater than the basal level of ATP turnover. The observation that supercoiled DNA is more effective than linear substrates in activating ATP turnover again indicates that topo VI interrogates DNA for specific topological features and further shows that its action is potentiated when these features are found.

ATP binding and hydrolysis by topo VI and many related GHKL-type ATPases (e.g., type IIA topoisomerases, Hsp90, MutL) rely on nucleotide-dependent dimerization of ATP-binding domains to elicit biological activity (Ali et al., 2006; Ban, Junop, & Yang, 1999; Ban & Yang, 1998; Dutta & Inouye, 2000; Shiau, Harris, Southworth, & Agard, 2006; Wigley et al., 1991). A mechanism in which supercoiled DNA binding, in particular T-segment engagement, promotes Top6B dimerization could thus explain why supercoiled DNA stimulates ATP turnover. To test this idea, we developed a Förster Resonance Energy Transfer (FRET) assay to monitor ATPase domain dimerization in the context of the topo VI holoenzyme. We first identified and mutated surface cysteines to non-reactive residues to create a fully functional "cys-lite" construct of the holoenzyme. Thr155 of top6B was then substituted with cysteine (**Figure S3.2a**). Dual labeling with donor (Alexa 555-maleimide) and acceptor (Alexa 647-maleimide) fluorophores yielded an enzyme population containing an expected labeled mixture of correctly labeled donor-acceptor enzymes (50%), and both acceptor-acceptor (25%) and donor-donor (25%) labeled enzymes (**Figure S3.2b**). The labeled topo VI holoenzymes were able to fully relax DNA, and showed only a slight impairment (~2-fold) for overall specific activity compared to wildtype topo VI (**Figure S3.2c**).

Using the labeled enzyme, bulk resting FRET efficiencies in the absence and presence of either linear or supercoiled DNA were first measured by scanning the spectral emission of both the donor and acceptor fluorophores under excitation at 530nm. The conformational response of the enzyme to AMPPNP, a non-hydrolyzable ATP analog, was then assessed for the enzyme alone and in the presence of each substrate both at a fixed point (**Figure 3.2d**) and over time (**Figure 3.2e**). The addition of linear DNA and to a greater extent, supercoiled DNA, was found to lead to small increases in FRET efficiency, suggesting DNA binding alone modestly alters the conformation of topo6B in the holoenzyme. The addition of AMPPNP, however, led to large differences in response, with FRET efficiency increasing rapidly with supercoiled DNA compared to linear DNA (AMPPNP produced detectable but minor changes when DNA was omitted). In conjunction with the greater stimulatory effect of supercoiled DNA on ATP hydrolysis, these data show that – unlike type IIA topoisomerases, whose ATPase regions efficiently dimerize in the absence of DNA (Gubaev & Klostermeier, 2011; Roca & Wang, 1992) (**Figure S3.3**) – topo VI utilizes the DNA geometries presented by supercoiled substrates to help favor nucleotide-dependent conformational changes associated with strand passage.

Three conserved elements in Top6B play a role in DNA binding, the sensing of DNA geometry, and the productive coupling of ATP hydrolysis to strand passage

Based on topo VI's ability to sense and utilize topological features in supercoiled DNA to promote activity, we set out to identify the structural elements responsible for this coupling. Working from an assumption that topology-sensing elements might consist in part of positively-charged residues on the B subunit, we mapped both the amino acid conservation derived from a multiple sequence alignment of top6B homologs and the electrostatic surface potential onto the known structure of *M. mazei* top6B using ConSurf and ABPS (**Figure 3.3a-c**)(Ashkenazy, Erez, Martz, Pupko, & Ben-tal, 2010; Baker, Sept, Joseph, Holst, & McCammon, 2001). By comparing positively-charged interfaces against sequence conservation, we were able to identify three different regions as candidate DNA interaction sites.

The first prospective locus consists of a trio of basic residues ($KGRR_{186\text{-}189}$) (**Figure 3.3d**) within the predicted T-segment binding cavity of topo VI. A second feature is a trail of conserved basic residues that runs from a C-terminal, α-helical stalk of Top6B (which connects the so-called "transducer" domain of the subunit to Top6A) to the lower surface of a Helix-2-turn helix (H2TH) domain that is embedded in the GHKL ATPase fold. Three amino acids in the C-terminal stalk stood out (R457, K399 and K401)(**Figure 3.3e**); of these, K401 comprises part of the so-called "WKxY motif", which is not only well conserved in Top6B, but is also a motif used to identify the Top6BL and Rec102 binding partners of Spo11 in metazoans (Robert et al., 2016). The third area of note, the H2TH domain, is of unknown function in topo VI, and serves as a nucleic acid-binding element in a diverse set of proteins such as FpG/Nei DNA glycosylases, s13 ribosomal proteins, and sIHF type nucleoid associated proteins (Brodersen, Jr, Carter, Wimberly, & Ramakrishnan, 2002; Sugahara et al., 2000; Swiercz, Nanji, Gloyd, Guarne, & Elliot, 2013; Zharkov et al., 2002). By comparing nucleic-acid bound structures of the H2TH domain from this broader set of proteins to top6B (**Figure S3.4**), we identified R263, K268 and K308 as candidate residues that might interact with DNA (**Figure 3.3f**).

Having identified three potential sites of supercoil sensing on the surface of top6B, six constructs were generated to assess the functional attributes of each region. Selected constructs included triple-neutral and triple-acidic mutations to the basic KGRR loop (KGRR→AGAA and EGEE, referred to as KGRR-AAA and KGRR-EEE), the C-terminal stalk (Lys399, Lys401, and Arg457 to alanine or glutamate, referred to as WKxY-AAA and WKxY-EEE), and the H2TH domain (Arg263, Lys268, and Lys308 to alanine or glutamate, referred hereafter as H2TH-AAA and H2TH-EEE). All six mutant topo VI holoenzymes were soluble upon expression, purified to homogeneity as judged by SDS-PAGE, and appeared well-behaved based on similar gel-filtration chromatography profiles as compared to the wildtype enzyme (**Figure S3.5**).

We next looked at the supercoil relaxation activity of the mutant enzymes compared to the wild-type as a function of enzyme concentration to assess overall activity. Both sets of KGRR and WKxY mutants (neutral and acidic) proved completely unable to relax supercoiled substrate (**Figure 3.4a**). By contrast, both sets of mutations to the H2TH region led to enzymes that were able to relax supercoiled DNA, but with ~20-30-fold lower efficiency than native topo VI. The

activity profiles seen in enzyme titration assays were corroborated by timecourse assays at fixed enzyme concentration (**Figure S3.6**). Collectively, these findings show that the Top6B KGRR loop and WKxY motif are essential components of the topo VI strand passage reaction, but that the H2TH domain, while important, is not strictly required for catalytic activity.

To further investigate the role of each DNA binding interface in the topo VI reaction cycle, the ATP hydrolysis activity of the six mutants was compared to wildtype enzyme in the presence of linear or supercoiled DNA. ATP hydrolysis rates were measured using an NADH coupled assay; however, for these experiments, ATP was held at 2mM, while the concentration of DNA substrate was varied to characterize the stimulatory effects of the substrate on each enzyme (**Figure 3.4b** and **Table 3.1**). No DNA-stimulated ATP turnover was observed for either the WKxY-AAA or WKxY-EEE mutants. Interestingly, the topo $VI^{H2TH\text{-}AAA}$ and topo $VI^{H2TH\text{-}EEE}$ enzymes, which exhibited large defects in strand passage, showed similar levels of ATP hydrolysis activity on both DNA substrates compared to wildtype topo VI. Moreover, whereas no ATP turnover was observed for the KGRR-AAA and KGRR-EEE mutants on linear DNA, both mutants showed an increased rate of ATP hydrolysis compared to wildtype on supercoiled DNA (albeit with a more weakly coupled response to DNA concentration than wildtype topo VI or the H2TH mutants as judged by K_m). Collectively, these data indicate that the abrogation of strand passage activity by the KGRR loop mutants stems in part from a loss of an essential DNA sensing motif required to complete strand passage. However, unlike the WKxY mutants, the KGRR loop mutants retain some feature which allows supercoiled DNA to promote ATP hydrolysis, resulting in pronounced futile cycling. Interestingly, mutations to the H2TH appear to largely decouple strand passage from ATP hydrolysis, yet do not appreciably alter the DNA dependence of ATPase activity, implying a role for this domain as well in facilitating A- and B-subunit coordination to minimize futile ATPase cycling.

Since all three interfaces identified affect strand passage activity and its coupling to ATP turnover, we next tested whether the observed differences in activity were a direct result of weakened binding to duplex DNA. Using fluorescence anisotropy, the affinity of each mutant was assessed for a range of duplex lengths (30, 40, 60, and 70 bp), which were found earlier to exhibit moderate-to-tight binding to wildtype topo VI (**Figure 3.1a**). Compared to the wildtype enzyme, the WKxY-AAA and WKxY-EEE mutants showed a marked defect in affinity for 40bp and longer DNAs, the magnitude of which was more severe for the acidic substitutions compared to the neutral changes (**Figure 3.5a** and **Figure S3.7**). This finding suggests the C-terminal stalk of Top6B constitutes an important DNA-binding interface, and that defects for both strand passage and ATP hydrolysis by the WKxY mutants may be explained in part by impaired DNA interactions. On the other hand, the KGRR loop and the H2TH domain mutants showed either small defects or no change in DNA affinity, suggesting that these regions play a role in sensing and coordinating T- and/or G-segment DNAs during strand passage, rather than contributing to tight substrate engagement *per se*.

Because the KGRR loop and H2TH domain mutants retained essentially wildtype affinity for short duplex DNAs, we wondered whether these motifs might instead play a role in the

preferential binding of topo VI to supercoiled DNA seen earlier (**Figure 3.1b**). To this end, the relative affinities of supercoiled plasmid and linear sheared salmon-sperm DNA were assessed for the more severe topo VI$^{KGRR\text{-}EEE}$ and topo VI$^{H2TH\text{-}EEE}$ mutants, using the fluorescence anisotropy-based competition assay described earlier (**Figure 3.5b**, and **Table 3.2**). Both substitutions resulted in a ~15-20-fold decrease of the overall affinity of topo VI for supercoiled DNA, with the topo VI$^{KGRR\text{-}EEE}$ adversely impacting the binding of linear DNA in a manner partially explained by small overall binding defects to short duplexes (**Figure 3.5a** and **Figure S3.7)**. Together, these data indicate that both the KGRR loop and H2TH domain contribute to preferential binding to supercoiled DNA, but that neither is solely responsible for the ability of topo VI to discriminate between different DNA topologies.

The KGRR loop specifically acts as a DNA crossing sensor, using T-segment engagement to promote Top6B dimerization

The biochemical and biophysical activities of our topo VI mutants directly implicate the KGRR loop and H2TH domain in coupling ATP hydrolysis to strand passage, rather than contributing to primary G-segment affinity. To test whether the KGRR loop or H2TH domain might thereby help to promote the DNA-dependent dimerization of Top6B upon ATP binding, we added the KGRR-AAA and H2TH-AAA mutations into the topo VI construct used to monitor the conformational status of the ATPase domain in our FRET-based assay. Following purification and labeling, we measured the emission spectra of both mutants alone and bound to supercoiled DNA. Similar to the wildtype construct, both the KGRR-AAA and H2TH-AAA mutants showed increased FRET efficiencies in the presence of supercoiled substrate, independent of nucleotide (**Figure S3.8**). The addition of AMPPNP produced a time-dependent FRET response in the H2TH-AAA mutant similar to that of native topo VI, indicating that the ATPase region of construct dimerizes in response to supercoiled DNA in a wildtype-like manner. By contrast, the addition of AMPPNP failed to elicit a FRET response for the KGRR-AAA mutant (**Figure 3.5c**). Given that the ATPase activity of the KGRR-AAA construct is actually more robust than wild-type topo VI in the presence of supercoiled DNA (**Figure 3.4b**), yet is catalytically dead for strand passage, this result indicates that the KGRR loop serves as a proofreading element to promote the formation of a stable, long-lived ATPase domain dimer in response to the binding of a supercoiled substrate, likely as means to mitigate futile ATPase cycling. In the absence of this interaction, top6B can reopen even if bound to nucleotide.

Although the KGRR loop in topo VI clearly senses some feature in supercoiled DNA that is used to promote strand passage activity, it was unclear whether these attributes might be DNA crossings or bends, both of which are present in plectonemic substrates. Based on the outcome of the competition assay, which showed a lower affinity of the KGRR-EEE mutant for supercoiled DNA, and on the physical location of the KGRR loop in the holoenzyme (**Figure 3.3**)), we hypothesized that this element might sense T-segment/G-segment crossings. To address this question, we designed a fluorescently-labeled, 20bp by 16bp Holliday junction substrate that can form a stacked-X structure (Duckett et al., 1988; Ortiz-Lombardía, González, Aymamí, Azorín, & Coll, 1999) as a mimic of a prospective duplex DNA crossover (**Figure S3.9a**). Using fluorescence anisotropy assays, wildtype topo VI was found to bind this substrate nearly

4-fold more efficiently compared to a single 20bp DNA duplex (**Figure 3.5d** and **Figure S3.9b**). We next asked whether mutations to the basic KGRR loop or the H2TH domain might interfere with binding of the Holliday junction substrate. Whereas both H2TH mutants showed similar affinities for the stacked-junction substrate as native topo VI, the KGRR mutants showed a clear, charge-dependent loss in affinity compared to a 20bp duplex (and little to no change in affinity for a 20 bp duplex alone) (**Figure 3.5d** and **Figure S3.9c-f**). When considered with our FRET data, this response implicates the KGRR loop as a DNA crossing sensor in topo VI, likely serving to engage a T-segment and couple that interaction to the control of coordinated ATPase domain function.

The H2TH interface engages an extended G-segment DNA to couple nucleotide-dependent Top6B dimerization with DNA cleavage.

Since the H2TH domain does not appear to participate in T-segment sensing (**Figure 3.5d**), yet is important for topo VI activity (**Figure 3.4a**), we considered whether the H2TH domain might interact with the G-segment instead. The H2TH domains reside far from the site of G-segment cleavage, which occurs in the Top6A subunits (Bergerat et al., 1997; Buhler et al., 1998; Corbett et al., 2007; K. D. Corbett & Berger, 2003; Graille et al., 2008; Nichols et al., 1999); however, a prior AFM study has observed that topo VI can bend DNA by 100-140° (Thomson et al., 2014). Based on this observation, we modeled duplexes of various bending angles into a structure of *Sulfolobus shibatae* topo VI that was captured with a fully open B-subunit conformation. This exercise suggested that a ~70bp DNA duplex with a smooth overall bend of ~100˚ could span the two H2TH domain present in the topo VI holoenzyme by running along the helical stalk of the Top6B transducer domains and through the topo VI A nucleolytic center (**Figure 3.6a**). Interestingly, the WKxY region resides along the modeled G-segment path, and a ~40bp DNA duplex appears sufficient to span between dimer-related WKxY motifs, a 50bp duplex sufficient to span to the edge of this region defined by Arg457. Interaction of the WKxY elements with G-segment DNA provides a structural rationale for the length-dependence of duplex DNA binding observed for wildtype topo VI (**Figure 3.1a**), and also explains the strong length-dependent DNA binding deficiencies observed for the WKxY-EEE mutant in particular (**Figure 5a**). This curved G-segment interface might also explain the impaired ability of nonspecific linear DNA to compete with our short duplex probe for topo VI$^{KGRR\text{-}EEE}$ binding (**Figure 3.5b**). Because the KGRR-EEE mutant appears to lack a T-segment binding interface (**Figure 3.5d**), any preference in the G-segment interface for bendable sequences (potentially the preferential cleavage sequence used as a probe in the competition experiments) over random sequences would be exacerbated for KGRR-EEE as compared to the native enzyme.

The minimal DNA size required for high-affinity binding of short, linear duplexes levels off around 40bp (**Figure 1a**). This finding indicates that if the H2TH domains do engage longer G-segment DNAs, they do not contribute appreciably to affinity, and instead suggests that the H2TH domains might help bend DNA, serve as sensors for pre-bent substrates, and/or help couple B-subunit dimerization to G-segment cleavage or strand passage. To test these ideas, we assessed the minimal length of DNA required for nucleotide-dependent G-segment cleavage. Topo VI was incubated with 40, 60, 70, or 80bp long fluorescently-labeled duplexes in the

absence of nucleotide, or with ATP or AMPPNP. To assess activity, reactions were analyzed by denaturing urea-formamide PAGE to separate cleaved and uncleaved oligonucleotide products. Topo VI produced clear products of the expected size for oligo-centered cleavage events in the presence of either ATP or AMPPNP on the 70bp duplex. Faint cleavage products were also produced on the 60bp duplex, but only in the presence of AMPPNP. No cleavage was seen for any condition on the 40bp duplex (**Figure 3.6b**).

To further test whether the H2TH domains might be responsible for the observed length dependence of the G-segment cleavage reaction, we assessed the nucleotide-dependent cleavage activity of our functional mutant panel on the 70bp duplex. Both topo VI$^{KGRR\text{-}AAA}$ and topo VI$^{KGRR\text{-}EEE}$ were competent for AMPPNP-dependent cleavage, whereas topo VI$^{WKxY\text{-}AAA}$ and topo VI$^{WKxY\text{-}EEE}$ showed decreased cleavage activity, with the triple glutamate substitution proving more severely compromised. These results are consistent with the relative affinities the mutant enzymes show for this DNA substrate (**Figure 3.5a**); by contrast, neither H2TH mutant proved capable of supporting DNA cleavage (**Figure 3.6c**). Collectively, these findings support the idea that for a G-segment to bind productively to the Top6A dimer, it must be sufficiently long to engage the H2TH domains on Top6B, and therefore be subject to conformational changes induced in this subunit upon binding ATP. The inability of a 40bp duplex to support cleavage, even though this DNA binds with higher affinity than a short duplex and is long enough to reach both WKxY motifs, suggests G-segment DNAs must engage both H2TH regions before strand scission can be triggered.

One implication of the H2TH contacts to the distal arms of an associated G-segment is that ATP-binding and ATPase domain dimerization might lead to more substantial G-segment bending. To test this prediction, we labeled opposing ends of the 70bp duplex with Cy5 and Cy5.5 and monitored changes in the end-to-end distance by FRET for native topo VI and our panel of mutants. Bulk FRET efficiencies in the absence and presence of enzyme were measured by exciting at 630nm and scanning the spectral emission of both the donor and acceptor fluorophores (**Figure 3.6d**). The time-dependent conformational response to the addition of AMPPNP was also assessed. The addition of wild-type topo VI led to a modest FRET increase, a result indicative of G-segment bending that also accords prior AFM data (Thomson et al., 2014). Addition of the KGRR mutants alone also showed a similar FRET increase, whereas both sets of WKxY and H2TH mutants yielded a nucleotide-independent response between that of wild-type topo VI and duplex alone. Upon adding AMPPNP, FRET efficiency rapidly increased further for duplex incubated with topo VI, topo VI$^{KGRR\text{-}AAA}$ or topo VI$^{KGRR\text{-}EEE}$, indicating that nucleotide-driven dimerization of the ATPase regions leads to additional DNA bending. Topo VI$^{WKxY\text{-}AAA}$ and topo VI$^{WKxY\text{-}EEE}$ also produced a FRET increase in the presence of AMPPNP, albeit with greatly slowed kinetics. By contrast, topo VI$^{H2TH\text{-}AAA}$ and topo VI$^{H2TH\text{-}EEE}$ were unable to support any nucleotide-dependent increase in FRET. Together, these observations both support a model where topo VI engages G-segment DNA with an interface spanning both H2TH domains, and that strand scission is stimulated by the bend induced upon Top6B dimerization.

Discussion

A new model for ATP-dependent coordination of strand passage by type IIB topoisomerases.

Type II topoisomerases are universally conserved molecular machines required for managing DNA topology. All cells utilize at least one type IIA or type IIB topoisomerase for catalyzing duplex strand passage events. These two enzyme families possess a common set of catalytic domains needed for ATPase activity and DNA cleavage, but diverge significantly in their overall tertiary and quaternary architecture. Numerous efforts have steadily revealed the finer details of DNA engagement, dimerization, allosteric communication, and subunit coordination for type IIA topoisomerases (Schoeffler & Berger, 2008; Vos et al., 2011); however, this understanding is largely lacking for the type IIB enzymes. This knowledge gap is unfortunate, as the type IIB topoisomerase scaffold is broadly used in nature – serving as the primary agent for DNA decatenation in archaea (Bergerat et al., 1997; Forterre et al., 2007), endoreduplication in plants (Hartung et al., 2002; Sugimoto-shirasu et al., 2002; Yin et al., 2002), and as part of the meiotic recombination initiation machinery in eukarya (Bergerat et al., 1997; Robert et al., 2016; Vrielynck et al., 2016) – and is further found in several bacteria species and plasmid-based integrated mobile elements (Forterre et al., 2007; Gadelle et al., 2014). Type IIB topoisomerases present a unique architectural and enzymatic solution to duplex strand passage by cleaving DNA in a stringently nucleotide-dependent manner requiring the regulatory B-subunit, a feature not true for type IIA systems (Buhler et al., 1998, 2001; Gellert et al., 1977; Kato et al., 1992; Sander & Hsieh, 1983; Sugino et al., 1977). It is how this regulatory B-subunit activates nucleolytic activity that remains poorly defined.

Using a range of biophysical and biochemical approaches, we show here that *M. mazei* topo VI, a prototypical type IIB topoisomerase, not only recognizes DNA crossings and bends of a supercoiled substrate, but in fact exploits these topological features to promote and tightly couple ATPase function and dynamics to DNA cleavage and strand passage. In doing so, topo VI has evolved elements that suppress futile ATP hydrolysis and promiscuous DNA cutting. We identified and validated three DNA binding interfaces on topo VI crucial for these coupling activities: a basic interface along the C-terminal stalk of the B-subunit that includes a conserved WKxY motif and is required for robust G-segment binding (**Figure 3.5a**, **Figure 3.7**, *step 1*), a basic loop that senses DNA crossings, engages T-segments and links strand passage to controlled ATP turnover(**Figure 3.4b**, **Figure 3.5b-d**, **Figure 3.7** step 2-3), and the H2TH DNA binding domain, which promotes G-segment bending and couples DNA cleavage with ATPase domain dimerization (**Figure 3.6**, **Figure 3.7**, step 3). All three DNA interacting elements reside on top6B, providing a molecular basis for why this subunit is absolutely essential for nucleolytic activity in the A-subunit (Buhler et al., 1998, 2001).

This model for type IIB topoisomerase strand passage provides a mechanism both for how ATP induced conformational changes between the transducer and GHL domain (Classen et al., 2003; Corbett & Berger, 2003; Lamour et al., 2002; Wigley et al., 1991) promote G-segment cleavage, and for how T-segment engagement prevents futile ATP hydrolysis and unnecessary strand scission events. Our data suggest that topo VI coordinates ATP binding with DNA break

formation through two forms of conformational gating. In the absence of DNA, top6B takes on a predominantly open conformation in the context of the holoenzyme (Corbett et al., 2007; Graille et al., 2008), but binding of an intrinsically bent G-segment (as found in supercoiled or catenated DNA) to an interface that extends to the H2TH domains in Top6B (**Figure 3.1a**, **Figure 3.6a**) allows topo VI to more readily access a dimerized B-subunit conformation (**Figure 3.2c-e**). Nucleotide binding subsequently induces a sharper bend in the G-segment through the H2TH domain (**Figure 3.6d**), an event directly correlated with G-segment cleavage (**Figure 3.6c**). This physically couples cleavage to ATP-dependent conformational changes, which in turn is dependent upon binding to bends present in supercoiled DNA.

In terms of T-segment coordination, our data show that topo VI physically couples T-segment engagement to both ATP hydrolysis and DNA cleavage. The KGRR loops in top6B bind T-segment DNA (**Figure 3.5b-d**), and this interaction promotes ATP binding and formation of the T-segment storage cavity, based on the loss of ATPase stimulation by linear DNA for the KGRR mutants (**Figure 3.4b**). While sufficient, T-segment engagement is not required for closure, as a pre-bent G-segment also promotes B-subunit dimerization and ATP hydrolysis (**Figure 3.4b**, **Figure 3.6d**). However, based on the ATPase and bulk FRET experiments, T-segment DNA additionally stabilizes gate closure and potentially promotes an additional conformational change subsequent to B-subunit dimerization (**Figure 3.2d-e**, **Figure 3.4b**, **Figure 3.5c**) with nucleotide-bound top6B quickly dissociating in the absence of a T-segment (**Figure 6b**). This minimizes the chances for spurious G-segment cleavage. Since the T-segment storage cavity is too small to accommodate duplex DNA when fully closed, the T-segment's role in stabilizing B-subunit dimerization may then also potentiate A-subunit opening (Corbett et al., 2007; Corbett & Berger, 2005; Graille et al., 2008).

Type IIA and IIB topoisomerases use alternative architectures to reach common solutions to the challenges of strand passage

Due to divergent architecture, it was unclear how closely type IIB topoisomerase coordination of strand passage might mirror type IIA topoisomerases. Our results reveal both convergent and divergent mechanisms. It is striking that both type II topoisomerase classes use DNA bending and deformation to promote G-segment cleavage. While it is well established that type IIA topoisomerases bend G-segment DNA to promote strand scission (Bax et al., 2010; Dong & Berger, 2007; Hardin et al., 2011; Laponogov et al., 2009; Lee et al., 2013; Lee et al., 2012), type IIB topoisomerases have only recently been proposed to bend DNA as well (Thomson et al., 2014). Our results both support this proposal that topo VI bends DNA, and further implicate bending as a critical step for activating top6A nucleolytic activity (**Figure 3.6**). The H2TH domain used by topo VI is unique to the type IIB enzymes, yet type IIA topoisomerases also use elements beyond their breakage-reunion core to bend G-segment DNA (McClendon et al., 2005; Papillon et al., 2013; Reece & Maxwell, 1991; Schmidt et al., 2012; Seol et al., 2013; Vos et al., 2013). That an extended G-segment interface has evolved multiple times suggests this feature imparts a functional advantage. Perhaps an extended interface generates more stringent control of G-segment cleavage, particularly if phosphate backbone deformation promotes TOPRIM/WHD nuclease activity (Lee et al., 2013; Lee et al.,

2012; Wu et al., 2011). This would suggests other TOPRIM containing nucleases (e.g. OLD family, spo11 (Aravind et al., 1998)) might also require DNA bending to promote strand scission.

Our data also provide new perspective on how the differing number of T-segment storage cavities present between type IIA and type IIB topoisomerases may reflect alternative approaches to T-segment engagement. Both classes share an N-terminal cavity formed by the ATP-gate and DNA-gate, but type IIA topoisomerases also have a second C-terminal cavity formed by a third dimer interface. Biochemical and structural evidence suggests this C-terminal cavity proof-reads T-segment DNA, allowing backtracking and biasing against re-catenation (Martinez-Carcia et al., 2014; Papillon et al., 2013; Roca, 2004; Roca et al., 1996; Schmidt et al., 2012). Our data suggest formation of the single topo VI storage cavity serves as a form of T-segment proof-reading as well. This proof-reading arises from two behaviors; the binding of DNA crossings promotes formation of the cavity, and cavity formation is otherwise stringently inhibited. This ensures hydrolysis is efficiently coupled with strand passage on supercoiled substrate (**Figure 3.2c-e**). Considering the N-terminal cavity of type IIA topoisomerases highlights the key importance of inhibited dimerization in topo VI. Type IIA enzymes in fact retain potential T-segment sensing elements in the N-terminal cavity ((Tingey & Maxwell, 1996) see **Figure S3.10** for other conserved residues) however this interface readily dimerizes in the absence of DNA ((Gubaev & Klostermeier, 2011; Roca & Wang, 1992), **Figure S3.3**). For yeast topo II this results in high levels of futile ATP hydrolysis (Lindsley & Wang, 1993). *E.coli* DNA gyrase and Topo IV show coupling of ATP hydrolysis to strand passage similar to that observed for topo VI (**Figure 3.2a,c**, (Basu, Schoeffler, Berger, & Bryant, 2012; Bates, O'Dea, & Gellert, 1996; Lee et al., 2013; Sugino & Cozzarelli, 1980)), however, both bacterial homologs accomplish this by engaging the T-segment with an additional DNA binding domain in the breakage-reunion region (a solution also employed by human topo IIα) for which there is no analog in topo VI (McClendon et al., 2008; Papillon et al., 2013; Reece & Maxwell, 1991; Vos et al., 2013).

Since both type II topoisomerase classes share an ancestral ATPase region that was likely recruited twice to two different breakage-reunion architectures (Forterre et al., 2007), it is interesting that T-segment engagement and proof-reading is primarily accomplished by the ATPase region for type IIB topoisomerases, and by the breakage-reunion region for type IIA topoisomerases. This suggests some sort of topology proof-reading was already present in the ancient type IIA breakage-reunion enzyme but not in the ancient type IIB breakage-reunion enzyme, and that topology sensing may have evolved in the top6B subunit subsequent recruitment of the A-subunit. Overall, specific and coordinated T-segment engagement by type II topoisomerases in both classes appear to arise not from a conserved architecture, but from distinct motifs that have convergently evolved to prevent aberrant DNA cleavage and minimize futile ATP hydrolysis.

Broader implications for the cellular context of topo VI

When considering *Mm* topo VI's role in addressing the topological strain induced by the temporally sensitive processes of transcription, replication and chromosome segregation *in*

vivo, two biochemical properties reported here are highly unusual. First, there is no clear advantage to topo VI's distributive supercoil relaxation activity (**Figure 3.2**), especially upon considering the clear advantage of processive strand passage for removing local build-up of super-helical tension produced by transcription or replication (Chong, Chen, Ge, & Xie, 2014; Khodursky et al., 2000; McClendon et al., 2005; Neuman, Charvin, Bensimon, & Croquette, 2009; Vos et al., 2013). Second, the maximal observed ATPase hydrolysis and strand passage rates for *Mm* topo VI (**Figure 3.2a,c**) are ~50-100-fold slower than rates generally observed for type IIA topoisomerases (Basu et al., 2012; Bates et al., 1996; Göttler & Klostermeier, 2007; Higgins, Peebles, Sugino, & Cozzarelli, 1978; I. Lee et al., 2013; Lindsley & Wang, 1993; Osheroff et al., 1983; Sugino & Cozzarelli, 1980; Vos et al., 2013). This difference raises the question of which cellular functions topo VI's slow activity is sufficient for in archaea. Directly comparing *in vitro* activity is inadequate to answer this question as variation in topoisomerases repertoires, genome sizes and generation times between species might account for the difference.

Based on the set of encoded topoisomerases in *M. mazei,* topo VI likely takes on similar cellular responsibilities to *E.coli* topo IV and *S. cerevisiae* Topo II and so may be compared against them (Bergerat et al., 1994; Corbett et al., 2007; Forterre et al., 2007; Goto & Wang, 1982; Holm et al., 1985; Schoeffler & Berger, 2008; Zechiedrich & Cozzarelli, 1995). Normalizing the strand passage rate of *Mm* topo VI, *Ec* topo IV and *Sc* topo II to genome size, copy number and doubling time may thus serve as a useful estimate of cellular workload required for each enzyme *in vivo*. Such an exercise (**Supplemental Materials**) yields workloads within ~20% for yeast and *E. coli* but would require ~50-fold greater activity from topo VI for it to accommodate a similar cellular role in *M. mazei.* While the *in vitro* topo VI activity reported here appears insufficient to perform the cellular roles required of the enzyme, a few modifications to some underlying assumptions may account for this discrepancy. For instance, the difference between the *in vitro* and *in vivo* rate of strand passage may be much greater for topo VI than for topo IV or topo II. Topo VI may have a higher cellular copy number than topo II or topo IV, or the relative balance between topo VI decatenase and topo III hemi-decatenase activity in chromosome unlinking may be greatly skewed towards topo III. Alternatively, a cellular factor not reconstituted in our biochemical assays might enhance topo VI activity. If true, this last explanation has intriguing ramifications.

One way an interacting factor might accelerate topo VI's strand passage rate would be by increasing enzyme processivity. The distributive behavior of the topo VI heterotetramer would then be understood as an additional auto-inhibitory mechanism, only released once topo VI is in the correct spatiotemporal or chromosomal context. Intriguingly, multiple protein factors in *Arabidopsis thaliana* bind topo VI, and mutating these factors impart endoreduplication deficient phenotypes similar to directly mutating *A. thaliana* top6B or *A. thaliana* top6A (Breuer et al., 2007; Hartung et al., 2002; Kirik, Schrader, Uhrig, & Hulskamp, 2007; Sugimoto-shirasu et al., 2005, 2002; Yin et al., 2002). It has been suggested these factors are obligate components of the topo VI machinery in plants (Forterre & Gadelle, 2009). If factors performing a similar role exist for archaeal topo VI, it may be that the top6A and top6B

subunits are simply the core of a larger complex which is the actual *bona fide* type IIB topoisomerase machinery in both archaea and in plants.

Implication for substrate and co-factor driven dimerization as a crucial feature of GHL ATPases.

The ATPase region of type IIA and type IIB topoisomerases appears in three other classes of molecular machines that perform cellular tasks distinctly unrelated to managing DNA topology, the Hsp90 protein-folding chaperones, the MutL mismatch repair (MMR) machinery mediating factor, and the microchidia (MORC) ATPases involved in transcriptional and chromatin control (Dutta & Inouye, 2000; Iyer et al., 2008). Together these enzymes comprise the historically termed "GHKL" (Gyrase, Hsp90, Histidine Kinase, MutL) superfamily, though when discussing just the ATPases "GHLM" (GHL, MORCs) is perhaps more accurate. The GHLM architecture retains well-conserved dimerization response to ATP binding across this diverse set of molecular machines, but hydrolysis rates vary greatly from class to class (Ban et al., 1999; Li et al., 2016; Prodromou et al., 2000; Wigley et al., 1991). Interestingly, topo VI's ATPase activity (**Figure 3.2c**) shows greater similarity to Hsp90, MutL, and MORC ATPases, namely a low basal hydrolysis rate and stringent dependence on proper substrates to stimulate ATPase activity, than to type IIA topoisomerases (Ban et al., 1999; Ban & Yang, 1998; Lindsley & Wang, 1993; Osheroff et al., 1983; Panaretou et al., 1998; Street, Lavery, & Agard, 2011; Sugino & Cozzarelli, 1980).

Topo VI's gate closure response to T-segment DNA (**Figure 3.2d-e**) parallels the behavior of Hsp90, for which client protein or co-chaperone engagement, as much if not more so than nucleotide binding, drive GHLM domain dimerization (Ali et al., 2006; Hessling, Richter, & Buchner, 2009; Wolmarans, Lee, Spyracopoulos, & Lapointe, 2016). While MutL ATP binding and hydrolysis is modulated by a broad array of MMR factors (Acharya, Foster, Brooks, & Fishel, 2003; Kadyrov, Dzantiev, Constantin, & Modrich, 2006; Kunkel & Erie, 2005; Pillon et al., 2010) this has not been directly linked to biasing ATPase dimerization. Based on the mechanistic parallels between Hsp90 and topo VI, it may be revealing to look at how MMR factor binding affects the conformation of the MutL GHLM domain, and whether these factors might promote dimerization. Initial characterization MORC ATPases also provides evidence of cofactors binding a GHLM dimer (Li et al., 2016). Topo VI's ATPase activity thus adds to a growing paradigm for GHLM ATPases, wherein basal ATP hydrolysis is inhibited, and it is conformational changes induced by substrate and co-factors that promote ATP binding. In such a paradigm, type IIA topoisomerases would provide an exception which proves the rule.

Similarities and differences to the MTopo6B/Topo6BL/Rec102-Spo11 meiotic recombination machinery

One of the great surprises from the discovery of topo VI was the existence of homology between top6A and the eukaryotic meiotic recombination protein Spo11 (Bergerat et al., 1997; Keeney et al., 1997), the protein which generates double strand DNA breaks for initiating meiotic recombination. The finding that top6A required top6B for generating double strand

breaks (Buhler et al., 1998) prompted the search for a similar regulatory factor in meiotic recombination. Structurally homologous counterparts to top6B (MTop6B in plants, Top6BL in mammals, Rec102 in *S. cerevisiae,* and Mei-P22 in *Drosophila*) have recently been found to partner with spo11 (Robert et al., 2016; Vrielynck et al., 2016). As our work shows that top6A-dependent cleavage relies on direct engagement and bending of target DNA by the top6B subunit (**Figure 3.5a**, **Figure 3.6**), this predicts that spo11 partner factors might directly bind to hotspot DNA and may bend or remodel target DNA in order to activate spo11 cleavage. Interestingly, the G-segment binding WKxY motif is the most stringently conserved feature between top6B and its meiotic counterparts (Robert et al., 2016), which suggests this element may play a similar role by binding target DNA in the meiotic recombination machinery.

In addition to binding DNA, Top6B dimerization bends DNA to potentiate cleavage. Might the meiotic top6B counterparts prompt spo11-mediated cleavage in a similar fashion? Surprisingly, two critical components for the top6B-mediated DNA bending are either degenerate or missing in meiotic top6B homologs. First, both Topo6BL and MTopo6B contain a highly degenerate GHLM domain which lacks essential elements required for both ATP binding and stable GHLM dimerization; in fact only the purine binding elements are conserved ((Ali et al., 2006; Ban et al., 1999; Corbett & Berger, 2003; Dutta & Inouye, 2000; Li et al., 2016; Wigley et al., 1991) and **Figure S3.11**). This suggests neither protein binds ATP or dimerizes, at least not in a fashion similar to top6B. Rec102 and Mei-P22 lack a GHLM domain entirely. Second, the H2TH domain which couples top6B dimerization to G-segment DNA bending is either missing or replaced by a structurally unrelated insert (Robert et al., 2016; Vrielynck et al., 2016). Perhaps the meiotic recombination machinery does not use a dimerization or bending mechanism to cleave hotspot DNA. However, this would be difficult to reconcile with top6A's clear reliance on top6B-mediated DNA bending to promote cleavage (**Figure 3.6**). Rather, our data would predict spo11 still requires DNA bending to cleave, however, this is likely accomplished by a structurally divergent mechanism. Potential mechanisms might include unidentified DNA binding elements in the meiotic top6B counterparts, additional partner factors for bending DNA or promoting dimerization, or some purine-containing effector other than ATP, which may bind to the degenerate GHLM domains in the meiotic topo6B counterparts.

Concluding remarks

Here, we have presented a fundamentally new model for how type IIB topoisomerases exploit the topological features of supercoiled DNA to coordinate nucleotide-dependent duplex strand passage activity in a manner that both protects against promiscuous DNA cleavage and minimizes futile ATP hydrolysis. We identified previously unrecognized elements in the regulatory B-subunit which engage both G-segment and T-segment DNA, and determined how this recognition allows DNA substrates to actively drive conformational changes in topo VI. These elements provide a rationale for why the B-subunit is stringently required for DNA cleavage by type IIB topoisomerases, but not by type IIA topoisomerases. Our work predicts a specific set of structural interactions between topo VI and DNA, yet to validate the model presented here an atomic resolution structure will be required. While no DNA-bound structure of a type IIB topoisomerase yet exists, the unanticipated extent of the enzyme-DNA interactions

hints at why such a structure may have eluded the field thus far. The possibility that the topo VI hetero-tetramer may only be the core of the *in vivo* type IIB topoisomerase machinery suggests a more concerted search for archaeal topo VI interacting partners and analysis known partners in plants is needed. Finally, while the meiotic top6B counterparts diverge from Top6B in several critical ways, the model presented here for topo VI delineate the set of activities that may be required to activate spo11-mediated cleavage. Further work will be required to determine how closely the Spo11 meiotic recombination machinery mirrors topo VI.

Materials and Methods

Cloning of M. mazei topo VI functional mutant vectors

Cloning of *M. mazei* topo6B in frame with an N-terminally fused His6-tobacco etch virus (TEV) protease-cleavable tag and *M. mazei* topo6A into a polycistronic expression vector was previously described (Corbett et al., 2007). Oligonucleotides used for mutagenesis were obtained from Integrated DNA Technology (IDT, Coralville, IA USA). Mutant constructs were generated using either PCR amplification of the expression vector with primers containing the desired point mutations in conjunction with blunt-end ligation, or by quick-change site-directed mutagenesis (Agilent, Santa Clara, CA). The following mutations were added to generate the "cys-lite" construct: C267S, C278A, C316A and C550A, all in top6B. Mutagenesis was verified by Sanger sequencing (Genewiz LLC, South Plainfield, NJ, USA).

Protein expression and purification

Topo VI and functional mutant variants were overexpressed in *E.coli* BL21codon-plus(DE3)-RIL cells (QB3-Macrolab, University of California, Berkeley) grown in ZYM-5052 auto-induction media (Studier, 2005). Wildtype topo VI was expressed in cultures grown at 37°C, whereas cultures expressing functional mutant constructs were shifted to 25°C upon reaching an OD_{600} of 0.4-0.6. The topo $VI^{KGRR\text{-}AAA}$ FRET construct was grown at 37°C to an OD_{600} of 2-3 in M9ZB media (Studier, 2005), cooled to 18^{o}C, and then induced with IPTG (250µM final concentration) and grown overnight. In all cases cultures were harvested by centrifugation at 24hrs following inoculation, resuspsended in buffer A [20mM HEPES-KOH pH 7.5, 800mM NaCl, 20mM Imidazole, 10%(v/v) glycerol, 1ug/mL pepstatin A, 1ug/mL leupeptin, 1mM PMSF], and frozen drop-wise into liquid nitrogen for storage at -80°C.

Proteins were purified as previously described ((Corbett et al., 2007), also see the **Supplemental Methods** for a more detailed protocol). Briefly, topo VI tetramer was purified from cell lysate using nickel-affinity chromatography, followed by cation and anion exchange in series to remove contaminants. Following tag removal by His_6-TEV protease and a second nickel-affinity step, untagged topo VI was polished by size-exclusion chromatography, concentrated, and flash frozen in storage buffer [HEPES-KOH pH 7.5, 300mM KCl, 30% (v/v) glycerol, 1mM Trisphosphine hydrochloride (TCEP)] for use in subsequent biochemical and biophysical studies.

DNA binding and competition

DNA substrates were resuspsended in ddH_2O and annealed from oligomers (**Table S3.1**) obtained from IDT. Annealing of stacked junction substrates followed previously published protocols (Duckett et al., 1988) with a few modifications. The junction was prepared in 25mM Tris HCl pH 7.9, 25mM NaCl, 10mM $MgCl_2$ and annealed by heating at 70°C for 2 hours, followed by cooling at 0.5°C/min to 4°C. Annealing reaction products were loaded onto a 5mL HiTrap-Q anion exchange column equilibrated in Holliday junction(HJ) buffer A [25mM NaCl, 25mM Tris-HCl pH 7.9, 10mM $MgCl_2$]. Contaminants were removed by washing with 55%/45% mix of HJ buffer A to HJ Buffer B[1M NaCl, 25mM Tris 7.9, 10mM $MgCl_2$] and correctly annealed substrate was eluted with 45%/55% Buffer A/Buffer B, pooled and dialyzed back into HJ buffer A, and concentrated by centrifugation (Millipore Amicon Ultra 3K MWCO). Proper annealing for all substrates was assessed by native 15% PAGE run in 0.5x Tris-Borate-EDTA (TBE) buffer.

DNA binding by topo VI and functional mutants was assessed using fluorescence anisotropy. Protein was serially diluted in two-fold steps in binding assay dilution buffer [250mM potassium glutamate, 5%(v/v) glycerol, 50mM HEPES-KOH pH 7.5 and 1mM TCEP] and incubated with DNA substrate in the dark on ice for 5 min. Reactions were diluted to final binding assay conditions [27µL, 0, 0.3-4000nM enzyme, 20nM labeled duplex, 50mM potassium glutamate, 5%(v/v) glycerol, 20mM HEPES-KOH pH 7.5, 1mM TCEP, 10mM $MgCl_2$ and 0.1mg/mL BSA], and incubated on ice an additional 10min. Fluorescence anisotropy was measured at ambient temperature using a Clairiostar microplate reader (BMG Labtech GmbH, Ortenberg, Germany) by exciting at 482nm (band pass 16nm) and measuring parallel and perpendicular emission intensity at 530nm (band pass 40nm), with an inline 504nm long pass dichroic filter. Data are the average of three independent experiments, with all points normalized to the DNA alone condition. Data were fit to the following single-site binding model:

$$\Delta FA = \Delta FA_{max}\left(\frac{[L]+[P]+K_{d,app}-\sqrt{([L]+[P]+K_{d,app})^2-4[L][P]}}{2[L]}\right) \quad (1)$$

where ΔFA_{max} is the maximal specific change in anisotropy, [L] is DNA substrate concentration, [P] is the concentration of topo VI construct, and $K_{d,app}$ is the apparent dissociation constant for DNA substrate and enzyme.

Competition assays were carried out similarly to binding assays, with protein diluted in binding assay dilution buffer and incubated with the 70bp FAM-labeled duplex and either negatively supercoiled pSG483 (pBluescript SK derivative, 2927bp) or linear sheared salmon sperm DNA (ThermoFisher Scientific) competitor. Reactions were diluted to final binding assay conditions, except enzyme concentration was set at 100nM, and competitor concentration varied from 0.026 µM bp to 106.5 µM bp DNA. Anisotropy data were fit to an explicit competition model, the details of which are described by Wang (Wang, 1995).

Supercoiled DNA relaxation

Topo VI holoenzyme was thawed and diluted in series with relaxation assay dilution buffer [300mM potassium glutamate, 10% (v/v) glycerol, 20mM HEPES-KOH pH 7.5 and 1mM

TCEP] and incubated with supercoiled pSG483 for 5min on ice before dilution into final relaxation assay conditions [30µL reactions, 0,0.3-20nM topo VI for titration, 2.5nM topo VI for time-courses, 50mM potassium glutamate, 10% (v/v) glycerol 20mM bis-tris-propane-HCl (BTP-HCl) pH 7.5, 2mM HEPES pH 7.5, 1mM TCEP, 10mM $MgCl_2$, 0.1mg/mL BSA, 3.5nM pSG483/10.2 uM bp DNA, and 1mM ATP]. Reactions were initiated with addition of ATP, incubated at 30°C, and quenched by addition of SDS and EDTA to final concentrations of 1% and 10mM respectively. Glycerol-based loading dye was added to samples which were run on a 1% (w/v) TAE agarose gel (40 mM sodium acetate, 50mM Tris-HCl, pH 7.9 and 1mM EDTA, pH 8.0) for 15 hours at ~2 V/cm. For visualization, gels were stained for 30min with 0.5ug/mL ethidium bromide in running buffer, de-stained in running buffer for 30min, and exposed to UV trans-illumination. Experiments were carried out similarly for the plasmid-chase experiments, except that a 13.5 kbp chase plasmid (pEAG-NC) was added with ATP to a final concentration of 10.2 µM bp when initiating reactions.

Steady-state ATP hydrolysis

ATP hydrolysis was measured using the established NADH-coupled assay (Morrical, Lee, & Cox, 1986; Tamura & Gellert, 1990). Topo VI was thawed and diluted with 300mM potassium glutamate, 10% (v/v) glycerol, 50mM BTP-HCl pH 7.5 and 5mM TCEP to 3.75 µM, mixed 1:2 with sheared salmon sperm DNA, supercoiled pSG483, or ddH_2O, and incubated for 5 min on ice. Enzyme/substrate mixes were diluted with NADH-PK/LDH coupling mix to final ATP hydrolysis assay conditions [100µL reactions, 3.75mM phosphoenolpyruvate, 150uM NADH, 24U pyruvate kinase and 36U lactate dehydrogenase (PK/LDH from rabbit muscle in buffered, aqueous glycerol solution, Sigma Aldrich, St Louis, MO, USA), 0.1mg/mL BSA, 50mM BTP-HCl, pH 7.5, 50mM potassium glutamate, 5mM TCEP, 10mM $MgCl_2$, 5% (v/v) glycerol, 500nM topo VI holoenzyme]. ATP titration reactions contained either 400 µM bp sheared salmon sperm DNA, 400 µM bp supercoiled pSG483 or no DNA, and were initiated by addition of ATP to a final concentration of 0mM or 62.5 µM-4mM diluted in two-fold steps. DNA titrations contained 3.12-800 µM bp DNA diluted in two-fold steps and were initiated by addition of ATP to a final concentration of 2mM. Reactions were incubated at 30°C and followed in clear 96-well plates (Corning Inc, Corning NY, USA) by absorbance at 340nm using a Clairiostar microplate reader. Raw absorbance values were converted to concentrations based on measurements from NADH standards in the final ATP hydrolysis assay condition buffer. ATP hydrolysis rates were determined by fitting to the linear portion of NADH consumption curves. Data representing three independent experiments were fit to a standard Michaelis-Menten model:

$$V_0 = \frac{k_{cat}[E_T][S]}{K_m + [S]} \quad (2)$$

where V_0 is the observed turnover rate, k_{cat} is the maximum turnover rate, $[E_t]$ is the total topo VI holoenzyme concentration, and [S] is the concentration of either substrate ATP or DNA affector, and K_m is either the Michaelis constant for ATP or the activation constant for either linear DNA or supercoiled DNA.

Top6B gate closure assessed by FRET

Following purification, topo VI FRET constructs were labeled by reacting enzyme with 5-fold molar excess to enzyme of both Alexa Fluor 555 C_2 maleimide and Alexa Fluor C_2 647 maleimide (ThermoFisher Scientific) in sizing buffer overnight at 4°C. TCEP was also added at 50-fold molar excess to enzyme. Reactions were quenched with 5mM DTT and applied to a HiPrep 26/10 Desalting column (GE) to separate protein from unreacted dye. Proper labeling was imaged by SDS PAGE using a Typhoon FLA 9500 laser scanner (GE). Labeling efficiencies were determined by comparing absorption at 280nm for protein to absorption at 555nm for Alexa555 and 650nm for Alexa647. Proteins were brought to storage buffer conditions, flash frozen as aliquots in liquid nitrogen and stored at -80°C.

For gate closure assays, labeled protein was diluted in [250mM potassium glutamate, 10% (v/v) glycerol and 20mM HEPES-KOH pH 7.5] to 1 µM, mixed 1:1 with 500uM bp DNA substrate or ddH_2O, incubated on ice for 5min, and diluted to final assay conditions [20µL reactions, 200 nM topo VI, 0 or 100 uM bp DNA, 50mM potassium glutamate, 1mM TCEP, 10% (v/v) glycerol, 20mM HEPES-KOH pH 7.5, 10mM $MgCl_2$ and 0.1mg/mL BSA]. Fluorescence emission spectra were measured by exciting samples at 530nm and measuring emission from 545nm to 700nm using a Fluoromax Fluorometer 4 (HORIBA Jobin Yvon, Edison, NJ, USA). Adenylyl-imidodiphosphate (AMPPNP) was added to a final concentration of 1mM and changes to emission spectra were measured over time. Spectra were normalized by total spectral emission. Plotted FRET efficiencies (E) were determined ratiometrically from donor (I_D) and acceptor (I_A) peak intensities:

$$E = \frac{I_A}{I_D + I_A} \quad (3)$$

Short DNA duplex cleavage

Topo VI was diluted in [250mM potassium glutamate, 10% (v/v) glycerol, 10mM $MgCl_2$ and 20mM HEPES-KOH pH 7.5] to 1 µM, mixed 1:1 with 500nM fluorescein-labeled duplex (**Table S3.1**) and incubated 5min on ice. Reactions were diluted to a final cleavage reaction condition [20µL reactions, 200 nM topo VI construct, 100 nM FAM-labeled duplex, 50mM potassium glutamate, 1mM TCEP, 10% (v/v) glycerol, 16mM BTP-HCl pH 7.5, 4mM HEPES-KOH pH 7.5, 10mM $MgCl_2$, 0.1mg/mL BSA and 15% DMSO]. ATP, AMPPNP or ddH_2O were added to initiate reactions. Reactions were incubated at 30°C for 2hrs then quenched with SDS to a final concentration of 1%. Protinase K was added to reactions at a final concentration of 0.3mg/mL and incubated at 45°C for 1 hour. Formamide was added 1:1 to samples and cleavage products were separated on 7M Urea-Formamide 0.5x TBE 12% PAGE. Gels were visualized using a Typhoon FLA 9500 laser scanner.

DNA bending assessed by FRET

DNA bending experiments used the same 70bp duplex sequence from binding and cleavage experiments, except the substrate was modified to have a Cy5 replace the 5'-fluorocein on strand 1 and Cy5.5 was added to the 5' end of strand 2 (**Table S3.1**). Reactions were prepared exactly as described for the DNA cleavage assays. Fluorescence emission spectra

were measured by exciting samples at 630nm and measuring emission from 645nm to 850nm using a Fluoromax Fluorometer 4. AMPPNP was added to a final concentration of 1mM and changes to emission spectra were measured over time. Spectra were normalized to by total spectral emission. Plotted FRET efficiencies were calculated as for the gate closure assays.

Data analysis and figure preparation

All data were plotted and fit using Prism Version 7 (GraphPad Software, La Jolla, CA, USA). and Mapping of sequence conservation in relation to tertiary structure was aided by the Consurf web server (Ashkenazy et al., 2010). Coordinates for bent DNA models were generated using the 3DNA web server (Zheng, Lu, & Olson, 2009). Pymol was used for structure visualization and comparison (The PyMOL Molecular Graphics System, Schödinger, LLC).

Figures and Tables

a

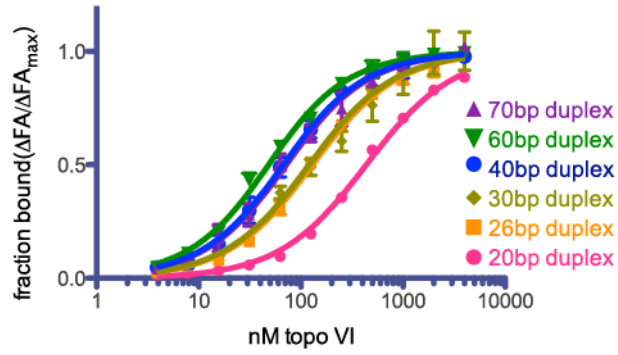

	Duplex length					
	20bp	26bp	30bp	40bp	60bp	70bp
$K_{d,\ app}$ (nM)	427±17	120±5	111±13	49 ±3	38±2	62±4

b

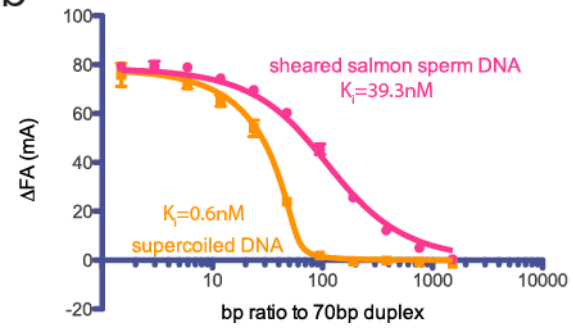

Figure 3.1. Topo VI engages longer duplexes and preferentially binds to supercoiled DNA.

(a) Binding of a 20, 26, 30, 40, 60 or 70bp fluorescein labeled duplex (20nM) to topo VI. Binding was observed as a change in fluorescence anisotropy (ΔFA) measured in milli-anisotropy units (mA) as a function of enzyme concentration, and converted to fraction bound ($\Delta FA/\Delta FA_{max}$) to more easily compare binding between substrates. Points and errors correspond to three independent experiments. Curves represent fits to a single site ligand depletion binding model. Apparent dissociation constants are reported below the plot.

(b) Binding assay to assess the ability of supercoiled DNA and sheared salmon sperm DNA to compete a fluorescein labeled 70 bp duplex (20nM duplex, 1.4 uM bp) from topo VI (100nM). Non-labeled DNA was titrated from 0.1 uM bp to 106.5 uM bp and competition was observed as a change in fluorescence anisotropy (ΔFA) as measured in milli-anisotropy units (mA). Data are plotted as a function of the base-pair ratio of competing DNA to a 70bp duplex. Points and error correspond to three independent experiments. Curves represent a fit to a competitive displacement model.

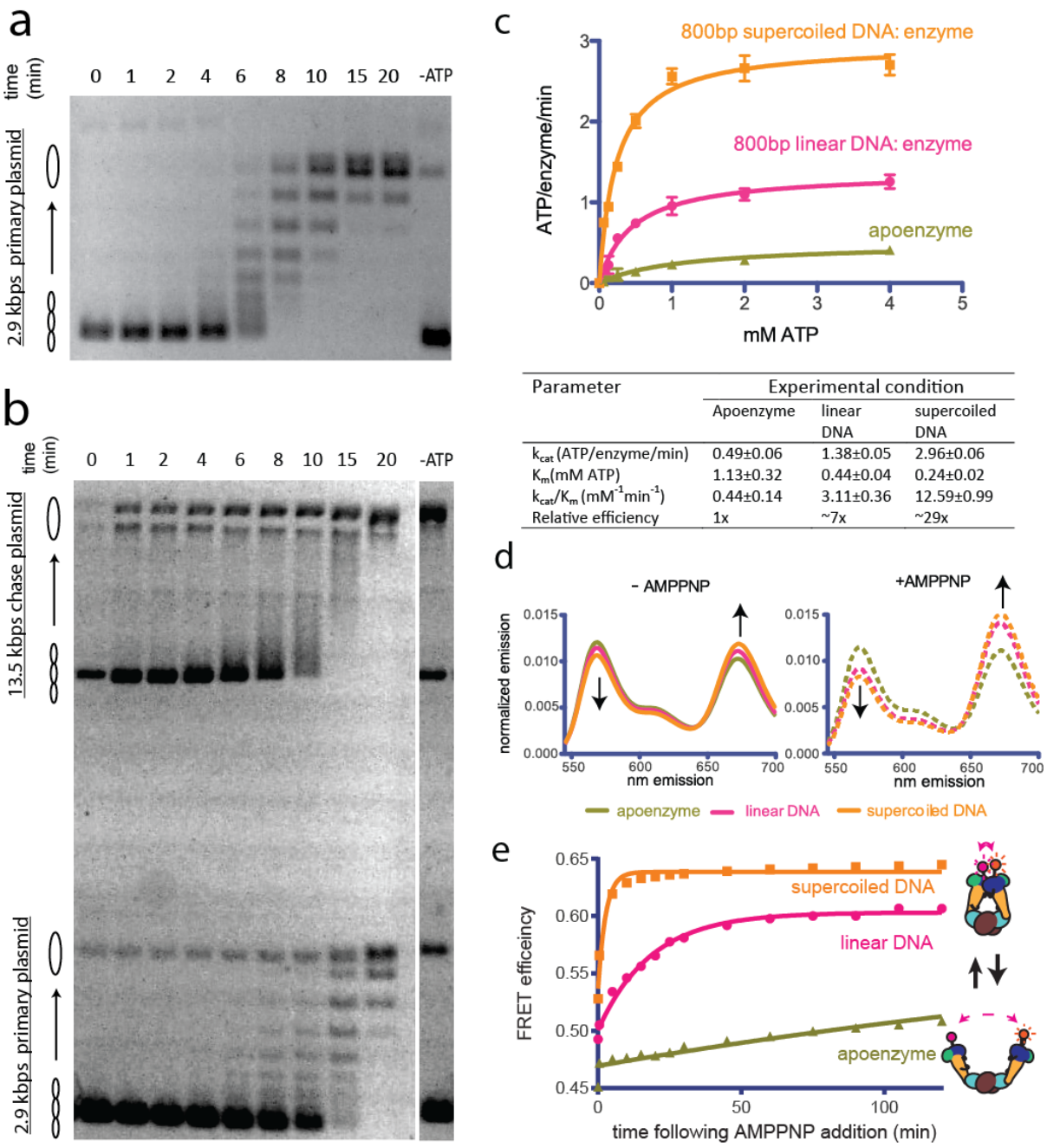

Parameter	Experimental condition		
	Apoenzyme	linear DNA	supercoiled DNA
k_{cat} (ATP/enzyme/min)	0.49±0.06	1.38±0.05	2.96±0.06
K_m(mM ATP)	1.13±0.32	0.44±0.04	0.24±0.02
k_{cat}/K_m ($mM^{-1}min^{-1}$)	0.44±0.14	3.11±0.36	12.59±0.99
Relative efficiency	1x	~7x	~29x

Figure 3.2. Topo VI coordination of ATP-dependent strand passage relies upon DNA substrate topology.

(**a-b**) Rate of negative supercoil relaxation by *M. mazei* topo VI on negatively supercoiled plasmid DNA. Topo VI was pre-incubated in a 1:1.4 ratio to a 2.9kbp negatively supercoiled plasmid (6.7 ng/µL in assay). Reactions were started by addition of either (**a**) ATP or (**b**) ATP and a 13.5 kbp "chase" plasmid (6.7 ng/µL in assay) to compete for unbound enzyme. Samples were quenched at 0, 1, 2, 4, 6, 8, 10, 15, and 20 min. Each condition was also incubated without ATP

for 20min as a negative control. Topoisomer species and identification of each plasmid are indicated on the left of each gel.

(**c**)Rate of steady state ATP hydrolysis catalyzed by topo VI alone, incubated with an 800:1 bp:enzyme ratio of linear sheared salmon sperm DNA, or an 800:1 bp:enzyme ratio of supercoiled plasmid as a function of ATP concentration. Rates were determined spectroscopically using an NADH coupled assay. Points represent mean and error of independent triplicate measurements. Curves represent a fit to a Michealis-Menten kinetics model reported below the plot.

(d) Fluorescence emission spectra produced by 530nm excitation of Alexa555/Alexa647 labeled topo VI$^{\text{cyslite-155C}}$ shows DNA binding modulates the conformation of the Top6B ATP gate in the absence of nucleotide (*left*, solid lines) as assessed by FRET. Upon addition of AMPPNP (*right*, dashed lines), only enzymes bound to DNA close in response, as accessed by the relative increase in acceptor emission and decrease in donor emission. Spectral emission was normalized by total emission from 545nm to 700nm.

(e) FRET efficiency was monitored over time after the addition of AMPPNP for enzyme bound to supercoiled DNA, linear DNA (sheared salmon sperm DNA), or enzyme alone. Curves represent a fit to an exponential single phase association model, with the upper plateau constrained to a FRET efficiency of 0.6 for the apoenzyme.

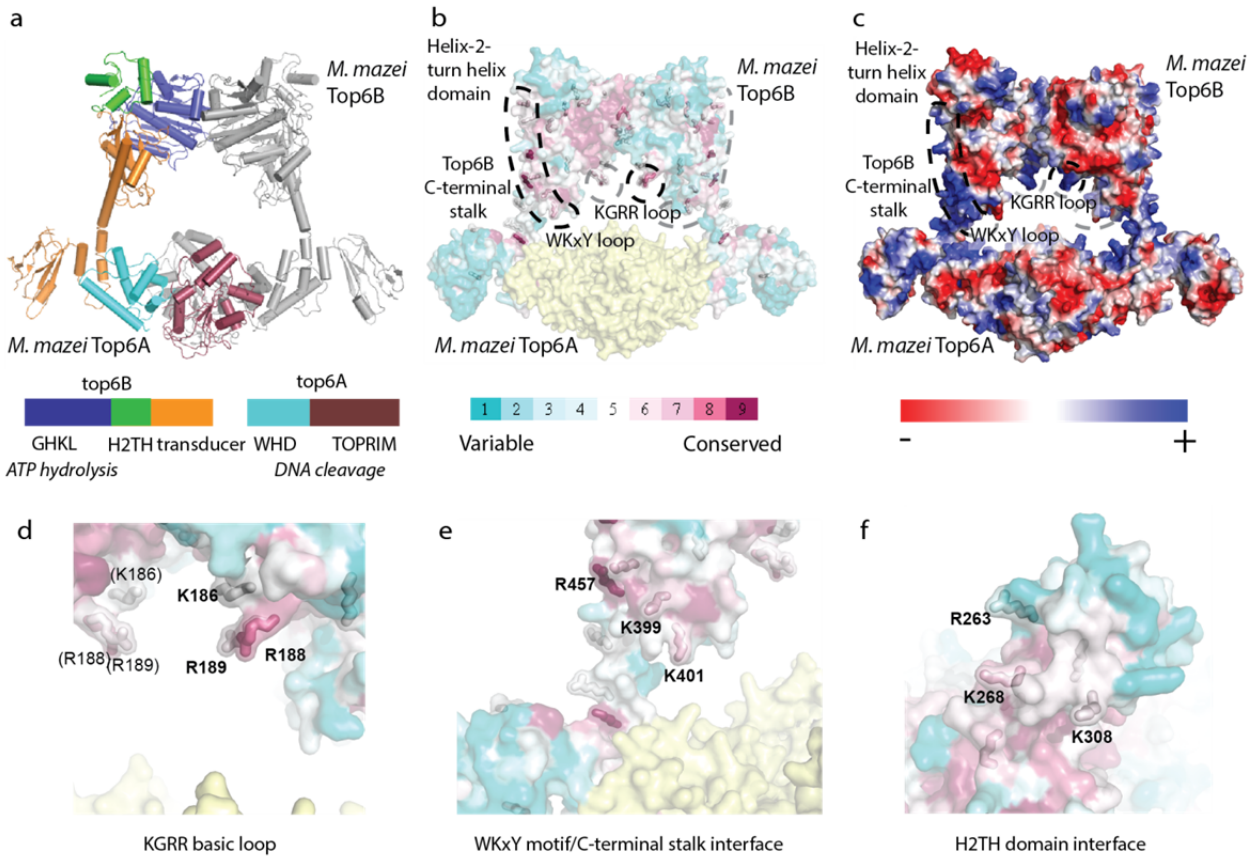

Figure 3.3. Identification of potential DNA binding elements in Top6B

(**a**) Primary and tertiary structure [Protein Data Bank (PDB) ID: 2Q2E] of the *Mm* topo VI heterotetramer. Domains for one top6A-topo6B heterodimer are colored as shown in the primary structure; the partner top6A-top6B heterodimer is shown in grey. Catalytic function is denoted in italics under primary structure. (**b**) Mapping of sequence conservation in Top6B based on a PSI-BLAST multiple sequence alignment. Conserved surface exposed arginine and lysine residues (ConSurf score of ≥ 6) are shown as sticks. Coloration is cyan to magenta for variable to conserved. Topo6A is represented in yellow. **(c)** Electrostatic surface representation of topo VI. A conserved basic loop in the T-segment storage cavity and conserved basic interface stretching from the WKxY motif and C-terminal stalk of top6B to the Helix-2-turn-helix (H2TH) domain of unknown function are labeled. (**d**) Zoomed in view of the KGRR basic loop motif. **(e)** Zoomed in view of the WKxY motif and C-terminal stalk interface. **(f)** Zoomed in view of the H2TH DNA binding interface, rotated 90^{o} towards the point of view as compared to **a-c**. See Figure S3.4 for a more detailed rationale for the functional importance of this interface. In **(d-f)** residues mutated to alanine or to glutamate for functional studies are labeled.

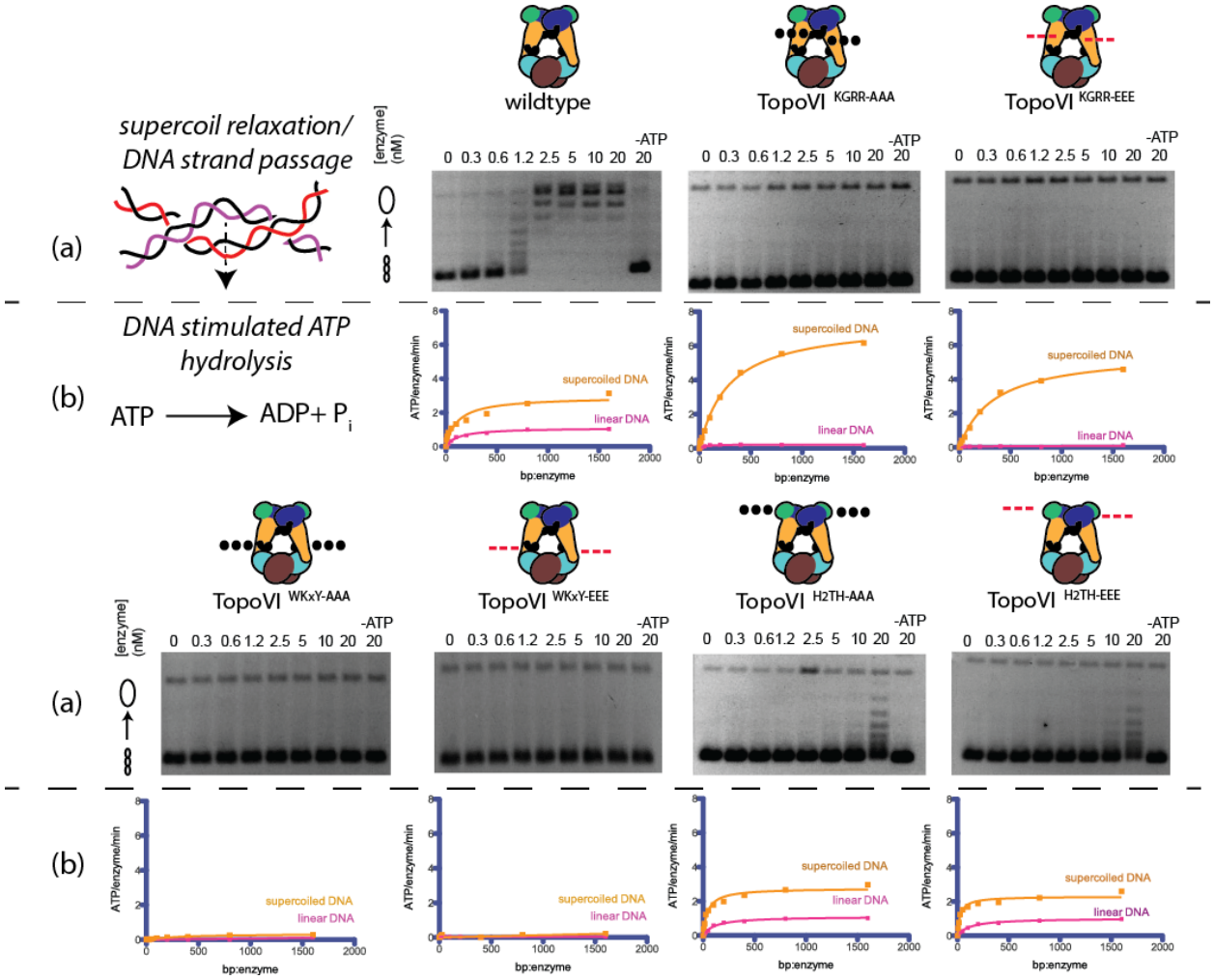

Figure 3.4. Effect of neutralization and charge reversal mutations to the KGRR loop, WKxY motif and H2TH DNA binding interface on topo VI supercoil relaxation activity and ATP hydrolysis.

(a) General activity of mutant topo VI constructs for relaxing supercoiled DNA as compared to wildtype a function of enzyme concentration. For the enzyme titrations (0.3-20nM in two-fold steps), each assay proceeded for 30 min prior to quenching with EDTA and SDS and contained 3.5 nM plasmid (10.2µM bp DNA). The placement and nature of mutations in each construct are depicted in the cartoons above each titration ("•••" - AAA; "---" – EEE). **(b)** Rate of steady state ATP hydrolysis catalyzed by wildtype topo VI as compared to mutant topo VI constructs, as a function of the basepair: enzyme ratio of sheared salmon sperm DNA concentration(pink), or supercoiled plasmid (orange). ATP was held at 2mM, and rates were determined spectroscopically using an NADH coupled assay. Curves represent a fit to a Michealis-Menten type kinetics model.

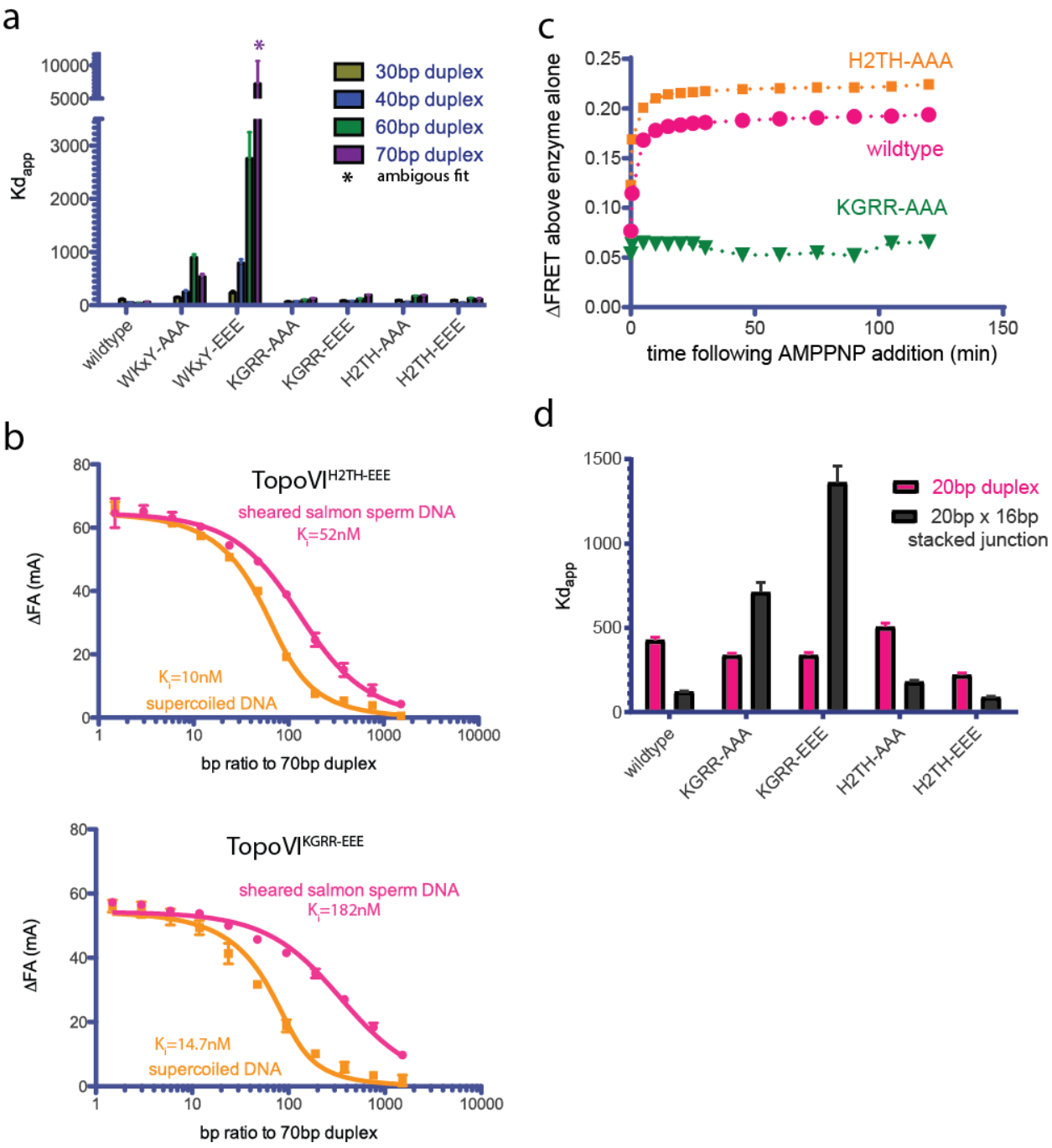

Figure 3.5. Effect of neutralization and charge reversal mutations on DNA binding affinity, topology sensing, and G-segment/T-segment crossing recognition

(a) Apparent binding constants of a 30, 40, 60 or 70bp fluorescein labeled duplex (20nM) to a panel of topo VI functional mutants. Binding was observed as a change in fluorescence anisotropy (ΔFA) and measured in milli-anisotropy units (mA) as a function of enzyme concentration as determined from independent triplicate (see Figure S3.7). Columns and error bars correspond to value and standard error of Kd_{app} for the indicated enzyme construct and

substrate derived from a single site ligand depletion binding model. An asterisk indicates an ambiguous fit as a result of a poorly defined maximum anisotropy change parameter, ΔFA_{max}.

(b) Binding assay to assess the ability of supercoiled DNA and sheared salmon sperm DNA to compete a fluorescein labeled 70 bp duplex (20nM duplex, 0.14 µM bp) from 100nM topo $VI^{H2TH\text{-}EEE}$ (*top*) or topo $VI^{KGRR\text{-}EEE}$ (*bottom*). Non-labeled DNA was titrated from 0.1 µM bp to 106.5 µM bp and competition was observed as a change in fluorescence anisotropy (ΔFA) as measured in milli-anisotropy units (mA). Data are plotted as a function of the base-pair ratio to a 70bp duplex. Curves represent a fit to a competitive displacement model.

(c) Increase in FRET efficiency above the signal for enzyme alone for the indicated Alexa555/647 labeled topo VI constructs incubated supercoiled DNA was monitored over time after the addition of AMPPNP. The H2TH-AAA mutant retains the rapid increase in FRET on seen for the wildtype topo VI on supercoiled DNA. The KGRR-AAA mutant, however, abolishes nucleotide-dependent increase in FRET on supercoiled substrate. As further detailed in **Figure S3.8**, supercoiled DNA alone, in the absence of nucleotide, increases the FRET efficiency for each construct.

(d) Kd_{app} derived from binding isotherms (**Figure S3.9b-f**) assessing the affinity of wildtype topo VI and functional mutants for a fluorescein labeled stacked junction as compared to a similar length duplex (20nM substrate). Binding was observed as a change in fluorescence anisotropy (ΔFA) as measured in milli-anisotropy units (mA) as a function of enzyme concentration. Columns and error bars correspond to value and standard error of Kd_{app} derived from a single site ligand depletion binding model.

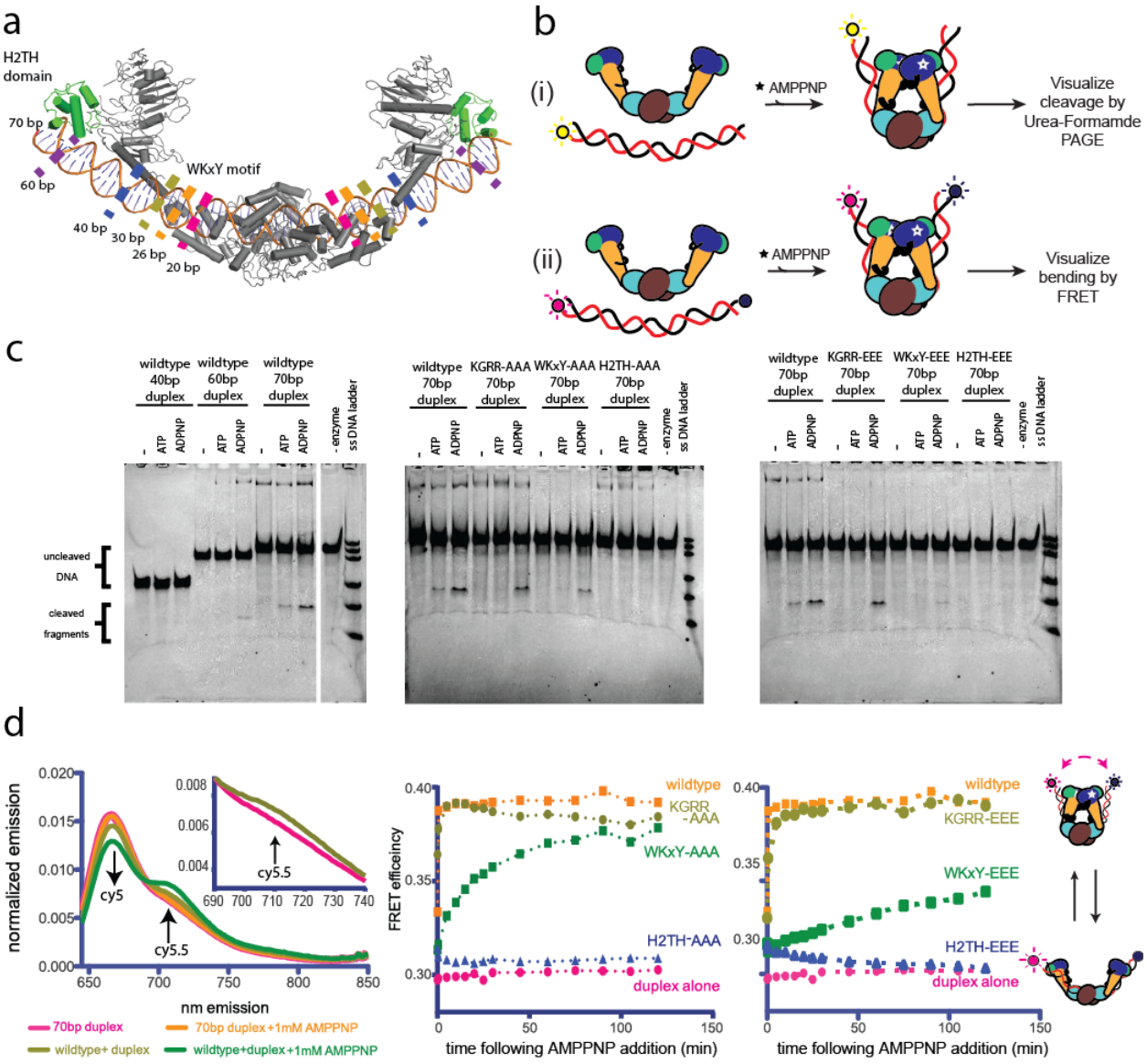

Figure 3.6. Topo VI requires H2TH-mediated, nucleotide-dependent bending of a 70bp duplex G-segment to induce cleavage.

(a) Modeling of a 70bp bent duplex spans from one H2TH domain to the other through the TOPRIM/WHD cleavage site of Topo6A (using a previously published SAXS model of *S. shibatae* topo VI with Topo6B in an open conformation (Corbett et al., 2007)(See also PDB ID: 2ZBK for a similar conformation, stabilized by the inhibitor radicicol (Graille et al., 2008)). H2TH domains are colored green. The length of other duplexes tested for binding are marked in relation to topo VI. DNA was modeled with a continuous bend using web 3DNA (Zheng et al., 2009).

(b) Schematic of the duplex cleavage assay (i) or bulk FRET assay (ii) used to test whether the H2TH-domain interacts with G-segment DNA.

(c) Nucleotide dependent cleavage of fluorescein labeled DNA duplexes by topo VI and mutant constructs. Length dependent cleavage by wildtype(*left*), cleavage of a 70bp duplex by basic to neutral functional mutants(*middle*), and cleavage by basic to acidic functional mutants(*right*) were tested. Cleavage reactions containing a 2:1 ratio of enzyme:duplex were run on denaturing PAGE to separate reaction products, and were visualized using a laser gel scanner. Enzyme construct (wildtype, topoVI$^{KGRR\text{-}AAA}$, topoVI$^{KGRR\text{-}EEE}$, topoVI$^{WKxY\text{-}AAA}$, topoVI$^{WKxY\text{-}EEE}$, topoVI$^{H2TH\text{-}AAA}$, or topoVI$^{H2TH\text{-}EEE}$), duplex length (40bp, 60bp, or 70bp), and addition of 1mM ATP or 1mM AMPPNP is noted above each lane. A no enzyme control containing 1mM AMPPNP and a single strand DNA ladder consisting of 20, 30, 40, 60, 70bp and 80bp oligonucleotides were run for reference.

(d) Nucleotide dependent bending of a Cy5/Cy5.5 labeled 70bp duplex was assessed using bulk FRET. Fluorescence emission spectra (*left*) produced by 630nm excitation Cy5-Cy5.5 labeled DNA show an increase in cy5.5 emission in the presence of topo VI and AMPPNP, but not in the presence of AMPPNP alone. Spectral emission was normalized by total emission from 645nm to 850nm. Ratiometric FRET efficiency ($I_A/(I_{A+}I_D)$) was monitored over time upon addition of AMPPNP for the noted basic to neutral mutant (*middle*) or basic to acidic topo VI functional mutant (*right*). Wildtype and duplex alone are shown in each case for comparison.

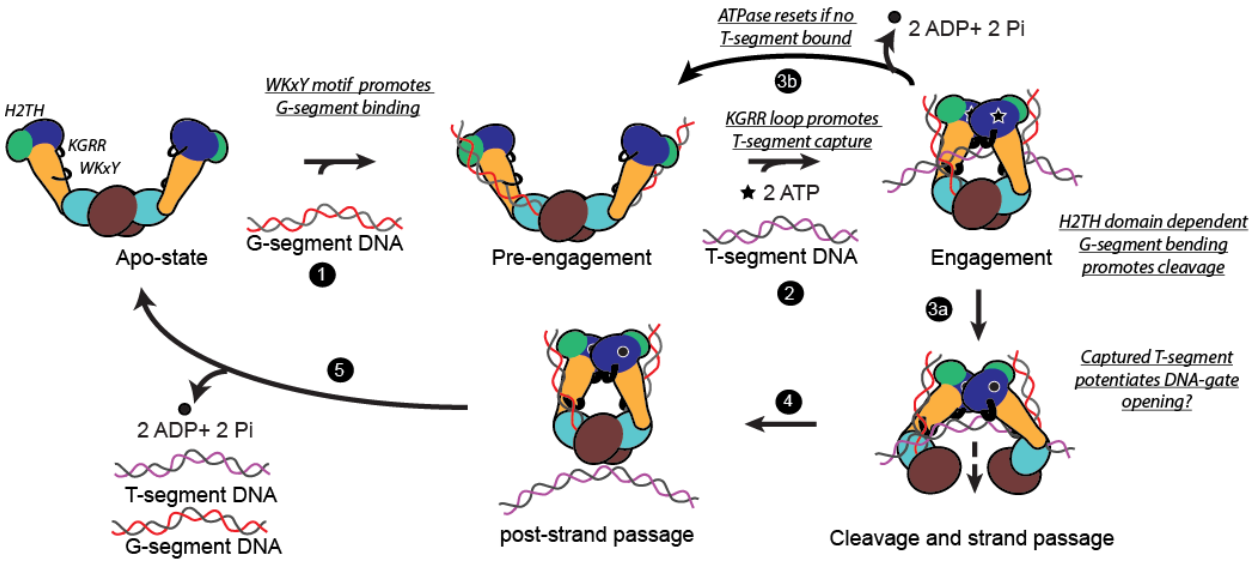

Figure 3.7. A new model for the type IIB topoisomerase catalytic cycle.

When not bound to DNA, topo VI populates a conformation with the B-subunit predominantly open, with low basal ATP hydrolysis. ***(1)*** Binding of G-segment DNA mediated by the WKxY motif bends the G-segment. ***(2)*** Both superhelical bending sensed by the H2TH domain and plectonemic crossings sensed by the KGRR loop allow top6B to close sufficiently to bind ATP. Dimerization of top6B induces a sharper bend in G-segment DNA through an H2TH domain mediated interaction, promoting cleavage and either: ***(3a)*** T-segment captured by the KGRR loop potentiates DNA gate opening or (***3b***) if a T-segment was not captured, ATP is hydrolyzed and the enzyme returns to the pre-engagement stage. ***(4)*** G-segment DNA is religated following T-segment passage. ***(5)*** G-segment dissociates and Top6B releases ADP and P_i.

Table 3.1. Kinetic parameters for DNA dependent stimulation of topo VI ATPase activity

Parameter	Topo VI construct						
	wildtype	KGRR-AAA	KGRR-EEE	WKxY-AAA	WKxY-EEE	H2TH-AAA	H2TH-EEE
Sheared salmon sperm DNA							
k_{cat} (ATP/enzyme/min)	1.11±0.03	N/A*	N/A*	N/A*	N/A*	1.11±0.03	1.03±0.03
K_m'(μM bp DNA)	122.4±12.7	N/A*	N/A*	N/A*	N/A*	112.4±12.2	120.4±13.3
Supercoiled plasmid DNA							
k_{cat} (ATP/enzyme/min)	2.93±0.14	7.40±0.11	5.60±0.11	N/A*	N/A*	2.76±0.07	2.30±0.05
K_m'(μM bp DNA)	113.7±19.7	285.3±12.0	336.3±18.8	N/A*	N/A*	44.6±4.73	26.5±2.9

*****data not fit to model due to undetectable ATP hydrolysis above basal rate.

******K_m' denotes the μM base pair concentration of DNA where half maximal ATP hydrolysis is attained. It therefore defines the concentration dependent stimulation of ATP hydrolysis, but is not a K_m in the classic sense, as DNA serves an allosteric effector, not substrate.

***Standard errors in fit parameters are reported.

Table 3.2. Affinities of topo VI$^{H2TH\text{-}EEE}$ and topo VI$^{KGRR\text{-}EEE}$ for supercoiled and linear DNA compared to wildtype

Substrate	Topo VI construct		
	Wildtype	H2TH-EEE	KGRR-EEE
$K_{I,app}$ of Supercoiled DNA (nM)	0.64±0.26	10.0±0.9	14.7±1.3
$K_{I,app}$ of linear DNA (nM)	39.3±2.6	52.1±2.8	181.7±10.0
Preference for supercoiled DNA	~60x	~5x	~12x

Supplemental Materials

Comparing the cellular workload of M. mazei topo VI to model type IIA topoisomerases

To assess whether the enzymatic activity reported for *Mm* topo VI could satisfy its cellular workload, we began by estimating the strand passage rate for topo VI. Assuming a super-helical density of σ = -0.06 on the substrate used in our relaxation time-courses (**Figure 3.2a**) yielded a bulk estimate of one supercoil relaxation event every 40-70s which agrees with the maximal ATPase rates observed (~3 ATP/min on supercoiled DNA, corresponding to one strand passage event every ~40s for an enzyme without futile cycling). These rates are ~50-100-fold slower than rates reported for a broad range of both bacterial and eukaryotic type IIA topoisomerases for which each strand passage takes ~0.5-1s on an optimal substrate (Basu et al., 2012; Higgins et al., 1978; Lindsley & Wang, 1993; Osheroff et al., 1983; Sugino & Cozzarelli, 1980; Vos et al., 2013).

We next considered the set of encoded topoisomerases in *M. mazei,* which include topo III, topo VI, and a DNA gyrase gained from bacteria by horizontal gene transfer (Forterre et al., 2007). If *M. mazei* employs its assortment of topoisomerases similarly to other organisms, then topo VI serves as a decatenase and assists in relaxing super-helical build-up (A Bergerat et al., 1994; K. D. Corbett et al., 2007), whereas topo III likely serves to resolve hemicatenanes and potentially to relax negative supercoils (DiGate & Marians, 1988; Harmon et al., 1999; Wallis et al., 1989), and DNA gyrase likely serves to relax positive supercoils and maintain an under-wound genome (Forterre & Gadelle, 2009; Forterre et al., 2007; Schoeffler & Berger, 2008). As *E.coli* topo IV and *S. cerevisiae* Topo II both serve as decatenases that are assisted by a hemi-decatenase, and may function as negative and positive supercoil relaxases in an assisting role, we deemed the cellular roles comparable (Forterre et al., 2007; Goto & Wang, 1982; Holm et al., 1985; Schoeffler & Berger, 2008; Zechiedrich & Cozzarelli, 1995).

We then normalized the strand passage rate of *Mm* topo VI, *Ec* topo IV and *Sc* topo II to genome size and doubling time under optimal growth conditions for each topoisomerase/organism pair. Using a genome size of 4.64 Mbp for *E.coli* (Blattner et al., 1997) with a doubling time of ~20 min (Schaechter, Williamson, Hood, & Koch, 1961), and a 12 Mbp genome for *S. cerevisiae* (Goffeau et al., 1996) with a ~90 min doubling time (Sherman, 2002) yielded relatively similar loads, within ~20% of each other. *M. mazei* have a ~8-16hrs doubling time in optimal conditions (Mah, 1980), and possess a ~4.1Mbp genome (Deppenmeier et al., 2002), however, the closely related *Methanoscarina acetivorans* maintains a chromosome copy number of ~16 in similar conditions, and maintenance of a large chromosome copy number appears to be a common trait in Euryarchota (Hildenbrand, Stock, Lange, Rother, & Soppa, 2011). Assuming *M mazei* possess a similar genome copy number in optimal conditions, this increases the amount of genetic material to process to 65.6 Mbp per cell. Such a burden would require ~50-fold greater activity from topo VI for it to accommodate a similar cellular role as topo II in yeast or topo IV in *E.coli.*

Detailed protocol for purification of wildtype topo VI and functional mutants

For topo VI purification, harvested cells were thawed and lysed by sonication, and lysate was clarified by centrifugation. Clarified lysate was applied to a 5-mL HiTrap Ni^{2+} column (GE) and washed with buffer A [20mM HEPES-KOH pH 7.5, 800mM NaCl, 20mM Imidazole, 10% (v/v) glycerol, 1µg/mL pepstatin A, 1µg/mL leupeptin, 1mM PMSF]. Following a subsequent wash with buffer B [20mM HEPES-KOH pH 7.5, 150mM NaCl, 20mM Imidazole, 10%(v/v) glycerol, 1ug/mL pepstatin A, 1ug/mL leupeptin, 1mM PMSF], bound proteins were eluted by a 15 column volume gradient from buffer B to buffer C [20mM HEPES-KOH pH 7.5, 150mM NaCl, 20mM Imidazole, 10%(v/v) glycerol, 1ug/mL pepstatin A, 1ug/mL leupeptin, 1mM PMSF]. Fractions containing the topo VI heterotetramer were applied to a 5-mL HiTrap SP cation exchange column (GE) and 5mL HiTrap Q anion-exchange column (GE) in series and washed with buffer B. Protein bound to the HiTrap Q column was eluted with a 10 column volume gradient from buffer B to buffer A. Peak fractions were concentrated by centrifugation (Millipore Amicon Ultra 30K MWCO) and incubated with 1.5mg of His_6-TEV protease (QB3-Macrolab, University of California, Berkeley) overnight at 4°C to remove His_6 tags. Uncleaved proteins and His_6-TEV protease were removed by applying the protease reaction to a HiTrap Ni^{2+} column equilibrated in buffer B. Flow-through was concentrated and applied to an Sephacryl-300 HR gel filtration column (GE) equilibrated and run in sizing buffer [HEPES-KOH pH 7.5, 300mM KCl, 10% (v/v) glycerol] and concentrated by centrifugation (Millipore Amicon Ultra 10K MWCO). Purity of peak fractions was assessed by SDS-PAGE and coomassie blue staining, and the concentration of tetramer was determined by absorbance at 280 nm using extinction coefficients determined by the ExPASY ProtParam webserver (Gasteiger et al., 2005). Proteins were flash frozen in a final storage buffer [HEPES-KOH pH 7.5, 300mM KCl, 30% (v/v) glycerol, 1mM Trisphosphine hydrochloride (TCEP)] and stored in aliquots at -80°C.

Expression and purification of S. cerevisiae topoisomerase II^{1-1177} (Sc topo II) and Sc topo $II^{1-1177,cyslite,180C}$

An *S. cerevisiae* topo II construct for labeling the N-terminal gate (N-gate) of with FRET pairs was generated from a topo II^{1-1177} construct by introducing the following mutations: C48A, C381A, C471A, and C731A. Proteins were overexpressed and purified using a previously described vector and protocol (Bryan H Schmidt et al., 2012). *S. cerevisiae* strain BCY123 was transformed with a GAL1 shuttle vector containing the yeast topo II^{1-1177} ORF and grown in CSM-Ura^- media with a 2% lactic acid and 1.5% glycerol carbon source at 30°C. Overexpression was induced by the addition of 2% galactose at A_{600}=0.8. Six hours following induction, cells were centrifuged, resuspended in 1mM EDTA and 250mM NaCl (1 mL per liter liquid culture), and flash frozen drop-wise in liquid nitrogen.

For purification, frozen cells were first lysed under liquid nitrogen using an SPEX SamplePrep 6870 Freezer Mill (SPEX SamplePrep, Metuchen, NJ , USA), and resultant powder was thawed and re-suspended in Buffer A300 [20mM Tris-HCl pH 8.5, 300mM KCl, 20mM imidazole, and 10% glycerol, 1mM PMSF, 1 µg/mL leupeptin, and 1 µg/mL pepstatin A]. Lysate was clarified by centrifugation and applied to a 5-mL HiTrap Ni^{2+} column equilibrated in buffer A. Following

washing with buffer A, protein was eluted with buffer B [20mM Tris-HCl pH 8.5, 100mM KCl, 200mM imidazole, and 10% glycerol, 1mM PMSF, 1 µg/mL leupeptin, and 1µg/mL pepstatin A], and applied to a 5-mL HiTrap SP cation-exchange column. Bound protein was eluted with buffer C [20mM Tris-HCl pH 8.5, 500mM KCl, 10% (v/v) glycerol, 1ug/mL pepstatin A, 1ug/mL leupeptin, 1mM PMSF]. Peak fractions were concentrated by centrifugation (Millipore Amicon Ultra 30K MWCO) and incubated with 1.5mg of His_6 TEV protease overnight at 4°C. Uncleaved proteins and TEV protease were removed by applying the protease reaction to a HiTrap Ni^{2+} column equilibrated in buffer A. Flow-through was concentrated and applied to an Sephacryl-300 HR gel filtration column (GE) equilibrated and run in Topo II sizing buffer [20mM Tris-HCl pH 7.9, 500mM KCl, 10% (v/v) glycerol]. Peak fractions were collected and concentrated (Millipore Amicon Ultra 30). Purity was estimated by SDS-PAGE and concentration was determined by absorbance at 280nm. Topo II was flash frozen in a final storage buffer containing [20mM Tris-HCl pH 7.9, 500mM KCl, 30% (v/v) glycerol] and stored in aliquots at -80°C.

Supercoiled DNA relaxation by S. cerevisiae topo II

Plasmid relaxation assays and chase assays with *Sc* topo II were carried out as described for topo VI, except that topo II was diluted in 500mM KCl, 10% (v/v) glycerol, 20mM Tris-HCl pH 7.9] and final relaxation assay conditions were 30mM Tris-HCl pH 7.9, 10mM $MgCl_2$, 0.05 mg/mL BSA, 0.5 mM TCEP, 100mM KCl, 10% (v/v) glycerol, 1mM ATP, 3.5nM (10.2 µM bp DNA) pSG483, and 2.5nM topo II, with 10. 2uMbp of the 13.5kbps plasmid added with ATP to initiate reactions for chase experiments.

S. cerevisiae topo II N-gate closure assessed by FRET

The N-gate of *Sc* topo II was labeled on a native cysteine residue (180C) with the Alexa Fluor 555 C_2 maleimide and Alexa Fluor C_2 647 maleimide FRET pair following the same procedure as for Top6B, except that the reaction was carried out in topo II sizing buffer and samples were flash frozen in the topo II storage buffer conditions.

Gate closure assays were performed similarly as with topo VI, except protein was diluted in 500mM KCl, 10% (v/v) glycerol and 20mM Tris-HCl pH 7.9, and final assay conditions were 200 nM topo II, 0 or 100 µM bp DNA, 100mM KCl, 2% (v/v) glycerol, 10mM Tris-HCl pH 7.9, 5mM $MgCl_2$ and either 0mM or 1mM AMPPNP. Fluorescence emission spectra were measured as with topo VI.

Table S3.1. Oligonucleotides used for fluorescence anisotropy and FRET experiments

Sequences of oligomers used for biophysical assays in this study. Sequences are based on a previously observed preferential cleavage site (site L) (Buhler et al., 2001).

Substrate; use	Oligonucleotide sequence
20bp duplex; binding assay	5’-FAM-CGGAAGAGTATGAGTATTCG-3’ 5’- CGAATACTCATACTCTTCCG-3’
26bp duplex; binding assay	5’-FAM-CCAAGGAAGAGTATGAGTATTCAAGC-3’ 5’-GCTTGAATACTCATACTCTTCCTTGG-3’
30bp duplex; binding assay	5’-FAM-CAA AAA GGA AGA GTA TGA GTA TTC AAC ATC-3’ 5’ GATGTTGAATACTCATACTCTTCCTTTTTG-3’
40bp duplex; binding assay, cleavage assay	5’-FAM- CTATTGAAAAAGGAAGAGTATGAGTATTCAACATTTCCGC-3’ 5’-GCGGAAATGTTGAATACTCATACTCTTCCTTTTTCAATAG-3’
60bp duplex; binding assay, cleavage assay	5'-FAM-CGCTTCAATAATATTGAAAAAGGAAGAGTATGAGTATTCAACATTTCCGTGTCGCCCTTC-3’ 5’- GAAGGGCGACACGGAAATGTTGAATACTCATACTCTTCCTTTTTCAATATTATTGAAGCG-3’
70bp duplex; binding assay, cleavage assay competition assay	5’ FAM-CCAAATGCTTCAATAATATTGAAAAAGGAAGAGTATGAGTATTCAACATTTCC GTGTCGCCCTTATTCCC-3’ 5’-GGGAATAAGGGCGACACGGAAATGTTGAATACTCATACTCTTCCTTTTTCAATATTATTGAAGC ATTTGG-3’
70bp duplex; FRET bending assay	5’ Cy5-CCAAATGCTTCAATAATATTGAAAAAGGAAGAGTATGAGTATTCAACATTTCC GTGTCGCCCTTATTCCC-3’ 5’Cy5.5-GGGAATAAGGGCGACACGGAAATGTTGAATACTCATACTCTTCCTTTTTCAATATTATT GAAGCATTTGG-3’
18bp by 20bp stacked junction; binding assay	5’-CGAATACTCAGCTCAACCGAAAGGTTGAGCCTTCGCTCGAAAGAGCGAAGTACTCTTCCG-3’ Annealed to oligomer 1 in the 20bp duplex substrate.

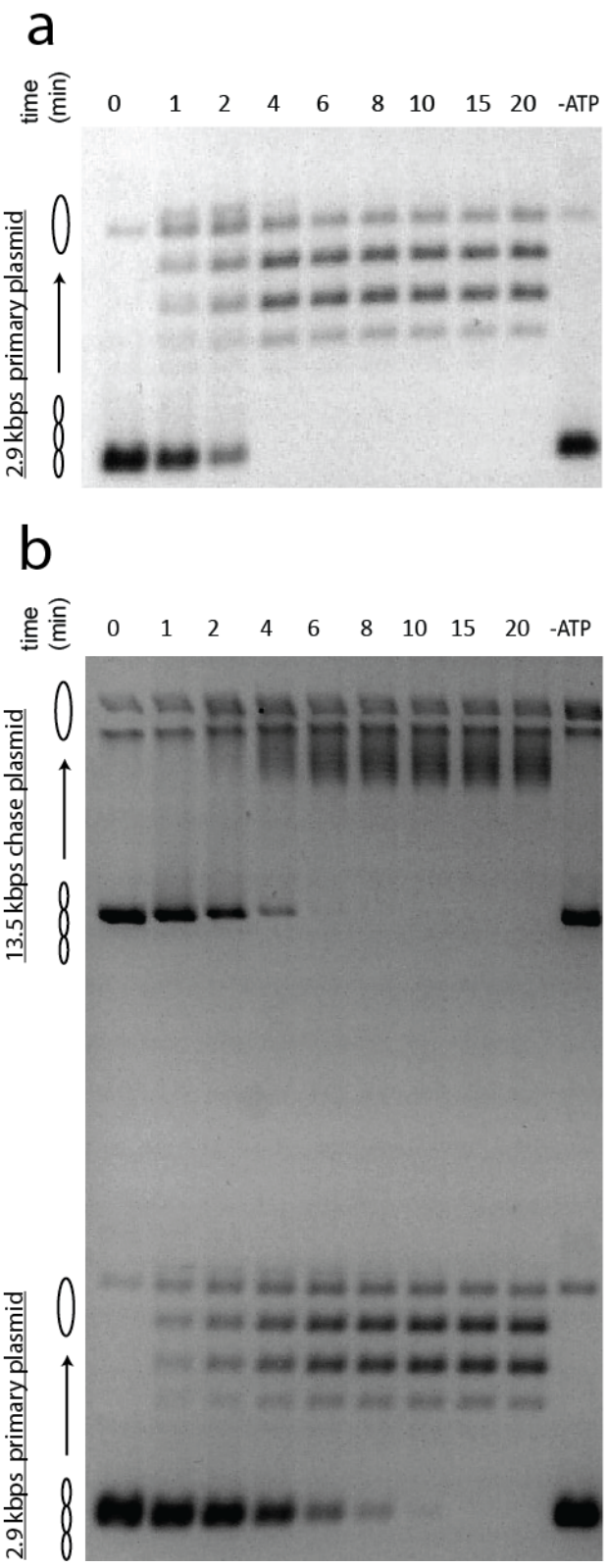
a
time (min)
0 1 2 4 6 8 10 15 20 -ATP
2.9 kbps primary plasmid
b
time (min)
0 1 2 4 6 8 10 15 20 -ATP
13.5 kbps chase plasmid
2.9 kbps primary plasmid

Figure S3.1. Topo II processively relaxes supercoiled DNA as compared to topo VI

An example of processive supercoil relaxation by *S. cerevisiae* topo II, as compared to topo VI in **Figure 3.2**. Topo II was pre-incubated in a 1:1.4 ratio to a 2.9kbp negatively supercoiled plasmid (6.7ng/µL in assay). Reactions were started by addition of either (**a**) ATP or (**b**) ATP and a 13.5 kbp "chase" plasmid (6.7ng/µL in assay) to compete for unbound enzyme. Samples were quenched at 0, 1, 2, 4, 6, 8, 10, 15, and 20 min. Each condition was also incubated without ATP for 20min as a negative control. Topoisomer species and identification of each plasmid are indicated on the left of each gel.

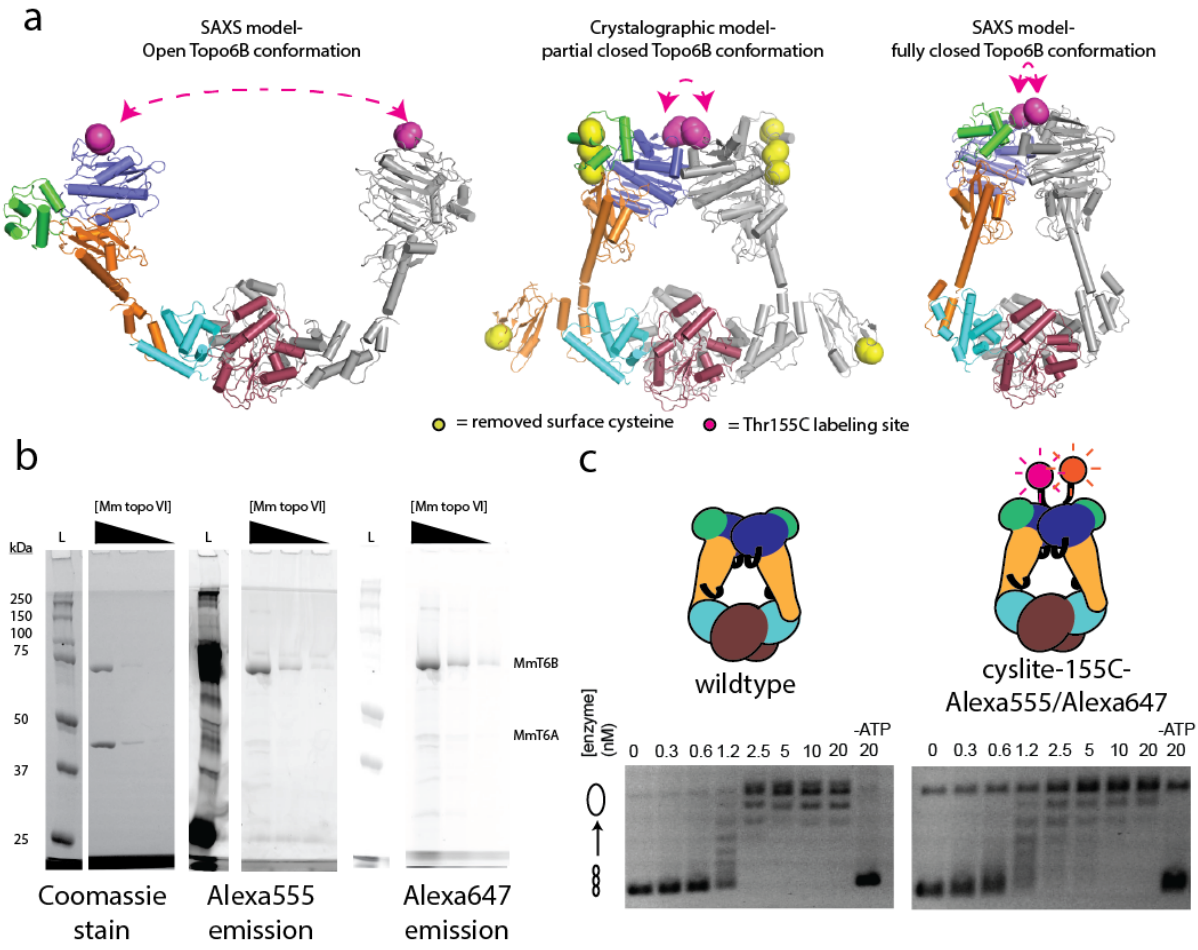

Figure S3.2. Design and production of a FRET pair labeled topo VI to report on B-subunit conformation.

(**a**) Three different conformations of the topo VI holoenzyme, an open SAXS model of *S. shibatae* topo VI, a partially closed crystallographic model of *M. mazei* topo VI, and a fully closed SAXS model of *Ss* topo VI are shown with Thr155 displayed in pink sticks and the distance between Thr155 dimer pairs shown by pink dashed arrows. Native cysteine residues mutated to alanine or serine residues to remove off target labeling sites are shown as yellow sticks on the *Mm* topo VI crystal structure.

(**b**)Purified topoVI$^{cyslite\text{-}155C}$ labeled with Alexa555 and Alexa647, separated on SDS-PAGE and stained for protein with Coomassie blue (*left)* after scanning for Alexa555 emission(*middle*), and Alexa647 emission (*right)*. A dilution series of enzyme (1ug, 0.1ug, 0.01ug) was run, along with a standards ladder(lane marked L, molecular weights in kDaltons labeled on left). Positions of *Mm*Top6B and *Mm*Top6A are labeled on the right.

(**c**)General activity of FRET pair labeled topo VI for relaxing supercoiled DNA as compared to wildtype a function of enzyme concentration. For the enzyme titrations (0.3-20nM in two-fold steps, marked above), each assay proceeded for 30 min prior to quenching and contained 3.5

nM plasmid (10.2 µM bp DNA). Topoisomer products were separated on agarose gel with the position of supercoiled and relaxed topoisomers marked on the left. Cartoons denote the construct used in each activity assay.

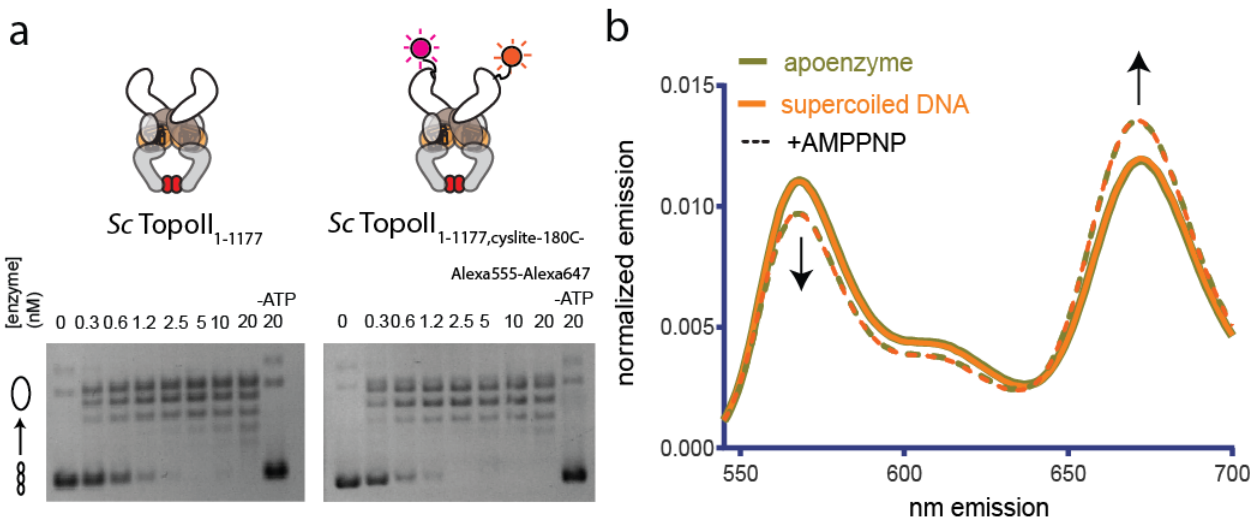

Figure S3.3. AMPPNP is sufficient to close the ATP gate of *Sc* Topo II.

(**a**) To assess conformation of the ATP gate of the type IIA topoisomerase *Sc* topo II, surface cysteine residues were mutated to alanine or valine, with the native C180 retained and labeled with Alexa-555-maleimide and Alexa-647-maleimide to generate *Sc* Topo II$^{1\text{-}1177,cyslite\text{-}180C\text{-}Alexa555\text{-}Alexa647}$ for ATP gate closure assays. Supercoil relaxation activity of the labeled *Sc* topo II$^{1\text{-}1177,cyslite\text{-}180C}$ was compared to wildtype as a function of enzyme concentration. For the enzyme titrations (0.3-20nM in two-fold steps, marked above), each assay proceeded for 30 min prior to quenching and contained 3.5 nM plasmid (10.2 µM bp DNA). Topoisomer products were separated on agarose gel with the position of supercoiled and relaxed topoisomers marked on the left. Cartoons denote the construct used in each activity assay.

(**b**) Fluorescence emission spectra produced by 530nm excitation of Alexa555/Alexa647 labeled *Sc* Topo II$^{1\text{-}1177,cyslite\text{-}180C}$ show that unlike topo VI, addition of AMPPNP (dashed line spectra), is sufficient to dimerize the ATP gate as accessed by the relative increase in acceptor emission and decrease in donor emission as compared to controls without nucleotide (solid line spectra). Presence (goldenrod spectra) or absence (pink spectra) of supercoiled DNA does not appreciably modify the conformational state of the ATP gate as accessed by FRET. Spectral emission was normalized by total emission from 545nm to 700nm.

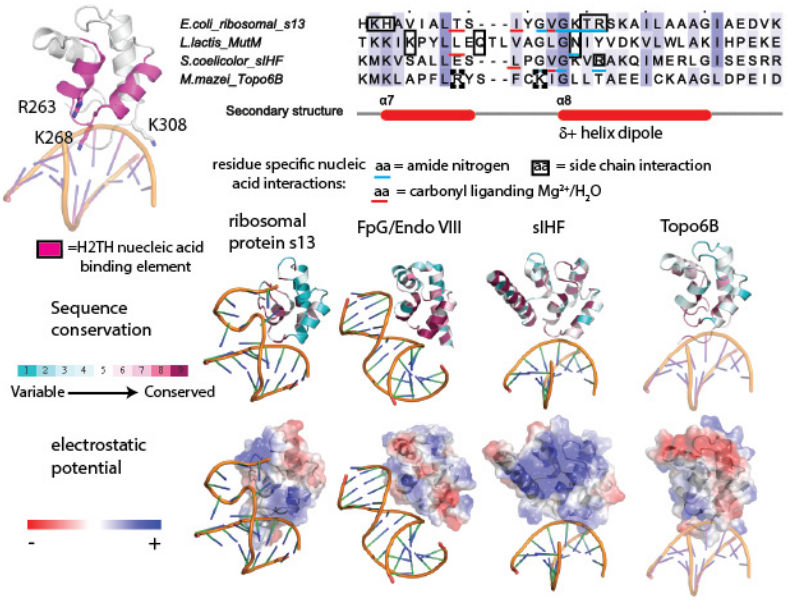

Figure S3.4. Comparison between H2TH domain homologs predicts a DNA binding interface in Top6B.

Representation of the H2TH domain with the nucleic acid binding element colored pink, potential DNA binding residues labeled, and DNA modeled based on a DNA-bound sIHF structure (*top left*). Structural comparison reveals ribosomal s13 (PDB ID=4YBB, (Noeske et al., 2015)), MutM (PDB ID=1TDZ, (Coste et al., 2004)) and sIHF (PDB ID=4ITQ, (Swiercz et al., 2013)) bind DNA or RNA through interactions with main chain amide nitrogens (blue underline) or bridging H_2O or Mg^{2+} liganded by main chain carbonyl oxygens(red underline). Side chain interactions (black box) are poorly conserved (*top right*). Nevertheless, the nucleic acid binding interface (*middle)* and electrostatic surface (*bottom*) is maintained within each family.

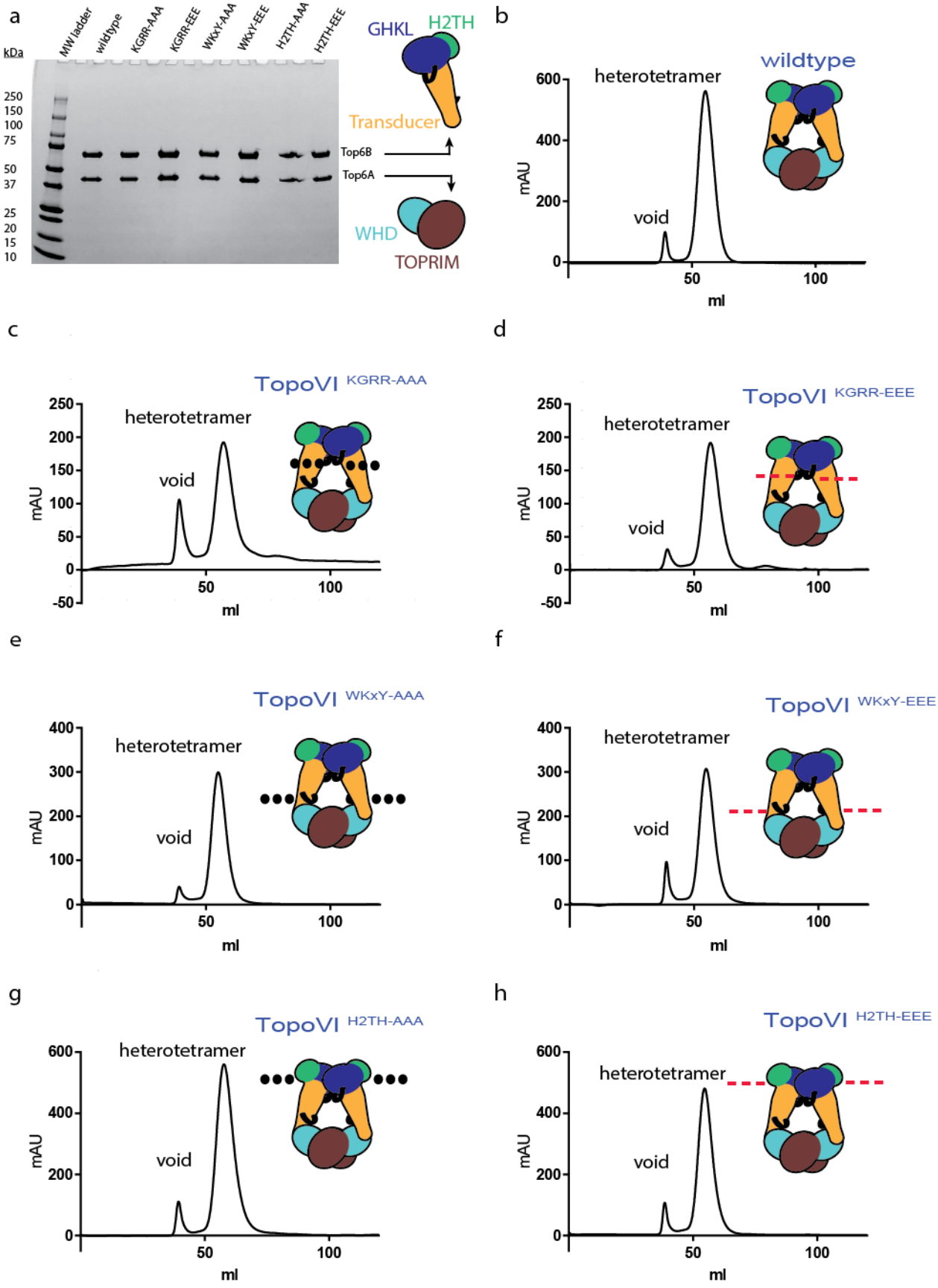
a
kDa
MW ladder
wildtype
KGRR-AAA
KGRR-EEE
WKxY-AAA
WKxY-EEE
H2TH-AAA
H2TH-EEE
250
150
100
75
50
37
25
20
15
10
GHKL
H2TH
Transducer
Top6B
Top6A
WHD
TOPRIM
b
wildtype
heterotetramer
void
mAU
ml
c
TopoVI KGRR-AAA
heterotetramer
void
mAU
ml
d
TopoVI KGRR-EEE
heterotetramer
void
mAU
ml
e
TopoVI WKxY-AAA
heterotetramer
void
mAU
ml
f
TopoVI WKxY-EEE
heterotetramer
void
mAU
ml
g
TopoVI H2TH-AAA
heterotetramer
void
mAU
ml
h
TopoVI H2TH-EEE
heterotetramer
void
mAU
ml

Figure S3.5. Topo VI functional mutants show similar solution properties to wild-type enzyme as judged by gel filtration.

(**a**) Purity of constructs in this study was assessed by running ~4ug of each construct on SDS-PAGE (4%-20% gradient) and staining with Coomassie Blue. Molecular weight standards (*left*) and subunit identity (*right*) are labeled. **(b-h)** Size exclusion chromatographs for wildtype **(b)** KGRR-AAA **(c)**, KGRR-EEE **(d)**, WKxY-AAA **(e)**, WKxY-EEE **(f),** H2TH-AAA **(g)**, and H2TH-EEE **(h)** topo VI constructs. Void and heterotetramer peaks are noted for each chromatograph. The placement and nature of mutations in each construct are depicted in the cartoons above each chromatograph ("•••" - AAA; "---" – EEE). Each protein preparation gives rise to a monodisperse peak eluting at the same expected volume.

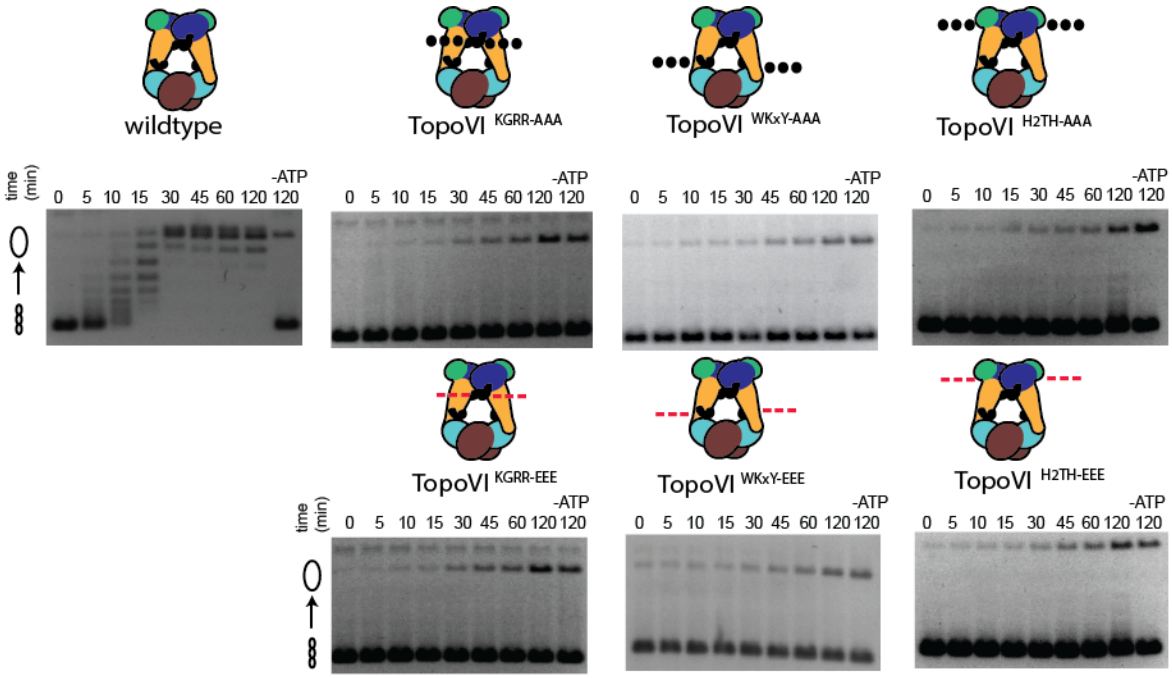

Figure S3.6. Supercoil relaxation activity of topo VI mutants as a function of time.
General activity of mutant topo VI constructs for relaxing supercoiled DNA as compared to wildtype as a function of time. In each time course experiment, 2.5nM of enzyme processed 3.5 nM of negatively supercoiled plasmid (10.2 µM bp) and was quenched with EDTA and SDS at the indicated time (0-120min). The placement and nature of mutations in each construct are depicted in the cartoons above each timecourse ("•••" - AAA; "---" – EEE).

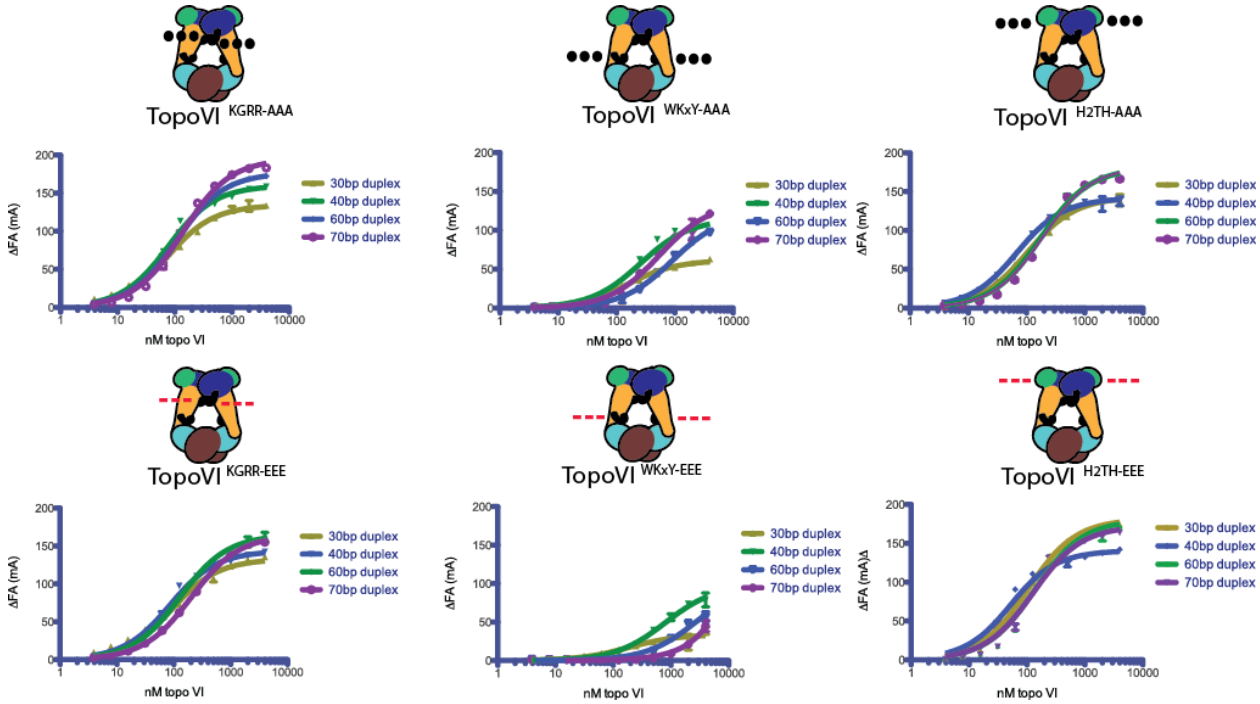

Figure S3.7. Affinity of topo VI mutants for longer duplexes as determined by fluorescence anisotropy

Binding of a 30, 40, 60 or 70bp fluorescein labeled duplex (20nM) to topo VI mutant constructs. Binding was observed as a change in fluorescence anisotropy (ΔFA) and measured in milli-anisotropy units (mA) as a function of enzyme concentration. Points and errors correspond to three independent experiments. Curves represent fits to a single site ligand depletion binding model. The placement and nature of mutations in each construct are depicted in the cartoons above each set of binding curves ("•••" - AAA; "---" – EEE).

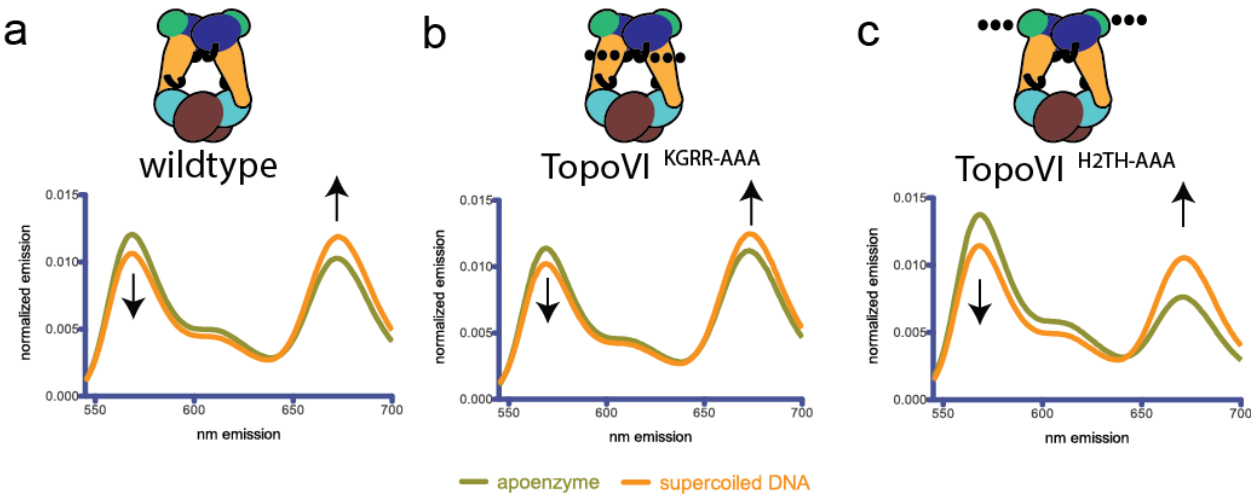

Figure S3.8. Conformational response of H2TH-AAA and KGRR-AAA constructs on different substrates as determined by FRET in the absence of nucleotide.

Comparison of the fluorescence emission spectra produced by 530nm excitation of Alexa555/Alexa647 labeled **(a)** TopoVI$^{\text{cyslite-155C}}$, **(b**) TopoVI$^{\text{cyslite-155C, KGRR-AAA}}$ and **(c)** TopoVI$^{\text{cyslite-155C, H2TH-AAA}}$ alone and on supercoiled DNA. For all three constructs, supercoiled DNA modulates the conformation of the Topo6B ATP gate in the absence of nucleotide as assessed by FRET. Spectral emission was normalized by total emission from 545nm to 700nm.

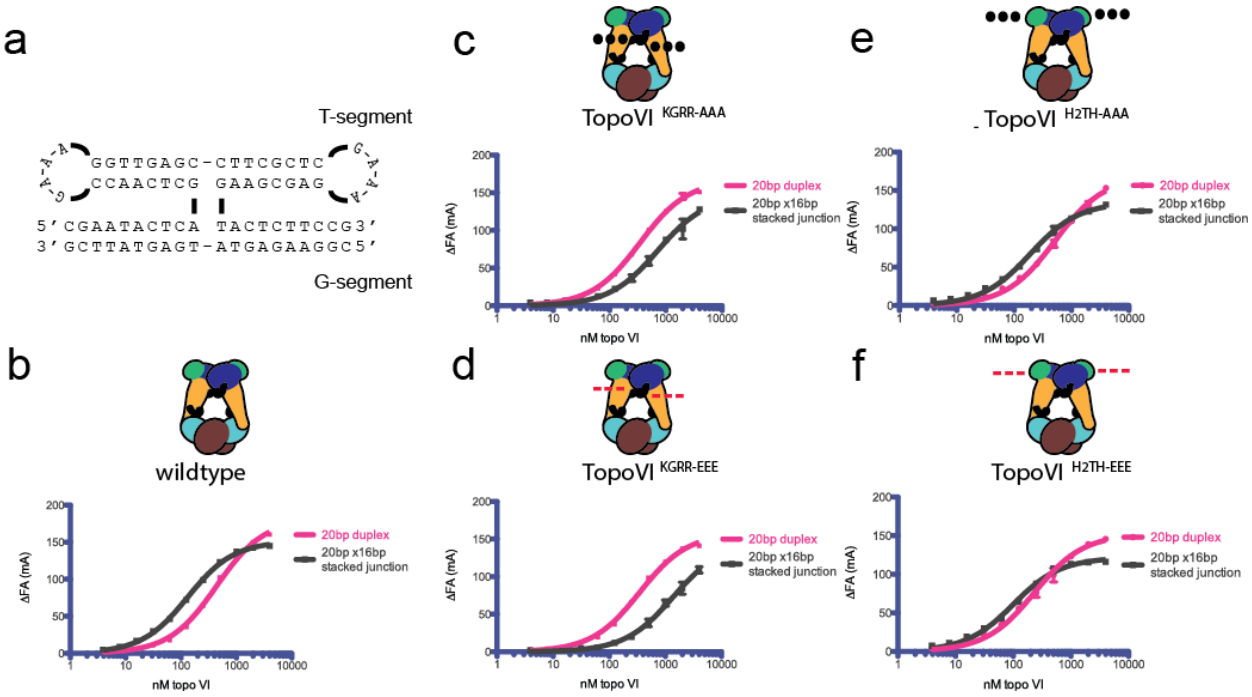

Figure S3.9. Affinity of KGRR loop and H2TH topo VI mutants for a 20bp x16bp stacked DNA junction as compared to a 20bp duplex as determined by fluorescence anisotropy.

(**a**) Schematic of the 20bp by 16bp stacked junction substrate used to mimic a T-segment/G-segment plectoneme crossing. (**b-f**) Binding of a 20bp fluorescein labeled duplex (20nM) or 20bp by 16bp fluorescein labeled stacked junction substrate to topo VI mutant constructs. Binding was observed as a change in fluorescence anisotropy (ΔFA) and measured in milli-anisotropy units (mA) as a function of enzyme concentration. Points and errors correspond to three independent experiments. Curves represent fits to a single site ligand depletion binding model. The placement and nature of mutations in each construct are depicted in the cartoons above each set of binding curves ("•••" - AAA; "---" – EEE).

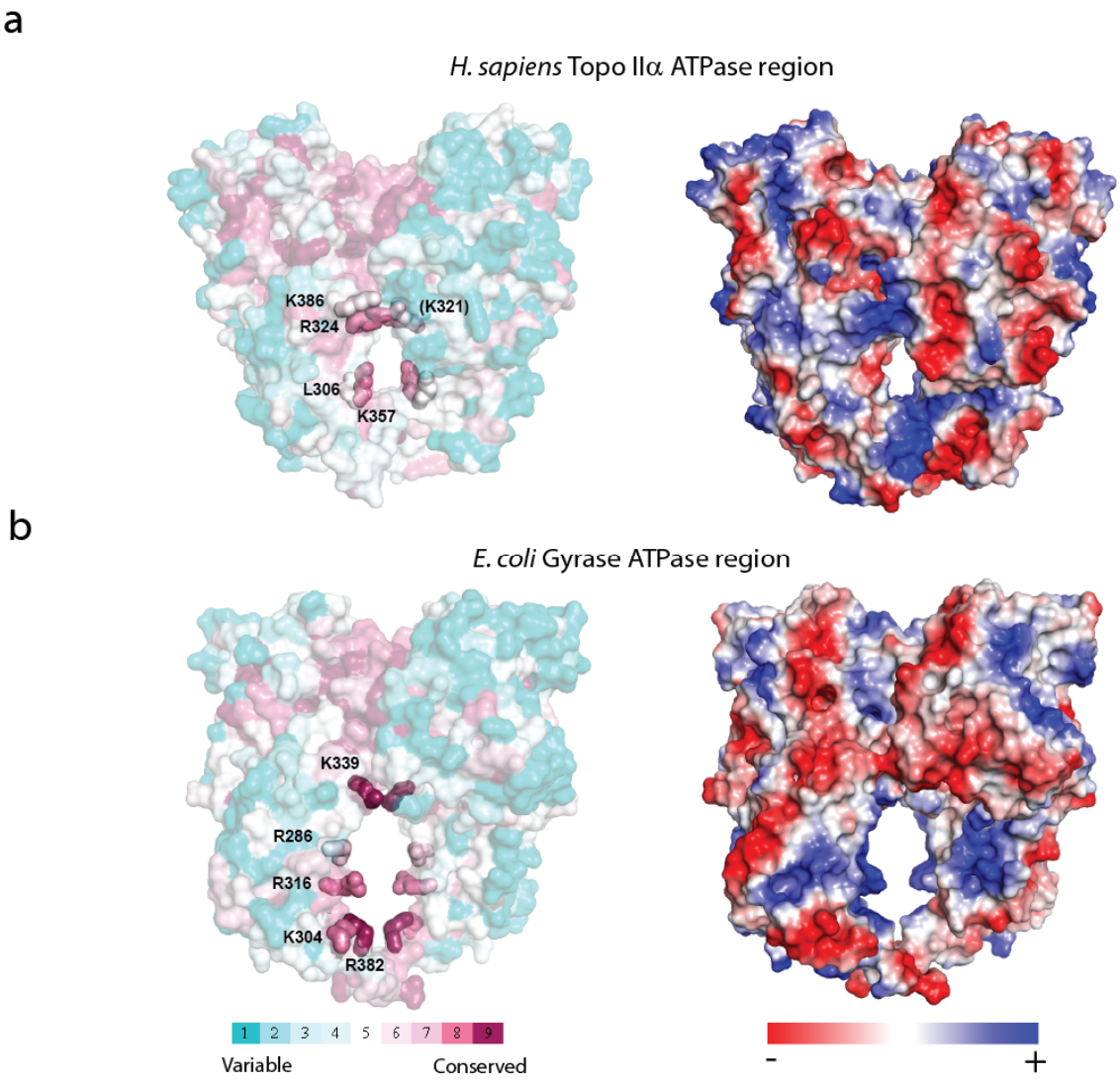

Figure S3.10. Conservation of basic residues in the N-terminal T-segment storage cavity of eukaryotic and bacterial type IIA topoisomerases

Sequence conservation and electrostatic potential are shown for the ATPase region (GHKL and transducer domain) of (**a**) eukaryotic type IIA topoisomerase (*H. sapiens* Topo IIα, PDB ID = 1ZXM) and (**b**) bacterial type IIA topoisomerase (*E. coli* DNA gyrase, PDB ID=4PU9). Conservation is based on a PSI-BLAST multiple sequence alignment. Conserved arginine and lysine residues (ConSurf score of ≥ 6) on the surface of the T-segment storage cavity are shown as sticks and labeled. Coloration is cyan to magenta for variable to conserved. Electostatic potentials were based on ABPS calculations.

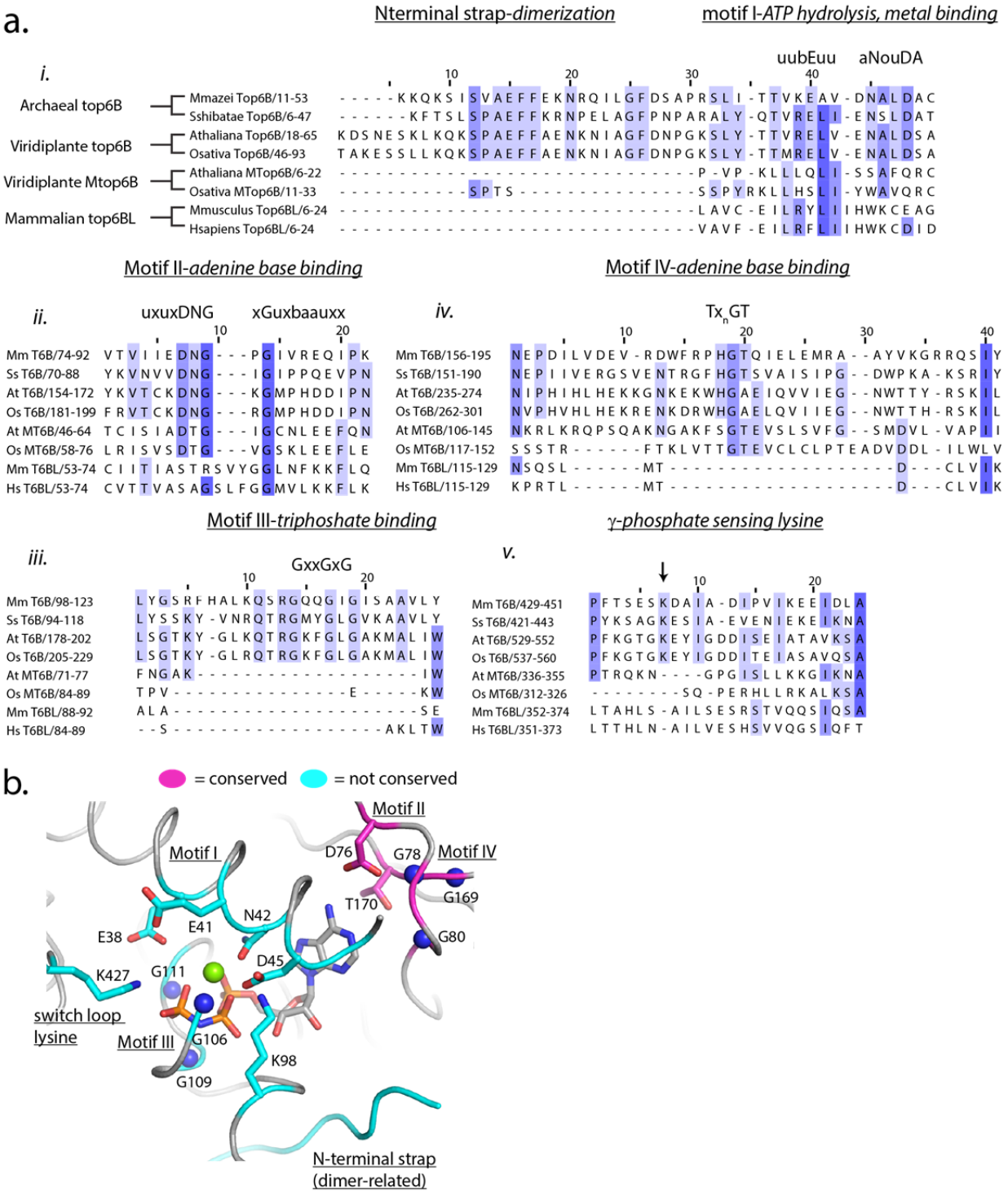

Figure S3.11. Conservation of DNA and ATP binding elements between Top6B, MTop6B, and Top6BL

(**a**) Alignment of archaeal top6B (*M. mazei, S. shibatae),* Viridiplante top6B (*A. thaliana, O. sativa*), Viridiplante Mtop6B (*A. thaliana, O. sativa*), and mammalian Top6BL (*Mus musculus,*

Homo sapiens) comparing motifs important for ATP hydrolysis. These include (***i***) the N-terminal dimerization strap and motif I, metal binding and ATP hydrolysis; (***ii***) motif II, adenine binding and base discrimination; (***iii***) motif III, triphosphate binding; (***iv***) motif IV, adenine binding and (***v***)transducer domain γ-phosphate sensor loop (Dutta & Inouye, 2000; Schoeffler & Berger, 2008; Thomsen & Berger, 2008) (**b**) Ribbon representation of the ATP binding pocket of *S. shibatae* top6B bound to the nonhydrolyzable ATP analog AMPPNP (PDB ID =1Mx0 (Corbett & Berger, 2003)) with the side chains of residues involved in hydrolysis(E38), metal binding(N42), triphosphate binding(G106, G109, G111, K98), adenine binding(D76, T170, G78, G80, G168) phosphate sensing(K427) or coordinating with other residues in the pocket (E41, D45) shown as sticks. The nitrogen atoms of denoted main chain glycine residues are shown as blue spheres. Residues that are generally conserved in the meiotic Top6B homologs are shown in magenta and poorly conserved residues are shown in cyan. GHKL motifs I-IV and the switch lysine residue are labeled. Residues are numbered according to *S. shibatae* Top6B.

Chapter 4 – Concluding Remarks and Future Directions

Conclusions

The aim of this dissertation has been to characterize and compare mechanisms of strand passage coordination specific to either type IIA or type IIB topoisomerases. Chapter 2 presented the first experimentally determined structure of the human topoisomerase IIα breakage-reunion region. Topo IIα assists in the unchecked proliferation of cancer cells and is the desired target of several chemotherapeutic regimes that use topoisomerase poisons, small molecules that convert topo IIα into a cytotoxic, DNA damaging agent (Boege et al., 1995; Fry et al., 1991). Unfortunately, topoisomerase poisons cross-react with human topo IIβ, an enzyme used for transcriptional control (Ju et al., 2006; King et al., 2013; Lin, Ho, Liu, & Lyu, 2013; Madabhushi et al., 2015; McNamara et al., 2008; Perillo et al., 2008), generating secondary malignancies (Azarova et al., 2007; Lyu et al., 2007). Comparison of our structure to an etoposide-bound human topo IIβ structure (Wu et al., 2011) revealed a similarly shaped and accessible etoposide binding pocket even though the two structures are in different conformational poses (Wendorff, Schmidt, Heslop, Austin, & Berger, 2012). This analysis both rationalized etoposide cross-reactivity and highlighted residues that might serve as potential handles for specifically targeting the topo IIα isoform.

In the context of the growing structural collection of type IIA topoisomerase breakage-reunion regions, a number of allosteric principles were determined for how DNA engagement, catalytic metal binding, and strand scission at the DNA are communicated to and affect the C-gate. First, constriction of the DNA-gate around a bound G-segment appears to generate structural strain in the α-helical coiled arms connecting the DNA gate to the C-gate that overcomes a predisposition for C-gate association. Nevertheless, binding of both active site metals and proper positioning of the active site tyrosine for catalysis require C-gate association. Upon strand scission, the DNA gate may dissociate to overcome strain produced by G-segment binding while the C-gate remains dimerized. Together, these principles directly link the open/closed status of the C-gate to G-segment cleavage status. Tellingly, binding of topoisomerase poisons appear to corrupt proper allosteric coordination in this network.

Whereas Chapter 2 focused on allosteric communication between the DNA-gate and C-gate specific to type IIA topoisomerases, Chapter 3 presented a set of biochemical studies supporting a new and unanticipated model for how type IIB topoisomerases bind DNA and coordinate communication between their ATPase and DNA cleavage regions. Results from this chapter show the functional status of two dimer interfaces – referred to as the ATP- and DNA-gates – are linked together by a variety of mechanisms, some of which are specific to type IIB topoisomerases and others that are shared with type IIA enzymes. For example, similar to eukaryotic topo II, topo VI bends a bound G-segment DNA, using an interface that includes contacts not only from the DNA-gate, but also the ATPase region. Interestingly, however, it is an H2TH domain – a fold specific to type IIB topoisomerases – that is necessary and required for G-segment bending. Contrariwise, a direct interaction between the Top6B transducer domain and Top6A inhibits Top6B dimerization in the absence of either a bent G-segment DNA or G-

segment/T-segment DNA crossing. Although both classes share DNA-dependent stimulation of ATP hydrolysis, an inhibitory mechanism appears specific to type IIB topoisomerases, as a flexible tethering element between the ATPase region and the breakage-reunion region of type IIA topoisomerases readily allows GHKL dimerization and ATP hydrolysis in the absence of a DNA substrate. Top6B also contributes a positively charged motif to the T-segment storage cavity – the KGRR loop – that senses DNA and is required for strand passage. Notably, the ATPase region of type IIA topoisomerases has similar positively-charged motifs, but these motifs have seen limited study (Tingey & Maxwell, 1996). It has been speculated that strain introduced by T-segment storage following ATP-gate closure potentiates DNA-gate opening (Corbett & Berger, 2005; Graille et al., 2008; Roca, 2004). If true, the results in Chapter 3 suggest the KGRR loop and functionally related elements may play an important role in potentiating and coordinating DNA-gate opening for both type II topoisomerase classes.

Future directions

Type IIA topoisomerases

The analysis presented in Chapter 2 lays the groundwork for two distinct avenues of further study. One centers on improving the therapeutic targeting of human topo IIα. The other is to gain a more comprehensive understanding of how conformational rearrangements in one region in a type IIA topoisomerase are structurally and dynamically communicated throughout the enzyme. The available human topo IIα and topo IIβ structures provides a starting point for identifying and designing topo IIα specific drugs by structure-activity relationships (SAR). Computational tools have already been used for virtual screening and to follow conformational trajectories of these regions *in silico* (Drwal, Marinello, & Manzo, 2014; Huang & Lin, 2015). Work by Nei Li Chan and colleagues also has revealed how numerous anti-tumor drugs, such as mAMSA, mixoantrone and ametantrone bind to the topo IIβ breakage-reunion regions (Wu, Li, Wang, Li, & Chan, 2013). One drawback to these efforts, however, is that with the exception of etoposide, the available structures have been determined by soaking compounds into pre-formed crystals of topo IIβ with etoposide, an approach that may bias the observed binding poses. Despite this concern, both computational modeling and certain previously-identified, drug-sensitizing mutations corroborate with the poses visualized (Huang & Lin, 2014; Leontiou, Lakey, & Austin, 2004). It is therefore unclear whether capturing *de novo* structures of eukaryotic topoisomerases bound these chemotherapeutic agents, even of topo IIα, is required to validate the poses determined by soaking methods.

One issue worth considering is whether the binding sites in topo IIα and topo IIβ for clinically-used therapeutics are divergent enough for small molecules to discriminate between the two isoforms. Structures of both the human topo IIα ATPase region (Wei et al., 2005) and breakage reunion region may allow computational techniques to virtually screen for compounds that can target critical functional sites where topo IIα and topo IIβ diverge in sequence. Such a goal would suggest that there is potential utility in determining an atomic structure of the topo IIβ ATPase region.

The most major differences between topo IIα and topo IIβ are found in the enzymes' non-conserved C-terminal regions (CTRs). This variability, coupled with the high hydrophilicity and general lack of *in vitro* function (particularly for topo IIβ), indicates that the CTRs are largely unstructured in eukaryotic topo IIs (Austin et al., 1993; Caron et al., 1994; Crenshaw & Hsieh, 1993; Jensen et al., 1996; McClendon et al., 2008). In topo IIα, however, the CTR imparts a preference for resolving positive DNA supercoils, an activity similar to the C-terminal domain of the topo IV ParC subunit (McClendon et al., 2008, 2005; Seol et al., 2013). This activity on the part of the topo IIα CTR is difficult to reconcile with a completely unstructured domain. Uncovering the biophysical basis for how the topo IIα CTR modulates topological preference could bridge a gap of understanding between how bacteria and eukaryotic type IIA topoisomerases utilize their auxiliary C-terminal regions to coordinate strand passage. It could also provide a specific way to target topo IIα if a sub-element of its CTR proves to be structured.

The analyses of Chapter 2 were only possible due to a diverse set of available structures that visualize different states of the type IIA breakage-reunion region. Recent structural studies of even larger fragments of type IIA topoisomerases have revealed additional unexpected conformations of this class of enzyme (Laponogov et al., 2013; Papillon et al., 2013; Schmidt et al., 2012), while single molecule studies predict that yet more poses remain to be visualized (Basu et al., 2012; Gubaev & Klostermeier, 2011; Lebel, Basu, Oberstrass, Tretter, & Bryant, 2014). Additional views of catalytically active type IIA topoisomerases, in particular with both G- and T-segment DNA, will be required to develop an atomic-resolution view of how substrate engagement and conformational changes in one region of these enzymes are communicated to and correlated with movements in distal regions. The ongoing "resolution revolution" in cryo-electron microscopy will make such studies more tractable (Callaway, 2015). Ultimately, however, there is a limit to visualizing static poses. Questions pertaining to relative timing of gate opening and closing events remain key barriers to understanding the concerted coordination of type II topoisomerase movement during strand passage. Also, although crystallography has answered the question of where topoisomerase II poisons bind, it has not sufficiently explained why certain poisons bind certain homologs, or why certain drugs are more effective than others. Rather, the kinetics of binding and dissociation appear important in a way that is not coupled to specific drug-protein interactions (Blower et al., 2016). Developing experimental approaches to follow type IIA topoisomerase conformational changes in real time is a critical next step for understanding how these enzymes facilitate the movement of one DNA duplex through another and for how small molecules corrupt such movements. The development of fluorescently labeled type IIA topoisomerases which report on the status of the different dimer gates (as reported in Chapter 3 and (Gubaev & Klostermeier, 2011)), coupled with DNA tethering geometries and single molecule microscopy setups to follow processive activity of single topoisomerases on topologically closed substrates, will be required to address these questions.

Type IIB topoisomerases

The studies described in Chapter 3 set out to better understand type IIB topoisomerase mechanism, and ultimately led to a new model for how these enzymes both engage DNA and

couple ATP/T-segment binding to efficient G-segment cleavage. Validating this model will require an atomic resolution structure of a DNA-bound enzyme intermediate. Visualizing such a complex was an original aim of my thesis research and the studies in Chapter 3 were prompted by efforts to understand why two tools I developed for determining such a structure failed. One of these tools was the stacked junction substrate, which was intended to mimic a crossed G- and T-segment but proved too sensitive to ionic strength for stabilizing a DNA-bound complex for crystallography. The other was a set of functional mutants (*M. mazei* Top6A^{E342Q}B and *M. mazei* top6A^{R209Q}B), which weakened the auto-inhibitory conformation of Top6A; although these mutants preferentially generated trapped cleavage complexes on plasmid DNA as I had hoped, they proved incapable of cleaving short (i.e. 20-26bp) DNA duplexes. The studies performed as part of Chapter 3 reveal that both approaches failed due to incorrect assumptions concerning the length and binding mechanism of a G-segment DNA. Both tools are now well positioned to aid with determining the structure of topo VI bound to DNA, either by cryo-electron microscopy or potentially by X-ray crystallography.

The FRET experiments in Chapter 3 revealed that topo VI uses topological features in supercoiled DNA to promote Top6B dimerization. However, the dynamics of gate closure and interface coordination cannot be readily determined from bulk measurements. The properties of ATP-gate closure and ATP hydrolysis found from my studies indicate that T-segment engagement stabilizes a closed conformation that is sampled by the enzyme when bound to a DNA crossing, but further suggest that T-segment binding promotes an intermediate conformational change prior to full ATP-gate closure. Considering the slow strand passage and ATP turnover rates observed for topo VI, it is unclear whether the binding of topo VI to DNA, Top6B dimerization, T-segment passage, Top6B gate opening, or topo VI dissociation from DNA act as a rate limiting step. A single molecule FRET assay using topologically closed DNAs would be the most direct method to answer these questions.

Topo VI's slow strand passage rate *in vitro* raises the intriguing possibility that type IIB topoisomerases may require other interacting partners for full functionality *in vivo*. Binding partners have already been identified for plant topo VI (Breuer et al., 2007; Kirik et al., 2007; Sugimoto-shirasu et al., 2005). However, no *in vitro* activity of plant topo VI has been reported in the literature, suggesting that reconstitution of this system might be quite challenging. Alternatively, archaeal genomes could be searched for potential partners, though the required computational and experimental interaction screening would be non-trivial.

Finally, the homology between topo VI to the Spo11 meiotic recombination machinery suggests several directions for future efforts. The studies outlined in Chapter 3 indicate that mutations specific to basic residues in the WKxY motif and/or basic amino acids that line the predicted C-terminal α-helix of meiotic Top6B homologs should be defective for DNA binding and meiotic recombination. MTop6B in plants also retains a domain insert between its GHKL and transducer domain; conserved motifs in this domain show some similarity to the DNA binding loop in H2TH family proteins, and it would be interesting to see whether point mutations to this sequence yield double-strand break deficient phenotypes. Surprisingly, the ATP binding and N-termini dimerization motifs in the GHKL fold of both MTop6B and Top6BL

are highly degenerate. Considering the importance of Top6B dimerization for promoting Top6A-dependent cleavage, this suggests some other signal, perhaps a post-translational modification or additional factors such as MEI4, REC114 and MEI1 in mice or the Rec114/Mei4/Mer2 complex in yeast (Lam & Keeney, 2014), might promote cleavage by facilitating dimerization. All of these studies would benefit from biochemical characterization *in vitro*. If co-expression of meiotic top6B homologs improves reconstitution of Spo11 activity, these systems may be compared biochemically to top VI directly.

Final remarks

It has been over forty years since the initial discovery of a type II topoisomerase (Gellert et al., 1976). Since that time, type II topoisomerases have been found to adopt two distinct architectures, each of which in turn has been fine-tuned by evolution to produce distinct activities in different cellular contexts. The activities and cellular roles of type II topoisomerases are versatile and varied, yet generally follow a paradigm of using chemical energy (in the form of ATP) to control activity and mitigate the potential to damage DNA. There remain many fundamental questions pertaining to *how* ATP hydrolysis couples to the concerted movements of discrete enzymatic elements and DNA substrates. Recent years have seen both breakthroughs in structural techniques that may make it tractable to image some of these fleeting intermediates, while improvements of single molecule techniques are likely to continue to provide new insights into chemo-mechanical coordination. Tackling these research directions remains important, both from a basic and biomedical perspective. Although the topoisomerase field is relatively mature, it is likely some of the most exciting discoveries pertaining to type II topoisomerase mechanism and regulation have yet to be made.

References

Acharya, S., Foster, P. L., Brooks, P., & Fishel, R. (2003). The Coordinated Functions of the E . coli MutS and MutL Proteins in Mismatch Repair. *Molecular Cell*, *12*, 233–246.

Adams, P. D., Afonine, P. V, Bunkóczi, G., Chen, V. B., Davis, I. W., Echols, N., … Zwart, P. H. (2010). PHENIX: a comprehensive Python-based system for macromolecular structure solution. *Acta Crystallographica. Section D, Biological Crystallography*, *66*(Pt 2), 213–21.

Ali, J. A., Orphanides, G., & Maxwell, A. (1995). Nucleotide Binding to the 43-Kilodalton N-Terminal Fragment of the DNA Gyrase B Protein. *Biochemistry*, *34*(30), 9801–9808.

Ali, M. M. U., Roe, S. M., Vaughan, C. K., Meyer, P., Panaretou, B., Piper, P. W., … Pearl, L. H. (2006). Crystal structure of an Hsp90 – nucleotide – p23 / Sba1 closed chaperone complex. *Nature*, *440*(April), 1013–1017.

Altschul, S. F., Madden, T. L., Schäffer, a a, Zhang, J., Zhang, Z., Miller, W., & Lipman, D. J. (1997). Gapped BLAST and PSI-BLAST: a new generation of protein database search programs. *Nucleic Acids Research*, *25*(17), 3389–402.

Altschul, S. F., Wootton, J. C., Gertz, E. M., Agarwala, R., Morgulis, A., Schäffer, A. a, & Yu, Y.-K. (2005). Protein database searches using compositionally adjusted substitution matrices. *The FEBS Journal*, *272*(20), 5101–9.

Anderson, V. E., Gootz, T. D., & Osheroff, N. (1998). Topoisomerase IV Catalysis and the Mechanism of Quinolone Action. *The Journal of Biological Chemistry*, *273*(28), 17879–17885.

Aravind, L., Leipe, D. D., & Koonin, E. V. (1998). Toprim--a conserved catalytic domain in type IA and II topoisomerases, DnaG-type primases, OLD family nucleases and RecR proteins. *Nucleic Acids Research*, *26*(18), 4205–13.

Arpa, P. D., Beardmore, C., & Liu, L. F. (1990). Involvement of Nucleic Acid Synthesis in Cell Killing Mechanisms of Topoisomerase Poisons. *Cancer Research*, *50*(21), 6919–6924.

Ashkenazy, H., Erez, E., Martz, E., Pupko, T., & Ben-tal, N. (2010). ConSurf 2010 : calculating evolutionary conservation in sequence and structure of proteins and nucleic acids. *Nucleic Acids Research*, *38*(May), 529–533.

Austin, C. A., Sng, J.-H., Patel, S., & Fisher, L. M. (1993). Novel HeLa topoisomerase II is the II beta isoform: complete coding sequence and homology with other type II topoisomerases. *Biochimica et Biophysica Acta*, *1172*(3), 283–91.

Austin, C., & Fisher, L. (1990). Isolation and characterization of a human cDNA clone encoding a novel DNA topoisomerase II homologue from HeLa cells. *FEBS Letters*, *266*(1–2), 115–7.

Azarova, A. M., Lyu, Y. L., Lin, C.-P., Tsai, Y.-C., Lau, J. Y.-N., Wang, J. C., & Liu, L. F. (2007). Roles

of DNA topoisomerase II isozymes in chemotherapy and secondary malignancies. *Proceedings of the National Academy of Sciences of the United States of America*, *104*(26), 11014–9.

Bachant, J., Alcasabas, A., Blat, Y., Kleckner, N., & Elledge, S. J. (2002). The SUMO-1 isopeptidase Smt4 is linked to centromeric cohesion through SUMO-1 modification of DNA topoisomerase II. *Molecular Cell*, *9*(6), 1169–82.

Baird, C. L., Harkins, T. T., Morris, S. K., & Lindsley, J. E. (1999). Topoisomerase II drives DNA transport by hydrolyzing one ATP. *Proceedings of the National Academy of Sciences of the United States of America*, *96*(24), 13685–90.

Baker, N. A., Sept, D., Joseph, S., Holst, M. J., & McCammon, J. A. (2001). Electrostatics of nanosystems : Application to microtubules and the ribosome. *Proceedings of the National Academy of Sciences*, *98*(18), 10037–10041.

Baldi, M. I., Benedetti, P., Mattoccia, E., & Tocchini-Valentini, G. P. (1980). In vitro catenation and decatenation of DNA and a novel eucaryotic ATP-dependent topoisomerase. *Cell*, *20*(2), 461–7.

Ban, C., Junop, M., & Yang, W. (1999). Transformation of MutL by ATP Binding and Hydrolysis : A Switch in DNA Mismatch Repair. *Cell*, *97*, 85–97.

Ban, C., & Yang, W. (1998). Crystal Structure and ATPase Activity of MutL : Implications for DNA Repair and Mutagenesis. *Cell*, *95*, 541–552.

Bandele, O. J., & Osheroff, N. (2008). The efficacy of topoisomerase II-targeted anticancer agents reflects the persistence of drug-induced cleavage complexes in cells. *Biochemistry*, *47*(45), 11900–8.

Basu, A., Schoeffler, A. J., Berger, J. M., & Bryant, Z. (2012). ATP binding controls distinct structural transitions of Escherichia coli DNA gyrase in complex with DNA. *Nature Structural & Molecular Biology*, *19*(5), 538–546.

Bates, A. D., Berger, J. M., & Maxwell, A. (2011). The ancestral role of ATP hydrolysis in type II topoisomerases: prevention of DNA double-strand breaks. *Nucleic Acids Research*, *39*(15), 6327–39.

Bates, A. D., & Maxwell, A. (2005). *DNA Topology* (2nd ed.). Oxford: Oxford University Press.

Bates, A. D., O'Dea, M. H., & Gellert, M. (1996). Energy Coupling in Escherichia coli DNA Gyrase : the Relationship between. *Biochemistry*, *35*, 1408–1416.

Bax, B. D., Chan, P. F., Eggleston, D. S., Fosberry, A., Gentry, D. R., Gorrec, F., … Gwynn, M. N. (2010). Type IIA topoisomerase inhibition by a new class of antibacterial agents. *Nature*, *466*(7309), 935–40.

Bender, R. P., Jablonksy, M. J., Shadid, M., Romaine, I., Anklin, C., Graves, D. E., & Osheroff, N. (2009). Substituents on Etoposide that Interact with Human Topoisomerase IIalpha in the Binary Enzyme-Drug Complex: Contributions to Etoposide Binding and Activity. *Biochemistry*, *47*(15), 4501–4509.

Berger, J. M., Gamblin, S. J., Harrison, S. C., & Wang, J. C. (1996). Structure and mechanism of DNA topoisomerase II. *Nature*, *379*, 225–232.

Bergerat, A., de Massy, B. de, Gadelle, D., Varoutas, P.-C., Nicolas, A., & Forterre, P. (1997). An atypical topoisomerase II from archaea with implications for meiotic recombination. *Nature*, *386*, 414–417.

Bergerat, A., Gadelle, D., & Forterre, P. (1994). Purification of a DNA topoisomerase II from the hyperthermophilic archaeon Sulfolobus shibatae. A thermostable enzyme with both bacterial and eucaryal features. *The Journal of Biological Chemistry*, *269*(44), 27663–9.

Blattner, F. R., Plunkett III, G., Bloch, C. A., Perna, N. T., Burland, V., Riley, M., … Shao, Y. (1997). The Complete Genome Sequence of Escherichia coli K-12. *Science*, *277*(5331), 1453–1462.

Blower, T. R., Williamson, B. H., Kerns, R. J., & Berger, J. M. (2016). Crystal structure and stability of gyrase – fluoroquinolone cleaved complexes from Mycobacterium tuberculosis. *Proceedings of the National Academy of Science USA*, *113*(7), 1706–1713.

Boege, F., Andersen, A., Jensen, S., Zeidler, R., & Kreipe, H. (1995). Proliferation-Associated Nuclear Antigen Ki-S1 is Identical with Topoisomerase IIalpha. *American Journal of Pathology*, *146*(6), 1302–1208.

Breuer, C., Stacey, N. J., West, C. E., Zhao, Y., Chory, J., Tsukaya, H., … Sugimoto-shirasu, K. (2007). BIN4 , a Novel Component of the Plant DNA Topoisomerase VI Complex , Is Required for Endoreduplication in Arabidopsis. *The Plant Cell*, *19*, 3655–3668.

Brill, S. J., DiNardo, S., Voelkel-Meiman, K., & Sternglanz, R. (1987). Need for DNA topoisomerase activity as a swivel for DNA replication for transcription of ribosomal RNA. *Nature*, *326*(6111), 414–416.

Brodersen, D. E., Jr, W. M. C., Carter, A. P., Wimberly, B. T., & Ramakrishnan, V. (2002). Crystal Structure of the 30 S Ribosomal Subunit from Thermus thermophilus : Structure of the Proteins and their Interactions with 16 S RNA. *Journal of Molecular Biology*, *316*, 725–768.

Brown, P. O., & Cozzarelli, N. R. (1979). A sign inversion mechanism for enzymatic supercoiling of DNA. *Science*, *206*(4422), 1081–1083.

Brown, P. O., & Cozzarelli, N. R. (1981). Catenation and knotting of duplex DNA by type 1 topoisomerases : A mechanistic parallel with type 2 topoisomerases. *Proceedings of the National Academy of Science USA*, *78*(2), 843–847.

Brown, P. O., Peebles, C. L., & Cozzarelli, N. R. (1979). A topoisomerase from Escherichia coli

related to DNA gyrase. *Proceedings of the National Academy of Science USA*, *76*(12), 6110–6114.

Buhler, C., Gadelle, D., Forterre, P., Wang, J. C., & Bergerat, a. (1998). Reconstitution of DNA topoisomerase VI of the thermophilic archaeon Sulfolobus shibatae from subunits separately overexpressed in Escherichia coli. *Nucleic Acids Research*, *26*(22), 5157–62.

Buhler, C., Lebbink, J. H., Bocs, C., Ladenstein, R., & Forterre, P. (2001). DNA topoisomerase VI generates ATP-dependent double-strand breaks with two-nucleotide overhangs. *The Journal of Biological Chemistry*, *276*(40), 37215–22.

Callaway, E. (2015). THE REVOLUTION WILL NOT BE CRYSTALLIZED. *Nature*, *525*(7568), 7–9.

Capranico, G., Tinelli, S., Austin, C. a, Fisher, M. L., & Zunino, F. (1992). Different patterns of gene expression of topoisomerase II isoforms in differentiated tissues during murine development. *Biochimica et Biophysica Acta*, *1132*(1), 43–8.

Caron, P. R., Wayt, P., & Wang, J. C. (1994). The C-Terminal Domain of Saccharomyces cerevisiae DNA. *Molecular and Cellular Biology*, *14*(5), 3197–3207.

Chan, K.-L., North, P. S., & Hickson, I. D. (2007). BLM is required for faithful chromosome segregation and its localization defines a class. *The EMBO Journal*, *26*(14), 3397–3409.

Chan, P. F., Srikannathasan, V., Huang, J., Cui, H., Fosberry, A. P., Gu, M., … Gwynn, M. N. (2015). Structural basis of DNA gyrase inhibition by antibacterial QPT-1, anticancer drug etoposide and moxifloxacin. *Nature Communications*, *6*, 1–13.

Charvin, G., Strick, T. R., Bensimon, D., & Croquette, V. (2005). Topoisomerase IV bends and overtwists DNA upon binding. *Biophysical Journal*, *89*(1), 384–92.

Chen, S. H., Chan, N., & Hsieh, T. (2013). New Mechanistic and Functional Insights into DNA Topoisomerases. *Annual Review of Biochemistry*, *82*, 139–170.

Chen, V. B., Arendall, W. B., Headd, J. J., Keedy, D. a, Immormino, R. M., Kapral, G. J., … Richardson, D. C. (2010). MolProbity: all-atom structure validation for macromolecular crystallography. *Acta Crystallographica. Section D, Biological Crystallography*, *66*(Pt 1), 12–21.

Chong, S., Chen, C., Ge, H., & Xie, X. S. (2014). Mechanism of Transcriptional Bursting in Bacteria. *Cell*, *158*(2), 314–326.

Chung, T. D., Drake, F. H., Tan, K. B., Per, S. R., Crooke, S. T., & Mirabelli, C. K. (1989). Characterization and immunological identification of cDNA clones encoding two human DNA topoisomerase II isozymes. *Proceedings of the National Academy of Sciences of the United States of America*, *86*(23), 9431–5.

Classen, S., Olland, S., & Berger, J. M. (2003). Structure of the topoisomerase II ATPase region

and its mechanism of inhibition by the chemotherapeutic agent ICRF-187. *Proceedings of the National Academy of Sciences*, *100*(19), 543–549.

Confalonieri, F., Eliet, C., Nadal, M., de La Tour, C. B., Forterret, P., & Duguet, M. (1993). Reverse gyrase : A helicase-like domain and a type I topoisomerase in the same polypeptide. *Proceedings of the National Academy of Sciences of the United States of America*, *90*(10), 4753–4757.

Corbett, A. H., Zechiedrich, E. L., & Osheroff, N. (1992). Communication A Role for the Passage Helix in the DNA Cleavage Reaction of Eukaryotic Topoisomerase II. *The Journal of Biological Chemistry*, *267*(2), 683–686.

Corbett, K. D., Benedetti, P., & Berger, J. M. (2007). Holoenzyme assembly and ATP-mediated conformational dynamics of topoisomerase VI. *Nature Structural & Molecular Biology*, *14*(7), 611–9.

Corbett, K. D., & Berger, J. M. (2003). Structure of the topoisomerase VI-B subunit: implications for type II topoisomerase mechanism and evolution. *The EMBO Journal*, *22*(1), 151–63.

Corbett, K. D., & Berger, J. M. (2005). Structural dissection of ATP turnover in the prototypical GHL ATPase TopoVI. *Structure*, *13*(6), 873–82.

Corbett, K. D., Schoeffler, A. J., Thomsen, N. D., & Berger, J. M. (2005). The structural basis for substrate specificity in DNA topoisomerase IV. *Journal of Molecular Biology*, *351*(3), 545–61.

Corbett, K. D., Shultzaberger, R. K., & Berger, J. M. (2004). The C-terminal domain of DNA gyrase A adopts a DNA-bending beta -pinwheel fold. *PNAS*, *101*(19), 7293–7298.

Coste, F., Ober, M., Carell, T., Boiteux, S., Zelwer, C., & Castaing, B. (2004). Structural Basis for the Recognition of the FapydG Lesion Formamidopyrimidine-DNA Glycosylase. *The Journal of Biological Chemistry*, *279*(42), 44074–44083.

Cowell, I. G., Sondka, Z., Smith, K., Lee, K. C., Manville, C. M., Sidorczuk-Lesthuruge, M., … Austin, C. a. (2012). Model for MLL translocations in therapy-related leukemia involving topoisomerase IIβ-mediated DNA strand breaks and gene proximity. *Proceedings of the National Academy of Sciences of the United States of America*, *109*(23), 8989–94.

Crenshaw, D. G., & Hsieh, T. (1993). Function of the Hydrophilic Carboxyl Terminus of Type II DNA Topoisomerase from Drosophila melanogaster. *The Journal of Biological Chemistry*, *117*(21), 21335–21343.

Crick, C. (1976). Linking numbers and nucleosomes. *Proceedings of the National Academy of Sciences USA*, *73*(8), 2639–2643.

Dawlaty, M. M., Malureanu, L., Jeganathan, K. B., Kao, E., Sustmann, C., Tahk, S., … van Deursen, J. M. (2008). Resolution of sister centromeres requires RanBP2-mediated

SUMOylation of topoisomerase IIalpha. *Cell*, *133*(1), 103–15.

Dedon, P. C., & Borch, R. F. (1987). Characterization of the Reactions of Platinum Antitumor Agents with Biological and Nonbiological Sulfur-containing Nucleophiles. *Biochemical Pharmacology*, *36*(12), 1955–1964.

Deppenmeier, U., Johann, A., Hartsch, T., Merkl, R., Schmitz, R. A., Martinez-Arias, R., … Gottschalk, G. (2002). The Genome of Methanosarcina mazei : Evidence for Lateral Gene Transfer Between Bacteria and Archaea. *Journal of Molecular Microbiology and Biotechnology*, *4*(4), 453–461.

Deweese, J. E., Guengerich, F. P., Burgin, A. B., & Osheroff, N. (2009). Metal ion interactions in the DNA cleavage/ligation active site of human topoisomerase IIalpha. *Biochemistry*, *48*(38), 8940–7.

Deweese, J. E., & Osheroff, N. (2009). The DNA cleavage reaction of topoisomerase II: wolf in sheep's clothing. *Nucleic Acids Research*, *37*(3), 738–48.

DiGate, R. J., & Marians, K. J. (1988). Identification of a Potent Decatenating Enzyme from Escherichia coli *. *The Journal of Biological Chemistry*, *263*(26), 13366–13373.

Dingemans, a M., Pinedo, H. M., & Giaccone, G. (1998). Clinical resistance to topoisomerase-targeted drugs. *Biochimica et Biophysica Acta*, *1400*(1–3), 275–88.

Dong, K. C., & Berger, J. M. (2007). Structural basis for gate-DNA recognition and bending by type IIA topoisomerases. *Nature*, *450*(7173), 1201–5.

Drake, F. H., Hofmann, G. A., Bartus, H. F., Mattern, M. R., Crooke, S. T., & Mirabelli, C. K. (1989). Biochemical and pharmacological properties of p170 and p180 forms of topoisomerase II. *Biochemistry*, *28*(20), 8154–8160.

Drlica, K., Hiasa, H., Kerns, R., Malik, M., & Mustaev, A. (2009). Quinolones : Action and Resistance Updated. *Current Topics in Medicinal Chemistry*, *9*, 981–998.

Drwal, M. N., Marinello, J., & Manzo, S. G. (2014). Novel DNA Topoisomerase II a Inhibitors from Combined Ligand- and Structure- Based Virtual Screening. *PloS One*, *9*(12), e114904.

Duckett, D. R., Murchie, A. I. H., Diekmann, S., Kitzing, E. Von, Kemper, B., & Lilley, D. M. J. (1988). The Structure of the Holliday Junction , and Its Resolution. *Cell*, *55*(1), 79–89.

Durand-Dubief, M., Persson, J., Norman, U., Hartsuiker, E., & Ekwall, K. (2010). Topoisomerase I regulates open chromatin and controls gene expression in vivo. *The EMBO Journal*, *29*(13), 2126–2134.

Dutta, R., & Inouye, M. (2000). GHKL , an emergent ATPase / kinase superfamily. *Trends in Biochemical Sciences*, *25*, 24–28.

Edwards, M. J., Flatman, R. H., Mitchenall, L. A., Stevenson, C. E., Le, T. B., Clarke, T. A., … Maxwell, A. (2009). A Crystal Structure of the Bifunctional Antibiotic Simocyclinone D8, Bound to DNA Gyrase. *Science*, *326*(5958), 1415–1418.

Emsley, P., Lohkamp, B., Scott, W. G., & Cowtan, K. (2010). Features and development of Coot. *Acta Crystallographica. Section D, Biological Crystallography*, *66*(Pt 4), 486–501.

Fass, D., Bogden, C. E., & Berger, J. M. (1999). Quaternary changes in topoisomerase II may direct orthogonal movement of two DNA strands. *Nature Structural Biology*, *6*(4), 322–6.

Felix, C. (1998). Secondary leukemias induced by topoisomerase-targeted drugs. *Biochimica et Biophysica Acta*, *1400*(1–3), 233–55.

Felix, C. (2001). Leukemias related to treatment with DNA topoisomerase II inhibitors. *Medical and Pediatric Oncology*, *36*(5), 525–35.

Forterre, P., & Gadelle, D. (2009). Phylogenomics of DNA topoisomerases : their origin and putative roles in the emergence of modern organisms. *Nucleic Acids Research*, *37*(3), 679–692.

Forterre, P., Gribaldo, S., Gadelle, D., & Serre, M.-C. (2007). Origin and evolution of DNA topoisomerases. *Biochimie*, *89*(4), 427–46.

Fry, A. M., Chresta, C. M., Davies, S. M., Lines, T. C., Walker, M. C., Harris, A. L., … Hickson, I. D. (1991). Relationship between Topoisomerase II Level and Chemosensitivity in Human Tumor Cell Lines. *Cancer Research*, *51*, 6592–6595.

Fuertes, M. a, Alonso, C., & Pérez, J. M. (2003). Biochemical modulation of Cisplatin mechanisms of action: enhancement of antitumor activity and circumvention of drug resistance. *Chemical Reviews*, *103*(3), 645–62.

Gadelle, D., Krupovic, M., Raymann, K., Mayer, C., & Forterre, P. (2014). DNA topoisomerase VIII : a novel subfamily of type IIB topoisomerases encoded by free or integrated plasmids in Archaea and Bacteria. *Nucleic Acids Research*, *42*(13), 8578–8591.

Gasteiger, E., Hoogland, C., Gattiker, A., Duvaud, S., Wilkins, M. R., Appel, R. D., & Bairoch, A. (2005). Protein Identification and Analysis Tools on the ExPASy Server. In *The Proteomics Protocols Handbook* (pp. 571–608).

Gellert, M., Fisher, L. M., & O'Dea, M. H. (1979). DNA gyrase : Purification and catalytic properties of a fragment of gyrase B protein. *Proceedings of the National Academy of Science USA*, *76*(12), 6289–6293.

Gellert, M., Mizuuchi, K., O'Dea, M. H., Itoh, T., & Tomizawa, J. I. (1977). Nalidixic acid resistance: a second genetic character involved in DNA gyrase activity. *Proceedings of the National Academy of Sciences of the United States of America*, *74*(11), 4772–6.

Gellert, M., Mizuuchi, K., O'Dea, M. H., & Nash, H. A. (1976). DNA gyrase : An enzyme that introduces superhelical turns into DNA. *Proceedings of the National Academy of Science USA*, *73*(11), 3872–3876.

Gentry, A. C., Pitts, S. L., Jablonsky, M. J., Bailly, C., Graves, D. E., & Osheroff, N. (2011). Interactions between the etoposide derivative F14512 and human type II topoisomerases: implications for the C4 spermine moiety in promoting enzyme-mediated DNA cleavage. *Biochemistry*, *50*(15), 3240–9.

Goffeau, A., Barrell, B. G., Bussey, H., Davis, R. W., Dujon, B., Feldmann, H., … Oliver, S. G. (1996). Life with 6000 Genes. *Science*, *274*(5287), 546 LP-567.

Goto, T., Laipiss, P., & Wang, J. C. (1984). The Purification and Characterization of DNA Topoisomerases I and II of the Yeast Saccharomyces cerevisiae. *The Journal of Biological Chemistry*, *259*(16), 10422–10429.

Goto, T., & Wang, J. (1982). Yeast DNA Topoisomerase II An ATP-dependent type II topoisomerase that catalyzes the catenation, decatenation, unknotting, and relaxation of double-stranded DNA Rings. *The Journal of Biological Chemistry*, *257*(10), 5866–5872.

Göttler, T., & Klostermeier, D. (2007). Dissection of the nucleotide cycle of B. subtilis DNA gyrase and its modulation by DNA. *Journal of Molecular Biology*, *367*(5), 1392–404.

Graille, M., Cladière, L., Durand, D., Lecointe, F., Gadelle, D., Quevillon-Cheruel, S., … van Tilbeurgh, H. (2008). Crystal structure of an intact type II DNA topoisomerase: insights into DNA transfer mechanisms. *Structure*, *16*(3), 360–70.

Grue, P., Grässer, a, Sehested, M., Jensen, P. B., Uhse, a, Straub, T., … Boege, F. (1998). Essential mitotic functions of DNA topoisomerase IIalpha are not adopted by topoisomerase IIbeta in human H69 cells. *The Journal of Biological Chemistry*, *273*(50), 33660–6.

Gubaev, A., & Klostermeier, D. (2011). DNA-induced narrowing of the gyrase N-gate coordinates T-segment capture and strand passage. *Proceedings of the National Academy of Sciences USA*, *108*(34), 14085–14090.

Haffner, M. C., Aryee, M. J., Toubaji, A., Esopi, D. M., Albadine, R., Gurel, B., … Yegnasubramanian, S. (2010). Androgen-induced TOP2B-mediated double-strand breaks and prostate cancer gene rearrangements. *Nature Genetics*, *42*(8), 668–75.

Hardin, A. H., Sarkar, S. K., Seol, Y., Liou, G. F., Osheroff, N., & Neuman, K. C. (2011). Direct measurement of DNA bending by type IIA topoisomerases: implications for non-equilibrium topology simplification. *Nucleic Acids Research*, *39*(13), 5729–43.

Harkins, T. T., Lewis, T. J., & Lindsley, J. E. (1998). Pre-steady-state analysis of ATP hydrolysis by Saccharomyces cerevisiae DNA topoisomerase II. 2. Kinetic mechanism for the sequential

hydrolysis of two ATP. *Biochemistry*, *37*(20), 7299–312.

Harkins, T. T., & Lindsley, J. E. (1998). Pre-steady-state analysis of ATP hydrolysis by Saccharomyces cerevisiae DNA topoisomerase II. 1. A DNA-dependent burst in ATP hydrolysis. *Biochemistry*, *37*(20), 7292–8.

Harmon, F. G., DiGate, R. J., & Kowalczykowski, S. C. (1999). RecQ Helicase and Topoisomerase III Comprise a Novel DNA Strand Passage Function : A Conserved Mechanism for Control of DNA Recombination. *Molecular Cell*, *3*, 611–620.

Hartung, F., Angelis, K. J., Meister, A., Schubert, I., Melzer, M., & Puchta, H. (2002). An Archaebacterial Topoisomerase Homolog Not Present in Other Eukaryotes Is Indispensable for Cell Proliferation of Plants. *Current Biology*, *12*(2), 1787–1791.

Hawtin, R. E., Stockett, D. E., Byl, J. A. W., McDowell, R. S., Nguyen, T., Arkin, M. R., … Fox, J. a. (2010). Voreloxin is an anticancer quinolone derivative that intercalates DNA and poisons topoisomerase II. *PloS One*, *5*(4), e10186.

Hay, R. T. (2005). SUMO: a history of modification. *Molecular Cell*, *18*(1), 1–12.

Hessling, M., Richter, K., & Buchner, J. (2009). Dissection of the ATP-induced conformational cycle of the molecular chaperone Hsp90. *Nature Structural & Molecular Biology*, *16*(3), 287–293.

Heyduk, T., & Lee, J. C. (1990). Application of fluorescence energy transfer and polarization to monitor Escherichia coli cAMP receptor protein and lac promoter interaction. *Proceedings of the National Academy of Sciences of the United States of America*, *87*(5), 1744–1748.

Hiasa, H., Yousef, D. O., & Marians, K. J. (1996). DNA Strand Cleavage Is Required for Replication Fork Arrest by a Frozen Topoisomerase-Quinolone-DNA Ternary Complex. *The Journal of Biological Chemistry*, *271*(42), 26424–26429.

Higgins, N. P., Peebles, C. L., Sugino, A., & Cozzarelli, N. R. (1978). Purification of subunits of Escherichia coli DNA gyrase and reconstitution of enzymatic activity. *Proceedings of the National Academy of Sciences of the United States of America*, *75*(4), 1773–1777.

Hildenbrand, C., Stock, T., Lange, C., Rother, M., & Soppa, J. (2011). Genome Copy Numbers and Gene Conversion in Methanogenic Archaea . *Journal of Bacteriology*, *193*(3), 734–743.

Holm, C., Goto, T., James, C., & Botstein, D. (1985). DNA Topoisomerase II Is Required at the Time of Mitosis in Yeast. *Cell*, *41*(June), 553–563.

Hsieh, T., Farh, L., Huang, W. M., & Chan, N. (2004). Structure of the Topoisomerase IV C-terminal Domain. *The Journal of Biological Chemistry*, *279*(53), 55587–55593.

Hsieh, T., & Plank, J. L. (2006). Reverse Gyrase Functions as a DNA Renaturase ANNEALING OF COMPLEMENTARY SINGLE-STRANDED CIRCLES AND POSITIVE SUPERCOILING OF A BUBBLE

SUBSTRATE. *The Journal of Biological Chemistry*, *281*(9), 5640–5647.

Huang, N., & Lin, J. (2014). Drug-Induced Conformational Population Shifts in Topoisomerase-DNA Ternary Complexes. *Molecules*, *19*, 7415–7428.

Huang, N., & Lin, J. (2015). Recovery of the poisoned topoisomerase II for DNA religation : coordinated motion of the cleavage core revealed with the microsecond atomistic simulation. *Nucleic Acids Research*, *43*(14), 6772–6786.

Inglese, J., Blatchly, R. A., & Benkovic, S. J. (1989). A Multisubstrate Adduct Inhibitor of a Purine Biosynthetic Enzyme with a Picomolar Dissociation Constant. *Journal of Medicinal Chemistry*, *32*(5), 937–940.

Iyer, L. M., Abhiman, S., & Aravind, L. (2008). MutL homologs in restriction-modification systems and the origin of eukaryotic MORC ATPases. *Biology Direct*, *9*, 1–9.

Jensen, S., Andersen, A. H., Kjeldsen, E., Biersack, H., Olsen, E. H. N., Andersen, T. B., … Jakobsen, B. K. (1996). Analysis of Functional Domain Organization in DNA Topoisomerase II from Humans and Saccharomyces cerevisiae. *Molecular and Cellular Biology*, *16*(7), 3866–3877.

Ju, B.-G., Lunyak, V. V, Perissi, V., Garcia-Bassets, I., Rose, D. W., Glass, C. K., & Rosenfeld, M. G. (2006). A topoisomerase IIbeta-mediated dsDNA break required for regulated transcription. *Science*, *312*(5781), 1798–802.

Kadyrov, F. A., Dzantiev, L., Constantin, N., & Modrich, P. (2006). Endonucleolytic Function of MutL a in Human Mismatch Repair. *Cell*, *126*, 297–308.

Kasahara, K., Fujiwara, Y., Sugimoto, Y., Nishio, K., Tamura, T., Matsuda, T., & Saijo, N. (1992). Determinants of response to the DNA topoisomerase II inhibitors doxorubicin and etoposide in human lung cancer cell lines. *Journal of the National Cancer Institute*, *84*(2), 113–8.

Kato, J., Nishimura, Y., Imamura, R., Niki, H., Hiraga, S., & Suzuki, H. (1990). New topoisomerase essential for chromosome segregation in E. coli. *Cell*, *63*(2), 393–404.

Kato, J., Suzuki, H., & Ikeda, H. (1992). Purification and characterization of DNA topoisomerase IV in Escherichia coli. *The Journal of Biological Chemistry*, *267*(36), 25676–84.

Keeney, S., Giroux, C. N., & Kleckner, N. (1997). Meiosis-Specific DNA Double-Strand Breaks Are Catalyzed by Spo11 , a Member of a Widely Conserved Protein Family. *Cell*, *88*(88), 375–384.

Khodursky, A. B., Peter, B. J., Schmid, M. B., Derisi, J., Botstein, D., Brown, P. O., & Cozzarelli, N. R. (2000). Analysis of topoisomerase function in bacterial replication fork movement : Use of DNA microarrays. *PNAS*, *97*(17), 9419–9424.

Kikuchi, A., & Asai, K. (1984). Reverse gyrase-a topoisomerase which introduces positive superhelical turns into DNa. *Nature*, *309*(5970), 677–81.

Kim, A., & Wang, J. C. (1989). Function of DNA Topoisomerases as Replication Swivels in Saccharomyces cerevisiae. *Journal of Molecular Biology*, *208*(2), 257–267.

King, I. F., Yandava, C. N., Mabb, A. M., Hsiao, J. S., Huang, H., Pearson, B. L., … Zylka, M. J. (2013). Topoisomerases facilitate transcription of long genes linked to autism. *Nature*, *501*(7465), 58–62.

Kirik, V., Schrader, A., Uhrig, J. F., & Hulskamp, M. (2007). MIDGET Unravels Functions of the Arabidopsis Topoisomerase VI Complex in DNA Endoreduplication , Chromatin Condensation , and Transcriptional Silencing. *The Plant Cell*, *19*(10), 3100–3110.

Kirkegaard, K., & Wang, J. C. (1985). Bacterial DNA Topoisomerase I Can Relax Positively Supercoiled DNA Containing a Single-stranded Loop. *Journal of Molecular Biology*, *185*, 625–637.

Klevan, L., & Wang, J. C. (1980). Deoxyribonucleic Acid Gyrase-Deoxyribonucleic Acid Complex Containing 140 Base Pairs of Deoxyribonucleic Acid and an α2β2 Protein Core. *Biochemistry*, *19*(23), 5229–5234.

Koster, D. A., Croquette, V., Dekker, C., Shuman, S., & Dekker, N. H. (2005). Friction and torque govern the relaxation of DNA supercoils by eukaryotic topoisomerase IB. *Nature*, *434*(7033), 1–4.

Kunkel, T. A., & Erie, D. A. (2005). DNA Mismatch Repair. *Annual Review of Biochemistry*, *74*, 681–710.

Lam, I., & Keeney, S. (2014). Mechanism and Regulation of Meiotic Recombination Initiation. *Cold Spring Harbor Perspectives in Biology*, *7*(1), 1–24.

Lamour, V., Hoermann, L., Jeltsch, J.-M., Oudet, P., & Moras, D. (2002). An Open Conformation of the Thermus thermophilus Gyrase B ATP-binding Domain. *The Journal of Biological Chemistry*, *277*(21), 18947–18953.

Laponogov, I., Pan, X.-S., Veselkov, D. a, McAuley, K. E., Fisher, L. M., & Sanderson, M. R. (2010). Structural basis of gate-DNA breakage and resealing by type II topoisomerases. *PloS One*, *5*(6), e11338.

Laponogov, I., Sohi, M. K., Veselkov, D. A., Pan, X.-S., Sawhney, R., Thompson, A. W., … Sanderson, M. R. (2009). Structural insight into the quinolone-DNA cleavage complex of type IIA topoisomerases. *Nature Structural & Molecular Biology*, *16*(6), 667–9.

Laponogov, I., Veselkov, D. A., Crevel, I. M., Pan, X., Fisher, L. M., & Sanderson, M. R. (2013). Structure of an " open " clamp type II topoisomerase-DNA complex provides a mechanism for DNA capture and transport. *Nucleic Acids Research*, *41*(21), 9911–9923.

Laponogov, I., Veselkov, D. a, Sohi, M. K., Pan, X.-S., Achari, A., Yang, C., … Sanderson, M. R. (2007). Breakage-reunion domain of Streptococcus pneumoniae topoisomerase IV: crystal structure of a gram-positive quinolone target. *PloS One*, *2*(3), e301.

Larkin, M. A., Blackshields, G., Brown, N. P., Chenna, R., McGettigan, P. A., McWilliam, H., … Higgins, D. G. (2007). Clustal W and Clustal X version 2.0. *Bioinformatics*, *23*(21), 2947–8.

Lebel, P., Basu, A., Oberstrass, F. C., Tretter, E. M., & Bryant, Z. (2014). Gold rotor bead tracking for high-speed measurements of DNA twist , torque and extension. *Nature Methods*, *11*(4), 456–462.

Lee, I., Dong, K. C., & Berger, J. M. (2013). The role of DNA bending in type IIA topoisomerase function. *Nucleic Acids Research*, *41*(10), 5444–5456.

Lee, M.-T., & Bachant, J. (2009). SUMO modification of DNA topoisomerase II: trying to get a CENse of it all. *DNA Repair*, *8*(4), 557–68.

Lee, S., Jung, S., Heo, K., Ann, J., Byl, W., Deweese, J. E., & Osheroff, N. (2012). DNA cleavage and opening reactions of human topoisomerase IIα are regulated via Mg2+ - mediated dynamic bending of gate-DNA. *Proceedings of the National Academy of Science USA*, *109*(8), 2925–30.

Leontiou, C., Lakey, J. H., & Austin, C. A. (2004). Mutation E522K in Human DNA Topoisomerase IIbeta Confers Resistance to Methyl N-(4'-(9-acridinylamino)-phenyl)carbamate hydrochloride and Methyl N-(4'-(9-acridinylamino)-3-methoxy-phenyl) methane sulfonamide but Hypersensitivity to Etoposide. *Molecular Pharmacology*, *66*(3), 430–439.

Li, S., Yen, L., Pastor, W. A., Johnston, J. B., Du, J., Shew, C. J., … Ho, J. (2016). Mouse MORC3 is a GHKL ATPase that localizes to H3K4me3 marked chromatin. *Proceedings of the National Academy of Sciences*, *113*(35), E5108–E5116.

Lin, R., Ho, C., Liu, L. F., & Lyu, Y. L. (2013). Topoisomerase IIbeta Deficiency Enhances Camptothecin-induced Apoptosis. *The Journal of Biological Chemistry*, *288*(10), 7182–7192.

Lindsley, J. E., & Wang, J. C. (1993). On the coupling between ATP usage and DNA transport by yeast DNA topoisomerase II. *The Journal of Biological Chemistry*, *268*(11), 8096–104.

Liu, L. F., Liu, C.-C., & Alberts, B. M. (1979). T4 DNA topoisomerase: a new ATP-dependent enzyme essential for initiation of T4 bacteriophage DNA replication. *Nature*, *281*, 456–461.

Liu, L. F., Liu, C., & Alberts, B. M. (1980). Type II DNA Topoisomerases : Enzymes That Can Unknot a Topologically Knotted DNA Molecule via a Reversible Double-Strand Break. *Cell*, *19*(March), 697–707.

Liu, L. F., & Wang, J. C. (1987). Supercoiling of the DNA template during transcription. *Proceedings of the National Academy of Sciences USA*, *84*(20), 7024–7027.

Lyu, Y. L., Kerrigan, J. E., Lin, C.-P., Azarova, A. M., Tsai, Y.-C., Ban, Y., & Liu, L. F. (2007). Topoisomerase IIbeta mediated DNA double-strand breaks: implications in doxorubicin cardiotoxicity and prevention by dexrazoxane. *Cancer Research*, *67*(18), 8839–46.

Lyu, Y. L., & Wang, J. C. (2003). Aberrant lamination in the cerebral cortex of mouse embryos lacking DNA topoisomerase IIbeta. *Proceedings of the National Academy of Sciences of the United States of America*, *100*(12), 7123–8.

MacDowell, A. a, Celestre, R. S., Howells, M., McKinney, W., Krupnick, J., Cambie, D., … Padmore, H. a. (2004). Suite of three protein crystallography beamlines with single superconducting bend magnet as the source. *Journal of Synchrotron Radiation*, *11*(Pt 6), 447–55.

Madabhushi, R., Gao, F., Pfenning, A. R., Cho, S., Madabhushi, R., Gao, F., … Rueda, R. (2015). Activity-Induced DNA Breaks Govern the Expression of Neuronal Early-Response Genes Article Activity-Induced DNA Breaks Govern the Expression of Neuronal Early-Response Genes. *Cell*, *161*(7), 1592–1605.

Mah, R. A. (1980). Isolation and Characterization of Methanococcus mazei. *Current Microbiology*, *3*, 3–8.

Martinez-Carcia, B., Fernandez, B., Diaz-Ingelmo, O., Rodriguez-Campos, A., Manichanh, C., & Roca, J. (2014). Topoisomerase II minimizes DNA entanglements by proofreading DNA topology after DNA strand passage. *Nucleic Acids Research*, *42*(3), 1821–1830.

McClendon, A. K., Gentry, A. C., Dickey, J. S., Brinch, M., Bendsen, S., Andersen, A. H., & Osheroff, N. (2008). Bimodal recognition of DNA geometry by human topoisomerase II alpha: preferential relaxation of positively supercoiled DNA requires elements in the C-terminal domain. *Biochemistry*, *47*(50), 13169–78.

McClendon, A. K., Rodriguez, A. C., & Osheroff, N. (2005). Human Topoisomerase II-alpha Rapidly Relaxes Positively Supercoiled DNA IMPLICATIONS FOR ENZYME ACTION AHEAD OF REPLICATION FORKS. *The Journal of Biological Chemistry*, *280*(47), 39337–39345.

McCoy, A. J., Grosse-Kunstleve, R. W., Adams, P. D., Winn, M. D., Storoni, L. C., & Read, R. J. (2007). Phaser crystallographic software. *Journal of Applied Crystallography*, *40*(Pt 4), 658–674.

McNamara, S., Wang, H., Hanna, N., & Miller, W. H. (2008). Topoisomerase IIbeta negatively modulates retinoic acid receptor alpha function: a novel mechanism of retinoic acid resistance. *Molecular and Cellular Biology*, *28*(6), 2066–77.

Miller, K. G., Liu, F., & Englund, P. T. (1981). A Homogeneous Type II DNA Topoisomerase from HeLa Cell Nuclei. *The Journal of Biological Chemistry*, *256*(17), 9334–9339.

Mizuuchi, K., Fisher, L. M., O'Dea, M. H., & Gellert, M. (1980). DNA gyrase action involves the

introduction of transient double-strand breaks into DNA. *Proceedings of the National Academy of Science USA*, *77*(4), 1847–1851.

Mizuuchi, K., O'Dea, M. H., & Gellert, M. (1978). DNA gyrase : Subunit structure and ATPase activity of the purified enzyme. *Proceedings of the National Academy of Sciences of the United States of America*, *75*(12), 5960–5963.

Mondal, N., Zhang, Y., Jonsson, Z., Dhar, S. K., Kannapiran, M., & Parvin, J. D. (2003). Elongation by RNA polymerase II on chromatin templates requires topoisomerase activity. *Nucleic Acids Research*, *31*(17), 5016–5024.

Morais Cabral, J. H., Jackson, a P., Smith, C. V, Shikotra, N., Maxwell, a, & Liddington, R. C. (1997). Crystal structure of the breakage-reunion domain of DNA gyrase. *Nature*, *388*(6645), 903–6.

Morrical, S. W., Lee, J., & Cox, M. M. (1986). Continuous Association of Escherichia coli Single-Stranded DNA Binding Protein with Stable Complexes of recA Protein and Single-Stranded DNA. *Biochemistry*, *25*, 1482–1494.

Morrison, A., & Cozzarelli, N. R. (1979). Site-Specific Gyrase Cleavage of DNA by E . coli DNA. *Cell*, *17*(May), 175–184.

Murzin, A. G. (1995). A ribosomal protein module in EF-G and DNA gyrase. *Nature Structural Biology*, *2*(1), 25–6.

Neuman, K. C., Charvin, G., Bensimon, D., & Croquette, V. (2009). Mechanisms of chiral discrimination by topoisomerase IV. *PNAS*, *106*(17), 6986–6991.

Nichols, M. D., DeAngelis, K., Keck, J. L., & Berger, J. M. (1999). Structure and function of an archaeal topoisomerase VI subunit with homology to the meiotic recombination factor Spo11. *The EMBO Journal*, *18*(21), 6177–88.

Niimi, A., Suka, N., Harata, M., Kikuchi, A., & Mizuno, S. (2001). Co-localization of chicken DNA topoisomerase IIα, but not β, with sites of DNA replication and possible involvement of a C-terminal region of α through its binding to PCNA. *Chromosoma*, *110*(2), 102–114.

Noble, C. G., & Maxwell, A. (2002). The role of GyrB in the DNA cleavage-religation reaction of DNA gyrase: a proposed two metal-ion mechanism. *Journal of Molecular Biology*, *318*(2), 361–71.

Noeske, J., Wasserman, M. R., Terry, D. S., Altman, R. B., Blanchard, S. C., & Cate, J. H. D. (2015). High-resolution structure of the Escherichia coli ribosome. *Nature Structural & Molecular Biology*, *22*(4), 336–341.

Nurse, P., Levine, C., Hassing, H., & Marians, K. J. (2003). Topoisomerase III Can Serve as the Cellular Decatenase in Escherichia coli. *The Journal of Biological Chemistry*, *278*(10), 8653–8660.

Olland, S., & Wang, J. C. (1999). Catalysis of ATP Hydrolysis by Two NH 2 -terminal Fragments of Yeast DNA Topoisomerase II. *The Journal of Biological Chemistry*, *274*(31), 21688–21694.

Ortiz-Lombardía, M., González, A., Aymamí, J., Azorín, F., & Coll, M. (1999). letters Crystal structure of a DNA Holliday junction. *Nature Structural Biology*, *6*(10), 913–917.

Osheroff, N., Shelton, E. R., & Brutlag, D. L. (1983). DNA Topoisomerase II from Drosophila melanogaster. Relaxation of supercoiled DNA. *The Journal of Biological Chemistry*, *258*(15), 9536–9543.

Otwinowski, Z., & Minor, W. (1997). Processing of X-Ray Diffraction Data Collected in Oscillation Mode. *Methods in Enzymology*, *276*(January 1993), 306–315.

Padget, K., Pearson, A., & Austin, C. (2005). Quantitation of DNA topoisomearse IIalpha and beta in human leukaemia cells by immunoblot. *Leukemia*, (July 2000), 1997–2005.

Painter, J., & Merritt, E. a. (2006a). Optimal description of a protein structure in terms of multiple groups undergoing TLS motion. *Acta Crystallographica. Section D, Biological Crystallography*, *62*(Pt 4), 439–50.

Painter, J., & Merritt, E. a. (2006b). TLSMD web server for the generation of multi-group TLS models. *Journal of Applied Crystallography*, *39*(1), 109–111.

Panaretou, B., Prodromou, C., Roe, S. M., Brien, R. O., Ladbury, J. E., Piper, P. W., & Pearl, L. H. (1998). ATP binding and hydrolysis are essential to the function of the Hsp90 molecular chaperone in vivo. *The EMBO Journal*, *17*(16), 4829–4836.

Papillon, J., Menetret, J.-F., Batisse, C., Helye, R., Schultz, P., Potier, N., & Lamour, V. (2013). Structural insight into negative DNA supercoiling by DNA gyrase , a bacterial type 2A DNA topoisomerase. *Nucleic Acids Research*, *41*(16), 7815–7827.

Pedersen-Bjergaard, J. (2002). Genetic pathways in therapy-related myelodysplasia and acute myeloid leukemia. *Blood*, *99*(6), 1909–1912.

Perillo, B., Ombra, M. N., Bertoni, A., Cuozzo, C., Sacchetti, S., Sasso, A., … Avvedimento, E. V. (2008). DNA oxidation as triggered by H3K9me2 demethylation drives estrogen-induced gene expression. *Science*, *319*(5860), 202–6.

Peter, B. J., Ullsperger, C., Hiasa, H., Marians, K. J., & Cozzarelli, N. R. (1998). The Structure of Supercoiled Intermediates in DNA Replication. *Cell*, *94*(6), 819–827.

Pillon, M. C., Lorenowicz, J. J., Uckelmann, M., Klocko, A. D., Mitchell, R. R., Chung, Y. S., … Guarne, A. (2010). Structure of the Endonuclease Domain of MutL : Unlicensed to Cut. *Molecular Cell*, *39*, 145–151.

Plank, J. L., Wu, J., & Hsieh, T. (2006). Topoisomerase IIIalpha and Bloom ' s helicase can resolve a mobile double Holliday junction substrate through convergent branch migration. *PNAS*,

103(30), 11118–11123.

Pommier, Y., Leo, E., Zhang, H., & Marchand, C. (2010). DNA topoisomerases and their poisoning by anticancer and antibacterial drugs. *Chemistry & Biology*, *17*(5), 421–33.

Prodromou, C., Panaretou, B., Chohan, S., Siligardi, G., Brien, R. O., Ladbury, J. E., … Pearl, L. H. (2000). The ATPase cycle of Hsp90 drives a molecular "clamp" via transient dimerization of the N-terminal domains. *The EMBO Journal*, *19*(16), 4383–4392.

Reece, R. J., & Maxwell, A. (1991). The C-terminal domain of the Escherichia coli DNA A subunit is a DNA-binding protein. *Nucleic Acids Research*, *19*(7), 1399–1405.

Robert, T., Nore, A., Brun, C., Maffre, C., Crimi, B., Guichard, V., … de Massy, B. (2016). The TopoVIB-Like protein family is required for meiotic DNA double-strand break formation. *Science*, *351*(6276), 943–949.

Roca, J. (2004). The path of the DNA along the dimer interface of topoisomerase II. *The Journal of Biological Chemistry*, *279*(24), 25783–8.

Roca, J., Berger, J. M., Harrison, S. C., & Wang, J. C. (1996). DNA transport by a type II two-gate mechanism topoisomerase : Direct evidence for a two-gate mechanism. *Proceedings of the National Academy of Sciences*, *93*(April), 4057–4062.

Roca, J., Ishidat, R., Berger, J. M., Andoht, T., & Wang, J. C. (1994). Antitumor bisdioxopiperazines inhibit yeast DNA topoisomerase II. *Proceedings of the National Academy of Sciences USA*, *91*(5), 1781–1785.

Roca, J., & Wang, J. C. (1992). The Capture of a DNA Double Helix by an ATP-Dependent Protein Clamp: A Key Step in DNA Transport by Type II DNA Topoisomerases. *Cell*, *71*, 833–840.

Roca, J., & Wang, J. C. (1994). DNA transport by a type II DNA topoisomerase: evidence in favor of a two-gate mechanism. *Cell*, *77*(4), 609–16.

Rodriguez, M. S., Dargemont, C., & Hay, R. T. (2001). SUMO-1 conjugation in vivo requires both a consensus modification motif and nuclear targeting. *The Journal of Biological Chemistry*, *276*(16), 12654–9.

Ryu, H., Furuta, M., Kirkpatrick, D., Gygi, S. P., & Azuma, Y. (2010). PIASy-dependent SUMOylation regulates DNA topoisomerase IIalpha activity. *The Journal of Cell Biology*, *191*(4), 783–94.

Sander, M., & Hsieh, T. (1983). Double Strand DNA Cleavage by Type I1 DNA Topoisomerase from Drosophila melanogaster ". *The Journal of Biological Chemistry*, *258*(13), 8421–8426.

Schaechter, M., Williamson, J. P., Hood, J. R., & Koch, A. L. (1961). Growth , Cell and Nuclear Divisions in some Bacteria. *Journal of General Microbiology*, *29*, 421–434.

Schmidt, B. H., Burgin, A. B., Deweese, J. E., Osheroff, N., & Berger, J. M. (2010). A novel and unified two-metal mechanism for DNA cleavage by type II and IA topoisomerases. *Nature*, *465*(7298), 641–644.

Schmidt, B. H., Osheroff, N., & Berger, J. M. (2012). Structure of a topoisomerase II – DNA – nucleotide complex reveals a new control mechanism for ATPase activity. *Nature Structural & Molecular Biology*, *19*(11), 1147–1154.

Schoeffler, A. J., & Berger, J. M. (2008). DNA topoisomerases : harnessing and constraining energy to govern chromosome topology. *Quarterly Reviews of Biophysics*, *1*, 41–101.

Schoeffler, A. J., May, A. P., & Berger, J. M. (2010). A domain insertion in Escherichia coli GyrB adopts a novel fold that plays a critical role in gyrase function. *Nucleic Acids Research*, *38*(21), 7830–44.

Seol, Y., Gentry, A. C., Osheroff, N., & Neuman, K. C. (2013). Chiral Discrimination and Writhe-dependent Relaxation Mechanism of Human Topoisomerase II-alpha. *The Journal of Biological Chemistry*, *288*(19), 13695–13703.

Sherman, F. (2002). Getting Started with Yeast. *Methods in Enzymology*, *350*(4), 3–41.

Shiau, A. K., Harris, S. F., Southworth, D. R., & Agard, D. A. (2006). Structural Analysis of E . coli hsp90 Reveals Dramatic Nucleotide-Dependent Conformational Rearrangements. *Cell*, *127*, 329–340.

Slesarev, A., Stetter, K. O., Lake, J. A., Gellert, M., Krah, R., & Kozyavkin, S. A. (1993). DNA topoisomerase V is a relative of eukaryotic topoisomerase I from a hyperthermophilic prokaryote. *Nature*, *364*(6439), 735–7.

Spell, R. M., & Holm, C. (1994). Nature and Distribution of Chromosomal Intertwinings in Saccharomyces cerevisiae. *Molecular and Cellular Biology*, *14*(2), 1465–1476.

Stein, N. (2008). CHAINSAW : a program for mutating pdb files used as templates in molecular replacement. *Journal of Applied Crystallography*, *41*(3), 641–643.

Street, T. O., Lavery, L. A., & Agard, D. A. (2011). Substrate Binding Drives Large-Scale Conformational Changes in the Hsp90 Molecular Chaperone. *Molecular Cell*, *42*(1), 96–105.

Studier, F. W. (2005). Protein production by auto-induction in high density shaking cultures. *Protein Expression and Purification*, *41*(1), 207–34.

Sugahara, M., Mikawa, T., Kumasaka, T., Yamamoto, M., Kato, R., Fukuyama, K., … Kuramitsu, S. (2000). Crystal structure of a repair enzyme of oxidatively damaged DNA , MutM (Fpg), from an extreme thermophile , Thermus thermophilus HB8. *The EMBO Journal*, *19*(15), 3857–3869.

Sugimoto-shirasu, K., Roberts, G. R., Stacey, N. J., Mccann, M. C., Maxwell, A., & Roberts, K. (2005). RHL1 is an essential component of the plant DNA topoisomerase VI complex and is required for ploidy-dependent cell growth. *PNAS*, *102*(51), 18736–18741.

Sugimoto-shirasu, K., Stacey, N. J., Corsar, J., Roberts, K., & Mccann, M. C. (2002). DNA Topoisomerase VI is Essential for Endoreduplication in Arabidopsis. *Current Biology*, *12*(2), 1782–1786.

Sugino, A., & Cozzarelli, N. R. (1980). The Intrinsic ATPase of DNA Gyrase. *The Journal of Biological Chemistry*, *255*(13), 6299–6306.

Sugino, A., Peebles, C. L., Kreuzer, K. N., & Cozzarelli, N. R. (1977). Mechanism of action of nalidixic acid: purification of Escherichia coli nalA gene product and its relationship to DNA gyrase and a novel nicking-closing enzyme. *Proceedings of the National Academy of Sciences of the United States of America*, *74*(11), 4767–71.

Suski, C., & Marians, K. J. (2008). Article Resolution of Converging Replication Forks by RecQ and Topoisomerase III. *Molecular Cell*, *30*(6), 779–789.

Swiercz, J. P., Nanji, T., Gloyd, M., Guarne, A., & Elliot, M. A. (2013). A novel nucleoid-associated protein specific to the actinobacteria. *Nucleic Acids Research*, *41*(7), 4171–4184.

Tamura, J. K., & Gellert, M. (1990). Characterization of the ATP Binding Site on Escherichia coli DNA Gyrase. *The Journal of Biological Chemistry*, *265*(34), 21342–21349.

Taneja, B., Schnurr, B., Slesarev, A., Marko, J. F., & Mondragon, A. (2007). Topoisomerase V relaxes supercoiled DNA by a constrained swiveling mechanism. *PNAS*, *104*(37), 14670–14675.

The PyMOL Molecular Graphics System, Version 1.5.x, Schödinger, LLC.

Thomsen, N. D., & Berger, J. M. (2008). Micro Review Structural frameworks for considering microbial protein- and nucleic acid-dependent motor ATPases. *Molecular Microbiology*, *69*(5), 1071–1090.

Thomson, N. H., Santos, S., Mitchenall, L. A., Stuchinskaya, T., Taylor, J. A., & Maxwell, A. (2014). DNA G-segment bending is not the sole determinant of topology simplification by type II DNA topoisomerases. *Scientific Reports*, *4:6158*.

Tingey, A. P., & Maxwell, A. (1996). Probing the role of the ATP-operated clamp in the strand-passage reaction of DNA gyrase. *Nucleic Acids Research*, *24*(24), 4868–73.

Toyoda, E., Kagaya, S., Cowell, I. G., Kurosawa, A., Kamoshita, K., Nishikawa, K., … Adachi, N. (2008). NK314, a topoisomerase II inhibitor that specifically targets the alpha isoform. *The Journal of Biological Chemistry*, *283*(35), 23711–20.

Tretter, E. M., & Berger, J. M. (2012). Mechanisms for Defining Supercoiling Set Point of DNA

Gyrase Orthologs. *The Journal of Biological Chemistry*, *287*(22), 18636–18644.

Tretter, E. M., Schoeffler, A. J., Weisfield, S. R., & Berger, J. M. (2010). Crystal structure of the DNA gyrase GyrA N-terminal domain from Mycobacterium tuberculosis. *Proteins*, *78*(2), 492–5.

Tropea, J. E., Cherry, S., & Waugh, D. S. (2009). Expression and Purification of Soluble His6 - Tagged TEV Protease. In S. A. Doyle (Ed.), *Methods in Molecular Biology:High Throughput Protein Expression and Purification* (Vol. 498, pp. 297–307). Totowa, NJ: Humana Press.

Tsai-Pflugfelder, M., Liu, L. F., Liu, a a, Tewey, K. M., Whang-Peng, J., Knutsen, T., … Wang, J. C. (1988). Cloning and sequencing of cDNA encoding human DNA topoisomerase II and localization of the gene to chromosome region 17q21-22. *Proceedings of the National Academy of Sciences of the United States of America*, *85*(19), 7177–81.

Tse, Y., Kirkegaard, K., & Wang, J. C. (1980). Covalent Bonds between Protein and DNA-Formation of phosphotyrosine linkage between certain DNA topoisomerases and DNA. *The Journal of Biological Chemistry*, *255*(12), 5560–5565.

Tsutsui, K., Okada, S., Watanabe, M., Shohmori, T., Seki, S., & Inoue, Y. (1993). Molecular cloning of partial cDNAs for rat DNA topoisomerase II isoforms and their differential expression in brain development. *The Journal of Biological Chemistry*, *268*(25), 19076–83.

Tsutsui, K., Sano, K., Kikuchi, a, & Tokunaga, a. (2001). Involvement of DNA topoisomerase IIbeta in neuronal differentiation. *The Journal of Biological Chemistry*, *276*(8), 5769–78.

Vaughn, J., Huang, S., Wessel, I., Sorensen, T. K., Hsieh, T., Jensen, L. H., … Nitiss, J. L. (2005). Stability of the Topoisomerase II Closed Clamp Conformation May Influence DNA-stimulated ATP Hydrolysis. *The Journal of Biological Chemistry*, *280*(12), 11920–11929.

Vos, S. M., Lee, I., & Berger, J. M. (2013). Distinct Regions of the Escherichia coli ParC C-Terminal Domain Are Required for Substrate Discrimination by Topoisomerase IV. *Journal of Molecular Biology*, *425*(17), 3029–3045.

Vos, S. M., Tretter, E. M., Schmidt, B. H., & Berger, J. M. (2011). All tangled up : how cells direct , manage and exploit topoisomerase function. *Nature Reviews. Molecular Cell Biology*, *12*(12), 827–841.

Vrielynck, N., Chambon, A., Vezon, D., Pereira, L., Chelysheva, L., De Muyt, A., … Grelon, M. (2016). A DNA topoisomerase VI-like complex initiates meiotic recombination. *Science*, *351*(6276), 939–944.

Wallis, J. W., Chrebet, G., Brodsky, G., Rolfe, M., & Rothstein, R. (1989). A Hyper-Recombination Mutation in S . cerevisiae Identifies a Novel Eukaryotic Topoisomerase. *Cell*, *58*, 409–419.

Wang, J. C. (1971). Interaction between DNA and an Escherichia coli protein [omega]. *Journal of Molecular Biology*, *55*(3), 523–533.

Wang, J. C. (2002). Cellular roles of DNA topoisomerases: a molecular perspective. *Nature Reviews Molecular Cell Biology*, *3*(6), 430–440.

Wang, Z. (1995). An exact mathematical expression for describing competitive binding of two different ligands to a protein molecule. *FEBS Letters*, *360*, 111–114.

Wasserman, R. a, & Wang, J. C. (1994). Mechanistic studies of amsacrine-resistant derivatives of DNA topoisomerase II. Implications in resistance to multiple antitumor drugs targeting the enzyme. *The Journal of Biological Chemistry*, *269*(33), 20943–51.

Wei, H., Ruthenburg, A. J., Bechis, S. K., & Verdine, G. L. (2005). Nucleotide-dependent Domain Movement in the ATPase Domain of a Human Type IIA DNA Topoisomerase. *The Journal of Biological Chemistry*, *280*(44), 37041–37047.

Wendorff, T. J., Schmidt, B. H., Heslop, P., Austin, C. A., & Berger, J. M. (2012). The Structure of DNA-Bound Human Topoisomerase II Alpha : Conformational Mechanisms for Coordinating Inter-Subunit Interactions with DNA Cleavage. *Journal of Molecular Biology*, *424*(3–4), 109–124.

Wentzell, L. M., & Maxwell, A. (2000). The Complex of DNA Gyrase and Quinolone Drugs on DNA Forms a Barrier to the T7 DNA Polymerase Replication Complex. *Journal of Molecular Biology*, *304*, 779–791.

West, K. L., Meczes, E. L., Thorn, R., Turnbull, R. M., Marshall, R., & Austin, C. a. (2000). Mutagenesis of E477 or K505 in the B' domain of human topoisomerase II beta increases the requirement for magnesium ions during strand passage. *Biochemistry*, *39*(6), 1223–33.

White, J. H. (1969). Self-Linking and the Gauss Integral in Higher Dimensions. *American Journal of Mathematics*, *91*(3), 693–728.

Wigley, D. B., Davies, G. J., Dodson, E. J., Maxwell, A., & Dodson, G. (1991). Crystal structure of an N-terminal fragment of the DNA gyrase B protein. *Nature*, *351*(20), 624–628.

Williams, N. L., & Maxwell, A. (1999). Locking the DNA Gate of DNA Gyrase : Investigating the Effects on DNA Cleavage and ATP Hydrolysis. *Biochemistry*, *38*(43), 14157–14164.

Williams, N. L., & Maxwell, a. (1999). Probing the two-gate mechanism of DNA gyrase using cysteine cross-linking. *Biochemistry*, *38*(41), 13502–11.

Willmore, E., Frank, A. J., Padget, K., Tilby, M. J., & Austin, C. A. (1998). Etoposide targets topoisomerase IIalpha and IIbeta in leukemic cells: isoform-specific cleavable complexes visualized and quantified in situ by a novel immunofluorescence technique. *Molecular Pharmacology*, *54*(1), 78–85.

Willmott, C. J. R., Critchlow, S. E., Eperon, I. C., & Maxwell, A. (1994). The Complex of DNA Gyrase and Quinolone Drugs with DNA Forms a Barrier to Transcription by RNA Polymerase. *Journal of Molecular Biology*, *242*, 351–363.

Wilstermann, A. M., Bender, R. P., Godfrey, M., Choi, S., Anklin, C., Berkowitz, D. B., … Graves, D. E. (2007). Topoisomerase II-Drug Interaction Domains : Identification of Substituents on Etoposide That Interact with the Enzyme †. *Biochemistry*, (29), 8217–8225.

Winn, M. D., Ballard, C. C., Cowtan, K. D., Dodson, E. J., Emsley, P., Evans, P. R., … Wilson, K. S. (2011). Overview of the CCP4 suite and current developments. *Acta Crystallographica. Section D, Biological Crystallography*, *67*(Pt 4), 235–42.

Wohlkonig, A., Chan, P. F., Fosberry, A. P., Homes, P., Huang, J., Kranz, M., … Bax, B. D. (2010). Structural basis of quinolone inhibition of type IIA topoisomerases and target-mediated resistance. *Nature Structural & Molecular Biology*, *17*(9), 1152–3.

Wolmarans, A., Lee, B., Spyracopoulos, L., & Lapointe, P. (2016). The Mechanism of Hsp90 ATPase Stimulation by Aha1. *Scientific Reports*, (April), 1–15.

Wu, C.-C., Li, T.-K., Farh, L., Lin, L.-Y., Lin, T.-S., Yu, Y.-J., … Chan, N.-L. (2011). Structural basis of type II topoisomerase inhibition by the anticancer drug etoposide. *Science*, *333*(6041), 459–62.

Wu, C., Li, Y., Wang, Y., Li, T., & Chan, N.-L. (2013). On the structural basis and design guidelines for type II topoisomerase-targeting anticancer drugs. *Nucleic Acids Research*, *41*(22), 10630–10640.

Yang, W. (2008). An equivalent metal ion in one- and two-metal-ion catalysis. *Nature Structural & Molecular Biology*, *15*(11), 1228–31.

Yin, Y., Cheong, H., Friedrichsen, D., Zhao, Y., Hu, J., Mora-Garcia, S., & Chory, J. (2002). A crucial role for the putative Arabidopsis topoisomerase VI in plant growth and development. *Proceedings of the National Academy of Sciences of the United States of America*, *99*(15), 10191–6.

Zechiedrich, E. L., & Cozzarelli, N. R. (1995). Roles of topoisomerase IV and DNA gyrase in DNA unlinking durping replication in Escherichia coli. *Genes and Development*, *9*, 2859–2869.

Zharkov, D. O., Golan, G., Gilboa, R., Fernandes, A. S., Gerchman, S. E., Kycia, J. H., … Shoham, G. (2002). Structural analysis of an Escherichia coli endonuclease VIII covalent reaction intermediate. *The EMBO Journal*, *21*(4), 789–800.

Zheng, G., Lu, X., & Olson, W. K. (2009). Web 3DNA — a web server for the analysis , reconstruction , and visualization of three- dimensional nucleic-acid structures. *Nucleic Acids Research*, *37*(May), 240–246.

Appendices

The appendices of this dissertation have been separated into two categories. Appendices 1-8 contain step-by-step protocols for both experimental methods and analyses described in the main text of this dissertation. Appendices 9-14 describe step-by-step protocols for experiments and preparations which were not included in the main text of this dissertation, but which may prove useful for future studies involving the conformational coordination of type IIA and type IIB topoisomerases, in particular for single molecule fluorescence experiments.

Appendix 1: Map of polycistronic vector containing Methanosarcina mazei top6A and top6B, with functional mutations annotated.

Following is the sequence of the polycistronic region of the *M. mazei* topo Vi expression vector used in Chapter 3, beginning with a T7 promoter and ending with a T7 terminator which containing both the open reading frame (ORF) for *M. mazei* Top6A and the ORF for *M. mazei* Top6B. Top6A is colored in cyan and Top6B in blue. Useful sequencing primer locations are in red, and sites for generally useful catalytic site mutations, or functional mutations used in Chapter 3 are colored in pink. An N-terminal His6-tag and TEV protease cleavable sequence on Top6B are colored in ruby and orange respectively. A graphical map of this expression vector (**Figure A1.1)** is labeled with the specific annotations for each feature highlighted in the sequence in the text.

Polycistronic transcribed region between T7 promoter and T7 terminator:

```
  27 taatacgactcactatagggagaccacaacggtttccctctagaaataat  76
  77 tttgtttaactttaagaaggagtacttccaATGGAAGGAGAAAAAGGCAG 126
 127 CAAAACAAGAAAGGGAGACGCCCTTGCCAGGGAAAAACTCCTTGAGATTG 176
 177 CAGAAAAGATCTATAACCAGTTTGAAGAGGAGGTTGTCCCGAGTGTCAGC 226
 227 CTTCCAAGCCGGACAAAAGCAAACCTGGAATATTCCGACGAGAGCGATGT 276
 277 CTGGGTCTACGGAGACAGGGAAAGCGAAAGAAGCGCAAAAACCGTAAAAG 326
 327 GTGCATTCCAGCTCCTGAAGACTACATATGCAACTGATTTTCTTATAAAC 376
 377 GAACATCTTGCCCGTAACCGTGGCTCAACACTTCGAGAACTTTATTATAT 426
 427 TTCCGAAGGCTGGGACTATGCCAAATTCAAAGAACAGGGTGAAAGCGACC 476
 477 GCCTGATAGAGGACCTGGAAATCCTGACCAGCCTCCAGAGAGAGTATTTC 526
 527 CATATGCGCCCTGAAGAAGACGGAGCCACGATGTTCGGGCCGATTGAGAT 576
 577 TACGGAACAGACAAAGCGCGGAGAGCGGAATATCCACTGCCAGAAGGATG 626
 627 TGGGAGAAGGTGGGTACCAGATCCCTTTCAATGTGGAAAACATAGAGTTT 676
 677 CAAAAGCACGATGCGAGCATGATTATTGCCATAGAAACCGGTGGTATGTA 726
 727 TGCGCGTTTAATGGAAAACGGGTTTGATGAGGCTTATAACGCAATCCTTG 776
 777 TCCACCTGAAAGGTCAGCCTGCACGGTCAACCCGCAGGATAATCAAGCGC 826
 827 ATGAACGAAGAACTCGGGATTCCCGTGGCAGTTTTTACTGACGGTGACCC 876
 877 TTGGTCTTACAGGATCTATGCCTCTGTTGCTTACGGAGCCATAAAAAGTG 926
 927 CTCACCTTTCGGAATTCATGGCAACACCGGCAGCCAAATTCCTGGGGCTT 976
 977 CAGCCTTCTGATATCGTGGAATACGAACTTTCAACCGATAAGCTCACAGA 1026
1027 GCAGGACGTAAGCGCTCTCCGGAGTGAGCTTTCCGACCCGCGTTTTGAGT 1076
```

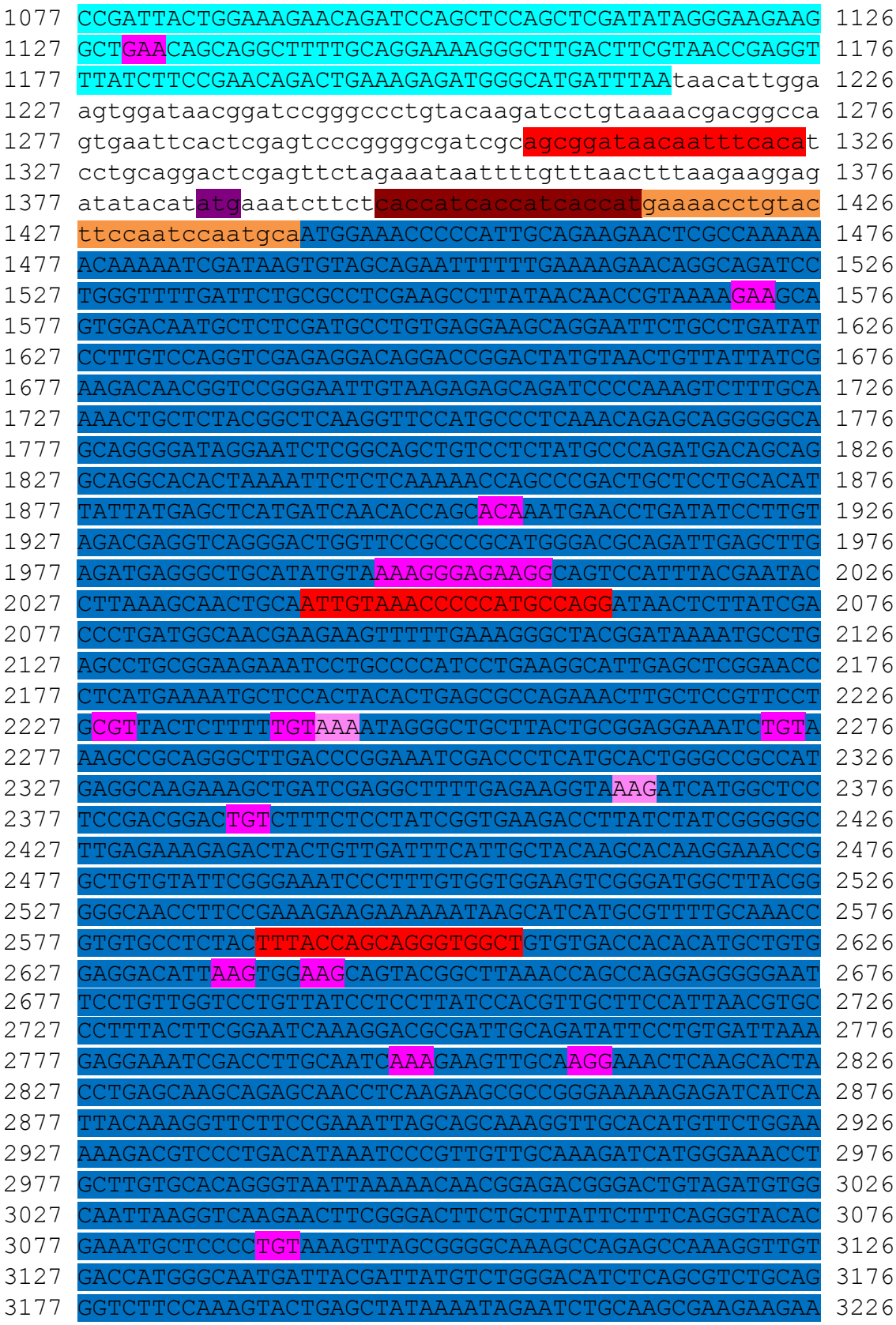
1077 CCGATTACTGGAAAGAACAGATCCAGCTCCAGCTCGATATAGGGAAGAAG 1126
1127 GCTGAACAGCAGGCTTTTGCAGGAAAAGGGCTTGACTTCGTAACCGAGGT 1176
1177 TTATCTTCCGAACAGACTGAAAGAGATGGGCATGATTTAAtaacattgga 1226
1227 agtggataacggatccgggccctgtacaagatcctgtaaaacgacggcca 1276
1277 gtgaattcactcgagtcccggggcgatcgcagcggataacaatttcacat 1326
1327 cctgcaggactcgagttctagaaataattttgtttaactttaagaaggag 1376
1377 atatacatatgaaatcttctcaccatcaccatcaccatgaaaacctgtac 1426
1427 ttccaatccaatgcaATGGAAACCCCCATTGCAGAAGAACTCGCCAAAAA 1476
1477 ACAAAAATCGATAAGTGTAGCAGAATTTTTTGAAAAGAACAGGCAGATCC 1526
1527 TGGGTTTTGATTCTGCGCCTCGAAGCCTTATAACAACCGTAAAAGAAGCA 1576
1577 GTGGACAATGCTCTCGATGCCTGTGAGGAAGCAGGAATTCTGCCTGATAT 1626
1627 CCTTGTCCAGGTCGAGAGGACAGGACCGGACTATGTAACTGTTATTATCG 1676
1677 AAGACAACGGTCCGGGAATTGTAAGAGAGCAGATCCCCAAAGTCTTTGCA 1726
1727 AAACTGCTCTACGGCTCAAGGTTCCATGCCCTCAAACAGAGCAGGGGGCA 1776
1777 GCAGGGGATAGGAATCTCGGCAGCTGTCCTCTATGCCCAGATGACAGCAG 1826
1827 GCAGGCACACTAAAATTCTCTCAAAAACCAGCCCGACTGCTCCTGCACAT 1876
1877 TATTATGAGCTCATGATCAACACCAGCACAAATGAACCTGATATCCTTGT 1926
1927 AGACGAGGTCAGGGACTGGTTCCGCCCGCATGGGACGCAGATTGAGCTTG 1976
1977 AGATGAGGGCTGCATATGTAAAGGGAGAAGGCAGTCCATTTACGAATAC 2026
2027 CTTAAAGCAACTGCAATTGTAAACCCCCATGCCAGGATAACTCTTATCGA 2076
2077 CCCTGATGGCAACGAAGAAGTTTTTGAAAGGGCTACGGATAAAATGCCTG 2126
2127 AGCCTGCGGAAGAAATCCTGCCCCATCCTGAAGGCATTGAGCTCGGAACC 2176
2177 CTCATGAAAATGCTCCACTACACTGAGCGCCAGAAACTTGCTCCGTTCCT 2226
2227 GCGTTACTCTTTTTGTAAAATAGGGCTGCTTACTGCGGAGGAAATCTGTA 2276
2277 AAGCCGCAGGGCTTGACCCGGAAATCGACCCTCATGCACTGGGCCGCCAT 2326
2327 GAGGCAAGAAAGCTGATCGAGGCTTTTGAGAAGGTAAAGATCATGGCTCC 2376
2377 TCCGACGGACTGTCTTTCTCCTATCGGTGAAGACCTTATCTATCGGGGGC 2426
2427 TTGAGAAAGAGACTACTGTTGATTTCATTGCTACAAGCACAAGGAAACCG 2476
2477 GCTGTGTATTCGGGAAATCCCTTTGTGGTGGAAGTCGGGATGGCTTACGG 2526
2527 GGGCAACCTTCCGAAAGAAGAAAAAATAAGCATCATGCGTTTTGCAAACC 2576
2577 GTGTGCCTCTACTTTACCAGCAGGGTGGCTGTGTGACCACACATGCTGTG 2626
2627 GAGGACATTAAGTGGAAGCAGTACGGCTTAAACCAGCCAGGAGGGGGAAT 2676
2677 TCCTGTTGGTCCTGTTATCCTCCTTATCCACGTTGCTTCCATTAACGTGC 2726
2727 CCTTTACTTCGGAATCAAAGGACGCGATTGCAGATATTCCTGTGATTAAA 2776
2777 GAGGAAATCGACCTTGCAATCAAAGAAGTTGCAAGGAAACTCAAGCACTA 2826
2827 CCTGAGCAAGCAGAGCAACCTCAAGAAGCGCCGGGAAAAAGAGATCATCA 2876
2877 TTACAAAGGTTCTTCCGAAATTAGCAGCAAAGGTTGCACATGTTCTGGAA 2926
2927 AAAGACGTCCCTGACATAAATCCCGTTGTTGCAAAGATCATGGGAAACCT 2976
2977 GCTTGTGCACAGGGTAATTAAAAACAACGGAGACGGGACTGTAGATGTGG 3026
3027 CAATTAAGGTCAAGAACTTCGGGACTTCTGCTTATTCTTTCAGGGTACAC 3076
3077 GAAATGCTCCCCTGTAAAGTTAGCGGGGCAAAGCCAGAGCCAAAGGTTGT 3126
3127 GACCATGGGCAATGATTACGATTATGTCTGGGACATCTCAGCGTCTGCAG 3176
3177 GGTCTTCCAAAGTACTGAGCTATAAAATAGAATCTGCAAGCGAAGAAGAA 3226

```
3227 CTCCAGAAGCTTCCTCAATTGATTGTAGAAGGGATTGAAGAAGAACTGGT 3276
3277 AACCGGGGCAAAAGCTTTCAAGGGTGTTTAAtaacattggaagtggataa 3326
3327 cggatccgcgatcgcggcgcgcccgccagggttttcccagtcgcggccgc 3376
3377 tcgcgcacctggtgccatcgccctgatagacgttaattaaagtactggcc 3426
3427 ggccacgcgtctcgagagatccggctgctaacaaagcccgaaaggaagct 3476
3477 gagttggctgctgccaccgctgagcaataactagc 3511
```

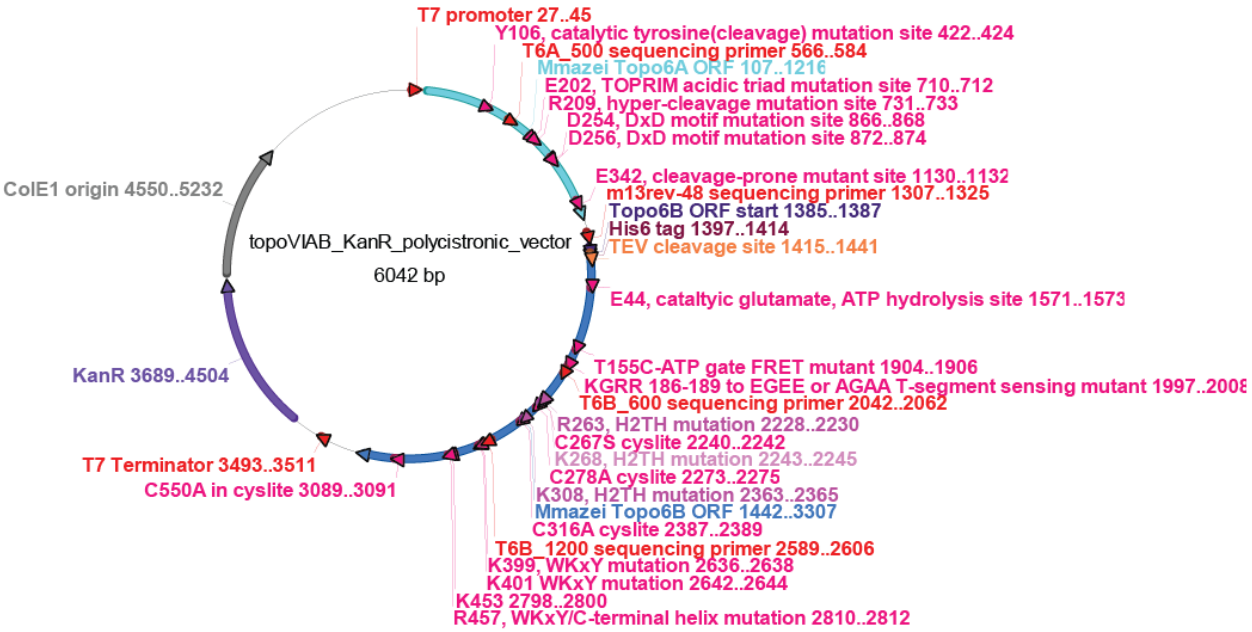

Figure A1.1. Graphical map of expression vector for M. mazei topo VI.

Origin (grey), resistance gene (purple), T7 promoter and terminator (red) open reading frames (cyan for Top6A, blue for Top6B), regions mutated for functional studies (pink) and useful regions for sequencing (red) are labeled.

Appendix 2: Step-by-Step Expression and Purification of Methanosarcina mazei topo VI holoenzyme

Materials

**note, for all solution stocks and buffers, 0.22 µm sterile filtering is assumed unless otherwise noted.*

M. mazei Top6A/Top6B expression vector (described in **Appendix 1**)
Chemically competent BL21 (DE3) Codon^{+} RIL *E.coli* cells
Sterile 1.5mL Eppendorf tubes
Autoclaved 2xYT (yeast extract/tryptone) media
Innova 4080 Incubator/Shaker (New Brunswick Scientific)
Innova 44 Incubator/Shaker (New Brunswick Scientific)
LB plates with 34µg/mL chloramphenicol and 30µg/mL kanamycin
30 mg/mL kanamycin (1000x stock)
34 mg/mL chloramphenicol (1000x stock)
6x 2L baffled flasks (number depends upon scale of preparation)
6x 1L ZYM-5052 auto-induction media (see Prepared media and buffers)
Steriflip 50 mL disposable Vacuum Filtration system tubes (Millipore)
Ultrospec 10 Cell density meter (Amersham Biosciences)
Disposable semi-micro UV cuvettes (BRAND GMBH+CO KG)
Avanti J-20 centrifuge (Beckman Coulter)
Avanti JL-8.1000 rotor and tubes (Beckman Coulter)
1M HEPES-KOH pH 7.5
5M NaCl
3M KCl
1M Imidazole pH 8.0
Reducing agent (BME or TCEP)
Glycerol
100 mM PMSF stock in 100% ethanol
1 mg/mL Leupeptin stock in H_2O
1 mg/mL Pepstatin A stock in 100% ethanol
Sonicator 3000 (Misonix, Inc)
RC5C centrifuge (Sorvall Instruments)
SS34 rotor and tubes (Sorvall Instruments)
2x Protein Loading Buffer
5mL Ni^{2+} Hi-Trap columns (GE)
5mL SP Hi-Trap columns (cation exchange, GE)
5mL Q Hi-Trap columns (anion exchange, GE)
Sterile 5, 10, 25 and 50mL serological pipettes
Barnstead Milli-Q purified ddH_2O
20% (v/v) ethanol
Manifold pump tubing PVC 1.52mm ID, Yellow-Blue 16'' long (ThermoFisher Scientific)
Minipuls 3 Peristaltic pump (Gilson)

Akta FPLC/Akta Pure chromatography system (GE)
13 x100mm PP Test Tubes (ThermoFisher Scientific)
Amicon Ultra 30K MWCO Concentrator (Millipore)
Sorvall Legend RT Tabletop Centrifuge
His_6-Tobacco Etch Virus(TEV) protease (UC Berkeley Macrolab)
BioRad protein assay dye reagent ("Bradford reagent")
MCT-200-NC-2.0 mL capless/clear homopolymer tubes (Axygen)
HiPrep 16/60 Sephacryl S-300 HR column (GE)
Precision Plus Protein Dual Color Standards (Biorad) or similar Protein MW standards
10% or 12% SDS-PAGE gels
1x Tris-Glycine running buffer
Nanodrop 1000 Spectrophotometer (Thermo Scientific)

Prepared media and buffers

ZYM-5052 auto-induction media. Adapted from: Studier, F.W. (2005) Protein Expr Purif. 41, 207-234). For a 1L culture:

1) Add 10 g N-Z amine or tryptone (1% w/v final) and 5 g yeast extract (0.5%w/v final) to 958mL distilled H_2O in a 2L baffled flask. Autoclave for 45min. This is the ZY stock.

2) Prior to inoculating cultures, add:
   20 mL 50x M stock solution
   20 mL 50x 5052 stock solution
   1 mL 2M $MgSO_4$
   1mL 1000x trace elements mix
   Antibiotics for resistance markers (2x for Kanamycin, 1x for all others)

50xM stock solution (500 mL). Add in sequence to 300mL milliQ purified H_2O while stiring:
88.73 g Na_2HPO_4 1.25 M final (note, may also come as a heptahydrate salt, modify mass added as required)
85 g KH_2PO_4, 1.25 M final
67 g NH_4Cl, 2.5 M final
17.75 g Na_2SO_4, 0.25M final
Add remaining volume to 500 mL, stir until dissolved. May require heat to enter solution. Sterile-filter solution once all components dissolved.

50x 5052 stock solution (500 mL). Add in sequence to 300mL milliQ purified H_2O while stirring:
125 g glycerol, 25% w/v final
12.5 g glucose, 2.5% w/v final
50 g α-lactose-monohydrate, 10% final
Lactose is slow to dissolve (will take hours), but may be expedited by heating. Sterile filter once all components dissolved.

1000x trace metals stock solution (100 mL)

1) Dissolve 0.811 g of $FeCl_3$ and 0.5 mL concentrated HCl in 50 mL of milliQ H_2O.

2) Add the following volumes of each of the following prepared stock solutions to the 0.1M $FeCl_3$ solution from step 1. 50mL stocks prepared by sterile filter using Steriflip 50 mL tube vacuum filtration (0.22 µm) works well:

2 mL 1.0 M CaCl2-2H2O	(7.9 g/50 ml)
1 mL 1.0 M MnCl2-4H2O	(9.9 g/50 ml)
1 mL 1.0 M ZnSO4-7H2O	(14.4 g/50 ml)
1 mL 0.2 M CoCl2-6H2O	(2.38 g/50 ml)
2 mL 0.1 M CuCl2-2H2O	(0.85 g/50 ml)
1 mL 0.2 M NiCl2-6H2O	(2.38 g/50 ml)
2 mL 0.1 M Na2MoO4-2H2O	(1.21 g/50 ml)
2 mL 0.1 M Na2SeO3	(0.87 g/50 ml)
2 mL 0.1 M H3BO3	(0.31 g/50 ml)
36 mL milliQ H_2O	

3) Sterile filter 1000x metals mix.

Mm Topo VI Buffer A: high salt/low imidazlole→Ni column wash

10mL 1M HEPES pH 7.5	20mM HEPES pH 7.5
80mL 5M NaCl	800mM NaCl
10 mL 1M imidazole 8.0	20mM Imidazole
100mL 50% (v/v) glycerol	10% glycerol
	To 500 mL

Mm Topo VI Buffer B: Low salt/low imidazole

10mL 1M HEPES pH 7.5	20mM HEPES pH 7.5
15mL 5M NaCl	150mM NaCl
10 mL 1M imidazole pH 8.0	20mM Imidazole
100 mL 50% (v/v) glycerol	10% glycerol
	To 500 mL

Mm Topo VI Buffer C: Low salt/high imidazole, elute tagged TopoVI

5 mL 1M HEPES pH 7.5	20mM HEPES pH 7.5
7.5 ml 5M NaCl	150mM NaCl
75 mL 1M imidazole pH 8.0	300mM Imidazole
50 mL 50% (v/v) glycerol	10% glycerol
	To 250mL

Mm Topo VI Buffer D: Sizing column buffer

50 mL 3M KCl	300mM KCl
10 mL 1M HEPES pH 7.5	20mM HEPES pH 7.5
100mL 50% (v/v) glycerol	10% glycerol

1 ml 1M DTT	1mM DTT
	To 500 mL

Bring to volume using Milli-Q H_2O. Sterile filter all buffers. Do not add reducing agents or protease inhibitors until immediately prior to use. Volumes should be sufficient for one preparation of *Mm* topo VI from 4-6 L of cell culture.

Mm Topo VI Storage Buffer
80% glycerol, 300mM KCl, 20mM HEPES pH 7.5, 1mM TCEP.

Added to protein in *Mm Topo VI Buffer D* in a 0.4:1 ratio to yield a 30% glycerol, 300mM KCl, 20mM HEPES pH 7.5, 1mM TCEP final solution.

2x SDS PAGE Loading Buffer
5% SDS, 0.01% Bromphenol Blue, 25% glycerol, 150mM Tris-HCl pH 6.8, 200mM βME.
Does not need to be sterile filtered.

Step-by-step protocol
Expression
Day 1-Transform chemically competent BL21DE3-Codon$^+$ RIL *E. coli* cells with wildtype *Mm*Top6A/Top6B expression vector:

1) Add ~50ng vector to ~50 µL competent cells (aliquots are usually 100 µL) in sterile 1.5mL Eppendorf tube and incubate on ice for ~30min.
2) Heat shock cells at 42°C for 45 seconds.
3) Allow recovery on ice for 2 minutes.
4) Add 900 µL autoclaved 2xYT media to cells and recover by shaking at 37°C in Innova 4080 Incubator-Shaker for at least 45 minutes.
5) Spread ~100 µL of cells on LB plate containing 30 µg/mL Kanamycin and 34 µg/mL chloramphenicol. Incubate overnight at 37°C in VWR Scientific Model 1565 incubator.

Note, certain Mm topo VI functional mutants, specifically Top6A^{R209Q}B is particularly toxic in E. coli. This construct will not grow in BL21DE3-Codon$^+$ RIL cells, but may be *expressed in Rosetta2 PLysS cells. Other methods that prevent leaky expression are likely also adequate for expressing this construct.*

Day 2-

1) Remove plates from incubator in morning. Keep on bench at room temperature.

2) Follow step 1 of preparing ZYM-5052 auto-induction media and autoclave needed ZY stock.

3) In afternoon, inoculate starter culture of 20 mL autoclaved 2xYT media +30 µg/mL Kanamycin and 34 µg/mL chloramphenicol with swath of colonies. Shake and incubate at 37°C in Innova 4080 Incubator-Shaker overnight.

Note, 1) size of starter culture may be scaled based on scale of final preparation. You will need 3 mL starter culture/ 1 L of auto-induction culture. 2) Original protocol by Studier calls for a starter culture using MDG media. In my experience, using 2xYT in the starter culture works as well for topo VI expression.

Day 3-

1) Follow step 2 of preparing ZYM-5052 auto-induction media, adding 60µg/mL Kanamycin and 34 µg/mL chloramphenicol as antibiotics.

Note, Kanamycin concentration is doubled for auto-induction media.

2) Inoculated 6x1L of ZYM-5052 auto-induction media + with 3 mL turbid starter culture each and grow by shaking in Innova 44 Incubator-Shakers at 37^{o}C for ~24hrs. Aeration of auto-induction cultures is critical to reach sufficient growth densities. The 2inch orbital of the Innova 44 shakers generates sufficient aeration at 160 rpm with baffled flasks.

Note, for certain topo VI constructs, decreasing the growth temperature to 25°C once cultures reach an OD_{600} of ~0.6-0.8 (~5 hours following inoculation) improves expression. This is useful for the cysteine-lite construct and any derivatives thereof, the KGRR T-segment sensing mutants, the H2TH domain mutants, and the WKxY and Top6B-C-terminal helix mutants.

3) Prepare Mm Topo VI Buffer A. Store at 4°C.

Day 4-Harvest cultures 24 hours following inoculation.

1) Transfer cultures to 1L bottles for JLA 8.1000 rotor and Avanti J-20 centrifuge. Spin cultures at 4500rpm for 20min at 4°C. Decant spent media, keep cell pellets on ice.

2) To ~100mL of Mm Topo VI Buffer A, add protease inhibitors to 1µg/mL pepstatin A, 1µg/mL leupeptin, 1mM PMSF.

3) For each liter of culture, resuspended cells with ~10mL Mm Topo VI Buffer A + protease inhibitors from previous step on ice. Use serological pipette and sterile cell scrapper to homogenize resuspended cells. Flash freeze dropwise into liquid nitrogen using a serological pipette and store in 50mL Falcon tubes at -80°C.

Note, 1) to measure culture growth at high ODs, first dilute 100uL of culture 10-fold to a 1mL volume in BRAND semi-micro UV cuvettes. 2xYT may be used to dilute. Then measure with Ultrospec 10 cell density meter. Scaled to the 1x volume, should

yield an OD_{600} of 5-8, though reasonable expression may be obtained from cultures outside this range (i.e. OD in range of 3-12).

2) Alternatively, instead of flash freezing cells continue directly with protein purification, from Day 1, step 2.

Purification

Day 0-

Make sure Mm Topo VI Buffer A, B, C, and D are prepared the day before starting a topo VI preparation and store buffers at 4°C. Do not add protease inhibitors at this time. Buffers may be made further in advance but run the risk of contamination if kept for long periods of time.

Day 1-

1) Place 50mL falcon tubes of frozen cells in beaker of room temperature H_2O. Once cell pellets have thawed, transfer cell resuspension to 250 mL metal beaker on ice.

2) To Mm Topo VI Buffer A, add protease inhibitors to 1µg/mL pepstatin A, 1µg/mL leupeptin, 1mM PMSF. Keep buffer at 4°C or on ice.

3) Prepare charged 5mL Ni^{2+} Hi-Trap columns stored in 20% ethanol by first equilibrating with 5 column volumes (CV) (25 mL) of miliQ-H_2O, followed by 5 CV (25 mL) of Mm Topo VI Buffer A + protease inhibitors. This may be done using a Minipuls 3 or alternative brand peristaltic pump and Manifold pump tubing PVC (Yellow-Blue, 1.52 mm inner diameter, 16 inches long). Two lines of pump tubing will likely need to be connected using 0.8mm barb-barb connectors. Run at a speed of ~10, this corresponds to ~2 mL/min for 1.52mm ID PVC tubing.

Alternatively, an FPLC/Akta Pure/Akta Prime may be used to equilibrate the column.

4) Add ~50 mL of Mm Topo VI Buffer A +protease inhibitors, to resuspsended cells. Make sure resuspension is homogenous and not overly dense. Using the Sonicator 3000, submerge the sonicator macro-horn (do not use the microtip) in resuspended cells. Make sure the horn does not touch the edge of the beaker, and make sure the beaker is well nestled in ice in an ice bucket. Apply six 20 second pulses, with 2min pauses between each pulse, at power setting 5.5.

Following sonication, take a 10 µL sample of lysate and add to 10 µL of 2x SDS PAGE loading buffer in case it is needed for diagnostic SDS-PAGE.

5) Transfer lysate into ss34 tubes and clarify by centrifugation at 15krpm at 4°C for 20 min in using an ss34 rotor and Sorvall Instruments RC5C centrifuge.

Alternatively, the JLA-25.50 rotor and Avanti J-20 centrifuge may be used for this step.
Following clarification, take a 15 µL sample of clarified lysate supernatant and add to 15 µL of 2x SDS PAGE loading buffer in case it is needed for diagnostic SDS-PAGE

6) Apply clarified lysate to the 5mL Ni-column equilibrated in Mm Topo VI Buffer A + protease inhibitors using peristaltic pump. A speed setting 10 (~ 2ml/min) is adequate. Collect and flow through.

Alternatively, clarified lysate may be applied to Ni^{2+} column using a FPLC/Akta Pure and a super-loop.

Take a 15 µL sample of lysate flow-through and add to 15 µL of 2x SDS PAGE loading buffer in case it is needed for diagnostic SDS-PAGE.

7) Wash Ni^{2+} column containing bound protein with a volume of Mm Topo VI Buffer A +protease inhibitors ~equal to the volume of clarified lysate applied to the column.

8) To Mm Topo VI Buffer B, and Mm Topo VI Buffer C, add protease inhibitors to 1µg/mL pepstatin A, 1µg/mL leupeptin, 1mM PMSF. On an Akta FPLC/Akta Pure, wash Pump A with Mm Topo VI Buffer B + protease inhibitors and Pump B with Mm Topo VI Buffer C + protease inhibitors. Make sure the flow path of the system is in buffer B, and the free column position (position 5 on the Akta Pure and valve 7 position 2 on the Akta FPLCs for instance) are inline of the system flowpath. Setup fraction collector to collect 5mL fractions in 12x 100 mm PP Test tubes.

9) Following sample application and washing, place Ni^{2+} column inline of the flow path on FPLC/Akta Pure. Applying flow of *Mm Topo VI Buffer B* at 2 mL/min, wash column with 5 CV (25 mL) of *Mm Topo VI Buffer B* + protease inhibitors, then elute bound protein by applying a 15 CV (75 mL) gradient from 100% *Mm Topo VI Buffer B* + protease inhibitors to 100% *Mm Topo VI Buffer* C+ protease inhibitors. Two peaks will elute off, one at ~2-4 CV (10 ml to 20mL) into the gradient and at 6 and 13 CV into the gradient (30 mL to 65mL). **Topo VI tetramer is in the second peak (6-13 CV into gradient)**. Pool peak fractions.

Take a 15 µL sample of pooled fractions from the 6-13 CV elution peak and add to 15 µL of 2x SDS PAGE loading buffer in case it is needed for diagnostic SDS-PAGE.

10) Prepare 5mL HiTrap-SP (cation exchange) and HiTrap-Q (anion exchange) columns stored in 20% ethanol by first equilibrating with 5 column volumes(CV) (25 mL) of miliQ-H_2O, followed by 5 CV of Mm Topo VI Buffer B + protease inhibitors. As with preparing the Ni^{2+} column, this may be done by peristaltic pump, using a flow rate of 2 mL/min (speed 10 on the Minipuls 3). Place the Hi-Trap-SP and Hi-Trap-Q columns in series, i.e. connect the peristaltic pump tubing to the inlet on the Hi-Trap-SP column and then attach the outlet of the Hi-Trap-SP **directly** to the inlet of the Hi-Trap-Q column. The Q-column should just screw on to the SP column.

Alternatively, an FPLC/Akta Pure may be used to equilibrate the columns and set them up in series.

11) Apply the pooled second peak from the Ni^{2+} column gradient elution onto 5mL Hi-Trap SP and 5 mL H-Trap Q column in series. Following protein application, wash Hi-Trap SP and 5 mL H-Trap Q in series with 30 mL Mm Topo VI Buffer B + protease inhibitors. Free Top6B

subunit will be bound to the Hi-Trap SP column, whereas **topo VI heterotetramer will be bound to the Hi-Trap Q** column.

12) On an Akta FPLC/Akta Pure, keep Pump A in *Mm Topo VI Buffer B + protease inhibitors*, and wash Pump B with *Mm Topo VI Buffer A + protease inhibitors*. Make sure the flow path of the system is in buffer B, and the free column position (position 5 on the Akta Pure and valve 7 position 2 on the Berger Lab Akta FPLCs for instance) are inline of the system flowpath. Setup fraction collector to collect 5mL fractions in 12x 100 mm PP Test tubes.

13) Following sample application and washing, place **only the Hi-Trap Q column** inline of the flow path on FPLC/Akta Pure/Akta Prime. Applying flow of *Mm Topo VI Buffer B* at 2mL/min, allow A_{280} to stabilize, then elute bound topo VI heterotetramer by applying a 10 CV (50 mL) gradient from of *Mm Topo VI Buffer B* + protease inhibitors to of *Mm Topo VI Buffer* A. **One major peak will elute off at ~2.5-5 CV (~12.5 mL to 25 mL) which contains Topo VI tetramer**. Pool peak fractions.

Take a 15 µL sample of pooled fractions from the 2.5-5 CV elution peak and add to 15 µL of 2x SDS PAGE loading buffer in case it is needed for diagnostic SDS-PAGE.
If the preparation is not progressing as expected, now is a good time to run a SDS-PAGE gel of collected samples from day 1 to determine where and how topo VI heterotetramer was lost.

14) Concentrate pooled elution fractions from the Hi-Trap Q elution gradient by centrifugation at 4000 rpm in a Sorvall Legend RT tabletop centrifuge using an Amicon Ultra 30K MWCO concentrator to ~1mL. Add 750uL 2mg/mL His6-TEV protease (3 aliquots from UC Berkeley Macrolab). Incubate at 4^{o}C overnight (usually 12-16 hours).

15) Prepare HiPrep 16/60 Sephacryl S-300 HR column on FPLC/Akta Pure/Akta Prime by equilibrating column with 1.25 CV (150 mL) of *Mm Topo VI Buffer D* at 0.5mL/min.

Day 2-

1) Prepare charged 5mL Ni^{2+} Hi-Trap column by equilibrating with 5 CV (25 mL) of Mm Topo VI Buffer B. I prefer to do this on the free column position of an Akta FPLC/Akta Pure, but a peristaltic pump may also be used. Setup fraction collector to collect 2mL fractions in 2.0 mL capless/clear tubes, which may be set in 12x 100 mm PP Test tubes.

2) Use 2 mL sample loop to apply TEV protease digest of topo VI heterotetramer to Ni^{2+} column and collect flow through, washing column with ~6 CV (30 mL) Mm Topo VI Buffer B. Tagless heterotetramer usually appears at ~0.5-4 CV (2.5-20 mL). Pool flow-through which contains protein.

Take a 15 µL sample of pooled fractions from flow through and add to 15 µL of 2x SDS PAGE loading buffer in case it is needed for diagnostic SDS-PAGE.
If using a peristaltic pump, collect 1.5mL fractions in Eppendorf tubes. Add 2µL of fraction to 48 µL Bradford reagent to determine peak fractions.

3) Concentrate pooled Ni^{2+} Hi-Trap column flow-through by centrifugation at 4000 rpm in a Sorvall Legend RT tabletop centrifuge using an Amicon Ultra 30K MWCO concentrator to <2.0 mL.

4) Wash Ni^{2+} Hi-Trap column with 5CV (25 mL) of Mm Topo VI Buffer C. TEV protease as tagged topo VI should elute at ~1CV (5mL) into wash.

Take a 15 µL sample of Ni^{2+} column elution and add to 15 µL of 2x SDS PAGE loading buffer in case it is needed for diagnostic SDS-PAGE.

5) Setup fraction collector to collect 2 mL fractions in 2.0 mL capless/clear tubes, and use the 2 mL sample loop to apply concentrated topo VI sample to HiPrep 16/60 Sephacryl S-300 HR equilibrated and run in *Mm Topo VI Buffer D* at a flow of 0.5mL/min. A void peak elutes at ~0.32-0.37 CV (38-44mL) and the topo VI heterotetramer elutes at 0.42-0.58 CV (50 mL-70 mL).

Take a 15 µL samples from each peak fraction and add to 15 µL of 2x SDS PAGE loading buffer. Run all fractions on a diagnostic SDS-PAGE (I find 10% or 12% SDS PAGE works well) with MW standards (I prefer Biorad Precision Plus Protein Dual Color Standards). Both SDS-PAGE gels and 1x Tris-Glycine running buffer are currently common lab stocks.

Top6B should run around 69 kDa, Top6A should run around 42 kDa. Sometimes the later eluting fractions contain degradation products running slightly faster than Top6B. As long as fractions from the s300 size exclusion chromatography run look as expected, I tend not to run the other diagnostic samples from the preparation.

6) Based on SDS-PAGE, pool concentrate peak fractions of topo VI heterotetramer by centrifugation at 4000 rpm in a Sorvall Legend RT tabletop centrifuge using an Amicon Ultra 10K MWCO concentrator to <500 µL.

7) Add 0.4x volume of *Mm topo VI storage buffer* to bring glycerol concentration to 30%. Measure protein concentration using the Edelhoch method (Edelhoch, 1967) by Nanodrop spectrophotometer. Use a topo VI tetramer extinction coefficient of 188010 A_{280}/cm/M. Aliquot protein in ~10 µL volumes, flash freeze in liquid nitrogen and store at -80°C.

Note, it has been shown the extinction coefficients generated from the ExPASy ProtParam server (Gasteiger et al, 2005) may be applied to native proteins as well, showing errors within 4%.

8) Strip and recharge Ni^{2+} HiTrap columns as per manufacturer's instructions. In brief, wash with 5 CV (25 mL) of Stripping Buffer (1M NaCl, 250mM EDTA), followed by 5CV (25 mL) of Mm Topo VI Buffer A, followed by 5CV (25 mL) of MilliQ-H_2O. If columns require extra cleaning, wash with 1M NaOH for precipitated proteins, or wash with 30% isopropanol for hydrophobically bound proteins or lipids. Apply 0.5CV (2.5mL) of Recharging buffer (0.2M $NiSO_4$), wash with 5CV (25 mL) of Mm Topo VI Buffer A, followed by 5CV (25 mL) of MilliQ-

H_2O and finish with 5CV (25 mL) of in 20% ethanol. Columns may be stored at room temperature until next use.

9) Elute and bound proteins from 5mL HiTrap SP and HiTrap Q columns with 5CV (25 mL) of Mm Topo VI Buffer A. Equilibrate with 5CV(25mL) of MilliQ H_2O and finish with 5CV (25mL) of 20% ethanol for HiTrap Q, and 5CV (25mL) of 20% ethanol/0.2M sodium acetate for HiTrap SP. Columns may be stored at room temperature until next use.

Appendix 3: Preparation and purification of stacked junction DNAs

This dissertation employed four-way junctions to assess modes of T-segment and G-segment DNA sensing and binding by type IIB topoisomerases. These junctions may be formed by four ssDNA oligomers to generate four duplex branches. In the presence of divalent cations, these junctions form a "stacked-X" structure where the four branches form two continuous duplexes, with two of the four strands crossing between these two duplexes (Duckett et al 1988, Ortiz-Lombardia et al 1999) (**Figure A3.1**). When designing these substrates, sequence specificity of the protein of interest (i.e. the cleavage hotspot sequence for topo VI, (Buhler et al 2001)) is the foremost consideration. More general considerations also include:

Design considerations

1) Make sure basepairs at the junction are non-equivalent in order to impede branch migration. An easy way to verify whether DNAs have been designed correctly is to draw out a four-way junction so that each of the four branches are directed either up, right, down, or left. Draw the result of a branch migration along the left/right axis (the up and down branches will each get one base pair shorter) or along the up/down axis (the left and right branches will each become one base pair shorter). Migration in either direction should result in unpaired bases at the junction.

2) The stacked-X junction forms two continuous duplexes, where two of the four ssDNA strands which make up the junction crossover between duplexes, and two strands do not. This may lead to two potential conformers. To bias which strands crossover, place a G or T at the second 3' position of a strand following the junction if you do not want it to crossover. Conversely, place a C at the second 3' position of a strand following the junction if you want it to crossover. The amine group of cytosine at this position of the crossing strand can coordinate the phosphate backbone at the crossing. G and T cannot assuage this interaction.

3) Placing a backbone spacer element (see IDT's C3 spacer /iSpC3/ as an example) on the crossover strands will both prevent branch migration, bias a specific stacking conformation, and allows the distance between stacked duplexes to be varied. However, this may generate too great a distance between the continuous stacked duplexes.

4) To decrease the complexity in annealing, connect the ends of two of the four strands with tetraloops. This generates a four way junction from two oligomers instead of four oligomers, and may be necessary when branches of the junction need to be short (i.e. less than 12 base pairs long).

Materials

DNA oligomer components of four-way junction (IDT). May add dyes or other modifications.
2-4 oligomers, designed by user. For the substrate used in Chapter 3:
5'-CGAATACTCAGCTCAACCGAAAGGTTGAGCCTTCGCTCGAAAGAGCGAAGTACTCTTCCG-3'
5'-CGGAAGAGTATGAGTATTCG-3'
MiliQ H_2O or equivalent
Junction Buffer A (25 mM Tris-HCl pH 7.9, 25mM NaCl, 10mM $MgCl_2$)
Junction Buffer B (25 mM Tris-HCl pH 7.9, 1M NaCl, 10mM $MgCl_2$)
Thin-wall PCR tubes
Mastercycler Gradient Thermocycler (Eppendorf) or equivalent thermocycler
5mL Hi-Trap Q (anion exchange) column (GE)
Akta FPLC/Akta Pure chromatography system (GE)
5x TBE (1.1M Tris, 900mM Borate 25mM EDTA, pH 8.3) buffer
0.5x TBE buffer
40% 19:1 acrylamide:bis solution
10% ammonium persulfate (APS)
TEMED
10,000x Sybr Gold DNA stain (ThermoFisher Scientific)
Nanodrop 1000 Spectrophotometer (Thermo Scientific)
T4 endonuclease VII (Molecular Cloning Laboratories)

Step-by-step protocol

Day 1-

1) Resuspend DNA oligomers in milliQ-H_2O or TE (10mM Tris-HCl pH 8.0, 1mM EDTA) to ~100 µM.

2) For a 100 µL of 20 µM junction, combine 10µL of each component oligomer, and dilute with 80 µL of Junction Buffer A in thin-wall PCR tubes. I usually prepare 500 µL of 20 µM junction and split into 5 tubes. The reaction is split because volumes greater than 100 µL will rise above the top of the thermocyler heat block and therefore not have full contact with the block.

3) In a thermocycler, setup a program to hold reactions at 70°C for 2hours, then cool reactions at 0.5°C steps per min until reactions reach 4°C, i.e.:

1) T=70.0°C		2:00:00
2) T=70.0°C		0:01:00
-0.5°C		+00:00
3) GOTO	2	REP 99
4) T=20.5°C		0:01:00
-0.5°C		+00:00
5) GOTO	4	REP 33
6) HOLD	4.0°C	

Day 2-

Alternatively to the following protocol, annealed junction substrates may be gel purified. In my experience, the chromatography based approach described below works as well as gel purification and recovers more junction substrate.

1) On an Akta FPLC/Akta Pure, wash Pump A with Junction Buffer A and Pump B with Junction Buffer B. Make sure the flow path of the system is in Junction Buffer A, and the free column position (position 5 on the Akta Pure and valve 7 position 2 on the Akta FPLCs for instance) are inline of the system flowpath. Setup fraction collector to collect 2mL fractions in 2.0 mL capless/clear tubes, which may be set in 12x 100 mm PP Test tubes.

2) Place a 5 mL Hi-Trap Q column inline, and equilibrate column at 2 ml/min with 5 column volumes (CV) (25 mL) of Junction Buffer A.

3) Use 2 mL sample loop to apply junction annealing reaction to 5 mL Q column. Wash with 5 CV (25 mL) of Junction Buffer A.

4) Start collecting 2 mL fractions. Wash Q column with 5 CV (25 mL) of 55%/45% Junction Buffer A/Junction Buffer B mix. Un-annealed DNAs will elute at the step.

5) Apply a 10 CV (50 mL) gradient from 55%/45% Junction Buffer A/Junction Buffer B to 45%/55% Junction Buffer A/Junction Buffer B. Additional un-annealed DNAs will elute during this gradient, and **the correct junction product may start eluting at the end of this gradient.**

6) Wash with 5 CV (25 mL) of 45%/55% Junction Buffer A/Junction Buffer B. **The correct junction product may continue to elute during this step.**

7) Wash with 5 CV (25 mL) of 100% Junction Buffer B. Higher order "daisy chain" products elute at this step.

   The described buffer steps and gradients are useful for purification of an untested junction product. Depending on the junction, optimizing steps and gradients may lead to a more efficient purification scheme.

8) Pour a native 0.5x TBE 15% (19:1 acryl:bis) PAGE gel. To prepare one, first setup a short glass plate and spacer plate in a Biorad Mini-Protean Handcast system. Mix 5.625 mL of 40% 19:1 Acrylamide:bis solution with 1.5 mL 5x TBE buffer, and 7.765 mL H_2O. Add 100 µL of 10% APS and 10 µL to start polymerization reaction and poor into prepared glass plates and add well comb. Gel will polymerize in ~20 min.

   These native TBE PAGE gels are not lab stocks, so you need to make one from scratch. I use them infrequently enough that I just prepare one when I need it.

9) Run a diagnostic 0.5x native TBE 15% (19:1) PAGE of peak fractions to identify correct products. Run at 90V at 4°C for ~4 hours. If junction contains a fluorophore, substrates may be imaged directly using a gel laser scanner (i.e. Typhoon FLA 9500 laser scanner. Place a transparency between your gel and the scanner, and select the correct laser and filter set wavelength for your fluorophore). Otherwise, stain gel with SybrGold. Allow stain to thaw at room temperature and then spin down with a tabletop microcentrifuge. Add 2.5 µL stain to gel in 25 mL of 0.5x TBE, cover with aluminum foil, and place on gel shaker for 10 min. No destain step is required. Image stained gel using a laser scanner (There should be setting in the Typhoon software for SybrGold). See **Figure A3.2** for an example chromatograph trace and diagnostic gel.

10) Combine fractions containing properly formed junctions and concentrate by centrifugation at 4000 rpm in a Sorvall Legend RT tabletop centrifuge using an Amicon Ultra 3K MWCO concentrator to <500 µL. Add fresh Junction Buffer A and concentrate to <500 µL to exchange junctions into a low salt condition by dialysis-filtration. Use a Nanodrop spectrophotometer to measure junction concentration by absorbance at 260nm. An online tool like (http://biophysics.idtdna.com/) may be used to determine an annealed junction's extinction coefficient.

11) Aliquot substrates as required (biochemical and biophysical assays will require different scales than structural assays) and flash freeze junction substrates in liquid nitrogen. They may be stored at -20°C. I prefer to store these substrates at -80°C.

12) While formation of a four way junction can be verified by electrophoretic mobility on a native TBE PAGE as described in step 9, it may also be verified enzymatically using T4 endonuclease VII which will cleave junctions, but not duplexes.

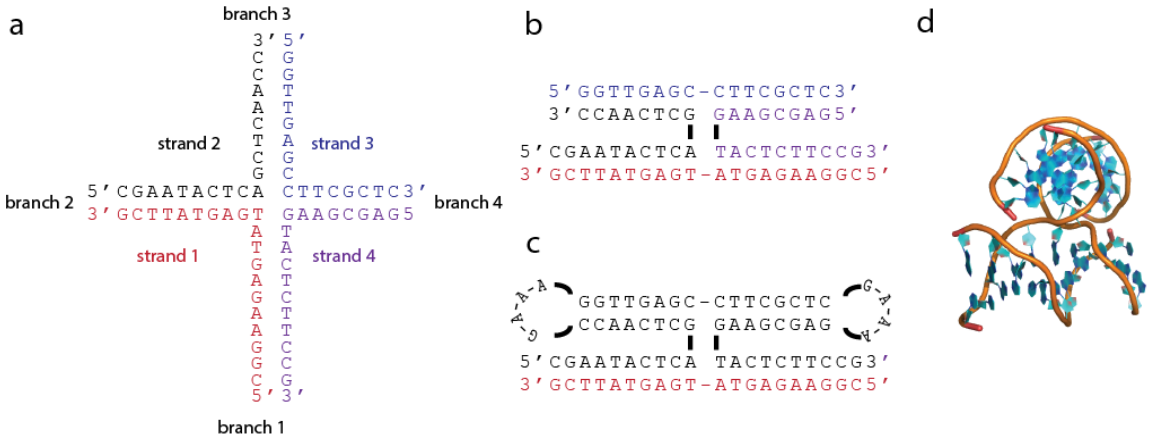

Figure A3.1. Design of four-way junctions.

a. Cartoon depicting how the four strands of a four-way junction substrate base pair to form four duplex branches. Note that branch migration on this junction results in unpaired bases.

b. Addition of divalent cations promotes folding of four-way junctions into a "stacked X" structure. Here, branch 1 and branch 2 form a continuous duplex; branch 3 and branch 4 form a second continuous duplex. Strand 2 and strand 4 are the crossing strands in this structure.

c. Tetraloop sequences may be used to link strand 2 to 3, and strand 3 to 4. This reduces the number of annealed oligomers in the four-way junction two.

d. A 3-dimensional representation of the "stacked-X" four-way junction (PDB ID = 467D).

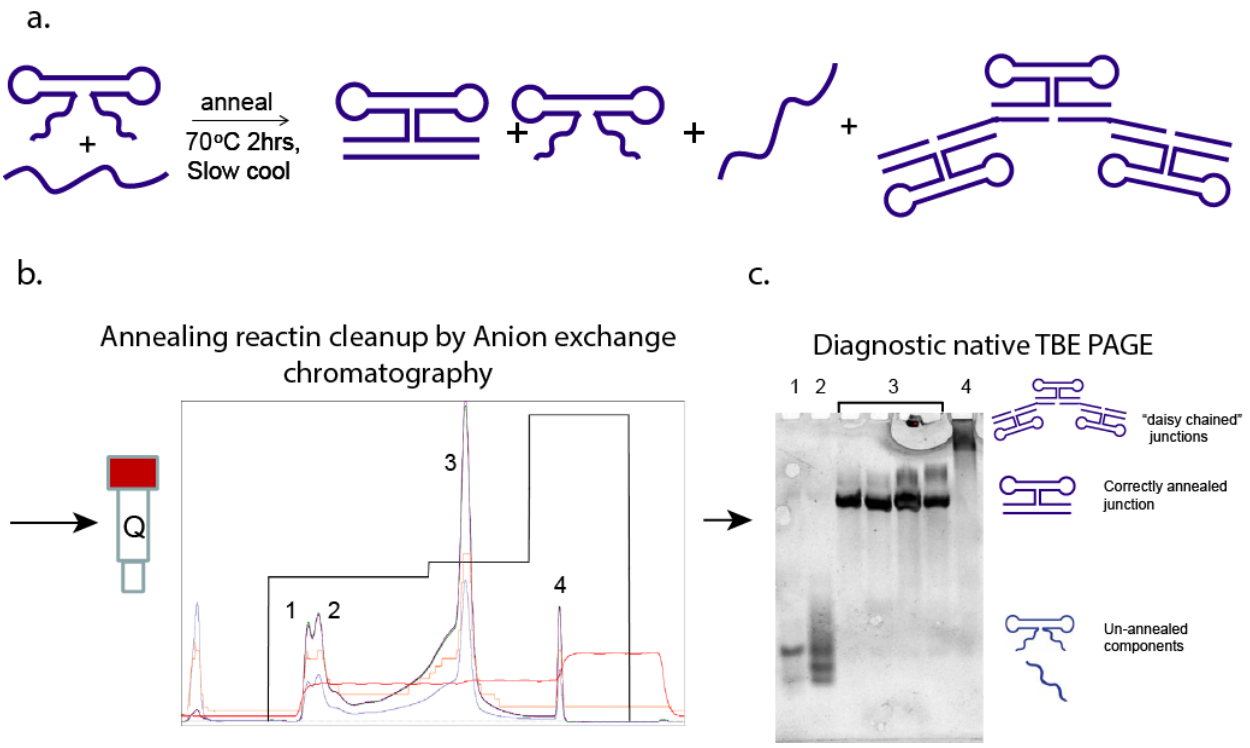

Figure A3.2. Annealing and purification of four-way junctions.
a. Cartoon depicting the annealing scheme for a four-way junction substrate where three of the four component strands are connected by tetraloop hairpins and annealed to the fourth oligomer. DNA oligomers are incubated at 70°C and slowly cooled to 4°C. This generates correctly annealed junctions, along with free un-annealed components and higher order "daisy chains" where the fourth DNA oligomer anneals to multiple tetraloop oligomers.
b. Anion exchange chromatography is able to separate distinct species from the annealing reaction. In the depicted trace, a multiple buffer ratio steps were used as opposed to the gradient described in the step-by-step protocol.
c. Diagnostic native 0.5x TBE shows distinct species in in each peak obtained by anion exchange chromatography.

Appendix 4: *M mazei* topo VI supercoil relaxation assays

This appendix provides a step-by-step guide for determining the specific activity of *M. mazei* topo VI enzyme preparation. Parameters which may be modified and the known effect of different components or component concentrations have been noted.

Materials

Supercoiled plasmid substrate resuspended in water (typically pSG483, 2927bps, typically in a ~500ng/µL stock from Maxiprep, 1ng/µL plasmid is 0.53 nM plasmid)
MilliQ H_2O
1.5mL Eppendorf tubes
96 well "U" bottom plate (vinyl) for mixing
8-tube strip PCR tubes
Metal tube racks/blocks
2M Potassium glutamate
1M HEPES-KOH pH 7.5
1mg/mL BSA
1M TCEP pH 7.0
1M $MgCl_2$
1M Bis-tris-propane-HCl (BTP) pH 7.5*

Modified from pH 6.5 used in KD Corbett's original assay. I have found pH 6.5, 7.0 and 7.5 yield similar topo VI activities. I use pH 7.5 to ensure compatibility with applications where pH 6.5 is sub-optimal.

50% (v/v) Glycerol
200mM ATP pH 7.0
Nanodrop (optional)
Mastercycler Gradient Thermocycler (Eppendorf) or equivalent thermocycler (optional)
0.5M EDTA pH 8.0
10% SDS
10X Glycerol DNA loading buffer
Invitrogen UltraPure agarose
8-12 channel 20µL multi-channel pipette
Ethidium Bromide
Plastic staining container (Rubbermaid or Tuperware)
UV trans-illuminator

Protocol

1. Prepare Topo VI dilution buffer:
[300mM potassium glutamate, 10% (v/v) glycerol, 20mM HEPES-KOH pH 7.5 and 1mM TCEP, ~500µL for one titration or time-course series]

and topo VI 2x assay buffer:

[0.2 mg/mL BSA, 20 mM $MgCl_2$, 40 mM BTP-HCl pH 7.5, 18% (v/v) glycerol, 40 mM potassium glutamate, 2mM TCEP, 13.3 ng/µL or 20.4 µM plasmid DNA (this is 7 nM pSG483), ~175 µL for one titration or time-course series].

Buffers may be prepared in larger stocks beforehand and frozen, as long as BSA and TCEP are withheld and added fresh.
**Note, I have tried a number of varied conditions from these buffers. To summarize: 1) 50 mM and 100 mM monovalent salt show similar activity, increasing concentration further decreases enzyme activity. 2) Activity with different monovalent salts shows the trend of potassium glutamate>KCl>potassium acetate. Nevertheless, enzyme is active in all three salts 3) Similar activity seen at 20 mM and 10 mM $MgCl_2$. Enzyme is active but shows slightly diminished activity at 5 mM $MgCl_2$. 4) Enzyme retains some nicking and cleavage activity in $CaCl_2$ and $MnCl_2$, but no longer relaxes DNA substrates. 5) Addition of BSA and increase of glycerol concentration compared to KD Corbett's original assay improves enzyme activity.*

2. Place buffers, H_2O (in an Eppendorf tube stock), 96 Well "U" bottom plate/vinyl for mixing, 8-tube strip PCR tubes, ATP aliquots and metal tube racks on ice. Add 15µL of 2x assay buffer to 8-tube strip PCR tubes, add H_2O to each well in an 8-well row on the mixing plate (need ~15 µL in each well for a single titration series reaction), dilute ATP to a 10 mM stock and add to each well in an 8-well row on the mixing plate (need ~6 µL in each well for a single titration series reaction), and add topo VI dilution buffer to in seven of the eight wells in an 8-well row, keeping an end well empty (10 µL in each well for a single titration series reaction).
Note, this setup is designed for a seven point titration series with a 0nM enzyme condition serving as the eighth condition, such that addition of reaction components is easily accomplished by multi-channel micropipette. Exact setup may be modified as required.

3. Thaw aliquot of topo VI enzyme on ice. Serially dilute with topo VI dilution buffer in 5-fold steps to achieve to 200nM tetramer* (need ~35 µL for single titration or timecourse assay), and add the 200nM enzyme stock to the empty well of the topo VI dilution series row in your mixing plate. Serially dilute 200nM tetramer stock in two-fold steps (i.e., pipette 10 µL of 200nM stock into 10 µL topo VI dilution buffer setup in step 2, mix, then pipette 10 µL of 100 nM stock generated into the next well, and so forth) for 6 steps. This will yield a 10x enzyme dilution series of 0 nM, 3.1 nM-200 nM enzyme. Make sure all volumes pipetted in this dilution scheme are ≥ 3µL to minimize inaccuracy. **Note**, especially when I am diluting from a highly concentrated stock, I try to check protein concentration by nanodrop once I've diluted to ~≤ 4 µM, using and extinction coefficient of 188010 A_{280}/cm/M.
**I find that titrating in two-fold steps from 200 nM to 3.1 nM (20nM to 0.31nM final reaction) gives a good range for assessing enzyme activity. This range and the number of experiments may be modified as required.*

4. Using a multichannel pipette, add 3 µL of protein dilution series from 96 well mixing plate to the 15 µL of 2x assay buffer added 8-tube strip PCR tubes in step 2. Incubate on ice for 5 min.

Make sure to set up an additional 0 mM ATP negative control reaction at the highest protein concentration.

5. Using a multichannel pipette, add 9 µL H_2O from mixing plate to 8-tube strip PCR tubes.

6. To initiate the reaction, add 3 µL 10mM ATP to 8-tube strip PCR tubes and incubate at 30°C* for 30 minutes. This may be done using the **Incubate** mode on a thermocycler machine. Final reaction condition is:
[30µL reactions, 0,0.3-20nM topo VI for titration, 2.5nM topo VI for time-courses, 50mM potassium glutamate, 10% (v/v) glycerol 20mM bis-tris-propane-HCl (BTP-HCl) pH 7.5, 2mM HEPES pH 7.5, 1mM TCEP, 10mM $MgCl_2$, 0.1mg/mL BSA, 3.5nM pSG483/10.2 µM bp DNA, and 1mM ATP].

**The optimal growth temperature for M. mazei is 30°C, however I have found the enzyme active from room temperature (25°C), to 42°C.*
Note,

7. Quench the reaction by adding 3µL stop buffer(10%SDS, 100 mM EDTA).

8. Add 3 µL of 10x Loading buffer [50% (v/v) glycerol, 0.2 M EDTA, 0.2% (w/v) bromphenol blue, 0.2% (w/v) xylene cyanol].

9. Run reactions on a 1% Tris-Acetate-EDTA (TAE) agarose gel at 35V (2-2.5 V/cm) for 15 hours. The quality of topoisomer bands will improve if gel electrophoresis is run in a more highly buffered TAE buffer. See Appendix 8 from SM Vos's dissertation for a more detailed protocol. In brief, set the gel in:

<u>Fresh TAE composition (1x):</u>
50mM Tris-HCl pH 7.9
40mM Sodium acetate
1mM EDTA pH 8.0

Run the gel in a TAE buffer created from a 1:1 mix of the Fresh TAE above, and the lab's traditional 1x TAE stock:

40mM Tris base
20mM glacial acetic acid
1mM EDTA pH 8.0

10. Following gel electrophoresis, place gel in plastic staining container. Submerge in running buffer (100 mL) and add Ethidium bromide to 0.5µg/mL. Stain gel on an orbital shaker for 30 min.

11. Remove staining buffer and submerge in ethidium bromide free running buffer (100 mL). Destain on an orbital shaker for 30 min.

12. Image under UV transilumination to visual DNA bands.

In general, wildtype topo VI will completely relax DNA substrate at 1.25-2.5 nM following this protocol.

To perform a time-course, a few adjustments to this protocol are made. Instead of setting up a 96 well mixing plate and performing volume transfers by multi-channel pipette, set up a single 10-fold volume reaction (300 µL), and set up 3 µL of stop buffer in 8-tube strip PCR tubes. In general, time-courses run at a final concentration of 2.5 nM topo VI with 3.5 nM plasmid will give best results, but use activity from a titration series as a guide. Dilute topo VI to a 25 nM stock and then add 30 µL of this stock to 150 µL of 2x assay buffer. Incubate for 5 min on ice as with the titration assay. Dilute with 90 µL H_2O, and start by mixing with 30 µL of 10 mM ATP. A second plasmid may be added at this point if performing a chase experiment. As with the titration, incubate at 30°C. Take time-points by transferring 30 µL of full reaction to 8-tube strip PCR tubes. For 2.5 nM topo VI, time-points at 0, 1, 2, 4, 6, 8, 10, 15, 20 and 30 min should adequately follow reaction progression. Modify as required.

Appendix 5: Designing fluorescence anisotropy based competition binding experiments using a probe of known affinity

Designing a fluorescence anisotropy based competition assay requires three practical considerations:
1) What substrate (i.e. labeled duplex DNA) should be used as a labeled probe?
2) What concentration of receptor (i.e. topoisomerase) should be used in the assay?
3) Over what range of competitor concentration should the competition assay be run?
4) Will a labeled probe substrate distinguish differences in affinity of different competitors?

Note that for anisotropy, the concentration of the labeled probe will not be able to vary outside 5-20 nM, so titration range of the competitors, concentration of receptor, and identify of the labeled probe (i.e. a ligand that binds more or less tightly to the receptor) are the main variables to alter.

Calculating theoretical competition curves using the explicit competitive binding model derived by Wang (Wang 1995), can help answer these questions (**Figure A5.1a-b**). Note that competitors with a $K_{d,app}$ more than 10-fold tighter than the probe ligand will be difficult to discriminate between. Decreasing receptor concentration may help (**Figure A5.1b**), but this decreases the overall ΔFA signal of the assay. To generate theoretical binding curves in numerical manipulation software, use this system of equations:

Using the parameters [A], total concentration of the competitor ligand; [B], total concentration of the labeled probe ligand; [P] total receptor concentration; K_A dissociation constant of the competitor ligand, and K_B, dissociation constant of the labeled probe ligand, and define:

$$a = K_A + K_B + [A] + [B] - [P]$$

$$b = K_B([A] - [P]) + K_A([B] - [P]) + K_B K_A$$

$$c = -K_A K_B [P]$$

Use these definitions of *a, b* and *c* to define:

$$\theta = \cos^{-1} \frac{-2a^3 + 9ab - 27c}{2\sqrt{(a^2 - 3b)^3}}$$

Fraction of labeled probe bound to the receptor is then:

$$y = \frac{2\sqrt{(a^2 - 3b)}\cos\frac{\theta}{3} - a}{3K_B + 2\sqrt{(a^2 - 3b)}(cos\frac{\theta}{3}) - a}$$

If a binding isotherm for the labeled probe has been determined, K_B and [B] may be defined. Multiplying *y* by the ΔFA_{max} for the labeled probe will then yield theoretical ΔFA values.

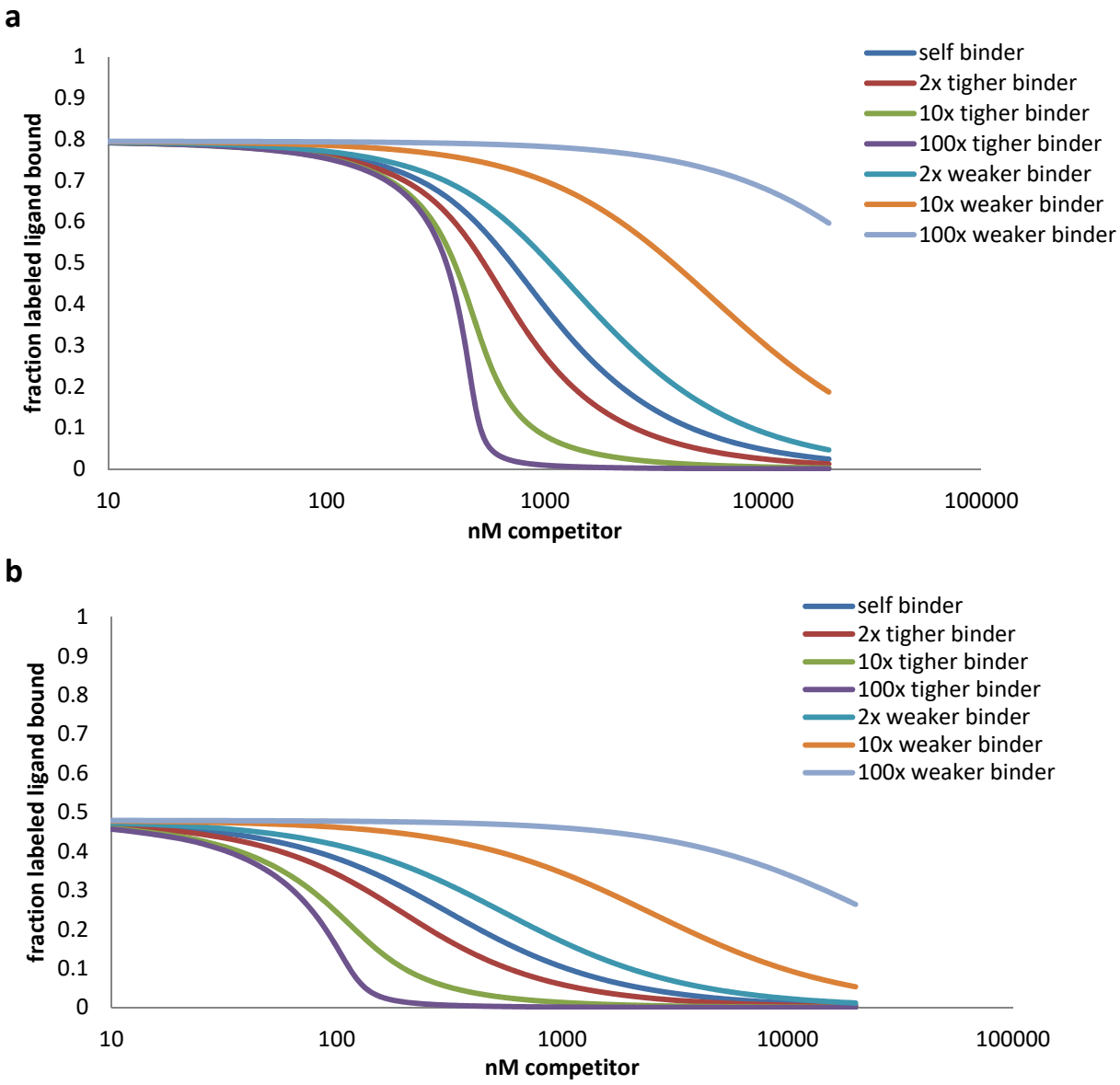

Figure A5.1. Theoretical curves for competitors with different relative affinities to a labeled probe.

a. Theoretical model of the fraction of labeled probe bound to a receptor as a function of competitor concentration for competitors with 0.01x, 0.1x, 0.5x, 1x, 2x, 10x and 100x the affinity of the probe. Protein concentration is 480 nM, 4-fold above the K_d of the probe ligand. **b**. The same exercise as in a, except protein concentration has been reduced to 120 nM, the 1x Kd of the probe ligand.

Appendix 6: *M mazei* topo VI NADH Coupled ATP hydrolysis assays

This appendix is a step-by-step guide for following the ATPase activity of *M. mazei* topo VI by an NADH coupled assay.

Materials

150mM phosphoenolpyruvate (Make PEP from dry stock, pH to 7.5, flash freeze and store at -80°C)
600-1000U/mL PK, 900-1400U/mL LDH Sigma enzyme mix (P0294). "100% stock" Can also make from lyophilized powders in buffered 50% glycerol. Store at -20°C
35mM NADH (pH to 7.5, flash freeze and store at -80°C)
10mg/mL BSA
1M Bis-tris-propane-HCl (BTP) pH 7.5
1M $MgCl_2$
50% (v/v) glycerol
2M potassium glutamate
1M TCEP pH 7.0
100 mM ATP
MilliQ H_2O
Topo VI holoenzyme (needs to be at 3.75 µM or greater)
DNA substrate (usually sheared salmon sperm for linear DNA or maxiprep plasmid DNA for supercoiled substrate. Need to be at 1950 ng/µL (3000 µM basepairs) or greater)
Eppendorf tubes (1.5, 2 or 5 mL depending upon number of reactions to run)
96-well clear, flat bottom, half area polystyrene plates (Corning Inc)
Clairiostar microplate reader (BMG Labtech GmbH)
96 well "U" bottom plate (vinyl) for mixing
Nanodrop spectrophotometer
8-12 channel 20µL multi-channel pipette
Prism (Graphpad)

Protocol

1. Make sure to set the incubator on the Clariostar plate reader to 30°C. This needs to be done ~5-10 mins before the reactions are ready to be initiated (in step 7). Also setup a collection program to read the A_{340} of wells containing your reactions and the frequency (in the range of 20-30 s) of and number of reads (240-360 reads, ~2 hour assay).

2. Set up an NADH/PEP/PK-LDH coupled assay mix on ice. I usually add all components except the LDH and NADH. Once I am close to mixing the coupled assay mix with the topo VI/DNA mix, I will add PK-LDH. Follow this, I reserve at least 165 µL of coupled mix for forming an NADH dilution standards, and then add NADH. The mix is:

[*7.5 mM PEP, *8% (v/v) PK/LDH stock, 0.2 mg/mL BSA, 60 mM BTP pH 7.5, 6 mM TCEP, 20 mM $MgCl_2$, 2% glycerol 20 mM potassium glutamate, 300 µM NADH]

**This the one of two concentration regimes for PEP and PK-LDH used in the lab. The other lab protocol uses a much lower set of concentrations, i.e. 4 mM PEP and 0.8% (v/v) PK-LDH stock. While both regimes work for topo VI, the higher concentration regime was used during initial troubleshooting, and is therefore the regime used in Chapter 3 to maintain similar assay conditions across all experiments. Nevertheless, for new experiments the lower concentration regime might be preferable, due to greater economy of stock components.*

Scale volume so there is 55 µL of this stock for each reaction to be run. Make sure to include enough volume for at least four NADH standards reactions. For these standards, set up a 4-well row on the mixing plate, with three of the four wells containing 55 µL of the reserved NADH-free coupling assay mix. Add 110 µL of the coupling mix+ NADH to the fourth well, then serially dilute in two-fold steps for two steps to make a series of standards from 300 µM NADH to 75 µM NADH, plus a 0 µM NADH standard.

3. If running a DNA titration, set up ATP stocks in a 10-well row in a 96 well "U" bottom mixing plate. Dilute ATP to 20 mM and add 15 µL per titration series to be run to each well. For ATP titrations, set up an 8-well row on the mixing plate and use H_2O to dilute ATP in two-fold steps starting at 40 mM and going to 0.62 mM (6 steps) plus a 0 mM ATP control. Make sure well volumes include at least 15 µL per titration series run.

4. Set up the enzyme/DNA mix on ice using a topo VI dilution buffer.

a) For DNA titrations, set up a dilution series in the mixing plate using H_2O that goes in two-fold steps starting at 1950 ng/µL (3000 µM basepairs) and going to 7.6 ng/µL (11.7 µM basepairs) (8 steps), plus a 0ng/µL DNA reaction. This sets up a 3.75x DNA titration series. Each stock in the dilution series requires ~40 µL/reaction.

For ATP titration reactions, make up a stock of DNA at 3.75x the desired assay concentration, and make sure the stock is scaled to ~40 µL/reaction.

**If checking DNA concentrations using the nanodrop, all concentrations above an A260 of ~8.0 (400 ng/µL) will be out of the linear range of the instrument and therefore inaccurate. Stocks will need to be diluted into this range for accurate measurements*

b) Using a topo VI dilution buffer:

[50 mM BTP-HCl pH 7.5, 5 mM TCEP, 10% (v/v) glycerol, 300 mM potassium glutamate]

Dilute topo VI to 3.75 µM in two-fold steps. Check concentration using the nanodrop and an extinction coefficient of 188010 A_{280}/cm/M. Make sure to blank using the

dilution buffer absorbance spectrum, as the dilution buffer has a small but significant absorbance at 280 nm. Scale topo VI stock to ~20 µL/reaction.

c) Aliquot 16 µL of 3.75 µM topo VI into a 10-well row on the mixing plate. Using a multichannel pipette, add 32 µL of 3.75x DNA titration series or stock to aliquoted topo VI. For reactions without DNA, add 32 µL H_2O at this point. Incubate on ice for 5 min.

5. For each ATPase reaction, add 50 µL of coupling assay mix to the 96-well clear, flat bottom, half area polystyrene plate. Using a multichannel pipette, add 40 µL of the topo VI/DNA mixes.

For NADH standards reactions, first dilute protein topo VI dilution buffer threefold with H_2O, then add 40 µL of the diluted buffer to the 96-well clear, flat bottom, half area polystyrene plate. Using a multichannel pipette, add 50 µL of the 4-well NADH standards series (300-75 µM NADH, 0 µM NADH) made in step 1.

6. Spin plate 2min at 1000 rpm in Sorvall Legend RT Tabletop Centrifuge using the microplate rotor adaptor.

7. Place plate in Clariostar plate reader, and allowing reactions to warm to 30°C (2-3 minutes). Start reaction by adding 10uL ATP stocks from step 3 using a multichannel pipette to initiate the reaction. Use the plunger to mix, but do not dispense to the second stop, otherwise bubbles will be introduced. Final reactions will be 100 µL* with the following conditions: [3.75mM PEP, 150uM NADH, 4% PK/LDH, 0.1mg/mL BSA, 50mM BTP pH 7.5, 50mM potassium glutamate, 5mM TCEP, 10 mM $MgCl_2$, 5% glycerol, 0.5uM Topo VI, Variable concentrations of DNA (800 µM to 3.1 µM bp in two fold steps and 0 µM in the example given here), Variable concentrations ATP(2 mM for DNA titrations, 4 mM to 0.062 mM and 0 mM for ATP titrations in the example given)]

**While lab protocols vary, I find 100 µL reactions yield smoother baselines, less background and require lower overall concentrations of enzyme and DNA. Because increasing volume increases path length, the same concentration of enzyme will generate double the signal in a 100 µL reaction vs. a 50 µL reaction. This is useful for slow ATPases, and for reaching large DNA:enzyme ratios when stock DNA concentration becomes limiting.*

8. Follow reactions by reading absorbance at 340 nm every 25s for 120 min.

9. Following the experiment, measure 340nm absorbance of NADH standards (300-75 µM NADH, 0 µM NADH) via nanodrop using $\varepsilon = 6220A_{340}/M/cm$ to calibrate absorbance readings in plate to actual NADH concentration.

10. Use NADH calibration to convert A_{340} curves into µM NADH. Use the slope of a linear regression fitting to NADH depletion to extrapolate reaction velocities for ATP consumption.

**Sometimes the initial region of the curve does not fit the linear relation of the rest of the curve and needs to be truncated. If all NADH is depleted over the course of the reaction (the consumption curve will look like a hockey stick), truncate this region as well.*

11. Apply any unit conversions desired (i.e. convert from velocity (μM ATP/min) to turnover number (ATP/enzyme/min), and then use Prism (or another non-linear regression software) to fit data to a kinetic model (i.e. Michalis-Menten kinetics).

Appendix 7: Performing and processing bulk FRET spectroscopy data

This appendix provides a step-by-step guide for performing and analyzing data from FRET-based topo VI gate assays using a fluorimeter.

Materials

500 µM bp DNA substrate (usually sheared salmon sperm for linear DNA or maxiprep plasmid DNA for supercoiled substrate, but also short DNAs or stacked junction substrates)
MilliQ H_2O
1.5mL Eppendorf tubes
96 well "U" bottom plate (vinyl) for mixing
Aluminum foil
2M Potassium glutamate
1M HEPES-KOH pH 7.5
1mg/mL BSA
1M TCEP pH 7.0
1M $MgCl_2$.
50% (v/v) glycerol
1 mg/mL BSA
Topo VI labeled on $Top6B^{T155C}$ with Alexa555 and Alexa 647
10mM AMPPNP
Fluoromax Fluorometer 4 (HORIBA Jobin Yvon)
12µL quartz cuvette (16.12F-Q-1.5/Z20, Starna)

Protocol

1. Prepare topo VI dilution buffer [250mM potassium glutamate, 10% (v/v) glycerol and 20mM HEPES-KOH pH 7.5], and 2.5x assay buffer [40 mM HEPES-KOH pH 7.5, 20% v/v glycerol, 25 mM $MgCl_2$, 0.25 mg/mL BSA, 2.5 mM TCEP]. Keep on ice.

2. When working with fluorescently labeled topo VI, always cover tubes with aluminum foil to protect from light. Thaw aliquot of fluorescently labeled topo VI and dilute to 1 µM in dilution buffer using 2-fold dilution steps.

3. To 8µL of 1 µM topo VI, add either 8µL of 500uM bp DNA substrate or H_2O and incubate on ice for 5min.

4. Add 16 µL of 2.5x assay buffer, then additionally dilute with 8µL H_2O. Keep on ice. Final reaction conditions are:
[200 nM topo VI, 0 or 100 µM bp DNA, 50mM potassium glutamate, 1mM TCEP, 10% (v/v) glycerol, 20mM HEPES-KOH pH 7.5, 10mM $MgCl_2$ and 0.1mg/mL BSA].

5) To use the Fluoromax, turn the instrument on, and launch the FluorEssence v3.5 software. Click **Experiment Menu**. The FluorEssence software should find all devices except for the Micromax. Choose to emulate and click **Next**. An experiment menu will come up, click **Spectra**,

then **Emission**. An experiment method may either be loaded, or defined by the user. For FRET experiments using a Cy3/Cy5 or Alexa555/Alexa647 pair, set the Excitation 1 to 530 nm, and set the emission range to 545 to 700 nm in the **monochromator tab**. In the **Detectors tab** integration time may be set. Increasing integration time decreases noise in the spectra at the expense of speed of collection. There are four spectra that the fluoromax will collect, **S1**, **S1c**, **S1/R1** and **S1c/R1c**. **S1** is the raw detector signal. **S1c** is the detector signal corrected for changes in the detector sensitivity as a function of emission wavelength. **S1/R1** and **S1c/R1c** scale each signal to a reference signal on the detector. For processing spectra, **S1c/R1c** should be used.

6) Use the 12 µL quartz cuvette to measure spectra. Fill with 16-18 µL of sample. Before testing samples, collect the spectra of an H_2O blank. In general, multiple rinses with MilliQ H_2O, followed by 100% ethanol and drying with the bench-top airline should be sufficient to clean the cuvette. If there is a significant background from the previous user, clean with nitric acid followed by thorough rinsing with water and ethanol. As a gauge of whether background is significant, peak S1c signals will be on the order of 10^6, S1c/R1c on the order of 10^5.

7) Measure multiple samples using **previous experiment setup**, cleaning the cuvette between samples. Alternatively spectra of the same sample may be measured over time.

Processing

Spectra from different samples usually show some variability in overall raw S1c/R1c emission intensities unrelated to anti-correlative donor peak quenching and acceptor peak sensitizing, and need to be normalized to directly compare spectra. Because top6B^{cyslite,T155C} labeling with Alexa555 and Alexa 647 produces a mixed population of donor-donor, donor-acceptor, acceptor-acceptor, singly labeled donor, and singly labeled acceptor enzyme, the best method for normalizing spectra to compare between samples is by excitation wavelength absorption. However, the Fluoromax does not measure absorption, so normalizing spectra by total spectral emission may serve as a proxy for absorption.

To perform this normalization, divide emission intensity at each measured wavelength by the sum of emission intensity at all emission wavelengths, i.e.

$$normalized\ emission(x) = I(x) \Big/ \sum_{x=545}^{700} I(x)$$

Where ***x*** is the emission wavelength, **I(x)** is the S1c/R1c emission intensity at x, and the summation bounds correspond to the range of the collected spectra. Note the units are arbitrary, and it may be appropriate to multiply the normalized emission by the range of the spectra.

Note, this method works well for the topo VI (and topo II) gate closure assays where the labeled enzyme sample remains constant across all conditions tested and for which a donor-only or acceptor-only controls would be non-trivial to produce. In experimental setups where the labeled biomolecule concentration is changes, or where donor-only and acceptor-only specimens would be trivial to make, the experimenter should reassess whether normalizing by donor only, acceptor only, or donor or acceptor specific excitation or emission spectra are more appropriate.

Ratiometirc FRET efficiencies (E) may be determined from donor (I_D) and acceptor (I_A) peak intensities:

$$E = \frac{I_A}{I_D + I_A}$$

Again, because labeled topo VI contains multiple different sub-populations, the FRET efficiencies determined in bulk cannot be directly related to distances, but due serve as readouts for conformational changes.

Appendix 8: Modeling curved DNA duplexes *in silico* using 3DNA

This appendix explains how to generate .pdb coordinate files of curved DNA duplexes using the w3DNA web server. This server builds DNAs based on local base-pair and base-step parameters, which requires these parameters for each base-pair in the DNA you wish to model. While there may certainly be more elegant ways to generate these models, once a parameter file template is set up this is a quick way to generate DNAs with varying bend angles.

I found this method to be the most straightforward way to generate curved DNA models for testing hypotheses pertaining G-segment bending by topo VI.

Setup

1) Generate a parameter file for the DNA sequence you wish to model. Even if you do not have specific sequence of interest or are using a random sequence, this will create a template with canonical basepair values. On the 3DNA web server (http://w3dna.rutgers.edu/) click **reconstruction**, then **Fiber model**, and **choose a fiber** of interest (i.e. B-DNA (generic)) from the drop down menu, then click continue. **Enter a sequence** of interest. Click **Build**. The page will then allow you to download a rebuilt pdb file.

2) Rename the generated .pdb file, then return to the 3DNA web server, but this time click **analysis**, then **Upload a PDB file**, and click **Analyze.** From the analysis page, either **download** the **Base pair and base-pair step parameter file**, or click **view** and copy and paste the text from the new window. This file will be in the form:

61 # base-pairs
*0 # ***local base-pair & step parameters****

#	Shear	Stretch	Stagger	Buckle	Prop-Tw	Opening	Shift	Slide	Rise	Tilt	Roll	Twist
T-A	-0.03	-0.10	0.09	0.04	-15.13	-1.88	0.00	0.00	0.00	0.00	0.00	0.00
T-A	-0.03	-0.10	0.09	0.04	-15.13	-1.88	0.01	0.45	3.36	-2.72	-0.43	35.97

…
…

A table formatted form of this file may also be opened from the links under the **Parameter** Tables heading and will be useful for modifying parameters in a spreadsheet program like Excel.

Note, the first six parameters are for the base pair, the second six parameters are base step. 3DNA will build whatever user specifies, with phosphate geometry defined by A-form, B-form, etc. For a continuously bent DNA, shear, stretch, stagger, buckle, propeller-twist, and opening are given canonical values for A-T or G-C pair. For step parameters, shift, slide, and rise are given canonical parameters**.**

3) Modify both **tilt and roll** parameters to generate a continuous bend. Since the step pair changes angular position relative to the helical axis, these two parameters are correlated and

vary as function of base-pair position in a sinusoidal fashion. The parameters for introducing a continuous curve can be generated in Excel or any similar program using:

$$Tilt = A \sin \frac{2\pi(bp)}{10.5\ bp/turn}$$

And

$$Roll = A \sin(\frac{\pi}{2} + \frac{2\pi(bp)}{10.5\ bp/turn})$$

Where ***bp*** is the step of the base-pair in question (i.e. for the third base-pair in a duplex sequence, bp=3), **10.5 *bp/turn*** scales for the helical periodicity of B-DNA, and ***A*** is a scaling factor for the degree of bending and should be the same for both parameters. As the parameter files give Tilt and Roll in terms of degrees, **A** approximates the bending angle/basepair.

4) To increase severity of bend, just increase the value of **A** in each function. Frequency should remain the same regardless of bend angle. These new values can be pasted into the **Base pair and base-pair step parameter file,** which should be saved as a plain text or [your name here].par file. Make sure to keep the text formatting of the file and make sure there are no empty lines before the header. Otherwise, the w3DNA web server will reject the file, giving no explanation.

5) By introducing a continuous bend, the DNA segment will now twist out of plane. To prevent this, decrease the ***Twist*** value for each base-pair step by a few degrees. How much this value needs to be decreased will depend upon the magnitude of bending.

6) On the web server, click **reconstruction**, then **customized model**, and choose **customized base pair step/nucleotide parameters** in the drop down menu, then click continue.

On **Please specify modeling information** you can choose between A-form, B-form or RNA backbone, and then upload the parameters text file and click **Build**. The webserver will then generate a PDB of the bent DNA. Modify parameters if the bend and twist of the DNA do not generate a satisfactory model.

Appendix 9: Improved Expression and Purification of catalytically active Sulfolobus shibatae topo VI holoenzyme

Previous expression protocols in the lab for *S. shibatae* topo VI have relied on using the *Ss* Top6A^{Y106F} mutation which results in a cleavage inactive mutant to overcome toxicity to host cells when expressed. This appendix presents a protocol to express and purify wildtype topo VI which overcomes these toxicity issues.

In brief, use of the Rosetta2(DE3)pLysS expression strain and ZYM-5052 autoinduction media overcomes toxicity issues. An in depth protocol follows.

Materials

**note, for all solution stocks and buffers, 0.22 µm sterile filtering is assumed unless otherwise noted.*

S. shibatae Top6A/Top6B expression vector (KD Corbett Freezer Stocks, box 1, B8)
Chemically competent **Rosetta2(DE3)pLysS** *E.coli* cells
Sterile 1.5mL Eppendorf tubes
Autoclaved 2xYT (yeast extract/tryptone) media
Innova 4080 Incubator/Shaker (New Brunswick Scientific)
Innova 44 Incubator/Shaker (New Brunswick Scientific)
LB plates with 34µg/mL chloramphenicol and 100 µg/mL carbenicillin
100 mg/mL ampicillin (1000x stock)
34 mg/mL chloramphenicol (1000x stock)
6x 2L baffled flasks (number depends upon scale of preparation)
6x 1L ZYM-5052 auto-induction media (see **appendix 2** for recipe)
Ultrospec 10 Cell density meter (Amersham Biosciences)
Disposable semi-micro UV cuvettes (BRAND GMBH+CO KG)
Avanti J-20 centrifuge (Beckman Coulter)
Avanti JL-8.1000 rotor and tubes (Beckman Coulter)
1M HEPES-KOH pH 7.5
5M NaCl
3M KCl
1M Imidazole pH 8.0
Glycerol
100 mM PMSF stock in 100% ethanol
1 mg/mL Leupeptin stock in H_2O
1 mg/mL Pepstatin A stock in 100% ethanol
Sonicator 3000 (Misonix, Inc)
RC5C centrifuge (Sorvall Instruments)
SS34 rotor and tubes (Sorvall Instruments)
2x Protein Loading Buffer
55°C or 65°C water bath
50 mL falcon tubes

5mL SP Hi-Trap columns (cation exchange, GE)
Sterile 5, 10, 25 and 50mL serological pipettes
Barnstead Milli-Q purified ddH_2O
20% (v/v) ethanol
Manifold pump tubing PVC 1.52mm ID, Yellow-Blue 16'' long (ThermoFisher Scientific)
Minipuls 3 Peristaltic pump (Gilson)
Akta FPLC/Akta Pure chromatography system (GE)
13 x100mm PP Test Tubes (ThermoFisher Scientific)
Amicon Ultra 30K MWCO Concentrator (Millipore)
Sorvall Legend RT Tabletop Centrifuge
BioRad protein assay dye reagent ("Bradford reagent")
MCT-200-NC-2.0 mL capless/clear homopolymer tubes (Axygen)
HiPrep 16/60 Sephacryl S-300 HR column (GE)
Precision Plus Protein Dual Color Standards (Biorad) or similar Protein MW standards
10% or 12% SDS-PAGE gels
1x Tris-Glycine running buffer
Nanodrop 1000 Spectrophotometer (Thermo Scientific)

Prepared media and buffers

Ss Topo VI Buffer A: high salt, resuspension buffer

10mL 1M HEPES pH 7.5	20mM HEPES pH 7.5
80mL 5M NaCl	800mM NaCl
100mL 50% (v/v) glycerol	10% (v/v) glycerol
1 mL 500 mM EDTA	1 mM EDTA
	To 500 mL

Ss Topo VI no salt dilution buffer:

10mL 1M HEPES pH 7.5	20mM HEPES pH 7.5
100 mL 50% (v/v) glycerol	10% (v/v) glycerol
	To 500 mL

Ss Topo VI Buffer B: Low salt buffer

10mL 1M HEPES pH 7.5	20mM HEPES pH 7.5
15mL 5M NaCl	150mM NaCl
100 mL 50% (v/v) glycerol	10% glycerol
	To 500 mL

Ss Topo VI Buffer C: Sizing column buffer

50 mL 3M KCl	300mM KCl
10 mL 1M HEPES pH 7.5	20mM HEPES pH 7.5
100mL 50% (v/v) glycerol	10% glycerol
	To 500 mL

Bring to volume using Milli-Q H_2O. Sterile filter all buffers. Do not add reducing agents or protease inhibitors until immediately prior to use. Volumes should be sufficient for one preparation of *Mm* topo VI from 4-6 L of cell culture.

Ss Topo VI Storage Buffer
80% glycerol, 300mM KCl, 20mM HEPES pH 7.5

Added to protein in *Ss Topo VI Buffer C* in a 0.4:1 ratio to yield a 30% glycerol, 300mM KCl, 20mM HEPES pH 7.5 final solution.

Step-by-step protocol
Expression
Day 1-4-Follow the step by step protocol from appendix 2 with the following alterations:

1) On day one, transform chemically competent **Rosetta2(DE3)pLysS *E. coli* cells** with **wildtype *S. shibatae* Top6A/Top6B expression vector**. Plate transformation onto LB plate containing **100 µg/mL carbenicillin** and 34 µg/mL chloramphenicol

2) On day 2, supplement starter culture with final concentrations of **100 µg/mL carbenicillin** and 34 µg/mL chloramphenicol.

3) On day 3, supplement ZYM-5052 media with **100 µg/mL carbenicillin** and 34 µg/mL chloramphenicol. Prepare *Ss Topo VI Buffer A.*

4) On day 4, substitute *Ss Topo VI Buffer A* for Mm Topo VI Buffer A when resuspending cultures.

Purification
Day 0-

Make sure Ss Topo VI Buffer A, no salt resuspension buffer, B,C, and C are prepared the day before starting a topo VI preparation and store buffers at 4°C. Do not add protease inhibitors at this time. Buffers may be made further in advance but run the risk of contamination if kept for long periods of time.

Prepare HiPrep 16/60 Sephacryl S-300 HR column on FPLC/Akta Pure/Akta Prime by equilibrating column with 1.25 CV (150 mL) of *Mm Topo VI Buffer C* at 0.5mL/min.

Day 1-

1) Place 50mL falcon tubes of frozen cells in beaker of room temperature H_2O. Once cell pellets have thawed, transfer cell resuspension to 250 mL metal beaker on ice.

2) To Ss Topo VI Buffer A, add protease inhibitors to 1µg/mL pepstatin A, 1µg/mL leupeptin, 1mM PMSF. Keep buffer at 4°C or on ice.

3) Add ~50 mL of Ss Topo VI Buffer A +protease inhibitors, to resuspsended cells. Make sure resuspension is homogenous and not overly dense. Using the Sonicator 3000, submerge the sonicator macro-horn (do not use the microtip) in resuspended cells. Make sure the horn does not touch the edge of the beaker, and make sure the beaker is well nestled in ice in an ice bucket. Apply six 20 second pulses, with 2min pauses between each pulse, at power setting 5.5.

Following sonication, take a 10 µL sample of lysate and add to 10 µL of 2x SDS PAGE loading buffer in case it is needed for diagnostic SDS-PAGE.

4) Transfer lysate into ss34 tubes and clarify by centrifugation at 15krpm at 4°C for 20 min in using an ss34 rotor and Sorvall Instruments RC5C centrifuge.

Alternatively, the JLA-25.50 rotor and Avanti J-20 centrifuge may be used for this step. *Following clarification, take a 15 µL sample of clarified lysate supernatant and add to 15 µL of 2x SDS PAGE loading buffer in case it is needed for diagnostic SDS-PAGE*

5) To Ss Topo VI Buffer B add protease inhibitors to 1µg/mL pepstatin A, 1µg/mL leupeptin, 1mM PMSF. Prepare 5mL HiTrap-SP (cation exchange) column stored in 20% ethanol by first equilibrating with 5 column volumes(CV) (25 mL) of miliQ-H_2O, followed by 5 CV of Ss Topo VI Buffer B + protease inhibitors. This may be done using Manifold pump tubing PVC (Yellow-Blue, 1.52 mm inner diameter, 16 inches long) and peristaltic pump, using a flow rate of 2 mL/min (speed 10 on the Minipuls 3).
Alternatively, an FPLC/Akta Pure/Akta Prime may be used to equilibrate the column.

6) Transfer clarified lysate to 50 mL falcon tubes and incubate in the 55°C water bath for 15 minutes. Then, incubate lysate on ice for 10 min.

7) Transfer heat treated lysate into ss34 tubes and clarify by centrifugation at 15krpm at 4°C for 20 min in using an ss34 rotor and Sorvall Instruments RC5C centrifuge.

Alternatively, the JLA-25.50 rotor and Avanti J-20 centrifuge may be used for this step. *Following clarification, take a 15 µL sample of clarified heat-treated lysate supernatant and add to 15 µL of 2x SDS PAGE loading buffer in case it is needed for diagnostic SDS-PAGE*

8) Add heat treated lysate to a beaker (600 mL should be adequate) and stir with a magnetic stir bar. Slowly add *Ss Topo VI no salt dilution buffer* with 1µg/mL pepstatin A, 1µg/mL leupeptin, 1mM PMSF to lower salt concentration. This will require ~5 fold volume dilution.

9) Apply diluted heat treated lysate to the 5mL Hi-Trap SP-column equilibrated in Ss Topo VI Buffer B + protease inhibitors using peristaltic pump. A speed setting 10 (~ 2ml/min) is adequate. Collect and flow through.

Alternatively, clarified lysate may be applied to SP column using a FPLC/Akta Pure and a super-loop.

Take a 15 µL sample of lysate flow-through and add to 15 µL of 2x SDS PAGE loading buffer in case it is needed for diagnostic SDS-PAGE.

10) Wash SP column containing bound protein with ~100 mL Ss Topo VI Buffer B +protease inhibitors.

11) On an Akta FPLC/Akta Pure, wash Pump A with Ss Topo VI Buffer B + protease inhibitors and Pump B with Ss Topo VI Buffer A + protease inhibitors. Make sure the flow path of the system is in buffer B, and the free column position (position 5 on the Akta Pure and valve 7 position 2 on the Akta FPLCs for instance) are inline of the system flowpath. Setup fraction collector to collect 5mL fractions in 12x 100 mm PP Test tubes.

12) Following sample application and washing, place SP column inline of the flow path on FPLC/Akta Pure. Applying flow of *Ss Topo VI Buffer B* at 2 mL/min, wash column until A_{280} baseline stabilizes, and then elute bound protein by applying a 20 CV (100 mL) gradient from 100% *Ss Topo VI Buffer B* to 100% *Mm Topo VI Buffer* A. *Ss* topo VI tetramer will elute at ~2-9 CV (10 ml to 45mL). Pool peak fractions.

Take 15 µL samples from each peak fraction and add to 15 µL of 2x SDS PAGE loading buffer. Run all fractions on a diagnostic SDS-PAGE (I find 10% or 12% SDS PAGE works well) with MW standards (I prefer Biorad Precision Plus Protein Dual Color Standards). Both SDS-PAGE gels and 1x Tris-Glycine running buffer are currently common lab stocks.

If the preparation is not progressing as expected, now is a good time to run a SDS-PAGE gel of all other collected samples from day 1 to determine where and how topo VI heterotetramer was lost.

13) Concentrate pooled elution fractions from the Hi-Trap SP elution gradient by centrifugation at 4000 rpm in a Sorvall Legend RT tabletop centrifuge using an Amicon Ultra 30K MWCO concentrator to ~2mL.

This will take a long time. This part of the preparation may require further optimization.

14) Prepare HiPrep 16/60 Sephacryl S-300 HR column on FPLC/Akta Pure/Akta Prime by equilibrating column with 1.25 CV (150 mL) of *Mm Topo VI Buffer D* at 0.5mL/min.

*For this protocol, the sizing column step (step 15) is usually started at the end of day 1, run overnight, and sample processing happens on day 2.

15) Setup fraction collector to collect 2 mL fractions in 2.0 mL capless/clear tubes, and use the 2 mL sample loop to apply concentrated topo VI sample to HiPrep 16/60 Sephacryl S-300 HR equilibrated and run in *Mm Topo VI Buffer C* at a flow of 0.5mL/min. A void peak elutes at ~0.32-0.37 CV (38-44mL) and the topo VI heterotetramer elutes at 0.42-0.58 CV (50 mL-70 mL).

Take a 15 µL samples from each peak fraction and add to 15 µL of 2x SDS PAGE loading buffer. Run all fractions on a diagnostic SDS-PAGE (I find 10% or 12% SDS PAGE works well) with MW standards (I prefer Biorad Precision Plus Protein Dual Color Standards). Both SDS-PAGE gels and 1x Tris-Glycine running buffer are currently common lab stocks.

Ss Top6B should run around 60 KDa, Ss Top6A should run around 45 kDa. Sometimes the later eluting fractions contain degradation products running slightly faster than Top6B. As long as fractions from the s300 size exclusion chromatography run look as expected, I tend not to run the other diagnostic samples from the preparation.

Day 2-

1) Based on SDS-PAGE, pool concentrate peak fractions of topo VI heterotetramer by centrifugation at 4000 rpm in a Sorvall Legend RT tabletop centrifuge using an Amicon Ultra 10K MWCO concentrator to <500 µL.

2) Add 0.4x volume of *Ss topo VI storage buffer* to bring glycerol concentration to 30%. Measure protein concentration using the Edelhoch method (Edelhoch, 1967) by Nanodrop spectrophotometer. Use a *Ss* topo VI tetramer extinction coefficient of 216140 A_{280}/cm/M. Aliquot protein in ~10 µL volumes, flash freeze in liquid nitrogen and store at -80°C.

Note, it has been shown the extinction coefficients generated from the ExPASy ProtParam server (Gasteiger et al, 2005) may be applied to native proteins as well, showing errors within 4%.

3) Equilibrate HiTrap SP column with 5CV(25mL) of MilliQ H_2O and finish with 5CV (25mL) of 20% ethanol/0.2M sodium acetate. Columns may be stored at room temperature until next use.

Appendix 10: Optimized *S. shibatae* topo VI supercoil relaxation assay

This appendix provides a step-by-step guide for determining the specific activity of an *S. shibatae* topo VI enzyme preparation. Note, the reaction conditions have been optimized and are slightly modified from conditions published by other groups (Buhler *et al* 1998, Buhler *et al* 2001).

Materials

Supercoiled plasmid substrate resuspended in water (typically pSG483, 2927bps, typically in a ~500ng/µL stock from Maxiprep, 1ng/µL plasmid is 0.53 nM plasmid)
MilliQ H_2O
1.5mL Eppendorf tubes
96 well "U" bottom plate (vinyl) for mixing
8-tube strip PCR tubes
Metal tube racks/blocks
1M KCl
1M Tris-HCl pH 7.5
1M DTT
1M $MgCl_2$
50% (v/v) Glycerol
200mM ATP pH 7.0
Nanodrop (optional)
Mastercycler Gradient Thermocycler (Eppendorf) or equivalent thermocycler (optional)
0.5M EDTA pH 8.0
10% SDS
10X Glycerol DNA loading buffer
Invitrogen UltraPure agarose
8-12 channel 20µL multi-channel pipette
Ethidium Bromide
Plastic staining container (Rubbermaid or Tuperware)
UV trans-illuminator

Protocol

1. Prepare *Ss* Topo VI dilution buffer:
[300 mM KCl, 10% (v/v) glycerol, Tris-HCl pH 7.5 and 1mM TCEP, ~500µL for one titration or time-course series]

and *Ss* topo VI 2x assay buffer:
[20 mM $MgCl_2$, 36 mM Tris-HCl pH 7.5, 8% (v/v) glycerol, 40 mM KCl, 2 mM DTT, 2 mM Spermidine-HCl, 13.3 ng/µL or 20.4 µM plasmid DNA (this is 7 nM pSG483), ~175 µL for one titration or time-course series].

Buffers may be prepared in larger stocks beforehand and frozen.

**Note, I have tried a number of varied conditions from these buffers. To summarize: 1)Spermidine-HCl is absolutely necessary for robust activity in my hands, 1mM is sufficient. 2) Tris-HCl pH 7.5 (room temperature) is preferential to HEPES pH 7.5 or BTP pH 7.5. 3) 35mM monovalent salt shows greater activity than 50 mM monovalent salt, increasing concentration further decreases enzyme activity. 4) Activity with different monovalent salts shows the trend of KCl>potassium glutamate>potassium acetate. 3) Similar activity seen at 20 mM and 10 mM $MgCl_2$. Enzyme is inactive at 5 mM $MgCl_2$.*

2-5. Refer to steps 2-5 in **Appendix 4** for setting up a topo VI activity assay. The primary alteration is using *Ss* topo VI dilution buffer and *Ss* topo VI 2x assay buffer, which differ from the *M mazei* topo VI buffers.

6. To initiate the reaction, add 3 µL 10mM ATP to 8-tube strip PCR tubes and incubate at 65°C* for 30 minutes. This may be done using the **Incubate** mode on a thermocycler machine. Final reaction condition is:
[30µL reactions, 0,0.3-20nM *Ss* topo VI for titration, 50mM KCl, 5% (v/v) glycerol, 20 mM Tris-HCl pH 7.5, 1mM DTT, 10mM $MgCl_2$, 1 mM Spermidine-HCl, 3.5nM pSG483/10.2 uM bp DNA, and 1mM ATP].

**The optimal growth temperature for M. mazei is 80°C. I have tested the enzyme at 75°C, 65°C and 55°C and found 65°C to be optimal.*

7-12. Refer to steps 7-12 in **Appendix 4.**

Appendix 11: Production and purification of biotinylated closed circle DNAs

This appendix describes a protocol for adding a biotin handle to closed circular DNA using a single strand nicking and ligation reaction adapted *Luzzietti N et al, NAR, 2011. V39:No3 e15.* The resulting topologically constrained DNA can then be immobilized on neutravidin functionalized surfaces for pulldown or single molecule experiments.

This protocol will be particularly useful for single molecule studies using the FRET-pair labeled *S. cerevisiae* topo II and *M. mazei* topo VI constructs described in Chapter 3.

Materials

Nicking cassette oligomers (IDT, see protocol text for sequences and description)
DNA primers for inserting nicking cassette into a vector of interest (IDT)
Vector of interest
T4 DNA Polymerase (NEB)
E. coli cloning strain
T4 Polynucleotide Kinase (NEB, optional)
10x PNK Buffer (NEB, optional)
Biotinylated insert oligomer (IDT, see protocol for sequence)
Nt.BbvCI restriction enzyme (NEB)
10x CutSmart Buffer (NEB)
Thin-wall PCR tubes
Mastercycler Gradient Thermocycler (Eppendorf) or equivalent thermocycler
100 mM ATP stock
T4 ligase (NEB)
DNA gyrase
2x gyrase reaction and gyrase dilution buffer (see protocol for details)
1x TAE agarose gel
Streptavidin HP SpinTrap (GE), streptavidin beads, or fluorescently labeled streptavidin

Protocol

Cloning nicking cassette into substrate vector

Order oligomers with the sequence:

Top: 5’ **cctca gc***tcatgtca t***cctcagc***ac acttgac***cct cagc***tcagct ag***cctcagc***c tacaatca***cc* **tcagc** 3’

Bottom: 5’**gctga gg**tgattgta g**gctgagg**ct agctga**gctg agg**gtcaagt gt**gctgagg**a tgacatga**gc tgagg** 3’

Bolded portions of the sequence are the NtBbvCI sites for the top strand, and Nb.BbvCI sites for bottom. Nt.BbvCI cuts:

5’ CC^{V}TCAGC 3’
3’ GG AGTCG 5’

This cassette may be inserted into a substrate vector of choice, using a number of cloning methods. One-step SLIC is the preferred method due to flexibility, especially if the sequence position of the biotin handle relative to another feature on the vector (i.e. transcription promotor, origin of replication) is important for a downstream application.

In addition to DNA oligomers with the cassette sequence, SLIC cloning will require:

1) DNA primers to linearize vector at the site of insertion using inverse PCR

2) DNA primers with an additional ~25 bp of homology to the vector insertion site to amplify the nicking cassette by PCR

3) T4 DNA polymerase

4) Cloning strain of *E.coli* (i.e. XL1-Blues) for transformation.

See *Jeong et al, Appl. Environ. Microbiol. 2012 vol. 78 no. 15, 5440-5443* for a detailed protocol.

Note, make sure to check whether the destination vector contains native Nt.BbvCI recognition sites!

Insertion of biotinylated handle to closed circular DNA

Note that these steps have been optimized for a ~14kbps plasmid, which required longer reaction times were for many of the steps to reach completion. From experience, shorter reaction times will suffice for smaller plasmid substrates. In this protocol, recommended volumes assume an initial input of 100 µL of 100 ng/µL plasmid stock (~10µg scale).* ***Units of enzymes* *and* ***amount of modified oligomer need to be scaled to the actual molar amount of plasmid*** *in initial reaction. When changing the volume scale of the reaction, enzyme buffers will need to be scaled as well.* **Figure A11.1a** depicts an overview of the insertion protocol.

1) 5'phosphorylate modified oligomer. This can either be added to the oligomer as ordered or phosphorylated using T4 Polynucleotide Kinase following the recommended protocol by NEB.

The biotinylated oligomer has a sequence:

5' tcagctcatg tcatcctcag cacacttgac cctcagctca gc CTGGGAG TTGCCGA/iBiodT/ /iBiodT/ /iBiodT/ TCGGCAACTC CCAGtagcc tcagcctaca atcacc 3'

This sequence replaces the top strand from the nicking cassette (i.e. it anneals to the bottom strand following Nt.BbvCI nicking), and contains a stemloop hairpin in the middle of the modified oligomer with Biotin-dT on the loop itself. This sequence binds to streptavidin very rapidly in the context of a supercoiled plasmid, without excess streptavidin. **The capitalized portion of the sequence is the stemloop**.

2) Nicking reaction. Combine in a thin wall PCR tube:

a) 100 µL of ~100 ng/µL plasmid substrate containing the nicking cassette (may need to Maxiprep to reach this scale)

b) 10µL of 10x NEB Cutsmart Buffer

c) 10U Nt.BbvCI/1µg plasmid (13.5kbps) or 15U/1 pmol cleavage sites. This ~10x recommended by NEB.

Incubate at 37°C for 8 hrs or overnight in a heat block or thermocycler.

3) Heat inactivate Nt.BbvCI by incubating reaction at 20 min at 80°C. Save 200ng DNA for diagnostic sample. There is no good way to tell whether all nicking sites have been processed. In experience, 8hrs appears to be best compromise of maximizing reaction time while minimizing accumulation of linearized product.

3) Annealing reaction. Add phosphorylated modified oligomer from step 1 to heat inactivated nicking reaction. The modified oligomer should be in 12.5 molar excess to plasmid substrate. To determine moles of substrate plasmid, use:

$$picomoles\ plasmid = \frac{10^{12} pmol\ plasmid}{mol\ plasmid} \times \frac{1\ mol\ plasmid}{\boldsymbol{x}\ mol\ basepairs} \times \frac{1\ mol}{650\ g} \times \frac{10^{-12}\ g}{ng} \times \boldsymbol{y}\ ng\ DNA$$

Where **x** is the basepair size of the plasmid used and **y** is the mass in ng of plasmid added in step 2.

Incubate 5min at 80°C, and then cool at 0.5°C/min to 4°C. This may be done with a thermocyler program:

1) T=80.0°C		0:05:00
2) T=80.0°C		0:01:00
	-0.5°C	+00:00
3) GOTO	2	REP 99
4) T=30.5°C		0:01:00
	-0.5°C	+00:00
5) GOTO	4	REP 53
6) HOLD	4.0°C	

Save 200ng DNA for diagnostic sample.

4) Ligation reaction. To ~ 120 µL annealing reaction, add ATP to 2 mM (i.e. 2.4uL of 100 mM stock). Add ligase to ~1U/µg plasmid, or 2-5U/pmol plasmid. Incubate at 16°C overnight or to 24hrs. Heat inactivate T4 ligase at 65°C for 10min. Save 200ng DNA for diagnostic sample.

If desired product is closed circular relaxed DNA, go to step 6). If desired product is negatively supercoiled closed circular DNA, continue with step 5)

5)Supercoiling reaction. Based on Berger lab protocol, using large excess of E. coli gyrase purified in lab. Alternatively, Topogen sells an E. coli gyrase assay kit (http://www.topogen.com/topoisomerase-enzymes/e-coli-bacterial-dna-gyrase.html)

For in house method:

2x Gyrase reaction buffer	Gyrase dilution buffer
80mM KGlutamate	150mM KGlutamate
50mM Tris HCl pH 7.9	25mM Tris HCl pH 7.9
20% glycerol	10% glycerol
10mM $MgCl_2$	2.5mM $MgCl_2$
0.2mg/mL BSA	
1mM TCEP	

Combine GyrA and GyrB in equimolar amounts, incubate on ice 5 min. Then, dilute in 2x steps using dilution buffer to 400nM tetramer. To ~130 µL ligation reaction, add 40 µL of 400 nM *Ec* Gyrase tetramer to ligation reaction product, incubate on ice 5min. Then, add 200 µL 2x Gyrase buffer. Start reaction with 40 µL of 10mM ATP to start. Incubate 30 min at 37^{o}C. Use EDTA (to 10 mM final) or heat (80°C) to stop. Save 200ng DNA for diagnostic sample.

6) Run an EtBr-free diagnostic 1xTAE 1% agarose gel of preparation (**Figure A11.1b**). If purity of product is sufficient for purposes, use PCR clean up, Phenol/Chloroform-extraction/EtOH-precipitation or preferred clean up method. If nicked and linear product needs to be remove from preparation, this can be done using either a Prep-cell type method (Prieto *et al,.* (2000). Biotechniques. 29(6), 1204-6) or by electro-eluting out of agarose gel.

If lacking an electro-eluter or prep cell, purification of closed circular DNA can be performed on a normal agarose gel box:

a) Run a diagnostic lane of final biotinylated plasmid product and a preparative lane of the rest of the product on a 1% agarose TAE gel overnight (15hrs) at low voltage (~ 2.6V/cm) in an EtBr free gel box.

b) In the morning, cut out and stain preparative lane of gel with EtBr. Use this to identify the position of supercoiled or relaxed bands on preparative lane of the gel.

c) Cut a trough in the agarose below band of interest. Drain buffer level in box below the top of the agarose gel. Place buffer in the trough, and continue to run gel, taking a fractions every 5min by removing buffer in trough, and replacing with fresh buffer. Continue to run gel and collect fractions until band of interest has been collected.

Note, marking the position of the band of interest with loading buffer dye before starting fraction collection can help in determining when the DNA of interest elutes into the trough in the

gel. If purifying relaxed plasmid product in this fashion, it may be necessary to run the gel in chloroquine to separate closed circular DNA from open circular DNA.

Note, while a gel extraction and clean up kit method would be technically simpler than the method described above, the biotinylated DNA product loses a majority of binding affinity to streptavidin when purified in this way, likely from carryover of an impurity from melting agarose.

7) Assess biotin labeling. This can be done with multiple methods, including:

a) Streptavidin pull down using Streptavidin HP SpinTrap (GE) or streptavidin beads (**Figure A11.1c**), or

b) Incubating plasmid with fluorescently (i.e. cy3 or cy5) labeled streptavidin, and running the reaction on a 1x TAE 1% agarose gel (**Figure A11.1d**).

Potential issues and troubleshooting solutions:

a) Incomplete ligation may be due to incomplete phosphorylation of insert sequence.

b) Poor Streptavidin binding may be due to carry over of excess modified oligomer. Minimize oligomer:plasmid ratio in annealing reaction and use a size or charged based purification method. Contamination with excess modified oligomer can be easily visualized by incubating with ~3-10-fold molar excess of fluorophore labeled streptavidin, running out on agarose gel, and then imaging the fluorophore. Free streptavidin runs at ~7kbps as a diffuse spot as opposed to a band, and contaminating modified oligomer will run at ~1.5-2kbps as a diffuse spot as well.

As a final note, this method can be used to add other modification besides biotin to a closed circular DNA, or to add multiple insertions. Other topological manipulations (i.e. positive supercoiling) could also be introduced.

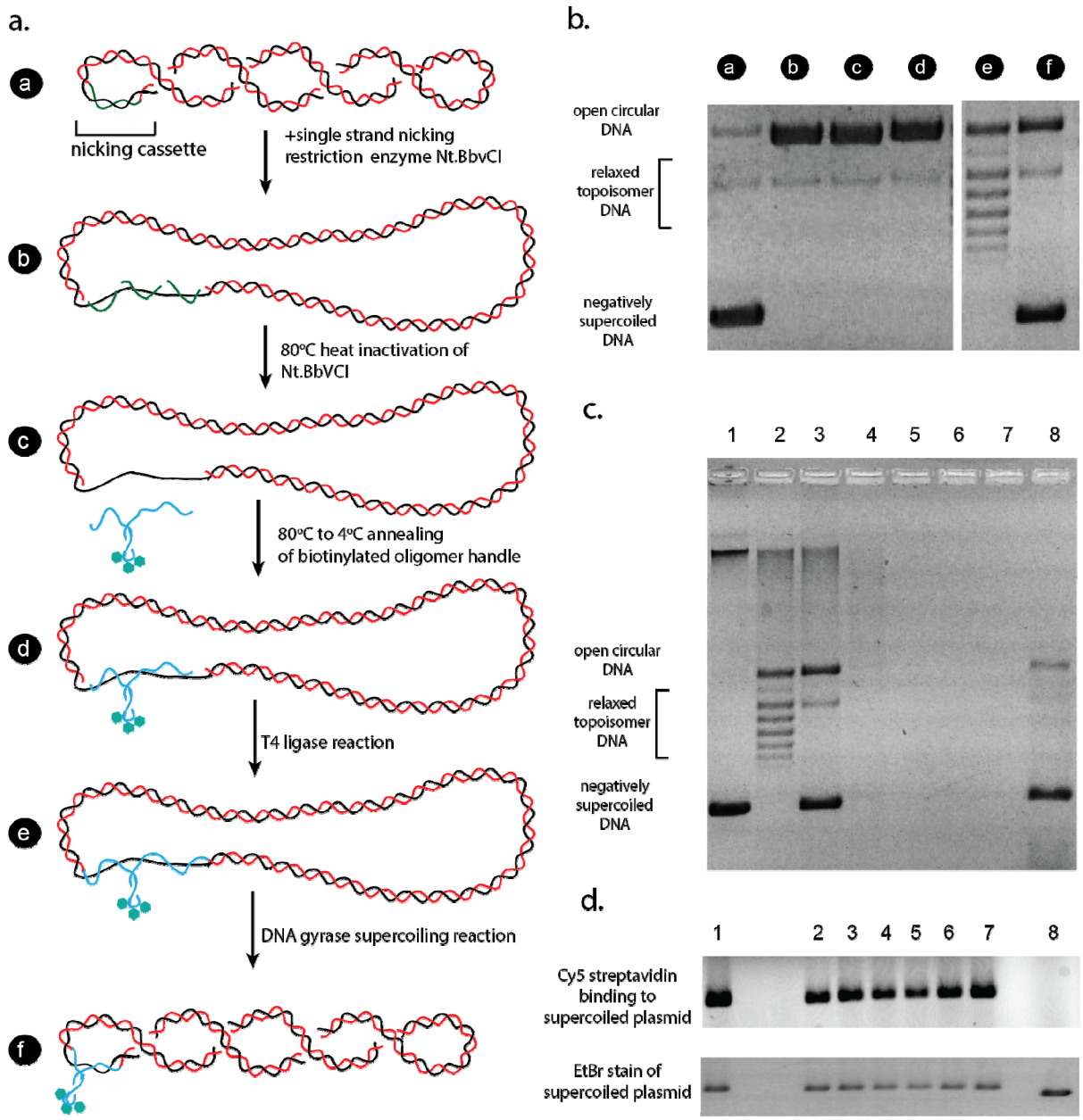

Figure A11.1. Production schematic and diagnostics for biotinylated closed circular DNA.

a. Cartoon scheme for generation of a closed circular DNA substrate with a biotin handle. The top strand of a cassette containing Nt.BbvCI restriction sites is colored in green, and an insert oligomer containing a stemloop modified with biotin is colored in cyan.

b. Diagnostic 1x TAE 1% agarose gel showing progression of the insertion preparation. Lanes a-f correspond to the steps labeled a-f in panel **a.**

c. Evaluation of plasmid biotinylation by a streptavidin pulldown experiment. Lanes correspond to 1)untreated plasmid, same as step (a) in panel **b**; 2)biotinylated plasmid following ligation, same as step (e) in panel **b**; 3)biotinylated plasmid following gyrase treatment, same as step (f)

in panel **b**; 4) Flow-through fraction for supercoiled biotinylated plasmid applied to a Streptavidin spin column (Streptavidin HP SpinTrap); 5-7)Wash 1-3 following application of biotinylated plasmid to a streptavidin spin column; 8)Elution of biotinylated plasmid from streptavidin spin column by boiling with an SDS elution buffer.

d. Evaluation of plasmid biotinylation by Cy5-streptavidin binding assay. Treated plasmids were incubated with a 25-fold molar excess of Cy5-streptavidin and run on a 1x TAE 1% agarose gel either without quenching(1); or were quenched with excess biotin after incubations of: 1 min (2); 30 min (3); 60 min (4); 120 min (5); 240 min (6); or 480 min (7). As a negative control, an **untreated** was incubated with 25-fold molar excess of Cy5-streptavidin and run on gel without quenching (8). The top panel shows a laser imager scan (Typhoon, GE) for cy5 streptavidin. The bottom panel shows an ethidium bromide stain of the same region.

Appendix 12: Production of PEGylated chambers for single molecule flow-based experiments

This appendix describes the preparation of polyethylene glycol (PEG) coated microscope chambers for single molecule based experiments:

Materials

1'' x 3'' x1mm slides (12-544-1, Fisherbrand)
24 mm x 40 mm-1.5 coverslips (12-544-C ThermoFisher Scientific)
Ultrasonic cleaner (Aquasonic 75HT, VWR Scientific)
Methanol
Alconox detergent
Ceramic slide and coverslip holders
0.030'' Diamond microtip drill bit (SMCDU30, UKAM Industrial Superhard Tools)
Dremel drill 3000
Dremel Drill Press
UKAM Industrial Tools Advanced Formula coolant solution
MilliQ H_2O
28% Ammonium hydroxide
30% hydrogen peroxide
Glacial acetic acid
Aminosilane
Biotin-PEG-SC-5000 (Laysan Bio)
MPEG-SC-5000 (Laysan Bio)
Fresh 0.1 M sodium bicarbonate, pH 8.5
Tabletop microcentrifuge
Micropipette tip boxes
Double-stick tape
FoodSaver Vacuum Sealer
Falcon tubes
FoodSaver 8'' rolls
N-333 - NanoPort Assembly Headless, 10-32 Coned, for 1/16" OD(IDEX).
F-247 - NanoTight™ Sleeve Green 1/16" OD x .033" ID x 1.6"
Syringe needle 7750-17 (Hamilton)
28 gauge Teflon tubing (Weico)
5-minute epoxy

Protocol

Day1-

Note, if recycling slides with inlet ports drilled in, perform step 1. To make new slides with inlet ports, perform step 2. Otherwise, start at step 3.

1. Place the slides in a ceramic holder, and place in a glass beaker. Holders take up to 12 slides. Add 2% alconox solution in water and sonicate the slides for 20 min or longer using an ultrasonic bath. Rinse the slides with a large quantity of tap water (2-4x rinses).

2. To make new slides with inlet ports, mark positions on glass slide and use a dremel to drill holes. **Make sure to wear safety glasses when doing this**.

a) Attach a 0.030'' diamond drill bit to the dremel tool, and screw the dremel into the drill press, making sure the dremel is secure.

b) Tape the glass slide on both sides to the base of the dill press, and lower the dremel to make sure it contacts the slide in the marked position.

c) Add ~50 µL of 1:50 dilution of UKAM coolant to the marked contact. Turn on the dremel at high speed, and slowly lower the dremel until the drill bit touches the glass surface. Do not push too hard or the glass may shatter and the diamond drill bit will dull quickly.

d) Add coolant as needed, and bring up dremel if either glass or drill bit start to heat up. Continue until glass is drilled through. **Working slowly, being patient, and adding a lot of coolant is key!**

3. RCA cleaning of slides and coverslips. DO THIS IN THE FUME HOOD.

a) To a 400 mL beaker, add stir bar, 250mL H2O, 50 mL Ammonium hydroxide (28%), add slides in slide holder, and then heat/stir until near boiling, using setting 5 for heat, about 5 for spinning. Then add 50 mL 30% hydrogen peroxide. Let clean for 1 hour, add a little water halfway through if necessary.

For coverslips, follow same protocol, but scale to a 250mL beaker, adding 125mL H2O, 25 mL Ammonium hydroxide (28%) and 25mL 30% hydrogen peroxide, following the protocol for the slides above.

Note, *while this has some similarities to a base type piranha wash, this IS NOT Piranha, it is much lower in concentration of reactive agents. Reaction should still be allowed to sit cooled, for full generation of* O_2 *before adding to waste jar.*

Alternatively, use a plasma cleaner, or KOH treatment to clean slides.

b) Let reaction beaker cool, then dump RCA into waste bottle, **do not tighten cap the whole way**.

c) Rinse the slides and coverslips twice with milliQ water.

d) Transfer slides to methanol, parafilm the top to prevent evaporation.

4. AminoSilanize the slides and coverslips –

a) For slides, prepare in a 400 mL beaker with stir bar 360mL methanol, 18 mL glacial Acetic Acid (5% final), allow to mix, and then add 3.6 mL amino-silane (1% final). After everything is mixed, transfer the slides from the methanol into the aminosilane solution. Let it go for 20 min. with stir bar at like 6 or 7 setting.

For coverslips in 250mL beaker, scale to 190mL MeOH, 9.5mL acetic acid, 1.9mL aminosilane.

b) Transfer slides back into methanol bath following 20min aminosilane reaction. They only need to sit in there for a minute or two.

c) Take the mPEG and biotinPEG out of the -20 freezer. They need to come up to room temperature before you weigh them out.

5. Remove a slide or coverslip from the methanol beaker and rinse both back and front thoroughly with milliQ water. Dry the slide off with tubing attached to air outlet on bench. Place rinsed slides in pipette tip boxes with milliQ H_2O in bottom as shown in **Figure A12.1a**.

6. After all slides are clean and ready to functionalize, prepare biotin-PEG/mPEG solutions:

a) Make a BiotinPEG stock solution at 6.25mg/mL in a 100mM NaHCO3 pH 8.5 solution. $NaHCO_3$ will be at 8.5, no need to adjust. ~20 µL stock is usually sufficient.

b) Make an mPEG solution to 250 mg/mL in a 100mM NaHCO3 pH 8.5 solution. ~400µL is usually sufficient.

c) Vortex the PEG solutions thoroughly. Then spin at 7500 RPM for 2 minutes in a tabletop micro-centrifuge to get rid of any of the bubbles.

d) For Slides, make an mPEG only solution by diluting from mPEG stock to a 125mg/mL solution. Use 100mM NaHCO3 pH 8.5 to dilute. Spot 70uL on to slide, then place second slide on top.

e) For coverslips, make a BiotinPEG:mPEG mix. May need to optimize with ratio depending upon how feature density in single molecule experiments. A 1:200 (125mg/mL mPEG, 0.625mg/mL biotinPEG) or 1:1000 (125 mg/mL mPEG, 0.125 mg/mL biotinPEG) ratio generally works. Spot 35 µL on to a coverslip, the place second coverslip on top.

f) Incubate slides and coverslip in coved pipette tip boxes in the dark for 3 hrs. Longer

incubations, i.e. overnight, also work.

7. After incubation, slowly pull the slides and coverslips apart, keeping track of PEGylated side. Use milliQ H_2O to rinse, dry with house air. Place double-stick tape on PEGylated side of slide to form channels from inlet to outlet port. Use razor to remove excess tape. Place coverslip with BiotinPEG/mPEG side facing tape. Press chamber to seal. This forms the slide/coverslip chamber. Place chamber in 50mL falcon tube,

8. Cut sections from 8'' food saver plastic roll that are long enough to fit falcon tubes. Use the Vacuum sealer to seal one end of each bag, place 50mL falcon tube containing a microscope chamber into the bag, then vacuum seal the other end and store in the -20°C freezer.

Assembly of Nano-port inlets and outlets for Slide-coverslip type chambers

1. To use chambers, remove vacuum sealed chambers from -20°C, and all chambers to warm to room temperature.

2. Cut open sealed bags and remove chambers from falcon tubes. Place N-333 Nanoport base with inset rubber O-ring over inlet ports (**Figure A12.1b**). Dispense and mix 5-minute epoxy. Use a p20 micropipette tip to apply epoxy to nanoport base, and along the edge of the coverslip. Wait for epoxy to harden.

3. Thread the 28 gauge Teflon tubing through F-247 nanotight sleeve, and thread sleeve through the N-333 nanoport top. Screw this assembly into the nanoport base (**Figure A12.1c**).

4) The other end of the 28 gauge Teflon tubing can be threaded over a syringe needle, and the syringe may now pull liquid through the chamber (**Figure A12.1c**). The example chamber has only one channel, but up to 4 channels may be easily placed on this chamber design.

a

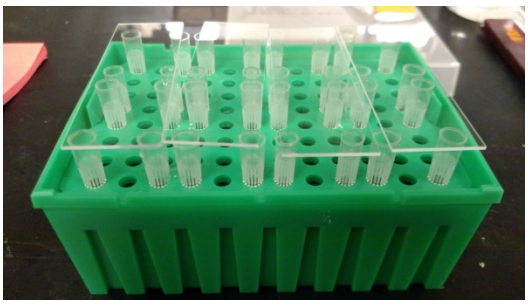

b

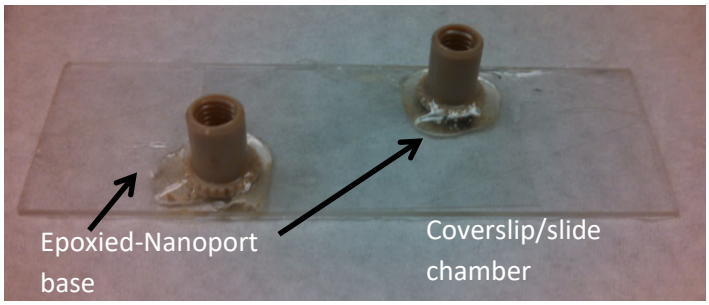

c

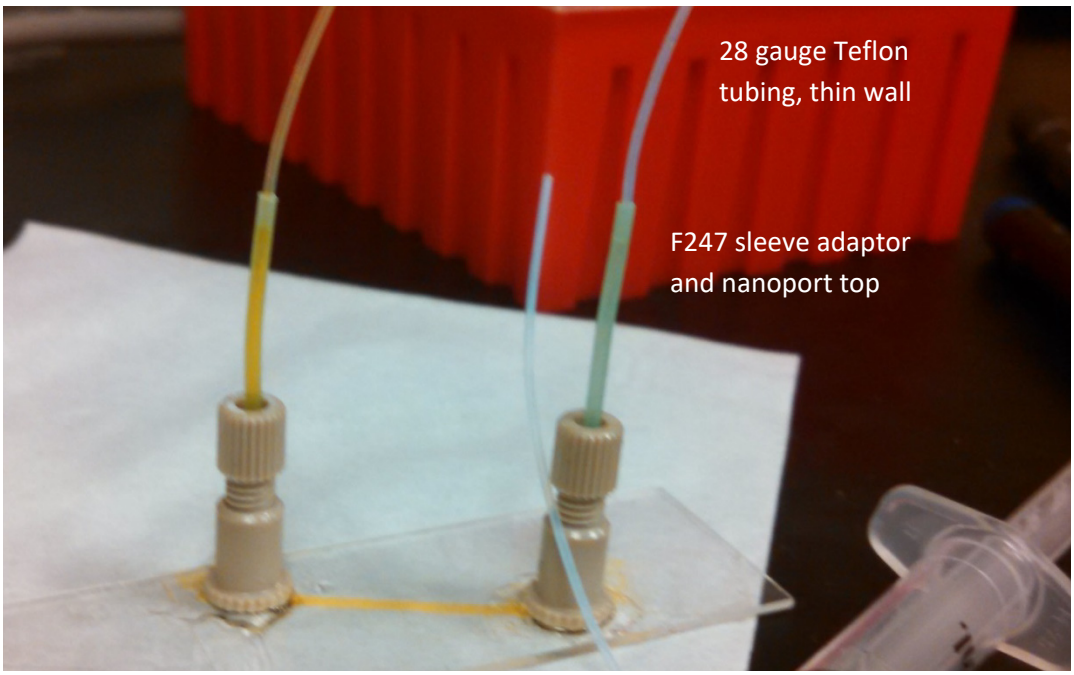

Figure A12.1. Assembly of slide/coverslip microscope sample chambers.
a. Pipette box setup for reacting aminosilane treated glass slides mPEG and biotinPEG/mPEG solutions.
b. Nanoport epoxied to slide/coverslip chamber assembly. Epoxy just gasket and port, without the Ferrule/Nut/tubing assembly. Also epoxy around coverslip, to seal the channel and chamber.
c. Assembled Nanoports. Note, threading nanoport presses in on ferrule on nut, locking tubing in place. Yellow food coloring is used to show channel. In practice device withstands flow rates up to 400uL/min, but for assays, 30ul/min-100uL/min range most used. Coverslip/slide assembly can accommodate multiple channels on a single device.

Appendix 13: Current (Spring 2017) setup and parts list for Berger Lab single molecule TIRF microscope

This appendix contains a parts list and cartoon schematic (**Figure A13.1**) for a fluorescence microscope setup designed to perform single molecule fluorescence localization and single molecule FRET experiments using objective-type total internal reflection fluorescence (TIRF) illumination.

Parts list:

Compass 315M 532nm solid state diode laser (Coherent)
Obis 640 LX 640nm solid state diode laser (Coherent)
Obis 488 100 LS 488 nm solid state diode laser (Coherent)
Olympus IX71 inverted microscope
Dual view optical splitter, Optosplit III, Cairn Research.
AC254-40-A, AC508-400A-ML, AC508-300A-ML achromatic focusing lenses, (Thorlabs)
3x 1in silver mirrors, (Thorlabs)
3x mounted achromatic half wave plate 400-800nm (AHWP05-600, Thorlabs)
1x mounted achromatic quarter wave plate 400-800nm (AQWP05M-600, Thorlabs)
3x Mechanical optical beam shutter, (SH1 Thorlabs)
2xT-cube Shutter Controller (TSC001, Thorlabs)
1x T-cube shutter Controller (KSC101, Thorlabs)
3x T-cube shutter AC adaptor (TPS001, Thorlabs)
4x 2in silver mirrors (Thorlabs)
3x 1 in mirror mounts (KS1, Thorlabs)
2x 2 in mirror mounts (KS2, Thorlabs,)
2x SM1-Threaded Kinematic Mount for Thin Ø1" Optics (KM100T, Thorlabs)
Mechanical Neutral Density Filter Wheel (FW102C, Thorlabs)
0.3, 0.6, 1.0, 2.0, 3.0 OD 25mm neutral density filters (NE03B-A, NE06B-A, NE10B-A, NE20B-A, NE30B-A Thorlabs)
3x Precision Cage Rotation Mount with Micrometer Drive, Ø1" Optics, 8-32 Tap for wave plates (CRM1P, Thorlabs)
3x Single Axis Translation Stage with Standard micrometer (PT1, Thorlabs)
25mm diameter 550 nm long-pass dichroic combining filter (ZT532rdc-UF2, Chroma)
25mm diameter 505 nm long-pass dichroic combining filter. (ZT488rdc, Chroma)
532/640 nm laser Dual Band emission and excitation optic set for TIRF applications, including excitation path filter cube and filters and dichroic mirrors for optical splitter emission path (TRF59907-EM-ET, Chroma)
488/532/640 nm laser custom emission and excitation optic set (zet405/488/532/642x, zet405/488/532/642m, zt405/488/532/642rpc-xt-uf2, ET510/20m short wave-pass, T550LPXR, Optosplit III emission dichroic. Chroma)
iXon Ultra EMCCD (Andor)
Dell Precision T7500

Objective extension tube, 12.5 mm, thread W0.8 x 1/36'' (P-721.90Q, Physik Instrumente)
ApoN 60xO TIRF objective (Olympus)
100x UPlanSApo Objective (Olympus)
MS-2000 Flattop XY Automated Stage for IX71/81 (Applied Scientific Instrumentation)
MS-2000-WK Multi-Axis Stage Controller (Applied Scientific Instrumentation)
PInano XYZ Piezo Stage and controller (P545.3R2, E545, Physik Instrumente)
Microscope Slide holder for PInano piezo stages (P-545.SH3, Physik Instrumente)
CRISP-780 Autofocus System (Applied Scientific Instrumentation)
Pump 11 Elite (Harvard Apparatus)
neMESYS Syringe Pump System (Cetoni)
Optical Table Isolator (Thorlabs, PFP52508 - 800 mm (31.5") SD Passive Frame, 1200 x 750 mm (4' x 2.5'))
MC 77-131-02 CleanTop Breadboard Optical Table 30 x 48 x 2 inch (Technical Manufacturing Corporation)
13U Smart Rack Open Frame rack (SR4POST13 Tripp Lite)
Custom optical table enclosure, 27'' x 24'' x 15'' (LxWxH) (Thorlabs)

Software:
Obis Connection (Coherent)
NIS Elements (Nikon)
Single (Ha laboratory)
PI Mikromove (Physik Instrumente)
Pump Terminal (Harvard Apparatus)
neMESYS User Interface (Cetoni)
ASI Console (Applied Scientific Instrumentation)
IDL (Harris Geospatial)
MATLAB (Mathworks)

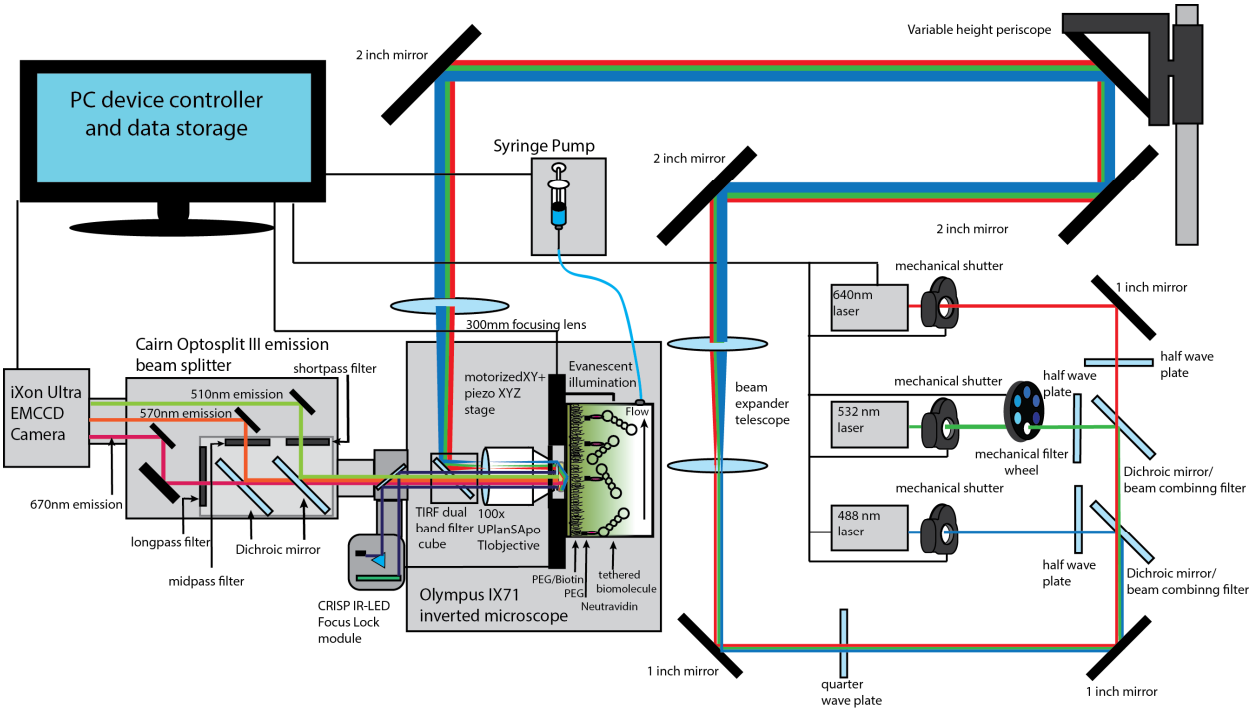

Figure A13.1. Schematic of the current microscope setup for performing single molecule experiments using TIRF illumination.

Excitation illumination at 488 nm (Coherent Obis 488 LS), 532nm (Coherent Compass 315M) and 640nm (Coherent Obis 640 LX) passes through a set of mechanical shutters and half wave plates and are combined using a pair of dichroic mirrors (Chroma, ZT532rdc-UF2, ZT488rdc). Circular polarization is introduced by a quarter wave-plate before the beams are expanded using a pair of achromatic lenses (Thorlabs, AC254-40-A and AC508-400A-ML). The beam-path is raised using a variable height periscope. A final mirror and achromatic lens (Thorlabs, AC508-300A-ML), mounted on a XY translational stage introduces the beam through the back port of an Olympus IX71 inverted microscope, and focuses the beam on the objective back focal plane (Olympus, 100x UPlanSApo). Translational of the achromatic lens allows movement from epifluorescence to TIR illumination. The microscope stage is equipped with a motorized XY (MS-2000, ASI) and piezo XYZ stage (PInano XYZ, Physik Instrumente) for translational movement and focusing of sample. Sample emission passes through an excitation and emission filter cube(either 532/640nm two color or 405/488/532/642 four color set) and fluorescent emission (i.e. from Alexa488/cy3/cy5 containing sample, 510nm, 570nm and 670nm emission) is split (Cairn Research, Optosplit III) into spatial distinct channels projected onto an EMCCD camera (Andor, iXon Ultra). Black lines denote equipment under PC/software control. The 488 nm and 640nm lasers intensity is controlled directly by the PC; 532nm laser intensity is controlled by a mechanical neutral density filter wheel.

Appendix 14: Determining common power and scale parameters for the Berger Lab single molecule TIRF microscope setup

This appendix explains how to determine a couple key parameters on our TIRF microscope setup, including:
1) The camera pixel to µm scale.
2) The illumination intensity on a coverslip immobilized sample.
3) Emission bleed-through between different fluorophore channels
4) Mapping between donor and acceptor channels for two color experiments.

Determining the camera pixel to µm scale

Materials
Microscope setup (Olympus IX71) with desired objective and Andor iXon Ultra EMCCD camera
Transmitted light (bright-field) illuminator (on microscope body, IX2-ILL 100, Olympus)
0.01 mm micrometer on 1x3'' slide (Fisher Scientific)
Immersion oil type F or type FF
ImageJ

Protocol
1) Place the emission path filter wheel on position 6 (brightfield/empty).
2) Apply immersion oil to objective, mount micrometer slide on stage.
3) Make sure camera is not in emission path (i.e. light-path selection lever is turned to the eyepiece). Turn on camera and allow it to cool to working temperature (~-75°C). Since imaging will be in bright-field, make sure EM gain is low/off, otherwise, camera will be damaged.
4) Turn bright-field/transmitted light illuminator. Adjust illumination with diaphragm. Find the micrometer markings and focus on micrometer slide surface. The stage may need to be moved to center on the micrometer. Finding the scale may be done either using the eyepiece, or with the camera. Turning off the lights in the room may help.
5) Once focused turn the light-path selection lever to the camera, and take an image of the slide surface, using a program like NIS Elements (or any program with drivers for the camera) (**Figure A14.1**). Do this both with, and without the 1.6x emission path magnifying lens. Save image as a TIF.
6) Repeat steps 2-5 for any additional objectives or emission path setups you wish to calibrate.
7) Open the saved TIF in ImageJ. Use the straight segment tool to draw a line along the micrometer ruler. The more tick marks covered by the segment, the more accurate the scaling conversion will be.
8) Under the **Analyze** drop down menu, click **Set scale**. "*Distance in pixels"* will be populated by the length of the line drawn in step 7. Each tick mark is 10 µm. Enter the *Known distance* of your line and enter the unit of length (i.e. µm). This will give you a pixel to distance ratio. You can now add a scale bar in ImageJ under the **Analyze** drop down menu, pick **Tools** and **Scale Bar**.

Determining the illumination intensity applied to a coverslip surface in TIR

Materials

Microscope setup (Olympus IX71) with desired objective and Andor iXon Ultra EMCCD camera, and associated excitation lasers (Coherent)
OD filter wheel (green laser) or Coherent OBIS Connection software to control blue/red laser
Power Meter PM100D and Photodiode Power Sensor, PM100D (Thorlabs)
Immersion oil type F or type FF
1'' x 3'' x1mm slide and 24 mm x 40 mm-1.5 coverslips
Fluorescent sample, i.e. FluoSpheres from ThermoFisher Scientific
Optosplit III
ImageJ

Protocol

1) Make sure the eyepiece of the microscope is blocked, and make sure all cameras are off/shuttered, and out of line of the emission path. Power on the lasers to be calibrated. Place the desired TIRF objective inline on the excitation path. Switch the filter wheel to a cube containing the correct excitation and emission filters (i.e. the two color FRET cube in position 5 or the three color fluorescence localization cube in position 4).

2) Shift the TIR lens in the laser path to the center of the back light port (horizontal translation stage at 4.61. Horizontal translation is at ~6.23 when beam is in TIR). The laser line should go directly through the objective, creating a spot on the ceiling. Use a power meter and photodiode sensor to measure the power of beam emitted from objective. Set the meter to measure at 532nm for the green laser and 635 nm for the red laser respectively. Measure the beam power for a range of different OD filter or power settings for each laser.

Note, the following steps (3-8) can also be done with a feature free surface using the background bleed-through of the laser, but I find the whole process is easier to do using fluorescent features.

3) Close the shutter on the microscope filter wheel. Prepare a fluorescent substrate (i.e. FluoSpheres, but in the example here I used biotinylated DNA bound to a PEG/neutravidin surface and stained with SYTOX Orange). Apply immersion oil to the objective, mount sample on the microscope stage. Turn on the Andor iXon Ultra EMCCD camera and allow the CCD chip to cool to working temperature (-75°C). Shift the final focusing lens back into TIR. Open the filter wheel shutter and raise the objective to focus on the coverslip surface. Look for the appearance of the reflected laser spot on the final 2-inch mirror in the excitation path as a sign that TIR has been achieved and the surface is in focus.

4) Turn off the room lights, and switch the emission path inline to the camera. Make any other fine adjustments to focus on the coverslip surface, and make sure you can see clear fluorescent features. Make sure the field of view contains the entire visible laser spot (see **Figure A14.2** for

an example). This will likely require modifying the emission path settings in the Optosplit III. This may require a combination of:

a) blocking the split image channels that do not correspond to the emission of the fluorescent specimen.

b) increasing the image size on the camera CCD with the aperture levers on the Optosplit. These are on the port where the emission path enters the Optosplit.

c) Changing the position of the image using the split control, V1, V2/H2, or V3/H3 adjusters.

5) Save an image (or better a series of different images) of this field of view as a TIF.

6) Using Image J and the scale calibration from "**Determining the camera pixel to µm scale**" to estimate the area of illumination. A rough estimate can be made by measuring the distance across the area of illumination, using the most distant identifiable fluorescent features from the center of the spot to define the edge of the laser spot. Then, use this diameter to determine the area of illumination, assuming a circular field of illumination:

$$A = 2\pi r^2$$

Where A is area in μm^2, and r is the radius of illumination determined in µm from the measured diameter.

7) For a more systematic and reproducible determination of the area of illumination, it is necessary to model illumination as a Gaussian function with respect to the pixel position or distance across the image. There are some imageJ plugins to do this sort of thing, but one can also use the **rectangle** or **segment** tool in ImageJ to define an area of interest, and then use **analyze** and **plot profile** to generate an intensity plot as a function of position. Doing this for an image which is the average of a number of fields of view will generate a smoother Gaussian curve. Fit the profile to:

$$I = k + ae^{-(x-b)^2/(2c^2)}$$

Where **I** is the measured intensity, **k** is background, **a** is the peak of the Gaussian curve, **b** is the peak center, and **c** is the standard deviation/width of the curve. From this fit the "full width half maximum" (FWHM) and "full width tenth maximum" (FWTM) may be estimated as 2.35**c** and 4.29**c** respectively. Note that estimating the diameter of illumination by eye generally agrees with the FWTM diameter. The area may then be used to estimate the intensity applied to a specimen at different intensities, as shown in **Table A14.1**.

Determining emission fluorescence leakage between spectral channels

Materials

Microscope setup (Olympus IX71) with desired objective and Andor iXon Ultra EMCCD camera, and associated excitation lasers (Coherent)
Immersion oil type F or type FF
1'' x 3'' x1mm slide and 24 mm x 40 mm-1.5 coverslips
Fluorescent sample, i.e. FluoSpheres from ThermoFisher Scientific
Correct filter cube (i.e. the two color FRET cube in position 5 or the three color fluorescence localization cube in position 4)
Optosplit III with properly aligned spectral emission channels and all filters in place.
ImageJ

Protocol

1) Make sure the eyepiece of the microscope is blocked, and make sure all cameras are off/shuttered, and out of line of the emission path. Power on the excitation lasers for the spectral channel to be tested. Place the desired TIRF objective inline on the excitation path. Switch the filter wheel to a cube containing the correct excitation and emission filters for the experiment type in question (i.e. the two color FRET cube in position 5 or the three color fluorescence localization cube in position 4). Make sure the emission path, in particular the Optosplit III, has every dichroic and filter inline that would be present in a single molecule experiment.

2) Prepare a fluorescent substrate (i.e. FluoSpheres, but in the example here I used biotinylated DNA bound to a PEG/neutravidin surface and stained with SYTOX Orange). Apply immersion oil to the objective, mount sample on the microscope stage. Shift the final focusing lens into TIR. Turn on the Andor iXon Ultra EMCCD camera and allow the CCD chip to cool to working temperature (-75°C). Open the filter wheel shutter and raise the objective to focus on the coverslip surface. Look for the appearance of the reflected laser spot on the final 2-inch mirror in the excitation path as a sign that TIR has been achieved and the surface is in focus.

4) Turn of the room lights, and switch the emission path inline to the Optosplit III and camera. Make any other fine adjustments to focus on the coverslip surface, and make sure you can see clear fluorescent features in the correct channel (in the current example, green laser excitation, SYTOX Orange emission). Collect an image where all features in the excited channel are in the linear range of the CCD camera, and where leakage into a second channel (in the current example the red laser emission channel) is visible.

5) Save an image of this field of view as a TIF.

6) Leakage between channels may be quantified in a number of ways.

a) An automatic spot picking program may be used to pick spots and correlate intensities in separate channels.

b) If leakage is low (as is the case for our green laser emission and red laser emission channel) correlated spots may need to be picked manual. This can be done in imageJ using the **rectangle tool** and either measuring maximum or mean intensity in a defined box for the spot and bleed through. An example is shown in **Figure A14.3**. The slope of the linear relation corresponds to leakage.

c) Alternative to step 6b, the **rectangle tool** may be used to define slices of each emission channel which correspond to the same surface. **Plot profile** may then be used to output intensity as a function of distance along the slice. The multiplicative factor of a linear scaling transformation which relates both plots corresponds to the leakage.

By this method, fluorescent leakage into the red laser emission channel from the green laser emission channel on our setup is ~ 3.75%. This is with the FRET filter wheel cube and two-color Optosplit III filters in line. This may change for the 3-color filter wheel cube and 3-color Optosplit III filters.

Mapping between donor and acceptor channels for two color experiments

Materials

Microscope setup (Olympus IX71) with desired objective and Andor iXon Ultra EMCCD camera, and associated excitation lasers (Coherent)
Immersion oil type F or type FF
1'' x 3'' x1mm slide and 24 mm x 40 mm-1.5 coverslips
Multi-labeled fluorescent sample, i.e. TetraSpeck Microspheres (ThermoFisher Scientific)
Correct filter cube (i.e. the two color FRET cube in position 5 or the three color fluorescence localization cube in position 4)
Optosplit III with properly aligned spectral emission channels and all filters in place.
Single and IDL scripts from (https://cplc.illinois.edu/software/) and IDL software

Protocol

1) Prepare the sample for visualization on the microscope as described in steps 1-4 in the **Determining emission fluorescence leakage between spectral channels** protocol. The sample must fluoresce brightly in all channels that need to be spatially correlated; otherwise the automated spot picking will not work correctly. A number of substrates may be used for this, including TetraSpeck Microspheres (ThermoFisher Scientific), a biotinylated DNA substrate containing multiple fluorophores of different wavelengths, or biotinylated long DNAs, stained with different emission wavelength dyes.

2) Use **Single** from https://cplc.illinois.edu/software/ to drive the Andor camera. Section 3 of the Single reference manual that comes with the program provides good documentation. A couple of additional hints:

a) make sure to open Single as an **administrator**, otherwise the camera will not run.
b) for downstream processing, make sure "Rotate -90°C is clicked in the Camera Configuration window which appears when **Camera** is selected from the **Devices** menu.
c) Our camera is different from the example given in the manual. We have 512 x 512 pixel resolution, pixel size is 16 µm x 16 µm, and Bit Depth is 16 bit per pixel.

3) Collect a .pma file (there are the movie files produced by **Single**, and are one long string of pixel data. They require downstream IDL scripts to be read) that is
a) at least 12 frames long,
b) has at least 16 paired features
c) has a good distribution of spots across the field of view,
d) has few or no overlapping spots, and
e) has similar spot intensity in the channels to be mapped.

Note that the downstream processing will exclude spots that overlap and will not pick spots if they are not bright enough compared to the background.

4) Use IDL (Interactive Data Language, Harris Geospatial) and scripts from https://cplc.illinois.edu/software/ to generate mapping function between two emission channels. We run IDL using a floating license setup, as a current user in the lab for details. The scripts expect all camera pixels where 1<x<256 to be the donor channel and 257<x<512 to be the acceptor channel. The **IDL scripts for PMA file analysis** document that comes with the scripts gives a good explanation of how the scripts work, as well as the workflow. In brief:
a) the script *maketiff* is used to generate a .tif image from the selected .pma file.
b) the script *calc_mapping2* uses the .tif from step (a) to allow the user to pick 3 correlated spots, which creates a .coeff file which is a linear transformation between the two emission channels
c) the script *nxgn1_cm* picks peaks from the .tif file generated by *maketiff*, and the uses the linear transformation generated by *calc_mapping2* to pair peaks. If more than 16 paired peaks are found, *nxgn1_cm* creates a .map file which contains a 2D polynomial mapping between the two channels.
d) This mapping function may then be used to correlate spots and generate multi-color trace files using the *ana_all* script. **Note**, as written, *ana_all* **requires the map file** generated in part (c) to **have the following directory location and name**:
C:\user\tir data\rough.map
If you want to modify this, change line 195 in the script *p_nxgn1_ffp*

From experience, the mapping between channels may drift over time. I have added a line after line 351 in the *p_nxgn1_ffp* script to save a .tif of the overlaid channels:
WRITE_TIFF, run + "_combined.tif", temp4, 1, RED = R_ORIG, GREEN = G_ORIG, BLUE = B_ORIG

This is useful for accessing whether mapping has drifted while processing data. **Figure A14.4** shows an example, where an incorrect mapping function may be distinguished from a correct mapping function due to elongation of the spots.
Note, that the scripts in this workflow are specific to two channel data collection and would need to be heavily modified to map between three channels. Additionally, the spot picking algorithm in the *p_nxgn1_ffp* script uses spot intensity in both channels. The script therefore requires modification for fluorescence localization experiments (LM Nevin, personal communication).

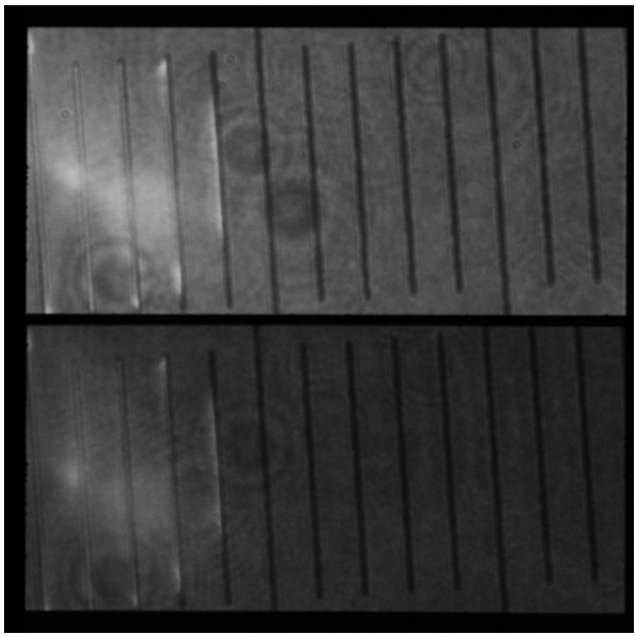

Figure A14.1. 0.01 mm micrometer slide imaged by bright-field illumination with a 60x TIRF objective and Cairns Optosplit III emission path on an Andor iXon Ultra EMCCD camera.
Example field of view of imaged micrometer slide for scale calibration. Optosplit III path is setup for cy3 emission (top) and cy5 emission (bottom).

a.

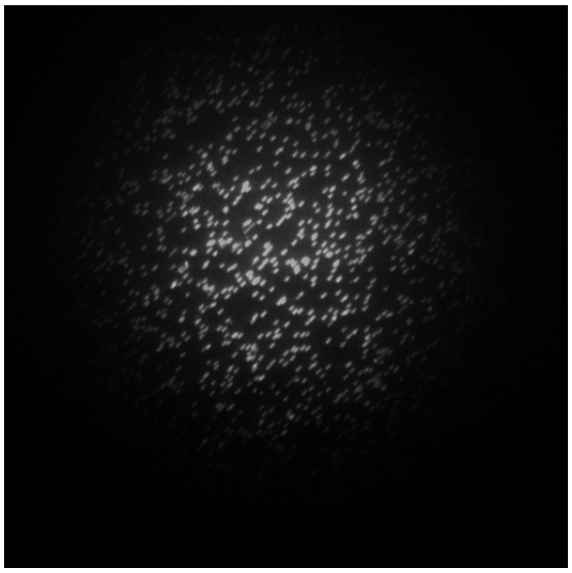

b.

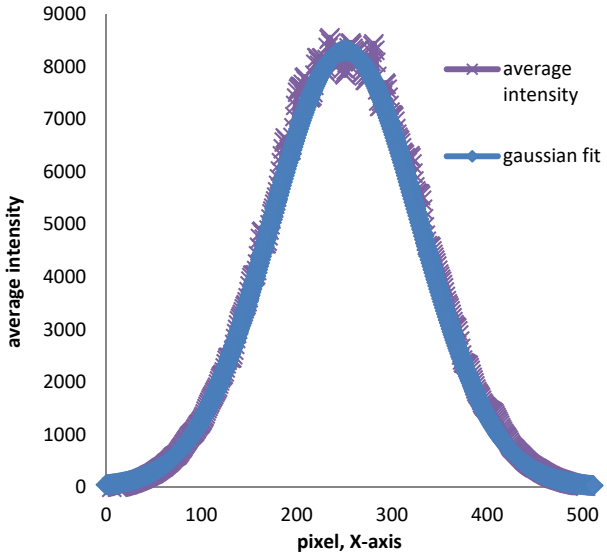

Figure A14.2. Determining laser spot size on the EMCCD camera.
a. A field of view of biotinylated plasmids tethered to a neutravidin functionalized coverslip. Plasmids are stained with SYTOX Orange and illuminated at 532nm. This image was used to measure the laser spot size.
b. Average pixel intensity over a number of fields of view as a function of X-axis pixel position. The pixel intensity is fit to a Gaussian curve.

a.

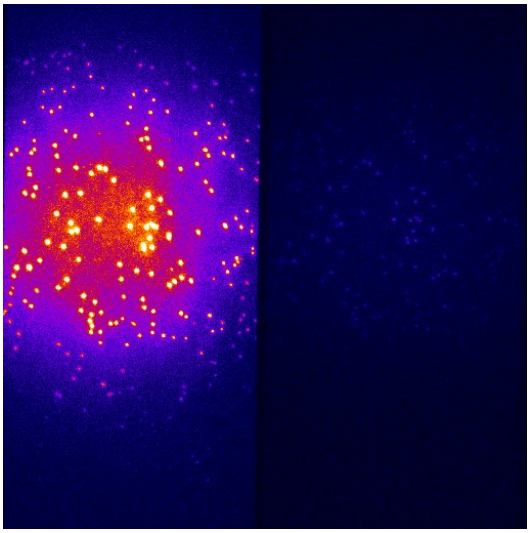

b.

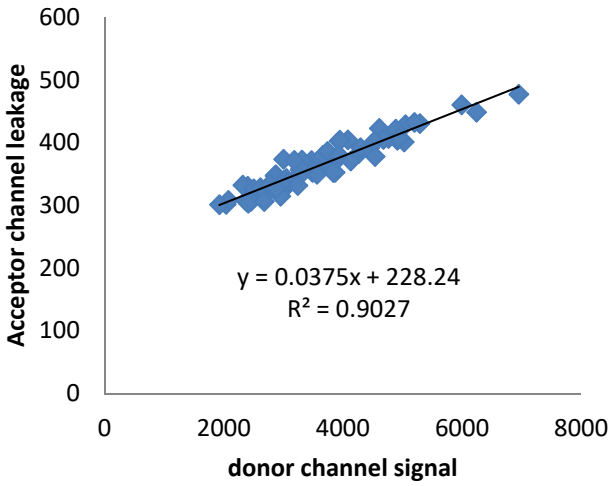

Figure A14.3. Determining donor channel leakage into the acceptor channel
a. A field of view of biotinylated plasmids tethered to a neutravidin functionalized coverslip. Plasmids are stained with SYTOX Orange and illuminated at 532nm. This image was used to calibrate leakage from the donor emission channel (532 nm excitation, 555-615nm emission) to the acceptor donor emission channel (640nm excitation, 660-700nm emission)
b. Mean intensity of selected paired features between donor and acceptor channel.

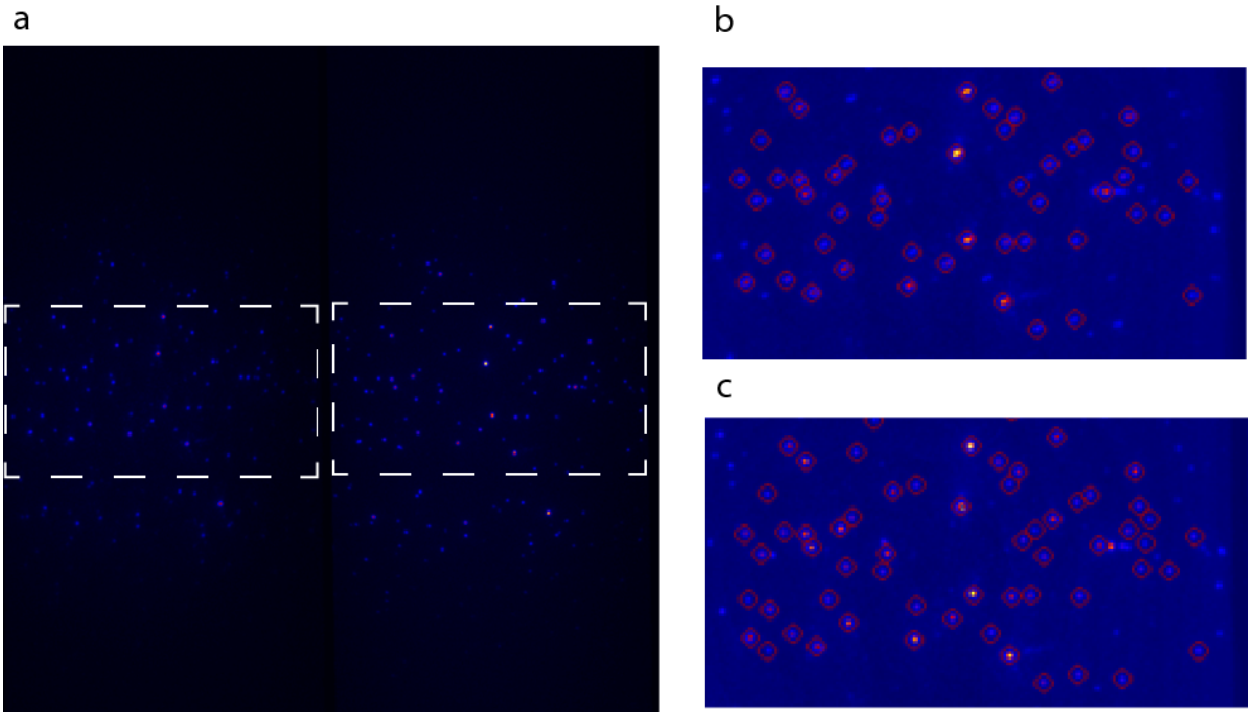

Figure A14.4. Evaluating channel mapping for a two color experiment
a. A field of view of biotinylated plasmids preincubated with yeast topo II labeled with Alexa555 and Alexa647 on the ATP gate. The topo II/plasmid complex is bound a neutravidin functionalized coverslip and illuminated at 532nm. Boxed areas are analyzed for channel mapping. Panel **b** shows channel overlay with an incorrect mapping function. Panel **c** shows overlay results with proper mapping.

Table A14.1. Comparison of laser power settings to laser power and intensity applied to coverslip surfaces on TIRF microscope.

Laser line(nm)	Setting	Power(mW) from objective	Power/area(W/mm^2)	kW/cm^2
532	0 OD	46	6.390	63.9
532	0.3 OD	22.2	3.084	30.84
532	0.6 OD	9.6	1.334	13.34
532	1 OD	3.75	0.521	5.21
532	2 OD	0.65	0.090	0.9
532	3 OD	0.027	0.004	0.04
640	80mW	28	3.889	38.9
640	40mW	12.2	1.695	17.0
640	20mW	6.6	0.917	9.17
640	10mW	3.2	0.445	4.45
640	5mW	1.54	0.214	2.14
640	2.5mW	0.78	0.108	1.08

*Intensities based on an area of illumination defined of ~7200µm^2.

*Intensities commonly cited in the literature for single molecule experiments range from 0.5-2 kW/cm^2.